
Electronic Thesis and Dissertation Repository

10-23-2012 12:00 AM

Calcium Phosphate-Based Resorbable Biomaterials for Bone Regeneration

Daniel O. Costa
The University of Western Ontario


Supervisor

Dr. Amin S. Rizkalla
The University of Western Ontario Joint Supervisor

Dr. S. Jeffrey Dixon
The University of Western Ontario

Graduate Program in Chemical and Biochemical Engineering
A thesis submitted in partial fulfillment of the requirements for the degree in Doctor of Philosophy

© Daniel O. Costa 2012
Follow this and additional works at: <https://ir.lib.uwo.ca/etd>

 Part of the [Biochemical and Biomolecular Engineering Commons](#), [Biological Engineering Commons](#), [Biology and Biomimetic Materials Commons](#), [Biomaterials Commons](#), [Biomedical Devices and Instrumentation Commons](#), [Ceramic Materials Commons](#), [Molecular, Cellular, and Tissue Engineering Commons](#), [Other Chemical Engineering Commons](#), [Other Engineering Science and Materials Commons](#), and the [Polymer and Organic Materials Commons](#)

Recommended Citation

Costa, Daniel O., "Calcium Phosphate-Based Resorbable Biomaterials for Bone Regeneration" (2012). *Electronic Thesis and Dissertation Repository*. 924.
<https://ir.lib.uwo.ca/etd/924>

This Dissertation/Thesis is brought to you for free and open access by Scholarship@Western. It has been accepted for inclusion in Electronic Thesis and Dissertation Repository by an authorized administrator of Scholarship@Western. For more information, please contact wlsadmin@uwo.ca.

CALCIUM PHOSPHATE-BASED RESORBABLE BIOMATERIALS FOR BONE
REGENERATION

(Spine title: Calcium Phosphate-Based Biomaterials for Bone Regeneration)

(Thesis format: Integrated-Article)

by

Daniel O. Costa

Graduate Program in Chemical and Biochemical Engineering

A thesis submitted in partial fulfillment
of the requirements for the degree of
Doctor of Philosophy

The School of Graduate and Postdoctoral Studies
The University of Western Ontario
London, Ontario, Canada

© Daniel O. Costa 2012

THE UNIVERSITY OF WESTERN ONTARIO
SCHOOL OF GRADUATE AND POSTDOCTORAL STUDIES

CERTIFICATE OF EXAMINATION

Supervisor

Dr. Amin Rizkalla

Joint Supervisor

Dr. S. Jeffrey Dixon

Supervisory Committee

Dr. Douglas Hamilton

Dr. Kibret Mequanint

Dr. Graeme Hunter

Examiners

Dr. Sean Peel

Dr. Peter Canham

Dr. Paul Charpentier

Dr. Lars Rehmann

The thesis by

Daniel O. Costa

entitled:

**Calcium Phosphate-Based Resorbable Composite Biomaterials for Bone
Regeneration**

is accepted in partial fulfillment of the
requirements for the degree of
Doctor of Philosophy

Date _____

Chair of the Thesis Examination Board

ABSTRACT

Bone defects are a prevalent problem in orthopedics and dentistry. Calcium phosphate-based coatings and nanocomposites offer unique solutions towards producing scaffolds with suitable physical, mechanical and biological properties for bone regeneration.

We developed a novel method to synthesize hydroxyapatite (HA) particles with high aspect ratio using sol-gel chemistry and hydrothermal treatment. We obtained tunable pure-phase carbonated-HA in the form of micro/nanorods and nanowires (diameters 25-800 nm). To mimic the structure of bone, HA nanowires were homogeneously mixed within poly(ϵ -caprolactone) (PCL) to produce nanocomposites with improved mechanical properties as determined by uniaxial tensile testing.

Surface chemistry and topography of biomaterials play prominent roles in regulating cell adhesion and differentiation. Bone-like apatite coatings, produced by incubating materials in a simulated body fluid (SBF), improve the osteoconductivity of scaffold materials. However, few studies have controlled the surface topography of biomimetic HA. We assessed the effect of SBF ion concentration and soaking time on the surface properties of apatite coatings. Calcium phosphates such as carbonated-HA with similar chemical composition and stiffness were deposited onto PCL films. Characterization of these coatings revealed an increase in topographical complexity and surface roughness with increasing ion concentration of SBF and soaking time.

To investigate their potential application in bone regeneration, we studied the influence of topography of biomimetic HA coatings on the behavior of osteoblasts and osteoclasts *in vitro*. Osteoblast attachment and differentiation were significantly greater

when cultured on rougher HA surfaces ($R_a \sim 2 \mu\text{m}$) than on smoother topographies ($R_a \sim 1 \mu\text{m}$). In contrast, activity of tartrate-resistant acid phosphatase (an osteoclast marker) was greater on smoother than on rougher HA surfaces. Furthermore, osteoclastic resorption lacunae were found exclusively on smoother HA coatings. Inhibition of resorption on rougher HA surfaces was associated with disruption of filamentous actin sealing zones. In conclusion, HA coatings can be prepared with different topographies, which regulate responses of osteoblasts and osteoclasts.

Thus, it may be possible to design HA-polymer composites and HA-coated polymers with physical, mechanical and biological properties suitable for tissue engineering. By modulating topography, rates of bone formation and biodegradation could be tailored for specific applications in orthopedics and dentistry.

KEYWORDS: bone regeneration; tissue engineering; hydroxyapatite; polycaprolactone; calcium phosphate; coatings; nanowires; nanorods; composite; biomaterial; osteoblast; osteoclast; surface topography; roughness;

CO-AUTHORSHIP STATEMENT

Chapter 1 entitled “Introduction” was written by D. O. Costa, with suggestions from A. S. Rizkalla, and S. J. Dixon. Sections 1.1, 1.2.1, 1.2.2, 1.3.1, 1.3.2, 1.3.3.1 are adapted from Allo, B. A., Costa, D. O., Dixon, S. J., Mequanint, K., and Rizkalla, A. S. (2012) *Journal of Functional Biomaterials* 3: 432-463, and reproduced here with permission from MDPI Publishing (see Appendix A). The publication was written by B. A. Allo, D. O. Costa, S. J. Dixon, K. Mequanint, and A. S. Rizkalla. B.A. Allo and D. O. Costa are co-first authors.

Chapter 2 entitled “One- and Three-Dimensional Growth of Hydroxyapatite Nanowires during Sol-Gel-Hydrothermal Synthesis” is adapted from Costa D. O., Dixon, S. J., and Rizkalla, A. S. (2012) *Acs Applied Materials & Interfaces* 4: 1490-1499, and reproduced here with permission from the American Chemical Society (see Appendix B). The publication was written by D. O. Costa, S. J. Dixon, and A. S. Rizkalla. All experiments were performed by D. O. Costa, and carried out in the laboratory of Dr. A. S. Rizkalla.

Chapter 3 entitled “Control of Surface Topography in Biomimetic Calcium Phosphate Coatings” is adapted from Costa, D. O., Allo, B. A., Klassen, R., Hutter, J. L., Dixon, S. J., and Rizkalla, A. S. (2012) *Langmuir* 28: 3871-3880, and reproduced here with permission from American Chemical Society (see Appendix C). The publication was written by D. O. Costa, S. J. Dixon and A. S. Rizkalla with suggestions from B. A. Allo. Dr. R. Klassen performed the nanoindentation experiments shown in Figure 3.5. Dr. J. L. Hutter conducted the atomic force microscopy measurements, shown in Figure

3.6, with assistance and analysis from D. O. Costa. All other experiments were performed by D. O. Costa, and carried out in the laboratory of Dr. A. S. Rizkalla.

Chapter 4 entitled “Surface Topography of Biomimetic Hydroxyapatite Coatings Differentially Regulates Osteoblast and Osteoclast Activity” was written by D. O. Costa and adopted from a submitted manuscript by Costa, D. O., Prowse, P. H. D., Chrones, T., Sims S. M., Hamilton, D. W., Rizkalla, A. S, and Dixon, S. J. The manuscript was written by D. O. Costa, A. S. Rizkalla, and S. J. Dixon with suggestions from P. D. H. Prowse, D. W. Hamilton and S. M. Sims. T. Chrones isolated osteoclasts from neonatal rabbits, and rat osteoblast isolation was conducted by P. D. H. Prowse and D. W. Hamilton with assistance from D. O. Costa. All experiments were performed by D. O. Costa, with the assistance of P. D. H Prowse (*in vitro* osteoblast experiments). Experiments were carried out in the laboratories of Dr. A. S. Rizkalla, Dr. D. W. Hamilton and Dr. S. J. Dixon.

ACKNOWLEDGEMENTS

I would like to thank Dr. Amin S. Rizkalla and Dr. S. Jeffrey Dixon for giving me the opportunity to work in their laboratory on these challenging research projects. I appreciate all the time and effort put towards my articles and thesis, and for all the valuable skills you have helped me develop.

Daniel O. Costa is supported in part by the Joint Motion Program – A CIHR Training Program in Musculoskeletal Health Research and Leadership. These studies were funded by the Natural Sciences and Engineering Research Council of Canada (NSERC) and the Canadian Institutes of Health Research (CIHR). Poly(ϵ -caprolactone) was generously donated by Solvay Chemicals Inc. SEM micrographs were taken by Dr. Todd Simpson and Tim Goldhawk of the Western Nanofabrication Facility. I would like to thank Dr. Alexey Pereverzev for expert technical assistance with adenovirus transduction studies, Tom Chrones for assistance with confocal microscopy and osteoclast isolations, and Barry Lai for helping with the quantification of focal adhesions. I would like to thank Dr. Douglas Hamilton, and Dr. Stephen Sims for their helpful advice and for generously allowing me to work in their laboratories.

Throughout my graduate studies, I had the pleasure to meet and work with several wonderful people. I would like to thank Paul Prowse, Deepta Srinath, Stephanie Grenier, Shaila, Bedilu Allo, Selma Saadaldin, Christopher Elliott, and Shawna Kim for valuable advice, stimulating discussion, and most of all, for their friendship.

I would like to thank Joey (Jonathan) Kim, Amy Robinson and Chris Troup for their much appreciated company. A special acknowledgement to my brother Filipe, hometown friends, and family – in particular, Claudio, Sergio, Mark, Chris, Andrew,

Jonathan, Simon, Mike, Marco, Pedro, the Galego family, the Oliveira family, and each of my grandparents.

Finally, I would like to extend my gratitude and sincere appreciation to my Mom and Dad, who have always given me unconditional support, love and the opportunity to do achieve everything.

TABLE OF CONTENTS

	Page
CERTIFICATE OF EXAMINATION	ii
ABSTRACT.....	iii
CO-AUTHORSHIP STATEMENT.....	v
ACKNOWLEDGEMENTS.....	vii
TABLE OF CONTENTS.....	ix
LIST OF TABLES.....	xiv
LIST OF FIGURES	xv
LIST OF APPENDICES.....	xvii
LIST OF ABBREVIATIONS.....	xviii
CHAPTER ONE - INTRODUCTION.....	1
1.1 Bone Tissue Regeneration	2
1.2 Regenerative Medicine	2
1.2.1 Autografts and Allografts.....	2
1.2.2 Scaffold-based Tissue Engineering.....	3
1.3 Bone Physiology	5
1.3.1 Structure and Composition.....	5
1.3.2 Bone Remodeling.....	7
1.4 Synthetic Biomaterials	11
1.4.1 Biocompatible and Biodegradable Polymers	11
1.4.2 Calcium Phosphate.....	14
1.4.3 Nanocomposites	21
1.5 Osteoblasts and their Interactions with Biomaterials.....	25
1.5.1 Origin and Differentiation of Osteoblasts	25
1.5.2 Adhesion and Morphology of Osteoblasts	27
1.5.3 Bone Formation.....	28
1.5.4 Interactions of Osteoblasts with Biomaterials.....	30

1.6	Osteoclasts and their Interaction with Biomaterials	34
1.6.1	Origin and Differentiation of Osteoclasts	34
1.6.2	Adhesion and Morphology of Osteoclasts	36
1.6.3	Bone Resorption	38
1.6.4	Interaction with Biomaterials	40
1.7	Rationale, Objectives and Hypotheses of the Research.....	42
1.7.1	Synthesis of High-Aspect Ratio Hydroxyapatite Nanowires and Fabrication of Hydroxyapatite/Polycaprolactone Composites	43
1.7.2	Control of Surface Topography in Biomimetic Calcium Phosphate Coatings	45
1.7.3	Surface Topography of Biomimetic Hydroxyapatite Coatings Differentially Regulates Osteoblast and Osteoclast Activity.....	46
1.8	References.....	49

CHAPTER TWO - ONE- AND THREE-DIMENSIONAL GROWTH OF HYDROXYAPATITE NANOWIRES DURING SOL-GEL-HYDROTHERMAL SYNTHESIS		64
2.1	Chapter Summary	65
2.2	Introduction.....	66
2.3	Materials and Methods.....	68
2.3.1	Materials.....	68
2.3.2	Preparation of dried Calcium Phosphate (CaP) Gel.....	68
2.3.3	Hydrothermal Treatment.....	69
2.3.4	Scanning Electron Microscopy (SEM) and Energy Dispersive X-ray Spectroscopy (EDX).....	70
2.3.5	X-ray Diffraction Analysis (XRD).....	70
2.3.6	Fourier Transform Infrared Spectroscopy (FTIR).....	70
2.3.7	Preparation of PCL and PCL/HA Composites	71
2.3.8	Mechanical Testing of PCL/HA Composites.....	71
2.4	Results.....	72
2.4.1	FTIR, XRD, and SEM Analysis of CaP Gel.....	72

2.4.2	SEM Analysis of Powders Produced by Hydrothermal Treatment.....	75
2.4.3	XRD Analysis of Nanoparticles Produced by Hydrothermal Treatment	83
2.4.4	FTIR Characterization of Nanoparticles Produced by Hydrothermal Treatment.....	85
2.4.5	EDX Elemental Analysis of Nanoparticles Produced by Hydrothermal Treatment.....	86
2.4.6	Characterization of PCL/HA Composites	88
2.5	Discussion	94
2.6	References.....	100

CHAPTER THREE - CONTROL OF SURFACE TOPOGRAPHY IN BIOMIMETIC CALCIUM PHOSPHATE COATINGS.....

3.1	Chapter Summary	104
3.2	Introduction.....	105
3.3	Materials and Methods.....	107
3.3.1	Polycaprolactone (PCL) Film Fabrication and Functionalization.....	107
3.3.2	Preparation of Modified Simulated Body Fluid (SBF) Solutions	107
3.3.3	Biomimetic Coating Process	108
3.3.4	Physical and Chemical Characterization of CaP Coatings.....	109
3.3.5	Young's Modulus (E_s) of CaP Coatings.....	110
3.3.6	Surface Roughness	111
3.4	Results.....	111
3.4.1	Characterization of Coating Morphology by SEM	111
3.4.2	XRD of CaP coatings	116
3.4.3	FTIR of CaP coatings.....	119
3.4.4	EDX elemental analysis of CaP coatings	121
3.4.5	Mechanical properties of CaP coatings	123
3.4.6	AFM imaging and surface roughness of CaP coatings	125
3.5	Discussion	128
3.6	References.....	135

CHAPTER FOUR - SURFACE TOPOGRAPHY OF BIOMIMETIC HYDROXYAPATITE COATINGS DIFFERENTIALLY REGULATES OSTEOBLAST AND OSTEOCLAST ACTIVITY	140
4.1 Chapter Summary	141
4.2 Introduction.....	142
4.3 Materials and Methods.....	144
4.3.1 Biomimetic HA coating process.....	144
4.3.2 Osteoblast isolation and culture	146
4.3.3 Osteoblast attachment and morphology	147
4.3.4 Osteoblast differentiation and quantitative assessment of osteoblast marker gene expression	148
4.3.5 Osteoclast isolation and culture.....	149
4.3.6 Tartrate-resistant acid phosphatase (TRAP) activity.....	150
4.3.7 Resorption Activity	151
4.3.8 Fluorescence microscopy	151
4.4 Results.....	153
4.4.1 Control of surface topography of biomimetic hydroxyapatite coatings.....	153
4.4.2 Effect of HA surface topography on osteoblast attachment, spreading and focal adhesion formation.....	156
4.4.3 Effect of HA surface topography on markers of osteoblast differentiation	158
4.4.4 Effect of HA surface topography on osteoclasts as revealed by staining for tartrate-resistant acid phosphatase (TRAP) activity	161
4.4.5 Effect of HA surface topography on osteoclastic resorption	164
4.4.6 Effect of HA surface topography on F-actin organization in osteoclasts....	169
4.5 Discussion	176
4.6 References.....	184
 CHAPTER FIVE - GENERAL DISCUSSION	 189
5.1 Summary and Conclusions	190
5.2 Contributions of the Research to the Current State of Knowledge.....	193
5.3 Limitations of the Research and Suggestions for Future Studies	197

5.4	References.....	202
	APPENDIX A.....	206
	APPENDIX B.....	224
	CURRICULUM VITAE.....	227

LIST OF TABLES

TABLE	Page
2.1 Particle Diameter of Sol-Gel-Hydrothermal Powders	82
2.2 Ca/P Atomic Ratio of Sol-Gel-Hydrothermal Powders	88
2.3 Mechanical Properties of PCL/HA Composites	93
3.1 Ionic concentrations of human blood plasma, SBF-A and SBF-B	109
3.2 Elemental atomic ratio of CaP coatings	122
3.3 Crystal phases of CaP coatings	123
3.4 Surface Roughness of CaP Coatings	128

LIST OF FIGURES

FIGURE	Page
1.1 The hierarchical levels of cortical bone	7
1.2 Crystal structure of stoichiometric hydroxyapatite	16
1.3 Schematic representation of a resorbing osteoclast	39
2.1 Dried CaP Gel	74
2.2 Hydrothermal synthesis at pH 5.20	76
2.3 Hydrothermal synthesis at pH 7.50	78
2.4 Hydrothermal synthesis at pH 13.70	80
2.5 SEM analysis of HA micro- and nanowires synthesized for 24 h	81
2.6 XRD spectra of the CaP gel after hydrothermal treatment	84
2.7 FTIR transmittance spectra of the CaP gel after hydrothermal treatment	87
2.8 SEM and EDX analysis of PCL/HA composites	90
2.9 Uniaxial tensile testing of PCL/HA composites	91
2.10 Compressive testing of PCL/HA composites	92
2.11 Schematic diagram of sol-gel-hydrothermal formation mechanism	97
3.1 SEM micrographs of CaP coatings	114
3.2 SEM micrographs showing cross-section of CaP coatings	115
3.3 XRD pattern of the CaP coatings	118
3.4 FTIR spectra of the CaP coatings	120
3.5 Nanoindentation measurement of E_s	124
3.6 Three-dimensional AFM images and mechanical stylus profilometer height profiles of surface topography of HA coatings	127
4.1 Scanning electron microscope (SEM) images of hydroxyapatite (HA) coatings	154
4.2 Elemental analysis of hydroxyapatite (HA) coatings as determined by energy dispersive X-ray spectroscopy (EDX)	155
4.3 Effects of HA surface topography on osteoblast attachment, spreading and focal adhesion formation	157
4.4 Effect of HA surface topography on expression of osteoblast differentiation markers	160

4.5 Effect of HA surface topography on osteoclasts as revealed by staining for tartrate-resistant acid phosphatase (TRAP) activity	163
4.6 Effect of HA surface topography on osteoclastic resorption	167
4.7 Osteoclastic resorption on the smooth HA1 coatings	168
4.8 Effect of HA surface topography on F-actin organization in osteoclasts	171
4.9 Quantification of the effect of HA surface topography on spreading of osteoclasts	172
4.10 Confocal microscopy of actin in living osteoclast adhering to micro-rough HA3 coating	173
4.11 Confocal microscopy of actin structures in osteoclast adhering to micro-rough HA3 coating	174

LIST OF APPENDICES

APPENDIX	Page
A. Copyright Permission.....	206
B. Animal Ethics Approval.....	224

LIST OF ABBREVIATIONS

3D	Three-dimensional
AA	Antibiotics and antimycotic
ACP	Amorphous calcium phosphate
AFM	Atomic force microscopy
ALP	Alkaline phosphatase
ANOVA	Analysis of variance
ATR	Attenuated total reflectance
BCP	Biphasic calcium phosphates
BMU	Basic multicellular unit
BSA	Bovine serum albumin
CaP	Calcium phosphates
COOH	Carboxylic acids
M-CSF	Macrophage colony-stimulating factor
DAPI	4',6 diamidino-2-phenylindole
DCPD	Dicalcium phosphate dihydrate
ECM	Extracellular matrix
EDX	Energy dispersive X-ray spectroscopy
E_r	Reduced Young's modulus
E_s	Young's modulus
F-actin	Filamentous actin
FBS	Fetal bovine serum

FDA	United States Federal Food and Drug Administration
FTIR	Fourier transform infrared spectroscopy
HA	Hydroxyapatite
HMDS	Hexamethyldisilazane
JCPDS	Joint Committee on Powder Diffraction Standards
α -MEM	minimum essential media
M_n	Number average molecular weight
OCN	Osteoclastin
OCP	Octacalcium phosphate
OH	Hydroxyl
OPG	Osteoprotegerin
PBS	Phosphate-buffered saline
PCL	Polycaprolactone
PFA	Paraformaldehyde
PGA	Polyglycolide
PLA	Poly lactides
PLLA	Poly-L-lactic acid
PU	Poly(ester urethane)
Ra	Average surface roughness
RANK	Receptor activator of nuclear factor- κ B
RANKL	Receptor activator of nuclear factor- κ B ligand
RCO	Rat calvarial osteoblasts
RFGD	Radio-requency glow discharge
RGD	Arginine-glycine-aspartic acid

Rq	Square root of the arithmetic mean of the squares of the deviations from the mean line
RT	Room temperature
RT-qPCR	Quantitative real-time polymerase chain reaction
Rz	Arithmetic mean of the maximum peak to valley deviation over five consecutive sampling lengths
SBF	Simulated body fluid
SEM	Scanning electron microscopy or standard error of the mean (depending on context)
S.E.M	Standard error of the mean
TCP	Tricalcium phosphate
TRAP	Tartrate-resistant acid phosphatase
XRD	X-ray diffraction

CHAPTER ONE

INTRODUCTION¹

¹Sections 1.1, 1.2.1, 1.2.2, 1.3.1, 1.3.2, 1.3.3.1 have been reproduced with permission from: Allo, B. A., Costa, D. O., Dixon, S. J., Mequanint, K., and Rizkalla, A. S. (2012). Bioactive and Biodegradable Nanocomposites and Hybrid Biomaterials for Bone Regeneration. *Journal of Functional Biomaterials*, 3(2), 432-463.

1.1 Bone Tissue Regeneration

Bone defects, ranging from small voids to large segmental defects are a prevalent and persistent problem in clinical orthopedics and dentistry. Bone defects and voids arise from a variety of causes including fracture nonunion [1, 2], dental and orthopedic implant fixation [2], trauma or tumour resection [1, 3, 4], periodontitis [5, 6], and musculoskeletal disorders such as rheumatoid arthritis [7]. In these and other clinical circumstances, bone repair and regeneration can be accelerated using natural and synthetic bone grafts, which are desired to ensure rapid restoration of skeletal function. Furthermore, intervention is necessary to repair nonunions or critical size defects, which are intraosseous wounds of a size that do not heal by regeneration, or in which some pathologic process exists that prevents regeneration. In these cases, bone-graft materials are often required to provide an osteogenic response promoting the formation of new bone [1].

1.2 Regenerative Medicine

1.2.1 Autografts and Allografts

Current standard procedures for bone defect repair include autografts and allografts [8, 9]. These are tissues harvested from one individual and implanted into the same or a different individual, respectively. Autografts such as those derived from aspirated bone marrow, cancellous or cortical bone, or vascularized grafts are osteogenic, osteoconductive and osteoinductive and are considered the gold standard [10, 11]. However, autografts are associated with high operating costs for harvesting the graft, limited availability, donor site morbidity and complications including infection, pain, and

hematoma [8, 9, 12-14]. On the other hand, allografts are subject to cleaning and preparation processes designed to remove cells to minimize immune response. These processing techniques potentially reduce the osteoinductivity, osteoconductivity and mechanical strength of the graft [8, 10]. To overcome these limitations, significant effort has been devoted to the development of biomaterials as bone-graft substitutes that can augment or regenerate bone [8].

1.2.2 Scaffold-based Tissue Engineering

Treatments based on the interdisciplinary field of tissue engineering may be useful for inducing the regeneration of bone. Regeneration as compared to repair is a relatively slow process, one which mimics many of the steps which normally occur during embryonic tissue development [15]. Tissue engineered regeneration is designed to inhibit the initial host rapid repair response, which typically results in scar tissue formation and can be a site for future failure [15].

Tissue-engineered regeneration of bone requires: (1) an osteogenic signal; (2) host cells that will respond to the signal; (3) a three-dimensional (3D) scaffold, designed to support the growth of responsive host cells and permit the formation of extracellular matrix (ECM); and (4) a vascularized host bed [8]. The scaffold serves as a space filling construct providing cell anchorage sites, structural cues, bioactive agents, and/or growth factors or stem cells, as well as inhibiting the formation of fibrous or bridging tissue (a consequence of the rapid repair sequence), while providing space for newly synthesized tissue and integration with surrounding host tissue [15, 16]. Ideally, the scaffold material provides mechanical stability to the individual cells, but also to the surrounding tissue

prior to the synthesis of functioning new tissue [16]. Therefore, it is advantageous to match the mechanical properties of the scaffold material to those of the target tissue in order to withstand *in vivo* stress and loading [12, 17].

Bone tissue engineering can be defined as the use of a scaffold to induce bone formation from the surrounding tissue *in vivo*, or to act as a delivery template for implanted bone cells and/or tissue, which have been grown and expanded *in vitro* [8]. A number of different strategies exist for the tissue engineering of bone. Hutmacher [12] describes one common strategy, which is subdivided into six phases: (1) fabrication of a bioresorbable scaffold; (2) seeding of osteoblasts into the scaffold in static culture; (3) growth of immature tissue in a dynamic environment (spinner flask); (4) growth of mature tissue in a physiologic environment (bioreactor); (5) surgical transplantation; and (6) tissue-engineered transplant assimilation/remodeling. However, a range of different tissue engineering concepts, varying from acellular scaffolds to cellular scaffold constructs, which are implanted with little or no *in vitro* culturing, have been studied in various situations including large animal models and clinical applications. In these studies, the animal or human body served as the bioreactor [8, 18, 19].

In order to promote bone healing, a scaffold construct must provide osteogenic, osteoconductive and/or osteoinductive activity to the specific defect site [10]. In the case of noncritical size defects, which heal naturally, tissue engineering principles can be used to accelerate bone regeneration by providing a construct to support attachment of osteoblasts and synthesis extracellular matrix (ECM) to bridge the defect. For nonunions and defects of critical size, often the osteogenic response is insufficient to promote complete healing. As such, the scaffold must provide an enhanced response by including

a sufficient number of osteoblast precursors and/or ideal concentrations of osteoinductive growth factors [9].

1.3 Bone Physiology

1.3.1 Structure and Composition

The skeletal system is highly dynamic and serves several important functions including: 1) protection of vital organs, 2) support of posture, musculature and teeth, 3) facilitation of movement, and 4) reservoir for bone marrow, and calcium, phosphate and magnesium ions. Functional demands present throughout life dictate the regulation of bone structure and mass via a remodeling process, in which old or damaged bone is replaced by new bone. The remodeling process, including bone repair and regeneration, is facilitated by an intricate balance between the function of different bone cell types: osteoblasts (bone-forming cells), osteocytes (terminally differentiated osteoblasts found within the bone matrix), and osteoclasts (bone-resorbing cells).

At the macroscopic level, bone can be subdivided into two distinct types: cortical (dense, compact) and trabecular (spongy, cancellous), which are easily distinguishable by the difference in macro-porosity [20]. Mature cortical bone (Fig. 1.1) consists of multiple dense and compact layers of mineralized ECM and bone cells, known as lamellae [21, 22]. The lamellae are organized in concentric layers surrounding a Haversian canal (blood vessel), and form a structure known as an osteon. Cortical bone is comprised of several densely packed osteons in parallel arrays. Trabecular bone is characterized by a honeycomb-like network with a large degree of macro-porosity and low bone density, wherein lamellae form individual trabeculae [20, 21]. Trabecular bone is interspersed in

the bone marrow compartment, whereas cortical bone surrounds the marrow of long bones and comprises the exterior of bones [21].

At the cellular level, bone is comprised of a highly organized and mineralized, inorganic-organic composite matrix. The organic component consists primarily of the major ECM protein collagen type I, and other non-collagenous proteins including osteocalcin (OCN) bone sialoprotein, osteopontin, osteonectin, as well as proteoglycans, and accounts for 20-40% of the wet weight of bone [21, 23]. The collagen I matrix is characterized by a unique fibril structure, which initially presents as non-oriented in woven bone, found during the development and healing of the skeleton [21]. As bone is remodeled, the collagen fiber network becomes highly organized and oriented as parallel layers, and woven bone is eventually replaced by lamellar bone. The mineralized collagen fibril structure, in combination with the highly organized manner in which bone is arranged, gives rise to bone's unique toughness and tensile strength [20, 23].

The inorganic component of bone consists predominately of a calcium-deficient and carbonated-HA (with respect to stoichiometric HA) mineral, which comprises approximately 60% of compact bone's wet weight [21]. The carbonated-HA nucleates and grows along the collagen fibers and forms as nano plate-like crystals, producing an inorganic-organic nanocomposite [20]. The HA mineralization of osteoid, the organic phase of bone matrix, contributes to bone mechanics and its high mechanical strengths in shear, compression and tension.

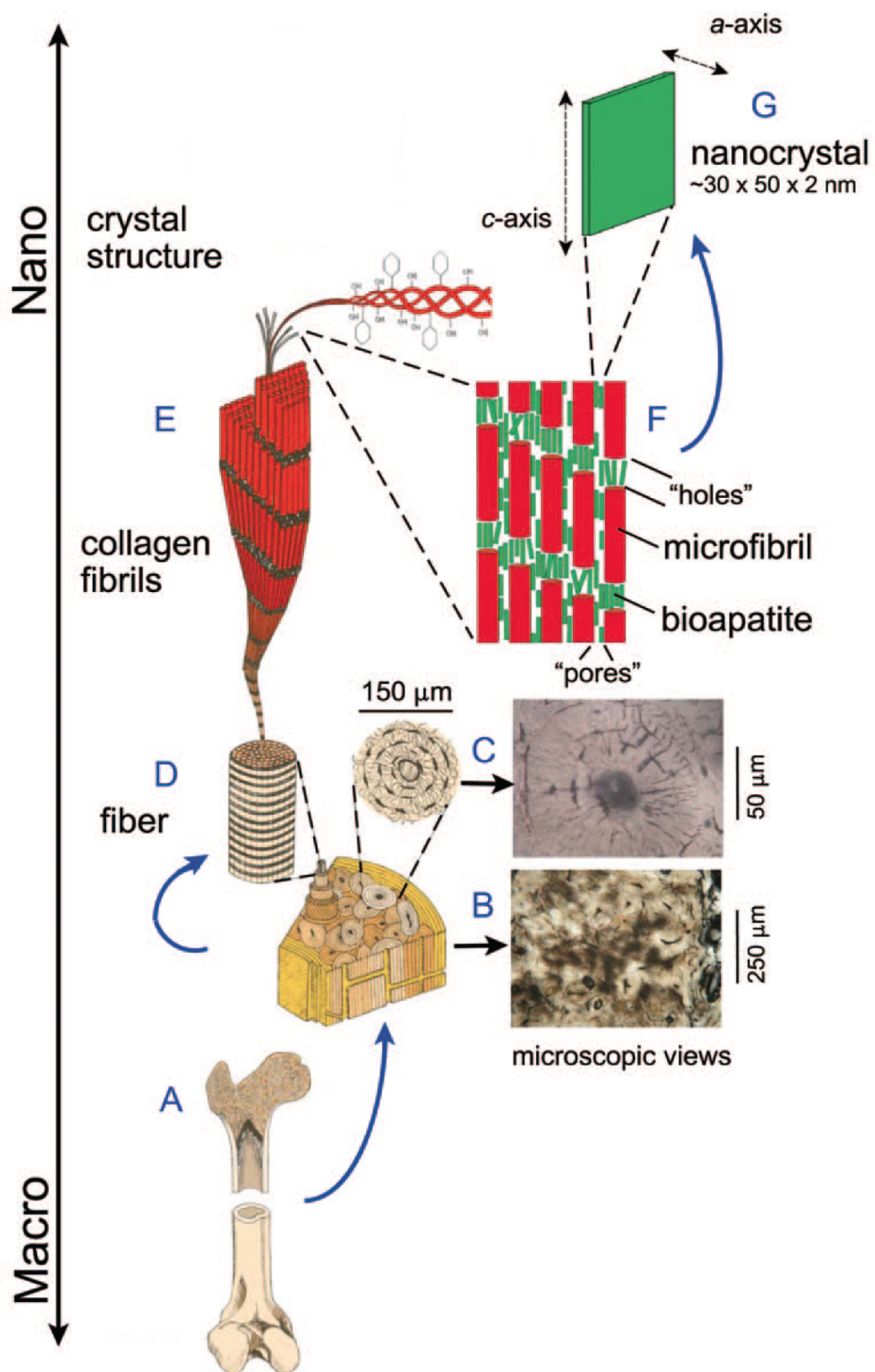


Figure 1.1 The hierarchical levels of cortical bone. (A) A longitudinal section of long bone; (B) Enlargement of a cross-sectional slice of cortical bone. Most of the volume of mature cortical bone consists of cylindrical osteons. Photomicrograph shows a thin-section of cortical bone with numerous osteons; (C) Enlargement of one osteon, consisting of a central vascular cavity with concentric lamellae. The black elliptical spots are osteocyte lacunae. Photomicrograph shows a single osteon; (D) One collagen fiber, created by the bundling of hundreds of fibrils, forms the structural framework of bone. Evenly spaced, dark bands represent periodic gaps (i.e., “holes” seen in F) that occur between the ends of collagen fibrils laid down in overlapping arrays; (E) The smallest unit of the organic component in bone is the triple-helix collagen molecule. Five collagen molecules are bundled side by side in a staggered array, forming a microfibril; (F) Microfibrils, in turn, are bundled into fibrils. Note that apatite crystallites (not to scale) form in voids. Each microfibril is ~300 nm long and ~4 nm thick; (G) An individual platelet of apatite. Reprinted from Reference [113] with permission (Appendix A).

1.3.2 Bone Remodeling

Bone is a highly dynamic tissue, constantly remodeling in response to mechanical stimuli, structural fatigue and damage. During bone remodeling, old bone is replaced by new bone, by sequential actions of the different bone cell types. The coordination of bone cells, particularly osteoblasts and osteoclasts, form a transient structure called a basic multicellular unit (BMU) [24]. Bone cells of the osteoblast lineage differentiate from mesenchymal stem cells and are characterized by their ability to synthesize organic matrix proteins, producing osteoid [21, 25]. Osteoblasts subsequently mineralize the osteoid by formation of HA. During matrix synthesis and mineralization, some mature osteoblasts become surrounded and entrapped in osteoid and terminally differentiate into osteocytes [21]. Osteocytes are thought to be responsible for mechanotransduction and cell communication [25]. Osteoclasts are large, multinucleated cells, which are derived from the fusion of monocytes and macrophages, and when active, are capable of resorbing bone by secreting protons and hydrolytic enzymes [21]. Active osteoclasts form a tight seal with the bone surface and release protons producing an acidic microenvironment, which dissolves HA, and proteases, which degrade the organic components of the bone ECM.

Bone remodeling is highly orchestrated and dictated by the sequential activity of the BMU. Remodeling is characterized by four distinct phases: activation, resorption, reversal and formation [21]. The *activation phase* marks the onset of remodeling, wherein osteoclast precursors are recruited to the bone site of interest. Osteoclastogenesis is induced by the interaction and binding of receptor activator of nuclear factor- κ B ligand

(RANKL), a membrane-bound or soluble protein produced by bone marrow stromal cells and osteoblast, to its receptor RANK found on osteoclast precursors [21, 25, 26].

During the *resorption phase*, active osteoclasts form a ruffled border, surrounded by a sealing zone on the bone surface. The resorption compartment within the sealing zone is the site where bone degradation occurs, resulting in formation of a resorption lacuna (or pit). Coupled with the acid conditions, enzymes are secreted that degrade the organic matrix. The resorption phase lasts for approximately 2-4 weeks and ends with the apoptosis of osteoclasts [21].

The *reversal phase* is the transition from resorption to formation of new bone, and includes the release of signaling molecules to recruit pre-osteoblasts to the remodeling site [21]. Furthermore, a layer of glycoproteins and proteoglycans known as the cement line matrix is deposited and delineates the old bone from the subsequently formed bone [27].

Recruited cells of the osteoblast lineage begin to proliferate and differentiate at the onset of the *formation phase*. Differentiated osteoblasts secrete organic matrix proteins forming the osteoid, which is eventually mineralized by HA [25]. The formation phase lasts approximately 4 months, during which osteoblasts either die through apoptosis, remain on the surface of bone as lining cells, or terminally differentiate into osteocytes [21]. *In vitro*, mineralization of osteoblast cultures represents the final stage of differentiation and correlates with osteoblast maturation [21, 28].

1.4 Synthetic Biomaterials

1.4.1 Biocompatible and Biodegradable Polymers

Scaffolds for tissue regeneration are required to be at the very least, capable of supporting cell attachment and provide sufficient mechanical strength to resist tractional forces produced by cells and contractile forces exerted by the natural healing process *in vivo* [16, 17]. For bone tissue engineering, the defect must be shielded from intrusion of competing cell types and formation of non-osseous tissue such as scar tissue [10, 29].

The scaffold material should be biodegradable and bioresorbable, allowing for excretion of the initial foreign material and its degradation by-products. Ideally, the scaffold degradation rate is expected to be similar to or lower than the remodeling rate of the tissue under physiological loading [12, 16]. Bone regeneration scaffolds are thought to maintain their physical and mechanical properties for 3–6 months with mass loss only to occur after 12–18 months [17]. The majority of degradable polymer systems undergo bulk degradation, which involves a two-stage degradation process [12]. Initially, biodegradation begins with slow reduction in viscosity and molecular weight of the polymer. The second stage results in mass loss characterized by the diffusion of molecular chains out of the bulk polymer, resulting in an accelerated degradation and resorption kinetics. The release of acidic by-products, often associated with mass loss degradation of polymer systems, could be a cause of inflammatory reactions [12].

A fundamental requirement for the design of a tissue engineering scaffold is the selection of a biocompatible material, which does not induce an immune response or a clinically detectable primary or secondary foreign body reaction [12]. A wide selection of naturally derived polymers (e.g., collagen, poly hyaluronic acid, chitosan, or alginate)

and synthetic polymers (polyglycolide (PGA), polylactides (PLA), or polycaprolactone (PCL)) may provide suitable matrix materials for scaffold fabrication [12, 30-33]. Due to concerns regarding the feasibility and availability of naturally derived polymers in large quantities for clinical applications, researchers are focusing on the use of synthetic polymers [34].

A commonly used class of synthetic polymers, polyesters, have found use as suture materials and have garnered attention for use as bone tissue regeneration scaffolds [34]. Polyesters are readily degraded by hydrolysis of the ester linkages and include PGA, PLA, PCL and their copolymers. The physical and degradation properties of synthetic polymers can be tailored to meet the requirements of specific orthopedic applications and have sufficient mechanical strength for use as screws and fixation devices [35].

1.4.1.1 Biodegradable Polyester: Polycaprolactone (PCL)

PCL is a biocompatible and bioresorbable polyester approved by the United States Federal Food and Drug Administration (FDA) for use in numerous medical and drug delivery applications [36]. *In vitro* cultures using PCL have showed good attachment and proliferation of human osteoblasts [36, 37]. Moreover, *in vivo* implantation revealed no inflammatory response with only a thin layer of connective tissue surrounding PCL capsules implanted for 480 days [38].

The degradation kinetics of PCL are suitable for bone tissue engineering applications, as studies have revealed molecular weight loss and loss of mechanical properties at 9 – 12 months, with mass loss occurring only after 24 – 36 months [12, 39]. The primary degradation mechanism of PCL is random hydrolytic chain scission of the

ester linkages with two distinct stages [36-38, 40]. Initially, water diffusion into the amorphous regions of the polymer results in cleavage of the ester bonds and a reduction in the molecular weight with little weight loss or deformation. The second stage, which typically occurs at a reduction of the molecular weight to 5000, involves degradation of the amorphous regions and hydrolysis of the crystalline phase leading to mass loss. Surface erosion by enzymatic hydrolysis and thermal degradation have also been suggested as contributing factors to the biodegradation of PCL *in vivo* [38, 41, 42]. The slow degradation kinetics of PCL make it suitable for bone tissue engineering applications as the scaffold is required to maintain its mechanical strength for the initial 12 months. The preservation of the mechanical properties has made PCL a candidate as a temporary joint spacer in total joint prostheses [39], and as scaffolds for applications where a resilient material is desired [43].

At the cellular level, the PCL macromolecules are ingested and degraded by phagocytes and giant cells [44]. *In vivo* studies involving rats indicated that PCL excretion occurred very rapidly, with radioactively traced PCL appearing in the blood stream, urine and feces virtually simultaneously [38]. The authors concluded that the excretion of PCL mainly occurs through the biliary or gastrointestinal route and occurred almost immediately after being metabolized in the body. Distribution studies revealed low levels of radioactivity, close to or below background values in various organs, indicating that the PCL does not bio-accumulate.

1.4.2 Calcium Phosphate

Calcium phosphates (CaP) are biocompatible and osteoconductive, and possess remarkable ability to bond directly to bone (bioactivity) [45, 46]. In particular, hydroxyapatite (HA) has attracted a great deal of attention for dental and orthopedic applications due to its similarity to the mineral phase of bone and teeth [47, 48]. Stoichiometric HA has the chemical formula, $\text{Ca}_{10}(\text{PO}_4)_6(\text{OH})_2$ with a hexagonal crystal structure (Fig. 1.2) [49, 50]. The mineral constituent of bone, enamel and dentin consists of one phase known as B-type HA, which consists of carbonate ion substitution for phosphate groups in the HA crystal lattice [5]. HA crystals grow along the *c-axis* when nucleated on collagen fibers in mineralized tissue (Fig. 1.2) [49, 50].

Synthetic HA powder can be produced by a variety of wet chemical methods and solid state reactions [5, 51]. Wet precipitation represents a common commercial route for HA production where the drop-wise addition of phosphoric acid to a suspension of calcium hydroxide, or reactions between calcium nitrate and ammonium phosphate (both under alkaline conditions) results in a calcium-deficient apatite precipitate [52, 53]. Hydrolysis methods are also used to prepare HA, using acid calcium phosphates such as dicalcium phosphate dihydrate (DCPD), octacalcium phosphate (OCP) or dicalcium phosphate anhydrous [5]. Commercially available CaP, such as beta-tricalcium phosphate (β -TCP), are also easily hydrolyzed to produce HA [54].

Sol-gel chemistry is a well-known and widely studied synthesis route. It involves the hydrolysis of phosphorous containing alkoxides and calcium salt and subsequent polycondensation. Advantages of sol-gel techniques include molecular level mixing providing a high degree of control over the composition and chemical homogeneity of

the final product. However, production of crystalline HA powders using sol-gel synthesis typically requires calcinations at elevated temperature, which are associated with the formation of secondary phases such as β -TCP and granular particle shapes [55, 56]. Alternatively, hydrothermal processes synthesize crystalline HA at relatively low temperatures (< 250 °C) by subjecting calcium and phosphorus precursors to high pressure steam in an acid digestion bomb [57, 58].

The synthesis of compact and dense HA and TCP scaffolds for bone regeneration often requires high temperature sintering. These are poorly degradable in their highly crystalline form, while their amorphous counterparts are mechanically too fragile to be used for fabrication of highly porous scaffolds. The dissolution rate for calcium phosphates is in the following order:

$$\text{amorphous HA} > \alpha\text{-TCP} > \beta\text{-TCP} > \text{crystalline HA.}$$

The crystalline HA, which is sintered at high temperature, has high chemical stability in contact with tissue fluids, which limits its bioactivity and osteoconductivity [59]. Alternatively, its amorphous counterpart is characterized by a high dissolution rate *in vivo*, which accelerates material desorption and can elicit immunologic responses. Consequently, the dissolution rate and subsequent bioactivity have been improved by synthesizing biphasic calcium phosphates (BCP) consisting of mixtures of HA and the more soluble β -TCP. BCP in the form of granules, blocks or specifically designed shapes are commercially available and are used in numerous orthopedic and dental applications [60].

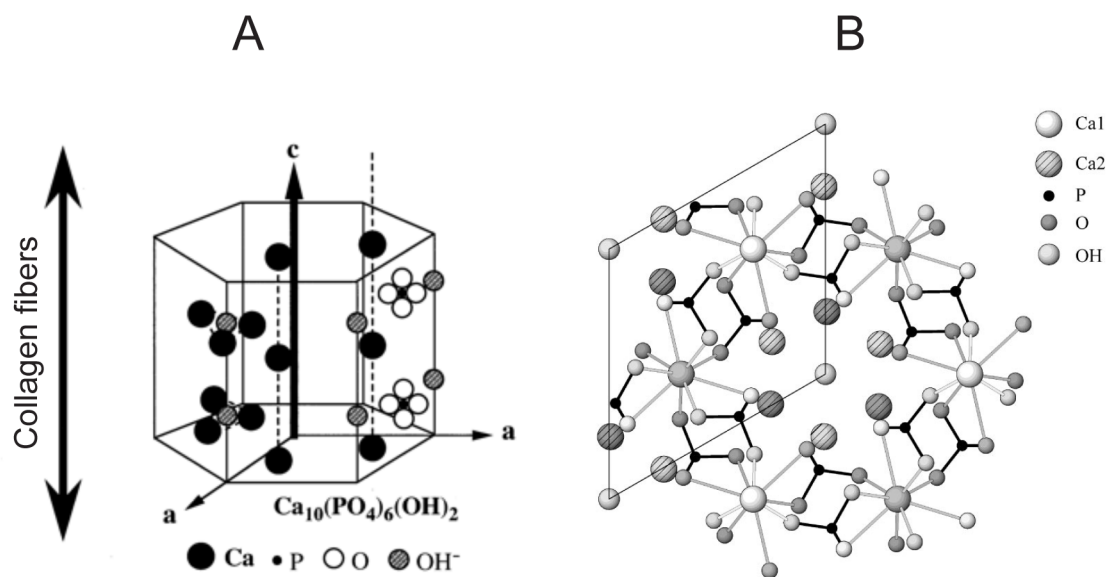


Figure 1.2 Crystal structure of stoichiometric hydroxyapatite. A) In mineralized tissues, apatite develops primarily along the c-axis of the hexagonal structure, and is oriented along the extended collagen microfibril. B) Hexagonal crystal structure of hydroxyapatite projected onto the 001 plane (as visualized down the c-axis). Reprinted from References 40 and 41, with permission (Appendix A).

In vitro studies using human bone marrow cells showed improved cellular attachment, proliferation and differentiation when cultured on HA as compared to other commonly used biomaterials – titanium and high molecular weight polyethylene [61]. *In vitro* culturing of osteoblast-like cells on porous PCL scaffolds showed significant increase in osteoconductivity and bone formation when the PCL was embedded with HA particles or coated with biomimetic HA [62].

Osteoconductivity is clearly evident from *in vivo* experiments. Improved bone ingrowth into porous implant materials was obtained when the implant was coated with CaP [63-70]. As well, CaP coatings as eliminated fibrous tissue encapsulation commonly seen at the tissue/material interface of implanted polymer scaffolds [71, 72]. Indeed, clinical applications of calcium phosphate coatings for total joint arthroplasty have shown improved osseointegration at the bone/implant interface resulting in superior implant stability [73]. Further, *in vivo* studies have shown potential osteoinductivity of biomimetic CaP coatings, where ectopic bone formation occurred when coated implants were inserted in nonosseous sites [74-76].

1.4.2.1 Micro- and Nano-Hydroxyapatite

Hydrothermal synthesis methods, utilizing high pressure conditions obtained in an acid digestion bomb, have been used to produce HA powders with controlled particle size, morphology and crystallinity [77-82]. The hydrothermal process operates at relatively low temperatures (< 200 °C) and HA nanorods and nanowires are produced from a variety of precursor materials, including mixtures of calcium hydroxide and phosphoric acid [80] or dicalcium phosphate dihydrate [81], calcium nitrate and tripolyphosphate gel [78] or ammonium hydrogen phosphate [77, 79, 82], and calcium

carbonate or calcium silicates with phosphate solutions [83, 84]. Traditionally, hydrothermal synthesis occurs in aqueous environments; however, various co-solvents [78, 80] or different organic additives, such as urea [77], citrate [82] and acetamide [79], are used to help control particle morphology. Furthermore, carbonated-HA is produced by hydrothermal systems containing urea as an additive, and the solubility of the carbonate-substituted HA is higher than phase-pure, highly crystalline HA [77, 85]. Carbonated-HA is expected to have dissolution rates comparable to TCP [85], and is considered more bioactive than stoichiometric HA [86].

In an effort to obtain a higher degree of control over particle morphology of the resulting HA powders, solvothermal processes have been used [87-89]. The solvothermal process is a modification of the traditional hydrothermal synthesis route, which utilizes organic solvents and surfactants to yield reverse micelle emulsions. The reverse micelle solutions provide an effective method to synthesize HA nanorods, nanowires and nanofibers of varying diameters and aspect ratios ($L/D = 100$). The organic surfactants in the solvothermal mixture provide organized micelle templates, which guide the synthesis of one-dimensional inorganic nanomaterials by controlling nucleation and growth through geometric and electrostatic interactions [90].

The diameter and aspect ratio of the HA powders are an important characteristic for biomedical applications, as diameters in the nano-scale are desirable for optimal biological and mechanical performance [91-93]. Nano-scale HA in the form of rods and wires has shown superior osteoconductive and bioactive properties as compared to their micron-scale counterparts [93]. *In vivo* experiments, using rabbit radius bone defects, showed greater osteoconductivity and bone ingrowth in defects treated with nano-HA, as compared to micro-HA or untreated groups [94]. In addition, nano-HA has been used to

produce nanocomposites and their mechanical properties and *in vivo* performance, assessed using an osteochondral rabbit defect model, were compared to microcomposites fabricated using micro-scale HA. The use of nano-scale HA yielded nanocomposites with superior stiffness and strength, and induced greater trabecular bone formation at the tissue-implant interface [95].

1.4.2.2 Biomimetic Surface Coatings

CaP coatings have the potential to improve the biocompatibility, bioactivity, and osteoconductive properties of scaffold surfaces [96, 97]. *In vitro* culturing of osteoblast-like Saos-2 cells on PCL porous scaffolds showed a significant increase in osteoconductivity and bone formation when PCL was embedded with HA particles or coated with biomimetic HA [62].

The commercial coating processes for deposition of CaP, such as HA, have traditionally used the plasma-spraying method [98]. However, plasma-spraying processes occur at elevated temperatures, and therefore, are not a suitable coating procedure for temperature sensitive materials such as most medical grade polymers [99].

A biomimetic process using a simulated body fluid (SBF) and operating at mild conditions (of temperature and pH) offers an economical method to apply a bone-like apatite coating to various materials, including polymers and metal alloys, with complex shapes and porous structures [100, 101]. SBF is a buffer solution containing ion concentrations similar to those found in human blood plasma. Kokubo et al. first demonstrated the ability of SBF to deposit surface layers of a calcium-deficient, carbonated HA onto material surfaces [102]. Advantages of biomimetic procedures include mild operating conditions at physiological pH (7.4) and temperature (37°C), and

an aqueous solution-based self-assembly system, which allows for coating complex surfaces and 3D porous structures.

Biomimetic processes using SBF solutions have successfully produced coatings of bone-like apatite on various material surfaces, including natural and synthetic polymers, metal alloys and titanium, in the presence of proper surface functional groups [103-108]. Negatively charged functional groups such as carboxylic acids (COOH) and hydroxyl (OH) groups act as nucleation sites, first by electrostatic attraction of Ca^{2+} ions, which culminate in the adsorption of PO_4^{3-} ions from the SBF solution [109]. Once critical size nuclei are formed on the material surface, the nuclei spontaneously grow into a dense apatite layer by further consuming calcium and phosphate ions from the SBF [109]. However, due to the low ionic activity product of traditional SBF (1x, 1.5x), lengthy incubation periods on the order of weeks are often required to achieve adequate surface coverage.

Recent efforts to accelerate the coating process have focused on increasing the supersaturation of the SBF solutions, specifically, the calcium and phosphate ion concentrations. Several studies have investigated the ability of a supersaturated SBF (e.g. 5xSBF) to depositing various crystalline CaP coatings. The careful design of SBF composition allows one to induce the deposition of coatings consisting of carbonated-HA [110-114], octacalcium phosphate (OCP) [111, 112, 115], and dicalcium phosphate dihydrate (DCPD) [110, 113], as well as an amorphous calcium phosphate (ACP) coating [110, 113-115] within 1 – 3 days incubation. The different CaP coatings were produced by varying the ionic composition of the 5xSBF solution, specifically, the concentration of crystal growth inhibitors, Mg^{2+} and HCO_3^- [110, 113]. The amorphous calcium phosphate coating, which is considered a precursor to other crystalline phases, can be

subsequently hydrolyzed into OCP and HA after incubating in concentrated SBF solutions devoid of crystal growth inhibitors [114-116]. Further increasing the ion concentration of the SBF 10-fold (10xSBF) induces apatite coatings within hours [117-120]. However, the increased supersaturation results in rapid solution precipitation and the 10xSBF must be replenished, and the incubation process repeated several times to promote formation of apatite over other crystalline phases [117, 119]. Moreover, subjecting material substrates to numerous incubation cycles results in an increase in coating thickness, which can mask designed surface features or block porous networks [119].

1.4.3 Nanocomposites

Currently, biomaterials for bone tissue regeneration suffer from the inability to satisfy every design consideration, including biodegradability, bioactivity, osteoconductivity, and mechanical competency. Biomaterials deemed to have sufficient mechanical properties are often bio-inert and nondegradable [121], whereas biodegradable polymers or resorbable, bioactive and osteoconductive bioceramics are inherently weak [33]. As such, nanocomposites – combining biodegradable, bioactive and mechanically resilient materials – offer a unique solution towards producing scaffold materials with suitable biological, physical and mechanical properties [34].

The rationale for the development of nanocomposites for bone tissue engineering was inspired by the natural physiological structure of bone tissue (Fig. 1.1), which consists of inorganic HA mineral embedded in a collagen-rich ECM [22, 34]. From this perspective, the different components of nanocomposites aim to mimic the organization

of bone tissue. Nanocomposites consist of inorganic reinforcing filler (nano-HA), resembling the mineral apatite crystals, embedded in an organic polymer matrix, resembling the collagen-containing ECM.

From a mechanical properties point of view, bioceramics such as HA, are inherently stiffer than polymers; however, their intrinsic brittleness and sensitivity to crack propagation and catastrophic failure limit their use as scaffold materials. On the other hand, synthetic polymers, including PCL, have suboptimal biocompatibility due to release of acidic degradation products, and limited strength and mechanical stability when fabricated with large degrees of macro-porosity, a fundamental design criterion for tissue regenerative scaffolds [34]. Furthermore, synthetic polymers are not osteoconductive or bioactive and, therefore, do not bond directly to bone and are typically encapsulated by fibrous tissue when implanted in vivo [38, 71].

Nanocomposites, prepared from biodegradable synthetic polymers in combination with bioresorbable HA, are ideal candidates for bone tissue engineering scaffolds. The bioresorbable HA component of nanocomposites imparts its bioactivity, osteoconductivity and mechanical strength to the more resilient biodegradable polymer matrix [34]. Furthermore, the basic resorption by-products of HA can potentially buffer the acidic polymer by-products, which are normally a cause of inflammatory reactions.

Inorganic nanoparticles, nanowires or nanofibers are added to different organic biodegradable polymer matrices to produce nanocomposite biomaterials. The particle size and morphology of the inorganic filler have a direct influence on its ability to reinforce materials [91, 122, 123]. In particular, smaller diameters and larger aspect ratios have the greatest beneficial effect on mechanical properties. Due to the large surface area of nano-sized fillers, an intimate interface with the polymer matrix is

formed, and the intrinsic properties of the fillers contribute to an increase in the mechanical strength and stiffness of composites [34].

1.4.3.1 Hydroxyapatite-based Nanocomposite

Recent studies have shown that HA powders consisting of micron-sized particles, were successful in improving the mechanical performance of high-density polyethylene-based materials [122, 123], silk-based porous scaffolds [124] and calcium phosphate cements [125]. The emergence of nanotechnology, coupled with the need for bioactive and biodegradable synthetic biomaterials, has led to the use of HA powders consisting of nano-sized particles, rods and wires for producing nanocomposites for bone regeneration [126-130].

Highly porous PLLA nanocomposite scaffolds have been prepared by a thermally induced phase separation technique [126]. Unfilled PLLA and HA/PLLA nanocomposite scaffolds with greater than 89% porosity and pores sizes ranging from 50–100 μm were produced. Compressive modulus of nanocomposites scaffolds were significantly higher (8.3 MPa) as compared to unfilled PLLA (4.3 MPa). Scaffolds with varying HA content were immersed in fetal bovine serum/phosphate buffer solution to evaluate protein adsorption, which is thought to be a determining factor for cell adhesion and survival. Composite scaffolds with high HA loading adsorbed 2–3 times more serum proteins than unfilled PLLA scaffolds. The authors proposed that greater HA loading was more effective in protein adsorption because the increased HA weight fraction allowed for more HA particles to be exposed on the surfaces of the pore walls. The authors further showed that, for high HA loading, composite scaffolds containing nano-HA improved

protein adsorption compared to scaffolds synthesized with micron-sized HA particles with similar loading rates.

Using a salt leaching and phase inversion process, Biossard *et al.* [127] developed porous nanocomposite scaffolds composed of biocompatible poly(ester urethane) (PU) and PCL with HA nano-particles. Micro-computed tomography (micro-CT) scans of scaffolds showed that scaffold pore size and porosity decreased with an increase in HA content, while the wall strut thickness increased. Results from the tensile testing indicated that the Young's modulus was moderately greater for the nanocomposites compared to polymer without HA. However, the authors did not address whether the improvement in mechanical properties of the composite was due to reinforcement of the polymer matrix by the HA filler, or by the decrease in porosity and increase in strut thickness as measured by the micro-CT analysis.

PU/HA nanocomposites were further evaluated *in vitro* by a protein adsorption study and *in vivo* by a mouse dorsal skin fold chamber model to assess the biocompatibility and vascularization [131]. The nanocomposite and the unfilled PU scaffolds adsorbed protein on their surfaces; however, the nanocomposite scaffolds exhibited greater levels of protein adsorption. Moreover, the *in vivo* results demonstrated that the host tissue response to the scaffolds were comparable for the PU/HA nanocomposites and the unfilled PU. The scaffolds promoted only a weak angiogenic host response; however, they showed favorable biocompatibility with little acute leukocytic inflammatory activity throughout the entire study period.

Prabhakaran *et al.* [132] fabricated nanofibrous PLLA and PLLA/collagen/HA nanocomposite scaffolds, containing HA nanoparticles, by electrospinning. *In vitro* experiments, using cultures of human fetal osteoblasts, showed that the inclusion of HA

nanoparticles in nanocomposite scaffolds enhanced cell proliferation, differentiation, and mineralization.

In summary, despite the multitude of nanocomposite technologies, most fail to combine the nano-scale and osteoconductive filler bioceramics, with scaffolds having the ideal surface chemistry and topography to promote bone forming stimulus and appropriate rates of biodegradation.

1.5 Osteoblasts and their Interactions with Biomaterials

1.5.1 Origin and Differentiation of Osteoblasts

Cells of the osteoblast lineage are derived from an osteoprogenitor cell, which originate from mesenchymal stem cells. Mesenchymal stem cells are capable of differentiating into bone, cartilage, fat or fibrous connective tissue, and are directed towards the commitment to the osteoblast phenotype through the canonical Wnt/ β -catenin pathway [21, 133]. In bone, transcription factors such as Runx2 and osterix have been identified as master regulators of osteoblast differentiation [133]. Runx2 directs mesenchymal progenitor cells towards preosteoblasts. Downstream, Runx2, β -catenin, and osterix further induce preosteoblasts to become immature osteoblasts, capable of expressing bone matrix protein genes, such as osteopontin [134].

Osteoblast differentiation towards mature osteoblasts and the subsequent matrix synthesis and mineralization of matrix is described by three distinct biological phases: 1) *cellular proliferation*, 2) *matrix maturation*, and 3) *matrix mineralization* [28, 135]. During these stages a host of collagenous, non-collagenous, and bone-related proteins are synthesized including type I collagen, alkaline phosphatase (ALP), OCN, osteopontin,

osteonectin, and bone sialoprotein [135]. These proteins are thought to serve multiple functions including regulation of mineral deposition, bone turnover and cell activity [21]. Therefore, no single specific gene can fully describe osteoblast differentiation, matrix synthesis, and mineralization, and as such, the gene expression of several different bone-related genes must be examined when investigating osteoblast differentiation.

During the initial stage of *cellular proliferation*, maximal expression of genes associated with ECM biosynthesis, are observed such as type I collagen and osteonectin [28]. Bone matrix is composed mostly of type I collagen, with small amounts of types III and V, whereas osteonectin is the most prevalent non-collagenous protein and is thought to influence osteoblast growth and proliferation [21]. The next phase, *matrix maturation*, is a post-proliferative stage highlighted by maturation of the ECM and is associated with maximal expression of ALP [21, 28]. ALP is a major glycosylated protein in bone, and is thought to increase local concentrations of inorganic phosphate, hydrolyze and inactivate inorganic pyrophosphate (an inhibitor of mineral deposition) and modify phosphoproteins to control HA nucleation [21]. The final stage of *matrix mineralization*, is characterized by gene expression of OCN, osteopontin and bone sialoprotein. It is believed that these proteins bind calcium and phosphate, and help regulate mineral deposition by controlling amount and size of the HA crystals formed [21, 28]. In this regard, OCN expression is considered a marker of osteoprogenitor differentiation to a mature osteoblast phenotype [134].

1.5.2 Adhesion and Morphology of Osteoblasts

Cell adhesion is typically divided into two phases – an attachment and an adhesion phase [136]. Attachment involves the short term interaction of cells with substratum via physiochemical linkages, whereas adhesion is described as a long-term phenomenon involving ECM proteins, cell trans-membrane proteins, and cytoskeletal proteins. Cell adhesion to ECM and synthetic material surfaces directly influences proliferation, ECM biosynthesis, and differentiation [137].

Adhesion is facilitated by various ECM proteins, including collagen, fibronectin, osteopontin, osteonectin and bone sialoprotein; however, *in vitro* osteoblast adhesion is mediated primarily by fibronectin and vitronectin [137]. These matrix proteins contain adhesive Arginine-Glycine-Aspartic acid (RGD)-peptide sequences, which facilitate specific interactions with cell membrane receptors, most notably, the integrin superfamily. Furthermore, the RGD-peptide motif is of critical importance for osteoprogenitor cell adhesion to various substrata [137].

Integrins are transmembrane adhesion molecules consisting of a large extracellular domain, a transmembrane domain and a short cytosolic domain [137]. Integrins are responsible for cell-substratum adhesion through interaction of their extracellular domain with extracellular ligands, and many have a high specificity for RGD sequences of ECM proteins [136]. The membrane-spanning domain links the external domain to the internal, cytosolic domain, which in turn is linked to intracellular proteins such as talin, paxillin and vinculin [136, 137]. After integrin binding to a ligand (RGD sequence of ECM protein), integrins cluster together and form focal adhesions [136]. Several other intracellular proteins will co-localize with vinculin and talin in the

adhesion plaque, including proteases, protein kinases, phosphatases, and other signaling molecules [137]. As such, integrin interaction with extracellular proteins can regulate not only cell adhesion, but motility, spreading, growth, signal transduction, and differentiation [136, 137]. Furthermore, vinculin and talin mediate interactions between integrins and actin filaments and, therefore, cellular adhesion and ECM proteins have a direct effect on cell morphology.

Osteoblast precursors initially present themselves as spindle-shaped osteoprogenitors and undergo changes in morphology and exist as large cuboidal cells when fully differentiated [21]. Mature osteoblasts have large nuclei, and Golgi structures and extensive endoplasmic reticulum [21]. The architecture and organization of filamentous actin (F-actin) dictates cell shape and morphology. When assembled in long bundles, F-actin promotes finger like projections of the plasma membrane known as filopodia. Furthermore, if bundles of F-actin are associated with focal adhesions, stress fibers are produced. Sheet-like protrusions, known as lamellipodia, result if F-actin is organized in a mesh-like structure [137].

1.5.3 Bone Formation

Skeletogenesis consists of four main phases – 1) mesenchymal cell migration to the targeted site of bone formation, 2) interactions between existing tissue and cells, 3) aggregation or condensation of mesenchymal cells, and 4) differentiation of mesenchymal cells into osteoblasts and/or chondroblasts [138]. Mesenchymal cell condensation is a necessary prerequisite for bone formation, which occurs through two distinct developmental processes, endochondral and intramembranous ossification [133,

138]. Endochondral ossification represents the most common pathway for bone formation, particularly for long bones, and occurs during development and through adolescence. In contrast, intramembranous ossification facilitates the majority of skull and flat bone synthesis.

During intramembranous ossification, osteoblasts differentiate from a condensed mesenchymal cell layer housed within a sheet of connective tissue. The differentiating osteoblasts synthesize and secrete a fibrillar, non-mineralized matrix (osteoid), which is later mineralized and reorganized into compact bone [133]. Similarly, endochondral ossification begins with an aggregated and condensed population of mesenchymal cells. However, the pluripotent mesenchymal cells first differentiate into chondrocytes, and then produce a cartilage template of the bone. Mesenchymal cells located on the periphery of the cartilage template, flatten and form the perichondrium, a condensed multilayered tissue. The cartilage matrix then mineralizes and is subsequently invaded by osteoclasts and blood vessels. Osteoblast precursors surrounding the blood vessels differentiate into osteoblast that then form bone on the remnants of calcified cartilage matrix. Ossification in the diaphysis and epiphyses of long bones gives rise to intermediate structure known as the growth plates. The growth plates are cartilaginous structures that serve as sites for the future longitudinal growth of long bones. In the region near the perichondrium, a host of signaling pathways induces the differentiation of osteoblasts and forms a region known as the periosteum. These differentiated osteoblasts begin to secrete osteoid, which is eventually mineralized and organized into compact bone [133].

In the context of bone regeneration therapies using scaffolds, or fracture repair systems (using intramedullary screws or fixation plates) bone formation and healing can

occur via intramembranous or endochondral ossification [139, 140]. Porous ceramic scaffolds, seeded with donor osteoblasts, produced bone via intramembranous ossification when implanted *in vivo*. However, identical scaffold constructs, loaded with mesenchymal cells and implanted *in vivo*, stimulated host bone formation through the activation of an endochondral process [140]. In a murine fracture model, femurs stabilized with an intramedullary screw showed considerable cartilaginous tissue within the newly formed callus, which was attributed secondary healing response through simultaneous endochondral and intramembranous ossification [139]. In contrast, femur fixation using a plate and screw system, showed accelerated bone formation bridging the fracture gap. The enhanced healing response was predominately by intramembranous ossification and was attributed to a more stable and improved fracture fixation as compared to the intramedullary screw [139].

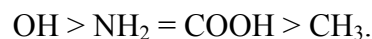
1.5.4 Interactions of Osteoblasts with Biomaterials

Cellular interactions with biomaterial surfaces are crucial for the success of any tissue engineering scaffold [16]. The scaffold is required to provide not only mechanical stability to the tissue engineering construct, but also cell anchorage sites and structural cues. Moreover, surface chemistry and topography play prominent roles in regulating cellular adhesion, proliferation and differentiation [8, 11]. The material surface also represents the interface between the scaffold and the tissue. Osseointegration, which is a phenomenon where bone forms within and at the endosseous implant surface, is a defining factor for the success of orthopedic and dental implants and tissue engineering scaffolds [141].

Osteoblast-biomaterial interaction is influenced by the biomaterial surface characteristics including chemistry and topography, which encompasses chemical composition, surface charge and energy, hydrophobicity/hydrophilicity, and roughness. These surface attributes determine the adsorption, orientation and conformation of ECM proteins, which influence osteoblast adhesion, proliferation, and differentiation on the biomaterial [137].

1.5.4.1 Surface Chemistry

Surface chemistry, through specific protein binding, controls focal adhesion assembly, composition and signaling [137]. Adsorbed proteins (such as immunoglobulins, vitronectin, fibrinogen, and fibronectin) can bind to integrins and distinctive biomaterial surface properties impart different integrin binding specificities through the presentation of various adsorbed proteins [142-145]. In particular, the presentation of the major integrin binding domain in fibronectin was found to be sensitive to material surface functional groups with specificity ranking as follows [143]:



Mineralization and matrix formation by osteoblast-like cells was also found to be dependent on surface chemistry and correlated well with the integrin binding capacity of different surface functional groups [143]. Studies investigating osteoblast attachment on materials with different surface functional groups have reported preference towards oxidized surfaces, corresponding well with reported protein binding preference [142]. Integrin function is dependent on divalent cations and the presence of charged elements plays a crucial role in bone remodeling and development. Ion implantation of Mg^{2+} on the surface of various biomaterials (such as titanium and Al_2O_3 bioceramics) has

improved osteoblast adhesion and differentiation and maintenance of the osteogenic phenotype [144-146].

1.5.4.2 Surface Topography

The surface topography of biomaterials is typically quantified in the form of numeric standard integral surface roughness parameters [147]. The most commonly used parameter is the average surface roughness (R_a), which is defined as the arithmetic mean of the absolute of the height (peak and valley) deviations from the mean value [147, 148]:

$$R_a = \frac{1}{m} \sum_{i=1}^m |z(x_i)|$$

where z is the height deviation from the mean line at each individual point (x_i) along the evaluation length having m number of ordered and equally spaced points. Several other parameters exist including R_q , which is the square root of the arithmetic mean of the squares of the deviations from the mean line, and R_z , the arithmetic mean of the maximum peak to valley deviation over five consecutive sampling lengths [147].

Numerous techniques exist for the characterization of surface roughness parameters, including mechanical and non-contact laser profilometry, interference microscopy, scanning tunneling microscopy, and atomic force microscopy (AFM) [147]. However, each system has its own vertical and lateral resolution limits and reported roughness parameters are scale-dependent and will vary with measurement scale and sampling length. Therefore, it is difficult to describe complex isotropic surfaces and fine nano-scale surface features, which are often masked by the coarser surface roughness [147]. As such, it is important to obtain scale-dependent roughness measurements at

several dimensional ranges, using different measurement techniques. As an example, coarse topographical features in the size range of micrometers to millimeters may be obtained using profilometry; whereas, AFM has sensitivity within the nanometer range and is suitable for assessing high resolution roughness.

Modification of biomaterial surface roughness, by imparting micro-, sub-micron and nanometer isotropic surface features, affects osteoblast adhesion, proliferation and differentiation. Formation of submicro- and nanometer surface features on titanium increased cellular adhesion when compared to flat surfaces [149]. In contrast, variation in micro- and nano-topography of gold coatings had negligible effect on cellular adhesion; however, increased proliferation and differentiation was observed on gold coatings with isotropic nano-topography [150].

Increase in surface porosity and roughness of sintered HA discs, improves cellular attachment, proliferation, differentiation and bone ingrowth [151, 152]. Osteoblast-like cells are capable of discerning the apatite microenvironment, and appear to favor large plate-like HA crystals over finer apatite crystals as indicated by elevated expression of osteocalcin and bone sialoprotein [153]. Bone-bonding at biomaterial surfaces is expected to occur if the material possesses topographical features at both the micrometer level and nanometer range [27]. It is believed that materials can be rendered bioactive given proper levels of surface complexity, and bone formation occurs through contact osteogenesis. Discrete nano crystals of CaP, deposited on titanium implants with micron-scale surface roughness, imparted a nano-scale surface complexity and improved the osseointegration of implants surfaces when implanted *in vivo* and at the posterior maxilla in a human clinical trial [154, 155].

The culmination of numerous *in vitro* and *in vivo* studies has identified an optimal Ra of biomaterials to be in the range of 1-7 μm for inducing maximal changes in cell behavior and bone formation [148, 156, 157]. On the other hand, bone nodule formation *in vitro* was limited to surfaces topographies having Ra $<0.3 \mu\text{m}$, and fibrous tissue encapsulation occurred for implants with Ra $<0.4 \mu\text{m}$, when placed in an osseous environment *in vivo* [148]. However it should be noted that conclusions on the effect of surface topography of biomaterials on the *in vitro* and *in vivo* success, should not be limited only to the measurement of the amplitude of the Ra. Osteoblastic activity is affected by subtle changes in surface architecture and other surface features, such as spatial distribution, aspect ratio, and curvature [148, 158]. Furthermore, bone formation is dependent on synergistic influences of surface roughness at different dimensional scales, i.e. micro-, sub-micrometer-, and nanometer range [158].

In summary, the osteoblast/biomaterial interface offers a distinctive opportunity to improve the performance of scaffolds and implants for applications in bone regeneration. Biomaterials with enhanced osteogenic stimulus may be achieved by combining appropriate surface chemistry, through the addition of bioactive and osteoconductive bioceramics, with ideal surface topographies having complex and isotropic nano-, sub-micrometer- and micro-scale features.

1.6 Osteoclasts and their Interaction with Biomaterials

1.6.1 Origin and Differentiation of Osteoclasts

The osteoclast is a multinucleated-giant cell, which is derived from the differentiation and fusion of mononuclear monocyte/macrophage precursor cells at or

near the bone surface [159]. Typically, osteoclasts are large cells having diameters ranging from 50-100 μm , and are characterized by having 3 or more nuclei, numerous mitochondria, lysosomes, and free ribosomes, and extensive Golgi complexes [160]. Furthermore, osteoclast precursors and mature osteoclasts have a significant level of the phosphohydrolase enzyme, tartrate-resistant acid phosphatase (TRAP), which is a marker commonly used for identifying osteoclasts.

The mononuclear osteoclast precursor develops from a myeloid hematopoietic progenitor that it shares with the granulocyte and monocyte lineages [160]. Osteoclastogenesis is dependent upon a permissive environment consisting of stromal, bone marrow and osteoblastic cells, and the presence of cell-associated or soluble hematopoietic factors – the cytokine RANKL and the polypeptide growth factor macrophage colony-stimulating factor (M-CSF) [159, 160]. RANKL exists as both a transmembrane and soluble protein (sRANKL), and along with M-CSF, is produced by stromal cells and osteoblasts in the bone marrow [159]. RANKL binds to and activates the transmembrane signaling receptor RANK found on osteoclast precursors. In combination with M-CSF, RANKL causes osteoclast differentiation and activation. TRAP-positive osteoclast precursors subsequently fuse together to form the multinucleated osteoclasts, which are considered terminally differentiated. In addition, M-CSF is crucial for the survival and proliferation of osteoclast precursors, as well as the survival of osteoclasts. In the case of mature osteoclasts, activation of RANK by its ligand triggers cytoplasmic signaling pathways, which control various functions including bone resorption and survival [159, 160].

Osteoclastogenesis, and subsequently bone resorption, are regulated by the decoy receptor osteoprotegerin (OPG) – a soluble tumor necrosis factor receptor-related protein

[159]. OPG inhibits osteoclastogenesis and prevents osteoclast formation *in vitro*, and bone resorption *in vivo*. The OPG decoy receptor binds to RANKL, effectively preventing RANKL interaction with RANK. Similar to the soluble form of RANKL, OPG is secreted by osteoblasts and, therefore, the expression of RANKL and OPG is coordinated to control the activation of RANK and subsequently, regulate bone resorption and density [159].

1.6.2 Adhesion and Morphology of Osteoclasts

Osteoclast-substratum interactions are mediated through the dynamic formation of specialized adhesion plaques known as podosomes. These are dot-like, discrete and conical structures, which function as short membrane protrusions and provide cell-substratum adhesion through contacts with gaps less than 10 nm [161]. Podosome structures are typically organized in clusters [162]. Inside the cell, podosomes consist of a central core of bundled F-actin microfilaments with a diameter of 0.3 μm and height of 0.6-1 μm , surrounded by a cloud of F-actin and actin monomers [163]. Encompassing the actin core is a ring comprised of integrins and their associated adaptor and signaling proteins, including vinculin, paxillin talin and different kinases [161, 163]. Through integrins osteoclast podosomes recognize the extracellular matrix via interaction with the RGD sequence of specific ECM adhesive macromolecules, such as fibronectin, vitronectin, osteopontin, collagen and bone sialoprotein. Furthermore, the interaction of integrins with RGD proteins has been shown to activate signal transduction mechanisms in osteoclasts [160]. In this regard, podosomes in osteoclasts are analogous to focal adhesions in osteoblasts, with main the difference attributed their organization and

dynamics, as podosome assembly and disassembly occurs within a few minutes [161]. *In vitro*, podosomes are constantly reorganizing during osteoclast differentiation, maturation and motility. Podosomes present initially as individual structures scattered throughout the osteoclast, which can then develop into rings, extend to the cell periphery, and eventually evolve into an F-actin belt or sealing zone [163].

During bone resorption, osteoclasts become functionally polarized with a basolateral membrane domain facing the vascular stream and an apical membrane facing the substratum. The basolateral cytoplasm contains the nuclei and organelles, whereas the apical cytoplasm towards the substratum contains lysosomes and a specialized structure at the periphery, known as the ruffled border (Fig. 1.3). The ruffled border is actively involved in bone resorption, and is formed by finger-like membrane interfoldings of the inner domain of the apical membrane. Protons are transported and enzymes are secreted extracellularly into the resorption compartment across the ruffled border. These protons and enzymes degrade the bone mineral and the organic ECM, respectively [161]. The resorbing compartment containing the ruffled border is enclosed by a unique and characteristic F-actin ring-like structure, called the sealing zone. The sealing zone is essential to segregate the resorption compartment from the extracellular fluid, in order to establish the conditions appropriate for bone resorption [161, 164]. When osteoclasts are not resorbing, they often exhibit a spread morphology and are highly motile [164].

1.6.3 Bone Resorption

During each remodeling cycle, osteoclast-mediated bone resorption requires approximately 2-4 weeks. As mentioned above, resorption requires the formation of a sealing zone. The sealing zone is composed of several condensed podosomes, cross-linked by interconnecting F-actin filaments [165]. The F-actin ring is surrounded on the inner and outer domains by rings of adhesive proteins, including vinculin and paxillin [164]. The interaction between F-actin and adhesive proteins in the interconnected sealing zone transmits the local properties of the substratum through the adhesion receptors (integrins), to the adhesion plaques (vinculin), and finally to the F-actin network, effectively sensing the condition of the substrate and thereby regulating the resorptive activity [163]. The uniformity and continuity of substrate adhesiveness is of critical importance for the formation of the sealing zone, and it has been shown that non-adhesive barriers as small as 1 μm can effectively inhibit the organization of a sealing zone [165].

Within the resorbing compartment, the ruffled border secretes hydrogen ions via a proton pump (H^+ -ATPase), which results in acidification of the resorption compartment, lowering the pH to ~ 4.5 (Fig. 1.3). The acidic conditions in the resorption compartment dissolve the HA mineral. The organic ECM is degraded by secretion of TRAP, cathepsin K, matrix metalloproteinase 9, and gelatinase and other enzymes, resulting in the formation of saucer-shaped Howship's lacunae on the surface of trabecular bone and dentin, and Haversian canals in cortical bone [21, 166].

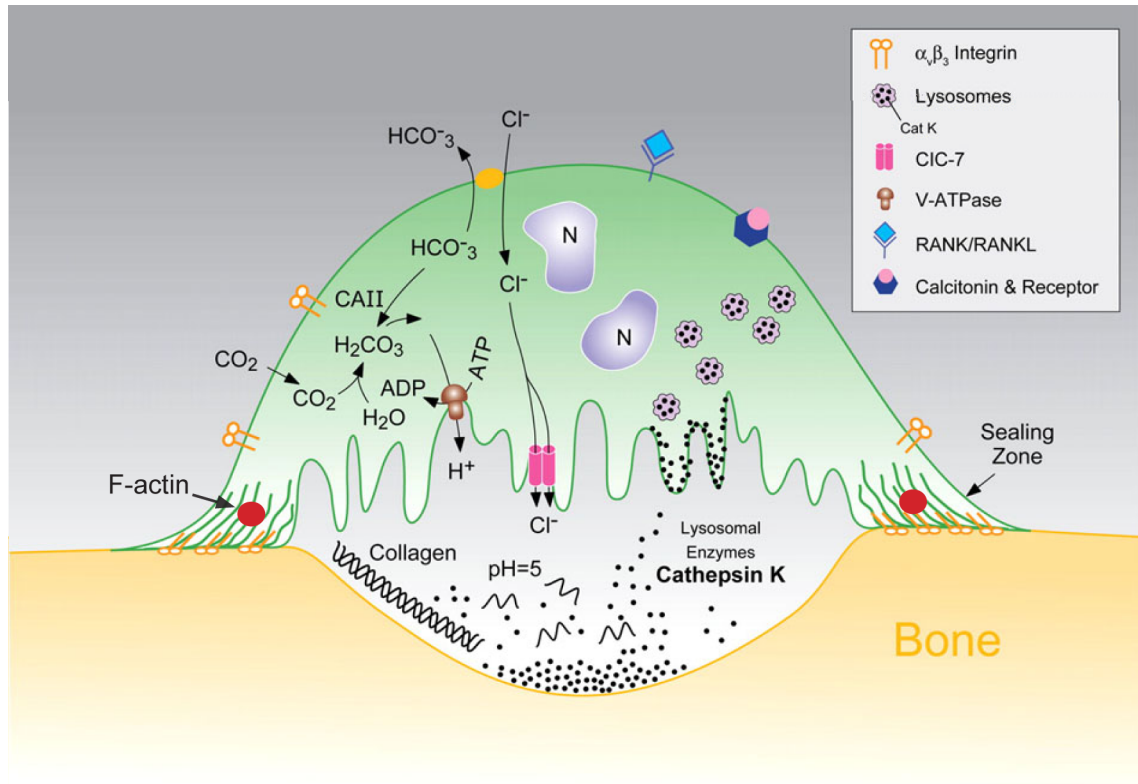


Figure 1.3 Schematic representation of a resorbing osteoclast. The osteoclast produces a sealing zone. The osteoclast acidifies the resorptive compartment by secreting H^+ and Cl^- ions for demineralization, and hydrolytic enzymes for degradation of type I collagen. Reprinted with permission from Reference [166] with permission (Appendix A).

1.6.4 Interaction with Biomaterials

The ideal resorbable biomaterial would be integrated into the physiological bone environment through “smooth assimilation”, wherein osteoblast bone formation occurs in concert with osteoclastic resorption of the biomaterial [167]. Degradation of resorbable biomaterials is mediated by cellular resorption and physiochemical dissolution [167]. A host of international standards on medical biomaterial resorption assays, characterize degradation under two separate conditions – degradation in an extreme environment (solution pH = 3) and degradation in a solution that mimics the common *in vivo* environment (pH = 7.4) [168]. However, many of the synthetic bone graft substitutes identified as resorbable are still present several years after implantation *in vivo* [168]. *In vivo* degradation consists of other factors beyond simply body fluid dissolution, including enzymes, body movements, and cell-mediated resorption [167, 168]. On the other hand, excessive *in vivo* biomaterial degradation prior to adequate bone formation can lead to detrimental results. As such, the determination of biomaterial resorbability using cell-based assays is an integral step prior to *in vivo* application [168].

1.6.4.1 Surface Chemistry

Osteoclast adhesion, differentiation and resorptive activity are influenced by the chemical composition of biomaterials. Chemical characteristics of bioceramics that affect osteoclast behavior *in vitro* include crystal phase [169-171], solubility [172] and carbonate content [173].

Bioceramics consisting of various CaP, such as monetite, TCP, DCPD, OCP, sintered HA and carbonated-HA have been investigated for their susceptibility to

osteoclastic resorption *in vitro*, with varying outcomes. Contradictory results regarding the resorption of sintered, crystalline HA have been reported [160]. Some investigators have shown osteoclastic resorption of sintered HA [174], while others have reported degradation of HA by osteoclasts only when in combination with TCP [170]. Furthermore, HA/TCP ceramics showed typical scallop-like resorption lacunae, whereas more soluble pure TCP ceramics had only island-like excavations. The difference in pit morphology was attributed to an inhibitory reaction to the increased release of Ca^{2+} from the more soluble, pure TCP.

Carbonate-substitution in biomimetic HA coating was shown to enhance resorption by osteoclasts *in vitro* in a particular study [171], whereas another study indicated that increased carbonate content in HA limited resorption [173]. The authors suggested that an increase in HA solubility (due to increase in carbonate substitution) does not necessarily correlate with increased osteoclastic resorption. Furthermore, a calcium-deficient HA also showed minimal degradation [169]. However, several other crystalline CaP (DCPD, OCP, monetite) undergo osteoclastic resorption *in vitro* [169, 171] and a decrease in CaP solubility inhibited osteoclastic resorption [172].

1.6.4.2 Surface Topography

Osteoclasts isolated from rat bone marrow [174], and osteoclast-like cells differentiated *in vitro* from human peripheral blood monocytes [175] showed increased adhesion and differentiation when cultured on surface-abraded sintered-HA discs with increased surface roughness. By contrast, osteoclast-like cells derived from human peripheral blood cells co-cultured with human bone marrow stromal cells, showed decreased TRAP activity when incubated on HA discs with increasing surface roughness

[175]. The area resorbed by osteoclasts was limited when rat bone marrow cells were cultured on rougher surfaces [174]. A similar effect was observed for osteoclast-like cells derived from human peripheral blood cells co-cultured with human bone marrow stromal cells, when plated on the rougher surfaces. Interestingly, the addition of M-CSF and RANKL negated any surface roughness influence of surface roughness. Furthermore, the opposite effect was reported for osteoclast-like cells cultured without supplementation with bone marrow cells [175]. However, the level of surface roughness of the sintered HA discs was well below the Ra value considered ideal for bone formation [148, 156]. Thus, the behavior of osteoclasts on optimal biomaterial surfaces remains poorly defined.

1.7 Rationale, Objectives and Hypotheses of the Research

The overall objective of this research was the synthesis of biomaterials for scaffolds for applications in tissue engineering and bone regeneration. In particular, our aim was to produce a composite biomaterial consisting of a PCL matrix reinforced with nano-scale HA to mimic the collagen and mineral organization of bone. The rationale was that composite biomaterials will have improved mechanical properties and will yield a mechanically competent material to maintain the porous structure of scaffolds *in vivo*. A further aim was to improve the biomaterial-cell interface by depositing a bone-like apatite coating on functionalized PCL substrates. Specifically, we sought to control the surface topography of biomimetic HA coatings to differentially regulate bone formation by osteoblasts and resorption by osteoclasts.

1.7.1 Synthesis of High-Aspect Ratio Hydroxyapatite Nanowires and Fabrication of Hydroxyapatite/Polycaprolactone Composites

Rationale – HA in the form of powders consisting of micro- and nano-sized particles, can be used as a reinforcing filler in polymer composites [123, 126], and calcium-phosphate bone cements [91, 176], and may impart their bioactive and osteoconductive properties [92, 177].

HA whiskers with high aspect ratios have been synthesized using a variety of hydrothermal precipitation methods [77-79]. However, the HA whiskers typically have diameter and length in the micrometer range. The current drive towards nanotechnology has shown that HA having at least one dimension in the nano-scale is required to obtain the high biological and mechanical functionality [92, 93, 95]. As such, nanowires and nanorods have been produced by hydrothermal processes utilizing surfactants and reverse micelle solutions, a method known as solvothermal synthesis [87-89]. However, concerns with use of solvothermal processes exists due to low aspect ratio [88, 89, 178], and the highly aggregated nature of the HA powders [87, 178]. As well, the use of surfactants and solvents may result in undesired organic impurities being incorporated into the final HA products [82, 89, 178].

Recently, HA nanowires and hollow microspheres were synthesized by hydrothermal processing of xonolite and calcium carbonate precursors of similar micro- and nano-scale dimensions and morphology [84]. It was suggested by these authors, that during hydrothermal processes, the scale and structure of the precursor starting material dictates the final morphologies of the HA product by dictating crystal nucleation and growth. Therefore, it would be beneficial to develop a method to produce phase pure HA

powders having nanowire morphology with high aspect ratio for use in nanocomposites. A novel method for the synthesis of nano-scale HA powders may be achieved by utilizing hydrothermal treatment in place of typical high temperature calcination of nano-scale amorphous CaP precursors produced via sol-gel chemistry.

Objectives

1. To develop a novel method for the synthesis of nano-scale HA by utilizing sol-gel chemistry in combination with hydrothermal processing.
2. To characterize morphology of sol-gel-hydrothermal synthesized powders, and quantitatively assess particle diameter distribution and aspect ratio.
3. To determine the effect of reaction pH and time on the control of particle diameter and length of sol-gel-hydrothermal synthesized powders.
4. To characterize HA crystals, presence of functional groups, and calcium to phosphorous ratio.
5. To fabricate HA/PCL nanocomposite biomaterials and assess HA particle distribution within the composite, and the resulting composite's mechanical properties.

Hypotheses

1. The nano-scale amorphous CaP precursors prepared by sol-gel chemistry provide a nano-precursor starting material for the synthesis of HA nano-wires.
2. The morphology of the HA powders, including particle diameter and length, can be controlled by adjusting hydrothermal reaction conditions and kinetics.
3. The nano-scale HA disperses homogeneously within a PCL matrix, and effectively reinforces the HA/PCL composites.

1.7.2 Control of Surface Topography in Biomimetic Calcium Phosphate Coatings

Rationale – The tailored design of surface topography offers an effective and facile strategy to improve the biological performance of implant and scaffold materials. *In vitro* cultures using osteoblasts have shown a remarkable osteogenic response to roughened biomaterial surfaces, with studies showing increased levels of differentiation and mineralization [157, 179]. Several *in vitro* and *in vivo* studies have identified an ideal surface roughness (Ra) in the range of 1 – 7 μm for inducing optimal changes in osteoblast behavior and stimulation of bone formation [148, 156, 157]. However, despite the multitude of research studies showing the potential of surface roughness to regulate osteogenic responses to biomaterials, few studies have attempted to directly design and control the surface topography of biomimetic coatings [180].

Objectives

1. To develop a method to control the surface topography and roughness of biomimetic HA coatings.
2. To assess the effect of SBF ion concentration and soaking time on the deposition of biomimetic CaP coatings.
3. To evaluate the CaP crystallography, presence of functional groups, and calcium to phosphorous ratio of deposited CaP coatings.
4. To evaluate and target HA coatings with isotropic surface topography and roughness at low and high resolution by characterization using profilometer and atomic force microscopy.

Hypotheses

1. The ionic concentrations of SBF and soaking time have controllable and reproducible effects on the surface topography of deposited CaP coatings.
2. HA coatings consisting of isotropic and complex surface topography can be deposited having surface roughness parameters within the range considered ideal for osteoblast differentiation and bone formation ($R_a = 1 - 7 \mu\text{m}$).

1.7.3 Surface Topography of Biomimetic Hydroxyapatite Coatings Differentially Regulates Osteoblast and Osteoclast Activity

Rationale – Biomaterials for orthopedic and dental applications may be coated with biomimetic HA to improve their bioactivity and osteoconductivity [96], and thus facilitating the *in vitro* differentiation of osteoblastic cells [181] and bone growth *in vivo* [66, 71, 182]. Furthermore, biomimetic carbonated-HA coatings are resorbed by osteoclasts *in vitro*, with classical resorption lacunae [171].

In vitro investigations using preosteoblasts cultured in osteogenic medium revealed differential cell viability, proliferation, and gene expression, towards biomimetic HA having varying crystal size [153]. The authors suggested that preosteoblasts respond to small changes in the apatite microstructure. However, the authors did not characterize the macroscopic surface topography and roughness. Therefore, it is not known whether changes in osteoblast behavior were due to differences in apatite crystal structure or the nano- and micro-topography of the HA coatings. Furthermore, the effect of surface topography on osteoclast activity remains poorly defined. Few studies have attempted to investigate the influence of biomaterial

surface roughness on osteoclast behavior. Those studies that have examined this question have reported widely varying results and utilized HA discs with roughness parameters well below those accepted as ideal for biomaterial design [174, 175].

Objectives

1. Determine the *in vitro* effect of surface topography of biomimetic HA on primary osteoblast attachment and focal adhesion formation.
2. Measure the gene expression of osteogenic marker genes (collagen I, alkaline phosphatases and osteocalcin) by osteoblasts cultured *in vitro* on biomimetic HA coatings with varying surface roughness considered ideal for biomaterial design.
3. Determine the effect *in vitro* of surface topography of biomimetic HA on TRAP activity and attachment of authentic osteoclasts.
4. Determine the effect of surface topography of biomimetic HA on osteoclast resorptive activity *in vitro*.
5. Assess the F-actin organization in the resorption apparatus of osteoclasts cultured on biomimetic HA with differential surface topographies.

Hypotheses

1. Biomimetic HA coatings with isotropic, complex and rough surface topography improve the attachment and differentiation of osteoblasts *in vitro*.
2. Surface roughness regulates the activity of authentic osteoclasts *in vitro*.

In Chapter 2, a novel synthesis method for the production of HA powders consisting of high aspect-ratio nanowires will be presented. The carbonated-HA

nanowires will be used as bioactive, reinforcing filler in a synthetic polymer matrix to yield nanocomposite biomaterials for application in bone regeneration. Chapter 3 will focus on the deposition of biomimetic CaP coatings on synthetic polymers. In particular, the control of surface topography of HA coatings will be demonstrated. Chapter 4 reports on the effect of the surface topography of these biomimetic HA coatings on the behavior of osteoblasts and osteoclasts. Chapter 5 will present our overall summary and conclusions, with a general discussion, as well as suggestions for future studies.

1.8 References

- [1] Einhorn TA. Clinically applied models of bone regeneration in tissue engineering research. *Clinical Orthopaedics and Related Research*. 1999:S59-67.
- [2] Bucholz RW. Nonallograft osteoconductive bone graft substitutes. *Clinical Orthopaedics and Related Research*. 2002:44-52.
- [3] Hak DJ. The use of osteoconductive bone graft substitutes in orthopaedic trauma. *The Journal of the American Academy of Orthopaedic Surgeons*. 2007;15:525-36.
- [4] Kelly CM, Wilkins RM. Treatment of benign bone lesions with an injectable calcium sulfate-based bone graft substitute. *Orthopedics*. 2004;27:s131-5.
- [5] LeGeros RZ. Calcium phosphates in oral biology and medicine. *Monographs in Oral Science*. 1991;15:1-201.
- [6] Nery EB, LeGeros RZ, Lynch KL, Lee K. Tissue response to biphasic calcium phosphate ceramic with different ratios of HA/beta TCP in periodontal osseous defects. *Journal of Periodontology*. 1992;63:729-35.
- [7] Woolf AD, Pflieger B. Burden of major musculoskeletal conditions. *Bull World Health Organization*. 2003;81:646-56.
- [8] Burg KJ, Porter S, Kellam JF. Biomaterial developments for bone tissue engineering. *Biomaterials*. 2000;21:2347-59.
- [9] Laurencin CT, Khan Y, Kofron M, El-Amin S, Botchwey E, Yu X, et al. The ABJS Nicolas Andry Award: Tissue engineering of bone and ligament: a 15-year perspective. *Clinical Orthopaedics and Related Research*. 2006;447:221-36.
- [10] Bauer TW, Muschler GF. Bone graft materials. An overview of the basic science. *Clinical Orthopaedics and Related Research*. 2000;371:10-27.
- [11] Salgado AJ, Coutinho OP, Reis RL. Bone tissue engineering: state of the art and future trends. *Macromolecular Bioscience*. 2004;4:743-65.
- [12] Hutmacher DW. Scaffolds in tissue engineering bone and cartilage. *Biomaterials*. 2000;21:2529-43.
- [13] Tomford WW. Transmission of disease through transplantation of musculoskeletal allografts. *Journal of Bone and Joint Surgery-American Volume*. 1995;77A:1742-54.
- [14] Laurencin C, Khan Y, El-Amin SF. Bone graft substitutes. *Expert Review of Medical Devices*. 2006;3:49-57.
- [15] Caplan AI, Goldberg VM. Principles of tissue engineered regeneration of skeletal tissues. *Clinical Orthopaedics and Related Research*. 1999:S12-6.

- [16] Vacanti CA, Bonassar LJ. An overview of tissue engineered bone. *Clinical Orthopaedics and Related Research*. 1999;S375-81.
- [17] Hutmacher DW, Schantz JT, Lam CX, Tan KC, Lim TC. State of the art and future directions of scaffold-based bone engineering from a biomaterials perspective. *Journal of Tissue Engineering and Regenerative Medicine*. 2007;1:245-60.
- [18] Cancedda R, Giannoni P, Mastrogiacomo M. A tissue engineering approach to bone repair in large animal models and in clinical practice. *Biomaterials*. 2007;28:4240-50.
- [19] Stevens MM, Marini RP, Schaefer D, Aronson J, Langer R, Shastri VP. In vivo engineering of organs: the bone bioreactor. *Proceedings of the National Academy of Sciences of the United States of America*. 2005;102:11450-5.
- [20] Rho JY, Kuhn-Spearing L, Zioupos P. Mechanical properties and the hierarchical structure of bone. *Medical Engineering & Physics*. 1998;20:92-102.
- [21] Clarke B. Normal bone anatomy and physiology. *Clinical Journal of the American Society of Nephrology : CJASN*. 2008;3 Suppl 3:S131-9.
- [22] Pasteris JD, Wopenka B, Valsami-Jones E. Bone and tooth mineralization: Why apatite? *Elements*. 2008;4:97-104.
- [23] Gelse K, Poschl E, Aigner T. Collagens--structure, function, and biosynthesis. *Advanced Drug Delivery Reviews*. 2003;55:1531-46.
- [24] Parfitt AM. Targeted and nontargeted bone remodeling: relationship to basic multicellular unit origination and progression. *Bone*. 2002;30:5-7.
- [25] Smith DW, Gardiner BS, Dunstan C. Bone balance within a cortical BMU: local controls of bone resorption and formation. *PLoS one*. 2012;7:e40268.
- [26] Lossdorfer S, Schwartz Z, Wang L, Lohmann CH, Turner JD, Wieland M, et al. Microrough implant surface topographies increase osteogenesis by reducing osteoclast formation and activity. *Journal of Biomedical Materials Research Part A*. 2004;70:361-9.
- [27] Davies JE. Bone bonding at natural and biomaterial surfaces. *Biomaterials*. 2007;28:5058-67.
- [28] Siggelkow H, Rebenstorff K, Kurre W, Niedhart C, Engel I, Schulz H, et al. Development of the osteoblast phenotype in primary human osteoblasts in culture: comparison with rat calvarial cells in osteoblast differentiation. *Journal of Cellular Biochemistry*. 1999;75:22-35.
- [29] Brekke JH, Toth JM. Principles of tissue engineering applied to programmable osteogenesis. *Journal of Biomedical Materials Research*. 1998;43:380-98.

- [30] Jayakumar R, Menon D, Manzoor K, Nair SV, Tamura H. Biomedical applications of chitin and chitosan based nanomaterials-A short review. *Carbohydrate Polymers*. 2011;82:227-32.
- [31] Thein-Han WW, Kitiyanant Y, Misra RDK. Chitosan as scaffold matrix for tissue engineering. *Materials Science and Technology*. 2008;24:1062-75.
- [32] Srinivasan S, Jayasree R, Chennazhi KP, Nair SV, Jayakumar R. Biocompatible alginate/nano bioactive glass ceramic composite scaffolds for periodontal tissue regeneration. *Carbohydrate Polymers*. 2011;87:274-83.
- [33] Rezwani K, Chen QZ, Blaker JJ, Boccaccini AR. Biodegradable and bioactive porous polymer/inorganic composite scaffolds for bone tissue engineering. *Biomaterials*. 2006;27:3413-31.
- [34] Allo BA, Costa DO, Dixon SJ, Mequanint K, Rizkalla AS. Bioactive and biodegradable nanocomposites and hybrid biomaterials for bone regeneration. *Journal of Functional Biomaterials*. 2012;3:432-63.
- [35] Puppi D, Chiellini F, Piras AM, Chiellini E. Polymeric materials for bone and cartilage repair. *Progress in Polymer Science*. 2010;35:403-40.
- [36] Kweon H, Yoo MK, Park IK, Kim TH, Lee HC, Lee HS, et al. A novel degradable polycaprolactone networks for tissue engineering. *Biomaterials*. 2003;24:801-8.
- [37] Corden TJ, Jones IA, Rudd CD, Christian P, Downes S, McDougall KE. Physical and biocompatibility properties of poly-epsilon-caprolactone produced using in situ polymerisation: a novel manufacturing technique for long-fibre composite materials. *Biomaterials*. 2000;21:713-24.
- [38] Sun H, Mei L, Song C, Cui X, Wang P. The in vivo degradation, absorption and excretion of PCL-based implant. *Biomaterials*. 2006;27:1735-40.
- [39] Elfick AP. Poly(epsilon-caprolactone) as a potential material for a temporary joint spacer. *Biomaterials*. 2002;23:4463-7.
- [40] Jones DS, Djokic J, McCoy CP, Gorman SP. Poly(epsilon-caprolactone) and poly(epsilon-caprolactone)-polyvinylpyrrolidone-iodine blends as ureteral biomaterials: characterisation of mechanical and surface properties, degradation and resistance to encrustation in vitro. *Biomaterials*. 2002;23:4449-58.
- [41] Tsuji H, Ishida T, Fukuda N. Surface hydrophilicity and enzymatic hydrolyzability of biodegradable polyesters: 1. Effects of alkaline treatment. *Polymer International*. 2003;52:843-52.
- [42] Tsuji H, Ishizaka T. Porous biodegradable polyesters. II. Physical properties, morphology, and enzymatic and alkaline hydrolysis of porous poly(epsilon-caprolactone) films. *Journal of Applied Polymer Science*. 2001;80:2281-91.

- [43] Agrawal CM, Ray RB. Biodegradable polymeric scaffolds for musculoskeletal tissue engineering. *Journal of Biomedical Materials Research*. 2001;55:141-50.
- [44] Woodward SC, Brewer PS, Moatamed F, Schindler A, Pitt CG. The intracellular degradation of poly(epsilon-caprolactone). *Journal of Biomedical Materials Research*. 1985;19:437-44.
- [45] El-Ghannam A. Bone reconstruction: from bioceramics to tissue engineering. *Expert Review of Medical Devices*. 2005;2:87-101.
- [46] Wilson J, Low SB. Bioactive ceramics for periodontal treatment: comparative studies in the Patus monkey. *Journal of Applied Biomaterials*. 1992;3:123-9.
- [47] Posner AS. Crystal chemistry of bone mineral. *Physiological Reviews*. 1969;49:760-92.
- [48] LeGeros RZ. Properties of osteoconductive biomaterials: calcium phosphates. *Clinical Orthopaedics and Related Research*. 2002:81-98.
- [49] Ivanova TI, Frank-Kamenetskaya OV, Kol'tsov AB, Ugolkov VL. Crystal structure of calcium-deficient carbonated hydroxyapatite. Thermal decomposition. *Journal of Solid State Chemistry*. 2001;160:340-9.
- [50] Nakano T, Kaibara K, Tabata Y, Nagata N, Enomoto S, Marukawa E, et al. Unique alignment and texture of biological apatite crystallites in typical calcified tissues analyzed by microbeam X-ray diffractometer system. *Bone*. 2002;31:479-87.
- [51] LeGeros RZL, J. P. Dense Hydroxyapatite. *Advanced Series in Ceramics*. 1993;1:12.
- [52] Pang YX, Bao X. Influence of temperature, ripening time and calcination on the morphology and crystallinity of hydroxyapatite nanoparticles. *Journal of the European Ceramic Society*. 2003;23:1697-704.
- [53] Jevtic M, Mitri, M., kapin, S., Janar, B. , Ignjatovi, N. and Uskokovi, D. Crystal Structure of Hydroxyapatite Nanorods Synthesized by Sonochemical Homogeneous Precipitation. *Crystal Growth and Design*. 2008;8.
- [54] Tas AC. Formation of calcium phosphate whiskers in hydrogen peroxide solutions at 90°C. *Journal of the American Ceramic Society*. 2007;90.
- [55] Liu DM, Troczynski T, Tseng WJ. Water-based sol-gel synthesis of hydroxyapatite: process development. *Biomaterials*. 2001;22:1721-30.
- [56] Taş AC. Molten Salt Synthesis of Calcium Hydroxyapatite Whiskers. *Journal of the American Ceramic Society*. 2001;84.

- [57] Ins S. N. YVK, Oleg I. L., Gustaaf V., Himadri S. G., Francisco G. and Masahiro Y. An Effective Morphology Control of Hydroxyapatite Crystals via Hydrothermal Synthesis. *Crystal Growth and Design*. 2009;9.
- [58] Kaili L JC, Yingjie Z, Wei W, Guofeng C, Yi Z and Meiling R. A Facile One-Step Surfactant-Free and Low-Temperature Hydrothermal Method to Prepare Uniform 3D Structured Carbonated Apatite Flowers. *Crystal Growth and Design*. 2009;9.
- [59] Oonishi H, Hench LL, Wilson J, Sugihara F, Tsuji E, Kushitani S, et al. Comparative bone growth behavior in granules of bioceramic materials of various sizes. *Journal of Biomedical Materials Research*. 1999;44:31-43.
- [60] LeGeros RZ, Lin S, Rohanizadeh R, Mijares D, LeGeros JP. Biphasic calcium phosphate bioceramics: preparation, properties and applications. *Journal of Materials Science-Materials in Medicine*. 2003;14:201-9.
- [61] Wilke A, Orth J, Lomb M, Fuhrmann R, Kienapfel H, Griss P, et al. Biocompatibility analysis of different biomaterials in human bone marrow cell cultures. *Journal of Biomedical Materials Research*. 1998;40:301-6.
- [62] Ciapetti G, Ambrosio L, Savarino L, Granchi D, Cenni E, Baldini N, et al. Osteoblast growth and function in porous poly epsilon -caprolactone matrices for bone repair: a preliminary study. *Biomaterials*. 2003;24:3815-24.
- [63] Li P. Biomimetic nano-apatite coating capable of promoting bone ingrowth. *Journal of Biomedical Materials Research Part A*. 2003;66:79-85.
- [64] Scaglione S, Iengo C, Fato M, Quarto R. Hydroxyapatite-coated polycaprolacton wide mesh as a model of open structure for bone regeneration. *Tissue Engineering Part A*. 2009;15:155-63.
- [65] Borsari V, Fini M, Giavaresi G, Tschon M, Chiesa R, Chiusoli L, et al. Comparative in vivo evaluation of porous and dense duplex titanium and hydroxyapatite coating with high roughnesses in different implantation environments. *Journal of Biomedical Materials Research Part A*. 2009;89:550-60.
- [66] Bigi A, Fini M, Bracci B, Boanini E, Torricelli P, Giavaresi G, et al. The response of bone to nanocrystalline hydroxyapatite-coated Ti13Nb11Zr alloy in an animal model. *Biomaterials*. 2008;29:1730-6.
- [67] Vasudev DV, Ricci JL, Sabatino C, Li P, Parsons JR. In vivo evaluation of a biomimetic apatite coating grown on titanium surfaces. *Journal of Biomedical Materials Research Part A*. 2004;69:629-36.
- [68] Schliephake H, Scharnweber D, Dard M, Robetaler S, Sewing A, Huttmann C. Biological performance of biomimetic calcium phosphate coating of titanium implants in the dog mandible. *Journal of Biomedical Materials Research Part A*. 2003;64:225-34.

- [69] Du C, Meijer GJ, van de Valk C, Haan RE, Bezemer JM, Hesselning SC, et al. Bone growth in biomimetic apatite coated porous Polyactive 1000PEGT70PBT30 implants. *Biomaterials*. 2002;23:4649-56.
- [70] Dekker RJ, de Bruijn JD, Stigter M, Barrere F, Layrolle P, van Blitterswijk CA. Bone tissue engineering on amorphous carbonated apatite and crystalline octacalcium phosphate-coated titanium discs. *Biomaterials*. 2005;26:5231-9.
- [71] Lickorish D, Guan L, Davies JE. A three-phase, fully resorbable, polyester/calcium phosphate scaffold for bone tissue engineering: Evolution of scaffold design. *Biomaterials*. 2007;28:1495-502.
- [72] Nagano M, Nakamura T, Kokubo T, Tanahashi M, Ogawa M. Differences of bone bonding ability and degradation behaviour in vivo between amorphous calcium phosphate and highly crystalline hydroxyapatite coating. *Biomaterials*. 1996;17:1771-7.
- [73] Geesink RG. Osteoconductive coatings for total joint arthroplasty. *Clinical Orthopaedics and Related Research*. 2002;53-65.
- [74] Barrere F, van der Valk CM, Dalmeijer RA, Meijer G, van Blitterswijk CA, de Groot K, et al. Osteogenicity of octacalcium phosphate coatings applied on porous metal implants. *Journal of Biomedical Materials Research Part A*. 2003;66:779-88.
- [75] Habibovic P, Van der Valk CM, Van Blitterswijk CA, De Groot K, Meijer G. Influence of octacalcium phosphate coating on osteoinductive properties of biomaterials. *Journal of Materials Science-Materials in Medicine*. 2004;15:373-80.
- [76] Habibovic P, Li JP, van der Valk CM, Meijer G, Layrolle P, van Blitterswijk CA, et al. Biological performance of uncoated and octacalcium phosphate-coated Ti6Al4V. *Biomaterials*. 2005;26:23-36.
- [77] Neira IS, Kolen'ko YV, Lebedev OI, Van Tendeloo G, Gupta HS, Guitian F, et al. An Effective Morphology Control of Hydroxyapatite Crystals via Hydrothermal Synthesis. *Crystal Growth & Design*. 2009;9:466-74.
- [78] Mizutani Y, Hattori M, Okuyama M, Kasuga T, Nogami M. Large-sized hydroxyapatite whiskers derived from calcium tripolyphosphate gel. *Journal of the European Ceramic Society*. 2005;25:3181-5.
- [79] Zhang H, Darvell BW. Synthesis and characterization of hydroxyapatite whiskers by hydrothermal homogeneous precipitation using acetamide. *Acta Biomaterialia*. 2010;6:3216-22.
- [80] Guo XY, Xiao P. Effects of solvents on properties of nanocrystalline hydroxyapatite produced from hydrothermal process. *Journal of the European Ceramic Society*. 2006;26:3383-91.

- [81] Liu JB, Ye XY, Wang H, Zhu MK, Wang B, Yan H. The influence of pH and temperature on the morphology of hydroxyapatite synthesized by hydrothermal method. *Ceramics International*. 2003;29:629-33.
- [82] Zhang CM, Yang J, Quan ZW, Yang PP, Li CX, Hou ZY, et al. Hydroxyapatite Nano- and Microcrystals with Multiformal Morphologies: Controllable Synthesis and Luminescence Properties. *Crystal Growth & Design*. 2009;9:2725-33.
- [83] Lin KL, Chang J, Liu XG, Chen L, Zhou YL. Synthesis of element-substituted hydroxyapatite with controllable morphology and chemical composition using calcium silicate as precursor. *Crystengcomm*. 2011;13:4850-5.
- [84] Lin KL, Liu XG, Chang J, Zhu YJ. Facile synthesis of hydroxyapatite nanoparticles, nanowires and hollow nano-structured microspheres using similar structured hard-precursors. *Nanoscale*. 2011;3:3052-5.
- [85] Mizutani Y, Hattori M, Okuyama M, Kasuga T, Nogami M. Carbonate-containing hydroxyapatite derived from calcium tripolyphosphate gel with urea. *Journal of Materials Science-Materials in Medicine*. 2005;16:709-12.
- [86] Gibson IR, Bonfield W. Novel synthesis and characterization of an AB-type carbonate-substituted hydroxyapatite. *Journal of Biomedical Materials Research*. 2002;59:697-708.
- [87] Cao MH, Wang YH, Guo CX, Qi YJ, Hu CW. Preparation of ultrahigh-aspect-ratio hydroxyapatite nanofibers in reverse micelles under hydrothermal conditions. *Langmuir*. 2004;20:4784-6.
- [88] Sun YX, Guo GS, Tao DL, Wang ZH. Reverse microemulsion-directed synthesis of hydroxyapatite nanoparticles under hydrothermal conditions. *Journal of Physics and Chemistry of Solids*. 2006;68:373-7.
- [89] Wei K, Lai C, Wang YJ. Solvothermal synthesis of calcium phosphate nanowires under different pH conditions. *Journal of Macromolecular Science Pure and Applied Chemistry*. 2006;43:1531-40.
- [90] Wang YJ, Lai C, Wei K, Chen XF, Ding Y, Wang ZL. Investigations on the formation mechanism of hydroxyapatite synthesized by the solvothermal method. *Nanotechnology*. 2006;17:4405-12.
- [91] Neira IS, Kolen'ko YV, Kommareddy KP, Manjubala I, Yoshimura M, Guitian F. Reinforcing of a Calcium Phosphate Cement with Hydroxyapatite Crystals of Various Morphologies. *Acs Applied Materials & Interfaces*. 2010;2:3276-84.
- [92] Sun F, Zhou H, Lee J. Various preparation methods of highly porous hydroxyapatite/polymer nanoscale biocomposites for bone regeneration. *Acta Biomaterialia*. 2011;7:3813-28.

- [93] Zhou H, Lee J. Nanoscale hydroxyapatite particles for bone tissue engineering. *Acta Biomaterialia*. 2011;7:2769-81.
- [94] Zhu W, Zhang X, Wang D, Lu W, Ou Y, Han Y, et al. Experimental study on the conduction function of nano-hydroxyapatite artificial bone. *Micro & Nano Letters*. 2010;5:19-27.
- [95] Chung EJ, Qiu H, Kodali P, Yang S, Sprague SM, Hwong J, et al. Early tissue response to citric acid-based micro- and nanocomposites. *Journal of Biomedical Materials Research Part A*. 2011;96:29-37.
- [96] LeGeros RZ. Properties of osteoconductive biomaterials: calcium phosphates. *Clinical Orthopaedics and Related Research*. 2002;395:81-98.
- [97] Barrere F, van Blitterswijk CA, de Groot K. Bone regeneration: molecular and cellular interactions with calcium phosphate ceramics. *International journal of nanomedicine*. 2006;1:317-32.
- [98] Ong JL, Appleford M, Oh S, Yang Y, Chen WH, Bunigardner JD, et al. The characterization and development of bioactive hydroxyapatite coatings. *Journal of the Minerals Metals and Materials Society*. 2006;58:67-9.
- [99] Sun L, Berndt CC, Gross KA, Kucuk A. Material fundamentals and clinical performance of plasma-sprayed hydroxyapatite coatings: a review. *Journal of Biomedical Materials Research*. 2001;58:570-92.
- [100] Kamitakahara M, Ohtsuki C, Miyazaki T. Coating of bone-like apatite for development of bioactive materials for bone reconstruction. *Biomedical Materials*. 2007;2:R17-23.
- [101] Ohtsuki C, Kamitakahara M, Miyazaki T. Coating bone-like apatite onto organic substrates using solutions mimicking body fluid. *Journal of Tissue Engineering and Regenerative Medicine*. 2007;1:33-8.
- [102] Kokubo T, Kushitani H, Sakka S, Kitsugi T, Yamamuro T. Solutions able to reproduce in vivo surface-structure changes in bioactive glass-ceramic A-W. *Journal of Biomedical Materials Research*. 1990;24:721-34.
- [103] Hata K, Kokubo T, Nakamura T, Yamamuro T. Growth of a Bonelike Apatite Layer on a Substrate by a Biomimetic Process. *Journal of the American Ceramic Society*. 1995;78:1049-53.
- [104] Kokubo T. Formation of biologically active bone-like apatite on metals and polymers by a biomimetic process. *Thermochimica Acta*. 1996;280:479-90.
- [105] Tanahashi M, Yao T, Kokubo T, Minoda M, Miyamoto T, Nakamura T, et al. Apatite Coating on Organic Polymers by a Biomimetic Process. *Journal of the American Ceramic Society*. 1994;77:2805-8.

- [106] Zhang RY, Ma PX. Porous poly(L-lactic acid)/apatite composites created by biomimetic process. *Journal of Biomedical Materials Research*. 1999;45:285-93.
- [107] Kim HM, Kishimoto K, Miyaji F, Kokubo T, Yao T, Suetsugu Y, et al. Composition and structure of the apatite formed on PET substrates in SBF modified with various ionic activity products. *Journal of Biomedical Materials Research*. 1999;46:228-35.
- [108] Uchida M, Kim HM, Kokubo T, Nawa M, Asano T, Tanaka K, et al. Apatite-forming ability of a zirconia/alumina nano-composite induced by chemical treatment. *Journal of Biomedical Materials Research*. 2002;60:277-82.
- [109] Tanahashi M, Matsuda T. Surface functional group dependence on apatite formation on self-assembled monolayers in a simulated body fluid. *Journal of Biomedical Materials Research*. 1997;34:305-15.
- [110] Barrere F, van Blitterswijk CA, de Groot K, Layrolle P. Nucleation of biomimetic Ca-P coatings on Ti6Al4V from a SBF x 5 solution: influence of magnesium. *Biomaterials*. 2002;23:2211-20.
- [111] Barrere F, van der Valk CM, Dalmeijer RAJ, van Blitterswijk CA, de Groot K, Layrolle P. In vitro and in vivo degradation of biomimetic octacalcium phosphate and carbonate apatite coatings on titanium implants. *Journal of Biomedical Materials Research Part A*. 2003;64A:378-87.
- [112] Wang J, Layrolle P, Stigter M, de Groot K. Biomimetic and electrolytic calcium phosphate coatings on titanium alloy: physicochemical characteristics and cell attachment. *Biomaterials*. 2004;25:583-92.
- [113] Barrere F, van Blitterswijk CA, de Groot K, Layrolle P. Influence of ionic strength and carbonate on the Ca-P coating formation from SBFx5 solution. *Biomaterials*. 2002;23:1921-30.
- [114] Habibovic P, Barrere F, van Blitterswijk CA, de Groot K, Layrolle P. Biomimetic hydroxyapatite coating on metal implants. *Journal of the American Ceramic Society*. 2002;85:517-22.
- [115] Barrere F, Layrolle P, van Blitterswijk CA, de Groot K. Biomimetic coatings on titanium: a crystal growth study of octacalcium phosphate. *Journal of Materials Science-Materials in Medicine*. 2001;12:529-34.
- [116] Chou YF, Chiou WA, Xu Y, Dunn JC, Wu BM. The effect of pH on the structural evolution of accelerated biomimetic apatite. *Biomaterials*. 2004;25:5323-31.
- [117] Tas AC, Bhaduri SB. Rapid coating of Ti6Al4V at room temperature with a calcium phosphate solution similar to 10x simulated body fluid. *Journal of Materials Research*. 2004;19:2742-9.

- [118] Zheng CY, Li SJ, Tao XJ, Hao YL, Yang R, Zhang L. Calcium phosphate coating of Ti-Nb-Zr-Sn titanium alloy. *Materials Science & Engineering C-Biomimetic and Supramolecular Systems*. 2007;27:824-31.
- [119] Yang F, Wolke JGC, Jansen JA. Biomimetic calcium phosphate coating on electrospun poly (epsilon-caprolactone) scaffolds for bone tissue engineering. *Chemical Engineering Journal*. 2008;137:154-61.
- [120] Li X, Xie J, Yuan X, Xia Y. Coating Electrospun Poly(epsilon-caprolactone) Fibers with Gelatin and Calcium Phosphate and Their Use as Biomimetic Scaffolds for Bone Tissue Engineering. *Langmuir*. 2008;24:14145-50.
- [121] Hench LL, Polak JM. Third-generation biomedical materials. *Science*. 2002;295:1014-7.
- [122] Wang M, Joseph R, Bonfield W. Hydroxyapatite-polyethylene composites for bone substitution: effects of ceramic particle size and morphology. *Biomaterials*. 1998;19:2357-66.
- [123] Roeder RK, Sproul MM, Turner CH. Hydroxyapatite whiskers provide improved mechanical properties in reinforced polymer composites. *Journal of Biomedical Materials Research Part A*. 2003;67:801-12.
- [124] Bhumiratana S, Grayson WL, Castaneda A, Rockwood DN, Gil ES, Kaplan DL, et al. Nucleation and growth of mineralized bone matrix on silk-hydroxyapatite composite scaffolds. *Biomaterials*. 2011;32:2812-20.
- [125] Muller FA, Gbureck U, Kasuga T, Mizutani Y, Barralet JE, Lohbauer U. Whisker-reinforced calcium phosphate cements. *Journal of the American Ceramic Society*. 2007;90:3694-7.
- [126] Wei G, Ma PX. Structure and properties of nano-hydroxyapatite/polymer composite scaffolds for bone tissue engineering. *Biomaterials*. 2004;25:4749-57.
- [127] Boissard CIR, Bourban PE, Tami AE, Alini M, Eglin D. Nanohydroxyapatite/poly(ester urethane) scaffold for bone tissue engineering. *Acta Biomaterialia*. 2009;5:3316-27.
- [128] Jack KS, Velayudhan S, Luckman P, Trau M, Grøndahl L, Cooper-White J. The fabrication and characterization of biodegradable HA/PHBV nanoparticle-polymer composite scaffolds. *Acta Biomaterialia*. 2009;5:2657-67.
- [129] Jayabalan M, Shalumon KT, Mitha MK, Ganesan K, Epple M. Effect of hydroxyapatite on the biodegradation and biomechanical stability of polyester nanocomposites for orthopaedic applications. *Acta Biomaterialia*. 2010;6:763-75.

- [130] Asran AS, Henning S, Michler GH. Polyvinyl alcohol-collagen-hydroxyapatite biocomposite nanofibrous scaffold: Mimicking the key features of natural bone at the nanoscale level. *Polymer*. 2010;51:868-76.
- [131] Laschke MW, Strohe A, Menger MD, Alini M, Eglin D. In vitro and in vivo evaluation of a novel nanosize hydroxyapatite particles/poly(ester-urethane) composite scaffold for bone tissue engineering. *Acta Biomaterialia*. 2010;6:2020-7.
- [132] Prabhakaran MP, Venugopal J, Ramakrishna S. Electrospun nanostructured scaffolds for bone tissue engineering. *Acta Biomaterialia*. 2009;5:2884-93.
- [133] Hartmann C. A Wnt canon orchestrating osteoblastogenesis. *Trends in Cell Biology*. 2006;16:151-8.
- [134] Komori T. Regulation of osteoblast differentiation by transcription factors. *Journal of Cellular Biochemistry*. 2006;99:1233-9.
- [135] Barrere F, van Blitterswijk CA, de Groot K. Bone regeneration: molecular and cellular interactions with calcium phosphate ceramics. *International journal of nanomedicine*. 2006;1:317-32.
- [136] Siebers MC, ter Brugge PJ, Walboomers XF, Jansen JA. Integrins as linker proteins between osteoblasts and bone replacing materials. A critical review. *Biomaterials*. 2005;26:137-46.
- [137] Anselme K. Osteoblast adhesion on biomaterials. *Biomaterials*. 2000;21:667-81.
- [138] Hall BK, Miyake T. All for one and one for all: condensations and the initiation of skeletal development. *Bioessays*. 2000;22:138-47.
- [139] Histing T, Garcia P, Matthys R, Leidinger M, Holstein JH, Kristen A, et al. An internal locking plate to study intramembranous bone healing in a mouse femur fracture model. *Journal of Orthopaedic Research*. 2010;28:397-402.
- [140] Tortelli F, Tasso R, Loiacono F, Cancedda R. The development of tissue-engineered bone of different origin through endochondral and intramembranous ossification following the implantation of mesenchymal stem cells and osteoblasts in a murine model. *Biomaterials*. 2010;31:242-9.
- [141] Mendonca G, Mendonca DB, Aragao FJ, Cooper LF. Advancing dental implant surface technology--from micron- to nanotopography. *Biomaterials*. 2008;29:3822-35.
- [142] Schweikl H, Muller R, Englert C, Hiller KA, Kujat R, Nerlich M, et al. Proliferation of osteoblasts and fibroblasts on model surfaces of varying roughness and surface chemistry. *Journal of Materials Science-Materials in Medicine*. 2007;18:1895-905.

- [143] Keselowsky BG, Collard DM, Garcia AJ. Surface chemistry modulates focal adhesion composition and signaling through changes in integrin binding. *Biomaterials*. 2004;25:5947-54.
- [144] Zreiqat H, Valenzuela SM, Nissan BB, Roest R, Knabe C, Radlanski RJ, et al. The effect of surface chemistry modification of titanium alloy on signalling pathways in human osteoblasts. *Biomaterials*. 2005;26:7579-86.
- [145] Zreiqat H, Howlett CR, Zannettino A, Evans P, Schulze-Tanzil G, Knabe C, et al. Mechanisms of magnesium-stimulated adhesion of osteoblastic cells to commonly used orthopaedic implants. *Journal of Biomedical Materials Research*. 2002;62:175-84.
- [146] Zreiqat H, Evans P, Howlett CR. Effect of surface chemical modification of bioceramic on phenotype of human bone-derived cells. *Journal of Biomedical Materials Research*. 1999;44:389-96.
- [147] Wieland M, Textor M, Spencer ND, Brunette DM. Wavelength-dependent roughness: a quantitative approach to characterizing the topography of rough titanium surfaces. *The International journal of oral & maxillofacial implants*. 2001;16:163-81.
- [148] Hacking SA, Tanzer M, Harvey EJ, Krygier JJ, Bobyn JD. Relative contributions of chemistry and topography to the osseointegration of hydroxyapatite coatings. *Clinical Orthopaedics and Related Research*. 2002;405:24-38.
- [149] Khang D, Lu J, Yao C, Haberstroh KM, Webster TJ. The role of nanometer and sub-micron surface features on vascular and bone cell adhesion on titanium. *Biomaterials*. 2008;29:970-83.
- [150] dos Santos EA, Farina M, Soares GA, Anselme K. Chemical and topographical influence of hydroxyapatite and beta-tricalcium phosphate surfaces on human osteoblastic cell behavior. *Journal of Biomedical Materials Research Part A*. 2009;89:510-20.
- [151] Deligianni DD, Katsala ND, Koutsoukos PG, Missirlis YF. Effect of surface roughness of hydroxyapatite on human bone marrow cell adhesion, proliferation, differentiation and detachment strength. *Biomaterials*. 2001;22:87-96.
- [152] Rosa AL, Beloti MM, van Noort R. Osteoblastic differentiation of cultured rat bone marrow cells on hydroxyapatite with different surface topography. *Dental Materials*. 2003;19:768-72.
- [153] Chou YF, Huang WB, Dunn JCY, Miller TA, Wu BM. The effect of biomimetic apatite structure on osteoblast viability, proliferation, and gene expression. *Biomaterials*. 2005;26:285-95.
- [154] Mendes VC, Moineddin R, Davies JE. The effect of discrete calcium phosphate nanocrystals on bone-bonding to titanium surfaces. *Biomaterials*. 2007;28:4748-55.

- [155] Orsini G, Piattelli M, Scarano A, Petrone G, Kenealy J, Piattelli A, et al. Randomized, controlled histologic and histomorphometric evaluation of implants with nanometer-scale calcium phosphate added to the dual acid-etched surface in the human posterior maxilla. *Journal of Periodontology*. 2007;78:209-18.
- [156] Hayes JS, Czekanska EM, Richards RG. The Cell-Surface Interaction. *Advances in Biochemical Engineering/Biotechnology*. 2012;126:1-31.
- [157] Bachle M, Kohal RJ. A systematic review of the influence of different titanium surfaces on proliferation, differentiation and protein synthesis of osteoblast-like MG63 cells. *Clinical Oral Implants Research*. 2004;15:683-92.
- [158] Wieland M, Textor M, Chehroudi B, Brunette DM. Synergistic interaction of topographic features in the production of bone-like nodules on Ti surfaces by rat osteoblasts. *Biomaterials*. 2005;26:1119-30.
- [159] Boyle WJ, Simonet WS, Lacey DL. Osteoclast differentiation and activation. *Nature*. 2003;423:337-42.
- [160] Minkin C, Marinho VC. Role of the osteoclast at the bone-implant interface. *Advances in Dental Research*. 1999;13:49-56.
- [161] Teti A, Marchisio PC, Zallone AZ. Clear zone in osteoclast function: role of podosomes in regulation of bone-resorbing activity. *American Journal of Physiology*. 1991;261:C1-7.
- [162] Destaing O, Saltel F, Geminard JC, Jurdic P, Bard F. Podosomes display actin turnover and dynamic self-organization in osteoclasts expressing actin-green fluorescent protein. *Molecular Biology of the Cell*. 2003;14:407-16.
- [163] Luxenburg C, Geblinger D, Klein E, Anderson K, Hanein D, Geiger B, et al. The architecture of the adhesive apparatus of cultured osteoclasts: from podosome formation to sealing zone assembly. *PloS one*. 2007;2:e179.
- [164] Saltel F, Destaing O, Bard F, Eichert D, Jurdic P. Apatite-mediated actin dynamics in resorbing osteoclasts. *Molecular Biology of the Cell*. 2004;15:5231-41.
- [165] Anderegg F, Geblinger D, Horvath P, Charnley M, Textor M, Addadi L, et al. Substrate adhesion regulates sealing zone architecture and dynamics in cultured osteoclasts. *PloS one*. 2011;6:e28583.
- [166] Rodan SB, Duong LT. Cathepsin K - A new molecular target for osteoporosis. *IBMS BoneKEy*. 2008;5:16-24.
- [167] Schilling A, Filke S, Brink S, Korbmacher H, Amling M, Rueger J. Osteoclasts and biomaterials. *European Journal of Trauma*. 2006;32:107-13.

- [168] Zhang Z, Egana JT, Reckhenrich AK, Schenck TL, Lohmeyer JA, Schantz JT, et al. Cell-based resorption assays for bone graft substitutes. *Acta Biomaterialia*. 2012;8:13-9.
- [169] Grossardt C, Ewald A, Grover LM, Barralet JE, Gbureck U. Passive and active in vitro resorption of calcium and magnesium phosphate cements by osteoclastic cells. *Tissue engineering Part A*. 2010;16:3687-95.
- [170] Yamada S, Heymann D, Bouler JM, Daculsi G. Osteoclastic resorption of calcium phosphate ceramics with different hydroxyapatite/beta-tricalcium phosphate ratios. *Biomaterials*. 1997;18:1037-41.
- [171] Leeuwenburgh S, Layrolle P, Barrere F, de Bruijn J, Schoonman J, van Blitterswijk CA, et al. Osteoclastic resorption of biomimetic calcium phosphate coatings in vitro. *Journal of Biomedical Materials Research*. 2001;56:208-15.
- [172] Winkler T, Hoenig E, Gildenhaar R, Berger G, Fritsch D, Janssen R, et al. Volumetric analysis of osteoclastic bioresorption of calcium phosphate ceramics with different solubilities. *Acta Biomaterialia*. 2010;6:4127-35.
- [173] Detsch R, Hagemeyer D, Neumann M, Schaefer S, Vortkamp A, Wuelling M, et al. The resorption of nanocrystalline calcium phosphates by osteoclast-like cells. *Acta Biomaterialia*. 2010;6:3223-33.
- [174] Gomi K, Lowenberg B, Shapiro G, Davies JE. Resorption of sintered synthetic hydroxyapatite by osteoclasts in vitro. *Biomaterials*. 1993;14:91-6.
- [175] Costa-Rodrigues J, Fernandes A, Lopes MA, Fernandes MH. Hydroxyapatite surface roughness: complex modulation of the osteoclastogenesis of human precursor cells. *Acta Biomaterialia*. 2012;8:1137-45.
- [176] Muller F, Gbureck U, Kasuga T, Mizutani Y, Barralet JE, Lohbauer U. Whisker-reinforced calcium phosphate cements. *Journal of the American Ceramic Society*. 2007;90:3694-7.
- [177] Okuda T, Ioku K, Yonezawa I, Minagi H, Gonda Y, Kawachi G, et al. The slow resorption with replacement by bone of a hydrothermally synthesized pure calcium-deficient hydroxyapatite. *Biomaterials*. 2008;29:2719-28.
- [178] Chen JD, Wang YJ, Wei K, Zhang SH, Shi XT. Self-organization of hydroxyapatite nanorods through oriented attachment. *Biomaterials*. 2007;28:2275-80.
- [179] Perizzolo D, Lacefield WR, Brunette DM. Interaction between topography and coating in the formation of bone nodules in culture for hydroxyapatite- and titanium-coated micromachined surfaces. *Journal of Biomedical Materials Research*. 2001;56:494-503.

- [180] Oyane A, Ishikawa Y, Yamazaki A, Sogo Y, Furukawa K, Ushida T, et al. Reduction of surface roughness of a laminin-apatite composite coating via inhibitory effect of magnesium ions on apatite crystal growth. *Acta Biomaterialia*. 2008;4:1342-8.
- [181] Hott M, Noel B, Bernache-Assolant D, Rey C, Marie PJ. Proliferation and differentiation of human trabecular osteoblastic cells on hydroxyapatite. *Journal of Biomedical Materials Research*. 1997;37:508-16.
- [182] Pek YS, Gao S, Arshad MS, Leck KJ, Ying JY. Porous collagen-apatite nanocomposite foams as bone regeneration scaffolds. *Biomaterials*. 2008;29:4300-5.

CHAPTER TWO

ONE- AND THREE-DIMENSIONAL GROWTH OF HYDROXYAPATITE NANOWIRES DURING SOL-GEL- HYDROTHERMAL SYNTHESIS¹

¹Chapter 2 has been reproduced (with some modifications) with permission from:
Costa, D. O., Dixon, S. J., and Rizkalla, A. S. (2012). One- and three-dimensional
growth of hydroxyapatite nanowires during sol-gel-hydrothermal synthesis. *Acs Applied
Materials & Interfaces*, 4(3), 1490-1499. Copyright © 2012, American Chemical
Society.

2.1 Chapter Summary

Nanoscale hydroxyapatite (HA) is an optimal candidate biomaterial for bone tissue engineering due to its bioactive and osteoconductive properties. In this study, micro- and nano-scale HA particles with rod and wire-like morphology were synthesized by a novel sol-gel-hydrothermal process. Sol-gel chemistry was used to produce a dry gel containing amorphous calcium phosphate (ACP), which was used as a precursor material in a hydrothermal process. The sol-gel-hydrothermal products were characterized by scanning electron microscopy (SEM), X-ray diffraction (XRD), and Fourier transform infrared spectroscopy (FTIR) to determine particle morphology, crystal structure, and the presence of chemical functional groups. A pure HA crystal was synthesized, which underwent both one- and three-dimensional growth, resulting in tunable microrod and nanorod, and wire morphologies. The effects of solution pH and reaction time on particle diameter and length were assessed. Particle diameter ranged from 25 nm to 800 nm and decreased with increase in solution pH, while both particle length and diameter increased as the hydrothermal process was prolonged. Nanowire HA powders (10-50 wt%) were mixed with poly(ϵ -caprolactone) (PCL) to produce PCL/HA composites. Fracture surfaces of PCL/HA composites showed a well-dispersed and homogeneous distribution of HA nanowires within the PCL matrix. Mechanical testing revealed a significant ($p < 0.05$) increase in the Young's and compressive moduli of PCL/HA composites compared to PCL alone, with 50 wt% HA producing a 3-fold increase in Young's modulus from 193 to 665 MPa and 2-fold increase in compressive modulus from 230 to 487 MPa. These HA nanowires can be used to reinforce polymer composites and are excellent biomaterials for tissue engineering of bone.

2.2 Introduction

Hydroxyapatite (HA), $\text{Ca}_{10}(\text{PO}_4)_6(\text{OH})_2$, is a synthetic ceramic that has attracted much attention for biomedical applications owing to its chemical and structural similarity to the mineral constituent of human bone and teeth [1]. HA is biocompatible and osteoconductive [2], serving as an excellent biomaterial for use as bone graft substitutes [3], and implant coatings [4]. In particular, HA powders consisting of micro- and nano-sized particles, can be used to reinforce polymer composites [5, 6], and calcium-phosphate bone cements [7, 8].

Two common methods of HA synthesis are sol-gel and hydrothermal processes. Sol-gel synthesis methods involve atomic level molecular mixing, providing control of composition and chemical homogeneity [9, 10]. However, sol-gel powders require calcination at high temperature in the presence of air to produce crystalline products. Moreover, sol-gel HA synthesis is often accompanied by the formation of secondary phases such as calcium oxide and tricalcium phosphate (TCP) [9, 10], and gives rise to granular particle shapes [10, 11]. Alternatively, HA powders with controlled particle size, morphology and crystallinity have been successfully synthesized by a variety of hydrothermal methods [12, 13]. Hydrothermal homogenous precipitation is capable of producing HA whiskers with high aspect ratio [14]. However, the HA whiskers have diameter and length scales in the micron-range, and it is known that having at least one dimension in the nano-scale size range optimizes the biological and mechanical functionality of HA [15-17]. Recently, HA nanowires and hollow microspheres were synthesized by hydrothermal processing of xonolite nanowire and calcium carbonate microsphere precursors of similar micro- and nano-scale dimensions [18]. It was found

that the scale and structure of the precursor material dictated the final morphologies of the HA product. Furthermore, hydrothermal treatment of calcium silicate-based starting materials can produce various element-substituted HA nano-structures [19]. Thus, in hydrothermal processes, characteristics of the precursors determine crystal nucleation and growth, and therefore dictate the final morphology of the product. Surfactants and reverse micelle solutions in solvothermal processes can be used to produce nanowires and nanorods of varying aspect ratios [20-22]. Surfactants provide organized organic templates that guide the synthesis and growth of inorganic nanomaterials through geometric, electrostatic and stereochemical interactions. However, HA products from solvothermal synthesis are typically of low aspect ratio [21-23], and highly aggregated [20, 23], and the presence of surfactants and solvents during the solvothermal process may result in undesired organic components being incorporated into the final HA products [21, 23, 24]. Therefore, the goal of the present study was to develop a method for the synthesis of HA nanowires with high aspect ratio.

In the present study, a novel method is presented for the synthesis of HA nanowires with high aspect ratio. Sol-gel chemistry was used to produce a nano-scale amorphous calcium phosphate (ACP). The subsequent nano-ACP was subjected to hydrothermal treatment in aqueous solvent to induce the formation of crystalline HA micro- and nanowires. To our knowledge, this is the first report of the synthesis of high purity HA nanowires by a tunable crystal growth mechanism using a combination sol-gel-hydrothermal method. By varying the initial pH of the aqueous solvent/sol-gel precursor mixture and the hydrothermal synthesis time, HA powders with varying particle diameters and lengths were obtained. This aqueous based hydrothermal treatment of a sol-gel product is a simple, cost effective, and environmentally friendly synthesis

route, offering a high degree of control on the particle morphology of the HA product. The as produced nano-scale HA powders were used as a reinforcing filler in polycaprolactone (PCL) composites. These nano-scale HA-embedded PCL composites mimic the nano-apatite/collagen composite of bone. Therefore, such materials are excellent candidates for the production of scaffolds for bone tissue engineering applications.

2.3 Materials and Methods

2.3.1 Materials

Triethyl phosphite (TEP, 98%), calcium nitrate tetrahydrate ($\text{CaNO}_3 \cdot 4\text{H}_2\text{O}$, 99%), sodium hydroxide (NaOH, 98.5%), ammonium hydroxide (NH_4OH , 30%), anhydrous ethanol (EtOH), and dichloromethane (DCM, 99.5%) were purchased from Sigma-Aldrich (Milwaukee, WI). Poly(ϵ -caprolactone) (PCL) (CAPA 6800, MW 80 000 g/mol) was generously donated by Solvay Chemicals Inc. (Houston, TX).

2.3.2 Preparation of dried Calcium Phosphate (CaP) Gel

A dry CaP gel was prepared by a sol-gel method similar to that developed by Liu et al [10]. Briefly, TEP solution was diluted in EtOH such that the concentration was 1.8 M. A small amount of water was added to the phosphite sol (6:1 molar ratio), and the mixture was sealed in a round-bottom flask and stirred vigorously for 30 min. The solution was allowed to age for 24 h to ensure complete hydrolysis of phosphite. A stoichiometric amount of $\text{CaNO}_3 \cdot 4\text{H}_2\text{O}$ dissolved in EtOH, was added drop-wise to the phosphite sol such that the Ca/P ratio was 1.67. The resulting mixture was stirred

vigorously for 30 min and aged at room temperature for 24 h. The sol was dried at 80 °C to produce a white gel which was ground to a fine powder using a mortar and pestle.

2.3.3 Hydrothermal Treatment

For hydrothermal treatment, 0.5 g of the dried CaP gel was suspended in 30 ml aqueous solution and vigorously stirred for 30 min. Aqueous solutions used as suspension medium were selected to achieve the desired pH. Aqueous solvents included deionized H₂O, NH₄OH (0.1 M) and NaOH (5 M). Suspensions were ultrasonically treated for 5 min and vigorously stirred for 30 min. The effect of pH on HA synthesis and particle morphology was determined by setting the initial pH of the CaP gel aqueous suspension to 5.20, 7.50 or 13.70. Suspensions were poured into a 125-ml Teflon-lined acid digestion bomb (Parr Instrumentation Company, Moline, IL) and heated to 170 °C using a band heater. Heating was regulated using a thermocouple, and a temperature and process controller (iSeries, Omega, Stamford, CT). For each initial pH condition, the hydrothermal treatment time was 6, 16 or 24 h. At the end of each time period, the bomb was cooled by means of a fan to room temperature and the product, which formed as white precipitates, had settled to the bottom of the Teflon liner. The aqueous solvent was carefully decanted and the particles were collected, washed with deionized H₂O several times and sedimented. The recovered pellet was dried at 50 °C and ground into a fine powder using a mortar and pestle.

2.3.4 Scanning Electron Microscopy (SEM) and Energy Dispersive X-ray Spectroscopy (EDX)

Particle morphology was examined using a FIB/SEM LEO 1540XB microscope (Carl Zeiss, Göttingen, Germany) equipped with an energy dispersive X-ray spectrometer for elemental analysis. Samples were first coated with 3 nm osmium metal using a Filgen OPC-80T instrument. Representative images were selected from three fields of view for each synthesis condition. Mean particle diameter calculations were determined by measuring a total of 300 particles from three fields of view ($n=300$) using *ImageJ* software (National Institutes of Health, USA). Elemental analysis of powders was performed by EDX on three fields of view for each synthesis condition ($n=3$).

2.3.5 X-ray Diffraction Analysis (XRD)

Crystal structures of the powders were determined by XRD using a Rotaflex RTP 300 RC (Rigaku Co., Japan) operating on $\text{CoK}\alpha$ radiation at 45 kV and 160 mA. Spectra were collected in the 2θ range between 5° and 65° , with 0.05° step and $10^\circ/\text{min}$ scan speed. 2θ for equivalent $\text{CuK}\alpha$ radiation was obtained using Bragg's Law, $\lambda = 2d \cdot \sin \theta$, where $\lambda = 1.54056$ and 1.79026 \AA for Cu and Co, respectively [25].

2.3.6 Fourier Transform Infrared Spectroscopy (FTIR)

Functional group identification of the CaP gel and hydrothermally synthesized powders were obtained by FTIR using a Bruker Vector 22 (Bruker Optics LTD, Milton, ON). Specimens were prepared by mixing 4 wt% of each sample with potassium bromide (KBr) and then pressing into a pellet. Specimens were analyzed at a resolution

of 4 cm^{-1} and transmittance spectrums from 4000 to 500 cm^{-1} wavenumbers were collected.

2.3.7 Preparation of PCL and PCL/HA Composites

PCL specimens were prepared by dissolving PCL pellets in DCM to produce a 12 wt% PCL mixture. The solvent was allowed to evaporate in a fume hood to yield a PCL film. The PCL film was heat-pressed at $100\text{ }^{\circ}\text{C}$ and 670 N for 2 min. PCL/HA composites were produced by adding HA powder, synthesized at a pH of 13.70 for 24 h, to DCM and stirring for 15 min, and sonicating for 5 min. PCL was then added to the HA/DCM suspension to produce a PCL/HA slurry containing 10-50 wt% HA. The PCL/HA slurry was cast in a glass dish and the solvent evaporated in a fume hood. The resulting PCL/HA films were heat pressed at $100\text{ }^{\circ}\text{C}$ and 670 N for 2 min. Fracture surfaces of PCL/HA composites were prepared for SEM analysis and EDX elemental mapping by submerging 60:40 (w/w) PCL:HA samples in liquid nitrogen and subsequent fracturing.

2.3.8 Mechanical Testing of PCL/HA Composites

Mechanical properties were determined using an Instron 3345 universal testing machine (Instron, Canton, MA) equipped with a 500 N (tension) and 5 kN (compression) load cell. For tensile testing, 10 mm x 30 mm specimens were cut from the PCL and PCL/HA films using a sharp blade. For compressive tests, cylindrical specimens (diameter=6 mm, length=5-9 mm) were prepared by slicing the PCL and PCL/HA films and adding 0.3 g to a stainless steel mold. The mold was heated at $100\text{ }^{\circ}\text{C}$ for 30 min and

heat pressed at 100 °C and 670 N for 2 min. Prepared specimens were soaked in deionized H₂O at 37 °C for 24 h prior to testing. For each group, 5 independent specimens ($n=5$) were tested in tension and compression at a crosshead speed of 1 mm/min. Stress-strain relationships were obtained from the load and displacement data. The Young's and compressive moduli were determined by calculating the slope of the linear portion of the stress-strain curves. The tensile strength, defined as the maximum stress achieved, and the compressive stress at 10% strain were obtained from the stress-strain curves of each specimen. Nonlinear regression analysis was performed to determine the correlation between HA content and the stiffness and strength of the PCL/HA composites.

2.4 Results

2.4.1 FTIR, XRD, and SEM Analysis of CaP Gel

Drying of the aged sol at 70 °C removed the EtOH solvent and produced a white gel. FTIR (Fig. 2.1 (a)) and XRD (Fig. 2.1 (b)) spectra of the CaP gel were obtained. From FTIR of the CaP gel (Fig. 2.1 (a)), typical peaks attributed to PO₄³⁻ groups are seen by the sharp ν_3 P-O asymmetric stretching band at 1040 cm⁻¹ and a broad band in the range of 600-500 cm⁻¹, characteristic of O-P-O bending of the ν_4 PO₄³⁻ groups in apatite [26]. This featureless broadband suggests a disordered phosphate structure in the CaP gel, indicating the presence of ACP in the CaP gel precursor [1]. Crystalline nitrate peaks are also evident at 730, 812, 1350, and 1420 cm⁻¹. P-H and P=O at 2450 cm⁻¹ and 1100 cm⁻¹, respectively, are characteristic of hydrolyzed phosphite. H₂O in the precursor produced a significant broad band at 3400 cm⁻¹ and sharp peak at 1630 cm⁻¹. XRD

spectra of the CaP gel (Fig 2.1 (b)) confirms the presence of a crystalline nitrate in the form of $\text{Ca}(\text{NO}_3)_2$ anhydride. All visible peaks in the XRD spectra could be ascribed to $\text{Ca}(\text{NO}_3)_2$, with the major peaks at $2\theta = 20.2, 26.2$ and 41.1° (JCPDS # 7-204) [27]. SEM was performed on a large particle of the CaP gel after being ground by mortar and pestle (Fig. 2.1 (c)). The surfaces of CaP gel particles were featureless, typical of amorphous products [28].

In summary, FTIR and SEM analyses of the CaP gel indicated the successful synthesis of an ACP precursor.

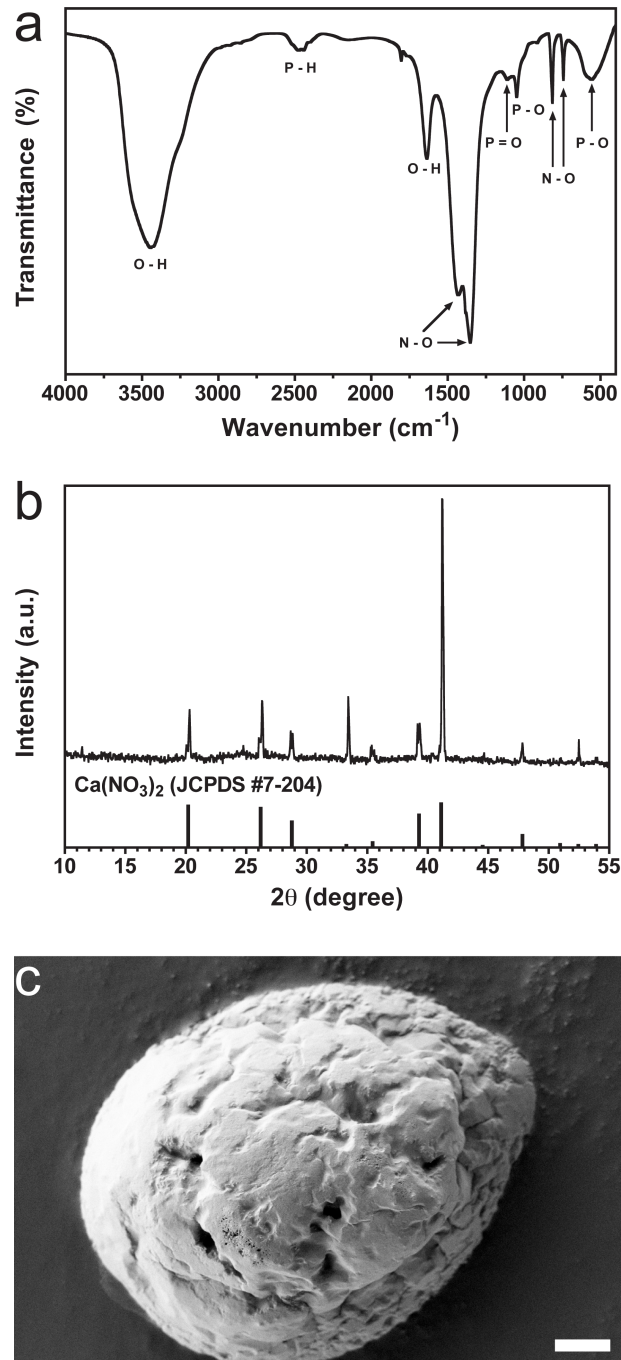


Figure 2.1 Dried CaP Gel. (a) FTIR, (b) XRD and (c) SEM of the CaP gel produced after drying the 24 h aged sol-gel at 70 °C. Representative of two independent samples. At the bottom of the XRD spectrum is the Joint Committee on Powder Diffraction Standards (JCPDS # 7-204) pattern for Ca(NO₃)₂ [27]. Scale bar = 1 μm.

2.4.2 SEM Analysis of Powders Produced by Hydrothermal Treatment

The combination of a sol-gel method with hydrothermal treatment produced powders consisting of particles having micro- and nanowire shapes. When the initial pH of the aqueous solvent/CaP gel suspension was slightly acidic at 5.20, powders consisting of particles with diameters ranging from 20 – 800 nm were produced (Fig. 2.2 (a-c)). The image and frequency distribution plot at 6 h (Fig. 2.2 (a)) revealed short nanorods with diameters of 30 nm as determined from the best fit value of the non-linear regression curve. Increasing the hydrothermal reaction time to 16 h (Fig. 2.2 (b)) resulted in growth of the long axis of the particle, with only a minor increase in the diameter. Further crystal growth was seen by extending the reaction time to 24 h, which increased particle length and radial growth (Fig. 2.2 (c)). The SEM images and corresponding frequency distribution plots highlight the dependence of particle morphology on hydrothermal time. Allowing the hydrothermal reaction to proceed to 24 h resulted in a large shift of the mean particle diameter to 300 nm and broadening of the particle diameter distribution plots (Fig. 2.2 (d)), indicating greater inhomogeneity in particle diameter. The particles varied from short nanorods with L/D (length/diameter) of ~ 9 at 6 h to nanowires and microwires with L/D in the range of 50 to 80 at both 16 and 24 h.

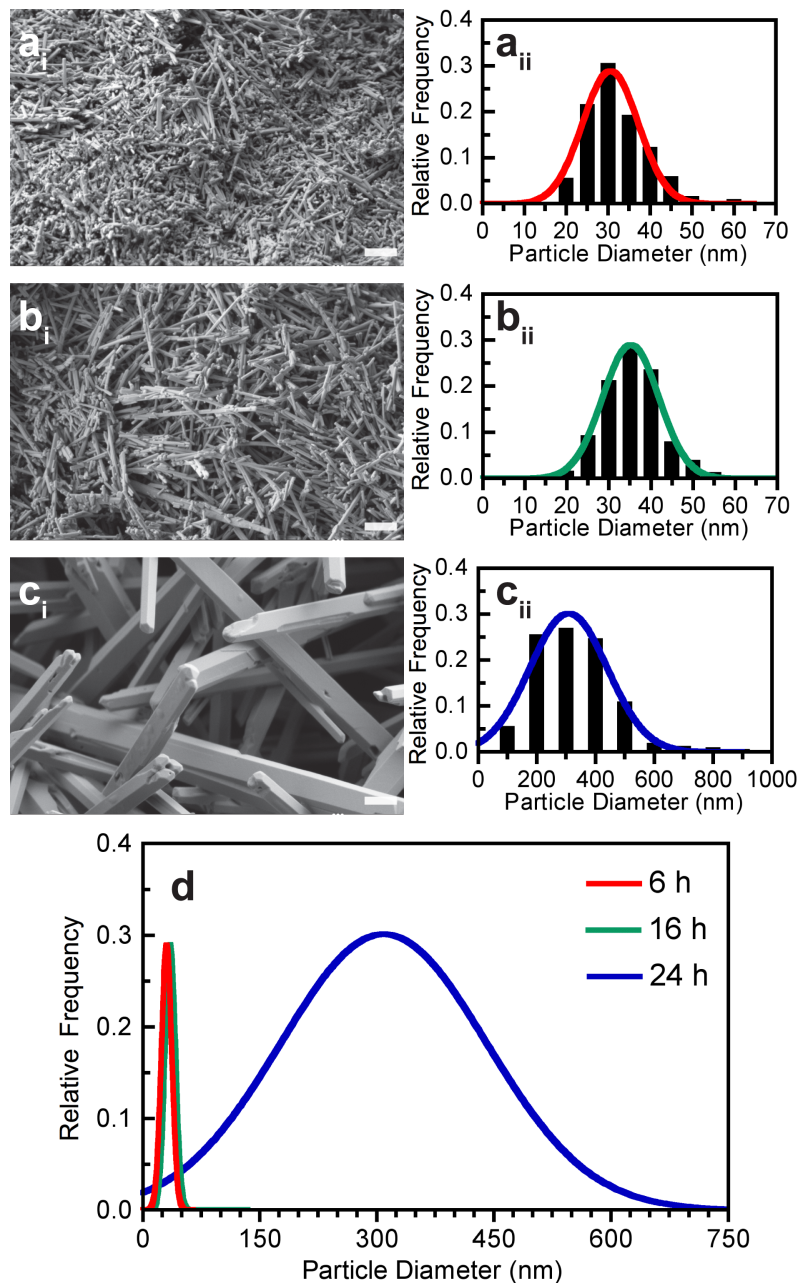


Figure 2.2 Hydrothermal synthesis at pH 5.20: (i) SEM images and (ii) particle diameter frequency distribution plots of CaP gel powders after hydrothermal treatment for (a) 6 h, (b) 16 h, and (c) 24 h. Hydrothermal time effect illustrated by (d) non-linear regression curves of the particle diameter distributions obtained from measuring 100 particle diameters for three fields of view ($n = 300$). Scale bar = 500 nm.

Increasing the initial pH using NH_4OH or NaOH permitted tuning of nanowire diameter. The addition of aqueous NH_4OH (0.1 M) to H_2O slurries was used to achieve a pH of 7.50. SEM micrographs (Fig. 2.3 (a-c)) showed substantial reduction in particle diameter compared to powders produced under acidic conditions, with particle diameters ranging from 20 to 200 nm. Six-h hydrothermal reaction produced short nanorods having diameters of 35 nm and a narrow size distribution (Fig. 2.3 (a)). Extending the hydrothermal time to 16 h resulted in the formation of nanowires with growth in the long axis (Fig. 2.3(b_i)), whereas little growth was seen in the radial direction as illustrated by the comparable distribution plots at 6 and 16 h (Fig. 2.3 (a_{ii}) *versus* Fig. 2.3 (b_{ii})). In contrast, crystal growth in both the long axis and radial directions occurred at 24 h (Fig. 2.3 (c)), giving rise to a broad distribution in particle diameter (Fig. 2.3 (c_{ii})). When compared to the particle morphology observed at earlier time points, the 24 h reaction time resulted in a distribution that was no longer represented by a Gaussian distribution, but rather was skewed to the right due to the crystal growth along the radial axis (Fig. 2.3 (d)). The particles varied from long nanorods with L/D of ~ 15 at 6 h to nanowires with L/D in the range of 60 to 90 at 16 and 24 h.

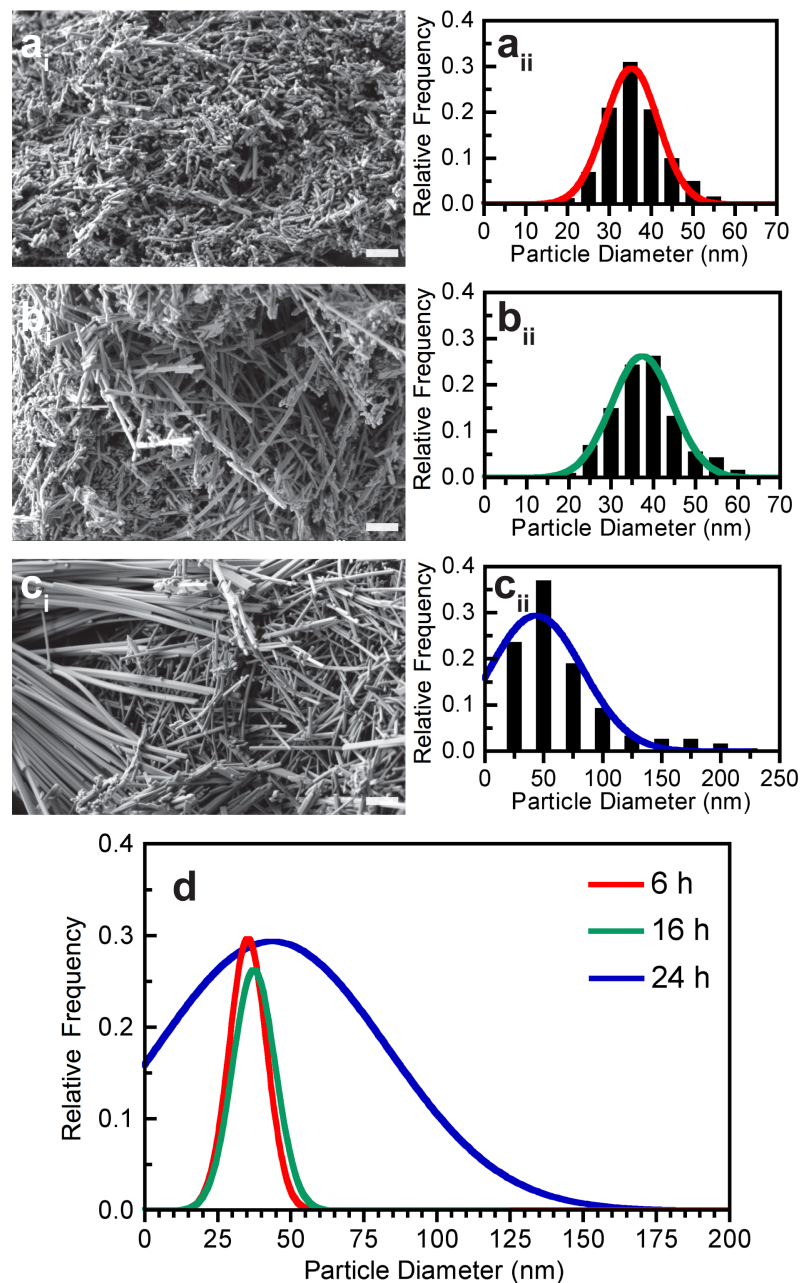


Figure 2.3 Hydrothermal synthesis at pH 7.50: (i) SEM images and (ii) particle diameter frequency distribution plots of CaP gel powders after hydrothermal treatment for (a) 6 h, (b) 16 h, and (c) 24 h. Hydrothermal time effect illustrated by (d) non-linear regression curves of the particle diameter distributions obtained from measuring 100 particle diameters for three fields of view ($n = 300$). Scale bar = 500 nm.

When aqueous 5 M NaOH was used to increase the initial pH to 13.70, there was a further reduction in particle diameter (Fig. 2.4 (a-c)), with the majority of particle diameters ranging from 15 to 100 nm. Nanorods produced after 6 h (Fig. 2.4 (a)), underwent crystal growth resulting in the formation of long nanowires by 16 h, the majority of which had diameters of ~ 25 nm (Fig. 2.4 (b)). Further hydrothermal treatment induced radial crystal growth resulting in a bimodal distribution of diameters, with nanowires having diameters in the ranges of 25 to 50 nm and 55 to 75 nm (Fig. 2.4 (c_i)). In contrast to the crystal growth observed at lower pH (5.20 and 7.50), the non-linear regression curves for pH 13.70 did not display as large an increase in breadth at 24 h (Fig 2.4 (d)), although there was a slight increase in mean diameter. Particles varied from long nanorods with $L/D \sim 17$ at 6 h to nanowires with L/D in the range of 60 to 100 at 16 and 24 h. We also assessed whether processing (sedimentation and grinding) affected the morphology of the micro- and nanowires. Using SEM, we found no apparent difference in the morphology of samples that were processed (Figs. 2.2-2.4) *versus* those that were not (Fig. 2.5).

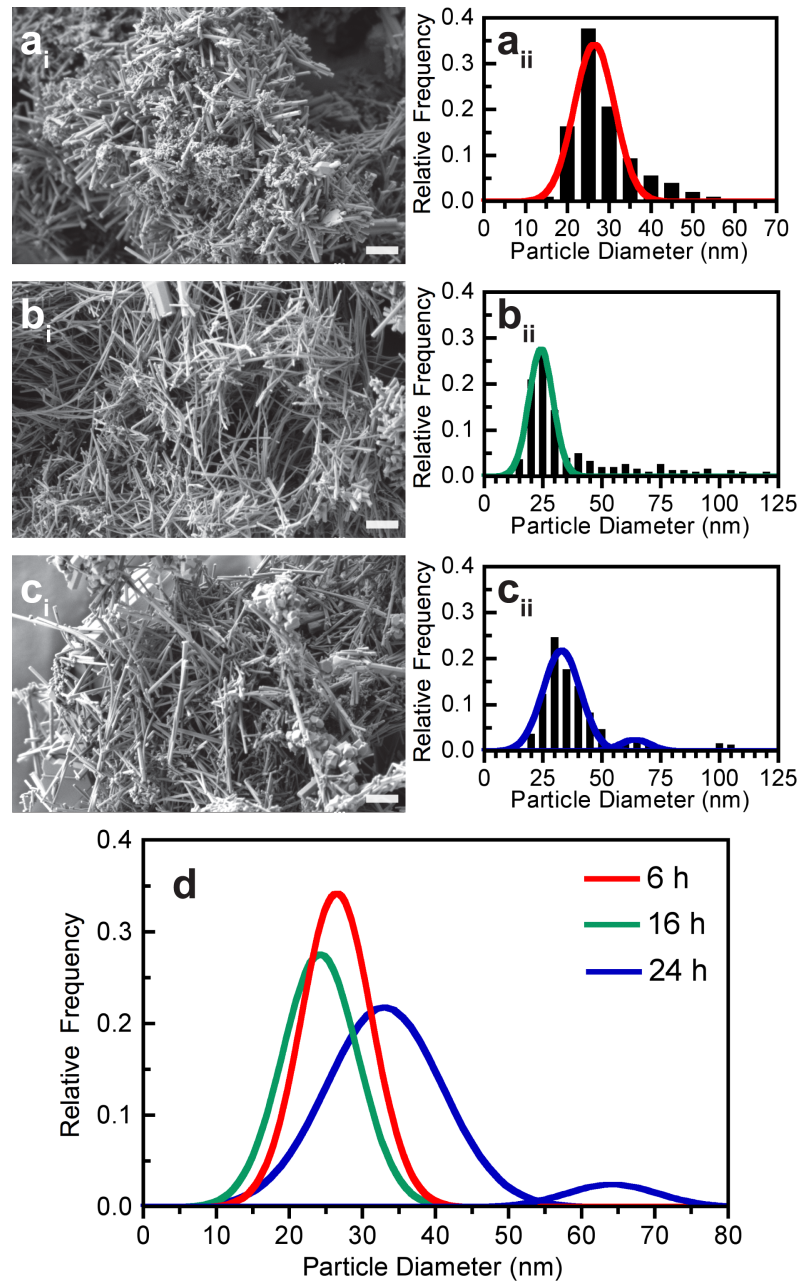


Figure 2.4 Hydrothermal synthesis at pH 13.70: (i) SEM images and (ii) particle diameter frequency distribution plots of CaP gel powders after hydrothermal treatment for (a) 6 h, (b) 16 h, and (c) 24 h. Hydrothermal time effect illustrated by (d) non-linear regression curves of the particle diameter distributions obtained from measuring 100 particle diameters for three fields of view ($n = 300$). Scale bar = 500 nm.

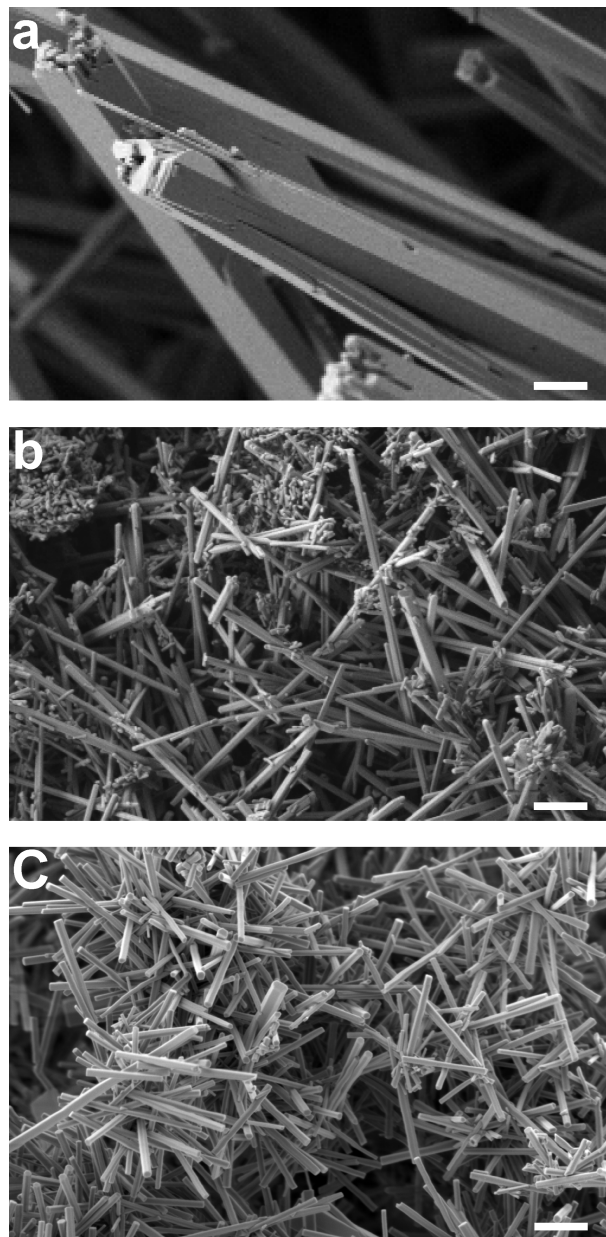


Figure 2.5 SEM analysis of HA micro- and nanowires synthesized for 24 h under hydrothermal conditions at initial pH of (a) 5.20, (b) 7.50, and (c) 13.70. SEM images reveal no observable difference in particle morphology as compared to powders that have been washed and recovered by centrifugation. Scale bar = 500 nm.

The average particle diameters (Table 2.1) showed no statistical differences ($p>0.05$) between powders produced at 6 and 16 h for any of the initial pH values, indicating that any observed growth occurs exclusively at the long axis of the particles. However, prolonging the hydrothermal treatment to 24 h resulted in significant increases ($p<0.05$) in the nanowire diameter as crystal growth occurred at the radial axes. The effect of initial pH on the particle diameter is not significant ($p>0.05$) at 6 and 16 h. However, at 24 h, there were significant decreases in diameter with increasing pH ($p<0.05$).

These results demonstrate the ability to produce nanorods and nanowires with tunable aspect ratios by applying a hydrothermal treatment to a dried sol-gel product composed of ACP.

Table 2.1 Particle Diameter of Sol-Gel-Hydrothermal Powders.

pH	Particle Diameter (nm)		
	6 h	16 h	24 h
5.20	32.6 ± 0.5 ^a	36.3 ± 0.6 ^a	343.2 ± 10.5 ^b
7.50	38.9 ± 1.3 ^a	38.9 ± 0.6 ^a	65.8 ± 2.3 ^c
13.70	29.8 ± 0.7 ^a	38.3 ± 1.5 ^{a,d}	44.2 ± 2.3 ^d

Particle diameter values are mean ± SD calculated from the average of 3 fields of view and 100 measurements per field of view ($n=300$). Statistical significance determined by a two-way ANOVA and a Bonferroni post-test. Effect of hydrothermal time and pH on particle diameter was determined, where matching letters indicate groups with no statistical difference ($p>0.05$) in particle diameter values as measured using ImageJ software.

2.4.3 XRD Analysis of Nanoparticles Produced by Hydrothermal Treatment

For all durations of hydrothermal treatment, the XRD spectra of powders produced with an initial pH of 5.20 or 7.50 revealed a crystalline and pure HA (Fig. 2.6 (a, b)). All visible peaks in the XRD spectra could be ascribed to HA, with the major peaks at $2\theta = 31.8, 32.2$ and 32.9° corresponding to the (211), (112) and (300) diffraction planes of crystalline HA (JCPDS # 9-432) [1, 27].

XRD spectra of the powders produced at an initial pH of 13.70 (Fig. 2.6 (c)) indicated the presence of Ca(OH)_2 in conjunction with HA at 6 h of hydrothermal treatment (revealed by peaks at $2\theta = 18.1, 34.5$ and 47.2° ; JCPDS # 44-1481) [27]. However, when the hydrothermal synthesis time was extended to 16 and 24 h, only HA was detected.

The HA powders produced after 24 h, independent of the initial pH, displayed a stronger preference for the (300) XRD reflection ($2\theta = 32.9^\circ$) compared to the JCPDS standard, consistent with crystal growth along the c-axis which leads to increased development of the a-plane [12]. The XRD spectra of the as produced powders indicated the successful synthesis of crystalline HA nano-rods and wires with varying aspect ratios.

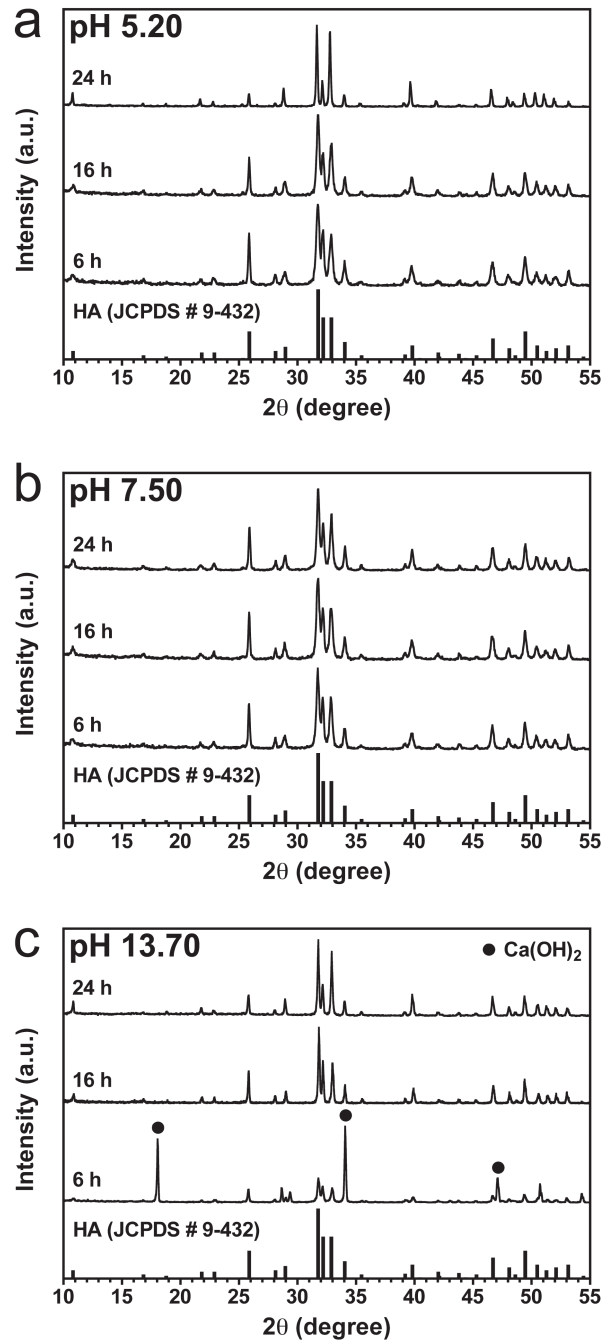


Figure 2.6 XRD spectra of the CaP gel after hydrothermal treatment in aqueous solvent at initial pH of (a) 5.20, (b) 7.50 and (c) 13.70 for 6, 16 and 24 h. Representative of two independent samples. At the bottom of each spectrum is the Joint Committee on Powder Diffraction Standards (JCPDS # 9-432) pattern for HA [27].

2.4.4 FTIR Characterization of Nanoparticles Produced by Hydrothermal Treatment

FTIR analysis confirmed the synthesis of HA after hydrothermal treatment of the CaP gel precursor (Fig. 2.7 (a-c)). Similar bands were observed for powders produced at the different initial pH values and spectra are in good agreement with IR data reported for HA [26]. Characteristic peaks of PO_4^{3-} groups are clearly visible at 1091 and 1028 cm^{-1} for the ν_3 asymmetric stretching mode of the P–O bond, and 960 cm^{-1} for the ν_1 symmetric stretching mode of the P–O bond. Additionally, the broad, featureless peak in the range 600-500 cm^{-1} , which was initially seen in the spectra of the CaP gel (Fig. 2.1(a)), resolved into well-defined bands at 600 and 561 cm^{-1} attributable to the ν_4 bending mode of the O–P–O bond of PO_4^{3-} groups found in apatite.

Hydroxyl (OH) groups were identified by peaks at 3570 and 631 cm^{-1} , ascribed to the stretching and librational modes of hydroxyl anions, the latter indicating a well-developed OH component in the apatite structure [26, 29]. CO_3^{2-} substitution in the HA lattice is noticeably absent for HA produced at pH 5.20 and 7.50. CO_3^{2-} substitution was only seen at the elevated pH of 13.70 (Fig. 2.7 (c)), signified by the presence of broad bands at 1450 and 1415 cm^{-1} (A and B-type HA), and sharp peak at 877 cm^{-1} (A-type HA), typical of partial CO_3^{2-} substitution [1, 26]. For pH 13.70, the absence of the librational band of OH^- (631 cm^{-1}) at 6 and 16 h suggests possible CO_3^{2-} substitution for OH groups characteristic of A-type HA [1]. The additional stretching peak at 3644 cm^{-1} (Fig. 2.7 (c)) at 6 h is associated with the presence of $\text{Ca}(\text{OH})_2$ [30]. The decrease in CO_3^{2-} bands at 1450, 1415 and 877 cm^{-1} from 6 to 24 h correlates with the appearance of the OH librational peak at 631 cm^{-1} , consistent with a decrease in CO_3^{2-} substitution.

CO_3^{2-} substitution is likely due to the presence of atmospheric CO_2 , which dissolved in the H_2O used for slurry preparation and hydrothermal processing.

2.4.5 EDX Elemental Analysis of Nanoparticles Produced by Hydrothermal Treatment

EDX elemental analysis was used to measure the calcium to phosphorous (Ca/P) atomic ratio of HA powders produced after hydrothermal treatment (Table 2.2), and indicate a predominately stoichiometric HA crystal ($\text{Ca/P} \approx 1.67$). There was no significant difference ($p > 0.05$) among the Ca/P ratios of the HA powders synthesized at different pH conditions or hydrothermal treatment times, with the exception of HA produced at pH 13.70 for 6 h ($p < 0.05$). The powder synthesized at pH 13.70 for 6 h is a mixture containing HA and $\text{Ca}(\text{OH})_2$, as determined by XRD (Fig 2.6 (c)), which accounts for the elevated Ca/P atomic ratio. Even at 16 and 24 h, the Ca/P atomic ratio of HA synthesized at pH 13.70 was higher compared to the other pHs (although this was not significant), likely reflecting lower PO_4^{3-} content. FTIR spectra of HA synthesized at pH 13.70 (Fig. 2.7 (c)) indicate the presence of CO_3^{2-} bands for both A and B-type HA. Therefore, it is possible that the higher Ca/P atomic ratios are attributed to partial substitution of CO_3^{2-} for PO_4^{3-} in the HA crystal lattice characteristic of B-type HA [31].

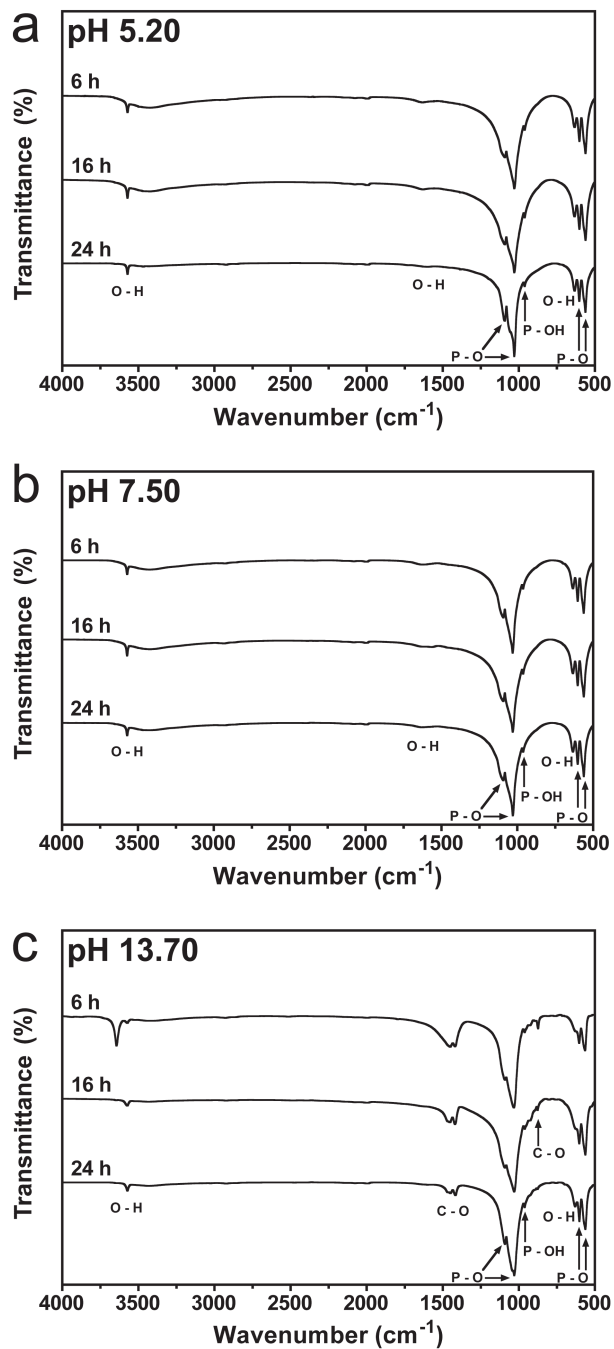


Figure 2.7 FTIR transmittance spectra of the CaP gel after hydrothermal treatment in aqueous solvent at initial pH of (a) 5.20, (b) 7.50 and (c) 13.70 for 6, 16 and 24 h. Representative of two independent samples.

In summary, the EDX analysis indicated the synthesis of stoichiometric HA at pH 5.20 and 7.50, whereas an initial pH of 13.70 appeared to yield a Ca-rich, B-type CO_3^{2-} -substituted HA. Thus, the EDX results, combined with SEM, XRD and FTIR, reveal a pH of 13.70 and hydrothermal treatment time of 16 – 24 h as ideal for the synthesis of A- and B-type CO_3^{2-} -substituted HA nanowires. In this regard, CO_3^{2-} -substituted HA is thought to be more bioactive than stoichiometric HA [31].

Table 2.2 Ca/P Atomic Ratio of Sol-Gel-Hydrothermal Powders.

pH	Ca/P		
	6 h	16 h	24 h
5.20	1.68 ± 0.03^a	1.60 ± 0.04^a	1.68 ± 0.04^a
7.50	1.66 ± 0.06^a	1.60 ± 0.06^a	1.71 ± 0.10^a
13.70	3.71 ± 1.62^b	1.89 ± 0.03^a	2.19 ± 0.23^a

Ca/P values are mean \pm SD calculated from the average of 3 fields of view ($n=3$). Statistical significance was determined by a two-way ANOVA and a Bonferroni post-test. Effect of hydrothermal time and pH on Ca/P was determined, where matching letters indicate groups with no statistical difference ($p>0.05$) in Ca/P values as measured using EDX.

2.4.6 Characterization of PCL/HA Composites

Composite biomaterials were prepared by combining HA nanowires as reinforcing filler with a PCL matrix. HA nanowires (produced by hydrothermal treatment at pH 13.70 for 24 h) were mixed with PCL in the following ratios (PCL:HA, w/w): 90:10, 80:20, 70:30, 60:40 and 50:50. Fractured surfaces of PCL/HA composites comprising 40 w/w % HA were characterized by SEM and EDX elemental mapping (Fig. 2.8) to determine the distribution of HA nanowires in the PCL matrix. SEM image (Fig. 2.8 (a)) of a fractured PCL/HA composite showed a uniform matrix, free of void

spaces. EDX elemental mapping of the same field demonstrates a relatively homogeneous distribution of carbon (Fig. 2.8 (b)), the major elemental component of PCL. Furthermore, EDX mapping of calcium (Fig. 2.8 (c)) and phosphorus (Fig. 2.8 (d)), found exclusively in HA, reveals a uniform distribution. Higher magnification SEM images (Fig. 2.8 (e, f)) clearly showed HA nanowires embedded isotropically within the PCL matrix and in intimate contact with the polymer (arrow). From the SEM analysis and EDX elemental mapping of PCL/HA composite fracture surfaces, we conclude that HA nanowires were uniformly and homogeneously distributed throughout the composite biomaterial.

The Young's modulus and tensile strength of PCL and PCL/HA composites were determined by uniaxial tensile testing (Fig. 2.9). An exponential increase ($p < 0.05$) in the Young's modulus was observed with increase in the HA content (Fig. 2.9 (a)). On the other hand, an increase in HA content resulted in an exponential decrease ($p < 0.05$) in the tensile strength of the composites compared to unfilled PCL (Fig. 2.9 (b)).

Similarly, compressive modulus and stress at 10% strain increased exponentially ($p < 0.05$) with HA content (Fig. 2.10 (a, b)). It was noted that during compressive testing of PCL and PCL/HA composites, bulging of the cylindrical specimens occurred resulting in an increase in the cross-sectional area of the specimens. This increase in cross-sectional area, and the ductile nature of PCL and PCL/HA composites produced a continuous increase in the measured stress during deformation. Therefore, the compressive stress at 10% strain was chosen to assess the strength of PCL and PCL/HA composites.

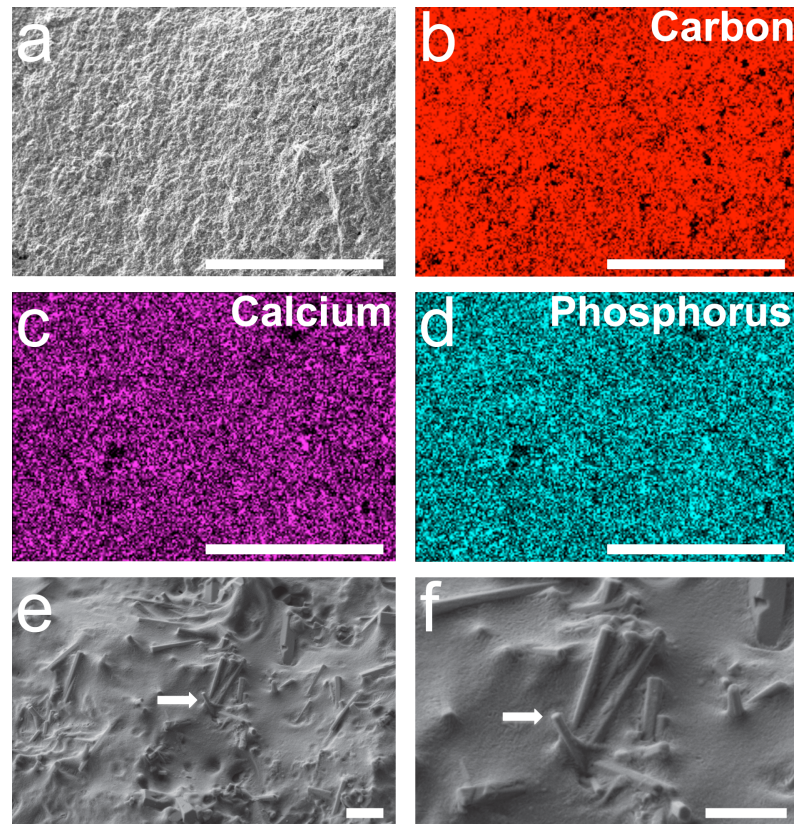


Figure 2.8 SEM and EDX analysis of PCL/HA composites: (a) SEM image, and EDX elemental mapping of (b) carbon, (c) calcium, and (d) phosphorus of fractured surface of PCL/HA composite (40% HA synthesized by sol-gel-hydrothermal process at pH 13.70 for 24 h) (scale bars = 400 μm). Higher magnification (e, f) SEM images of fractured surface show HA nanowires (e.g. arrow) embedded in the PCL matrix (scale bars = 500 nm).

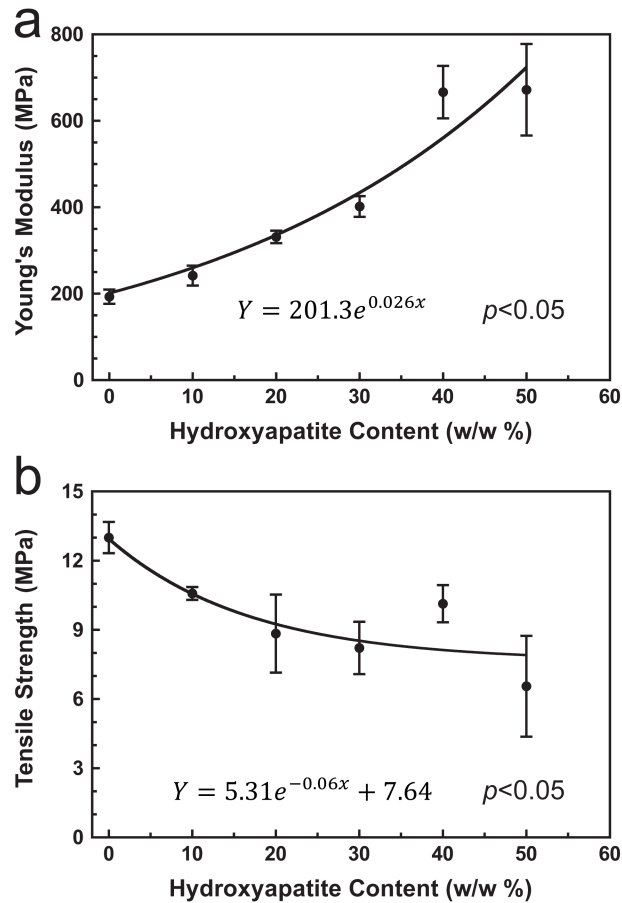


Figure 2.9 Uniaxial tensile testing of PCL/HA composites: (a) Young's modulus and (b) tensile strength of PCL/HA composites comprising 0-50 w/w % HA synthesized by sol-gel-hydrothermal process at pH 13.70 for 24 h. Young's modulus and tensile strength values are the mean calculated from five independent samples ($n=5$) measured under uniaxial tension. Error bars are standard deviation. The solid line represents the nonlinear regression analysis fit of tensile test data ($p < 0.05$).

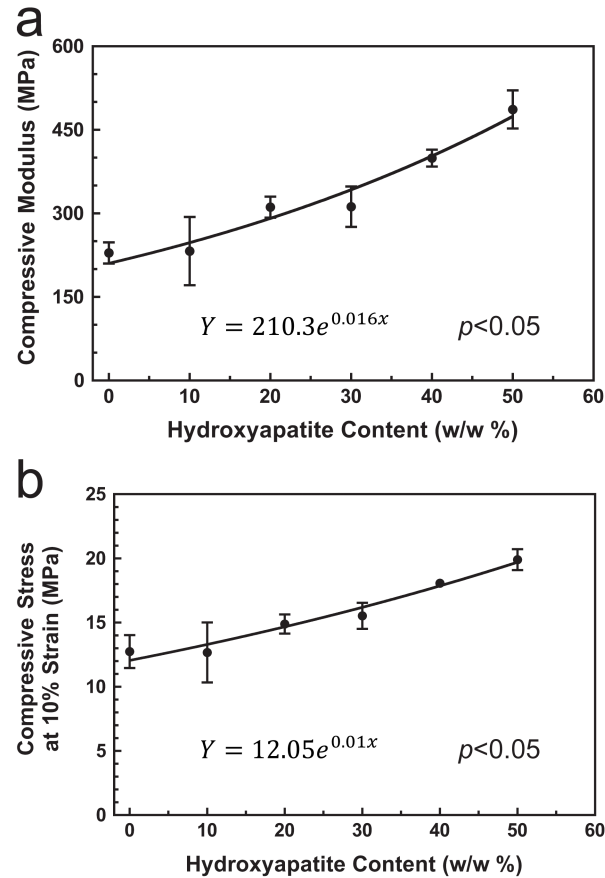


Figure 2.10 Compressive testing of PCL/HA composites: (a) Compressive modulus and (b) compressive stress at 10% strain of PCL/HA composites comprising 0-50 w/w % HA synthesized by sol-gel-hydrothermal process at pH 13.70 for 24 h. Young's modulus and tensile strength values are the mean calculated from five independent samples ($n=5$) measured under compression. Error bars are standard deviation. The solid line represents the nonlinear regression analysis fit of the compressive test data ($p < 0.05$).

There was a significant increase in Young's modulus ($p<0.05$) after the addition of 20-50% (w/w) HA, with more than a 3-fold increase from 193 MPa for unfilled PCL, to 665 MPa for specimens containing 40-50% (w/w) HA (Table 2.3). However, a significant decrease in tensile strength ($p<0.05$) is seen after the addition of 20% (w/w) HA.

Comparable to its effect on Young's modulus, the addition of 20-50% (w/w) HA to PCL significantly increased the compressive modulus ($p<0.05$) of the composites, with a maximum compressive modulus achieved with 50:50 (w/w) PCL/HA at 487 MPa (Table 2.3). Furthermore, a significantly greater compressive stress at 10% strain ($p<0.05$) was observed after the addition of 30-50% (w/w) HA (Table 2.3). The largest stress value was observed for composites containing 50% (w/w) HA, with a value of 19.9 MPa as compared to 12.7 MPa for unfilled PCL.

Table 2.3 Mechanical Properties of PCL/HA Composites

PCL:HA (w/w)	Young's Modulus (MPa)	Tensile Strength (MPa)	Compressive Modulus (MPa)	Compressive Stress at 10%
100:0	193.1 ± 14.7 ^a	13.0 ± 0.6 ^a	229.0 ± 17.0 ^a	12.7 ± 1.1 ^a
90:10	241.8 ± 20.7 ^{a,b}	10.6 ± 0.2 ^{a,b}	232.3 ± 54.7 ^a	12.7 ± 2.1 ^a
80:20	331.3 ± 12.8 ^{b,c}	8.8 ± 1.5 ^{b,c}	311.3 ± 17.0 ^b	14.9 ± 0.7 ^{a,b}
70:30	401.8 ± 21.5 ^c	8.2 ± 1.0 ^{b,c}	312.0 ± 32.5 ^b	15.5 ± 0.9 ^b
60:40	666.4 ± 54.3 ^d	10.1 ± 0.7 ^b	399.2 ± 13.6 ^c	18.1 ± 0.2 ^c
50:50	671.8 ± 94.6 ^d	6.6 ± 2.0 ^c	486.5 ± 30.5 ^d	19.9 ± 0.7 ^c

Mechanical properties are mean ± SD calculated from the average of five independent specimens ($n=5$) measured under uniaxial tension and compression. Statistical significance determined by a one-way ANOVA and Tukey's multiple comparison test. Effect of HA filler content on mechanical properties of PCL/HA composites was determined, where matching letters indicate groups with no statistical difference ($p>0.05$).

2.5 Discussion

The synthesis of HA with nanowire morphology has been the subject of extensive research. The sol-gel-hydrothermal process described in the present study provides a novel method for the synthesis of HA with micro- and nanowire morphologies, without the use of organic solvents or surfactants. The synthesis of an amorphous precursor via a sol-gel approach in combination with hydrothermal crystallization results in a high-purity product and provides control over HA particle diameter and length.

The formation of ACP in the sol-gel process occurs via the following stages: 1) hydrolysis of the phosphite sol, 2) interaction with the Ca^{2+} sol to produce colloidal CaP intermediates consisting of Ca–O–P bonds, which are thought to be stabilized by electrostatic repulsive forces and have oligomeric dimensions on the order of a few nanometers (polycondensation) [29], and 3) drying of the sol at 80 °C where ethanol and H_2O are removed, resulting in thermal dehydration and further polycondensation of the colloidal CaP intermediates forming more Ca–O–P bonds and producing a dried CaP gel [10]. FTIR spectra of the CaP gel revealed that the CaP intermediates are amorphous. The spectra also suggested an incomplete reaction between the hydrolyzed phosphite and Ca^{2+} sol during the 24 h aging process. The visible P=O and P–H bands are likely due to the presence of hydrolyzed phosphite precursors in the CaP gel [29]. However the presence of the hydrolyzed phosphite precursor does not seem to disturb the formation of HA during the hydrothermal process.

The 24 h aging step during sol-gel preparation is sufficient to produce a pure apatite-like ACP intermediate as shown in a previous study [32], and confirmed by FTIR of the CaP gel in the present study. The dried CaP gel is an agglomeration of small

particles with dimensions in the nano-scale range (~ 8 nm in diameter) [29]. These particles are assembled through weak van der Waals attractive forces, which allow for their facile dispersion and dissolution in aqueous solvents prior to hydrothermal processing [29]. It is this critical feature of the CaP gel precursor that allows for the successful synthesis of HA nanowires by hydrothermal processing [33].

Typical hydrothermal crystallization involves a transformation process via dissolution and precipitation where amorphous nano-particles act as a precursor for the formation of small crystalline nuclei (Fig. 2.11(a)) [23]. In the present study, the dissolution of the ACP intermediate in the hydrothermal solution provided a supersaturated medium containing apatite precursors. Subsequently, upon heating of the hydrothermal vessel, the energy input and high-pressure conditions produced crystalline nuclei that grew to form HA nano-rods and wires.

The growth of the HA nanowires and the resulting particle morphology is governed by an Ostwald ripening process and diffusion-controlled crystal growth (Fig. 2.11). The Ostwald ripening and Gibbs-Thompson theory state that larger crystals grow at the expense of dissolving smaller crystals, which are inherently less stable than the larger ones [34]. In diffusion-controlled crystal growth, the concentration of the ACP in the bulk solution is a critical factor [35].

During crystal growth, the ACP diffuses from the bulk solution and approaches the solution-crystal interface. The autogenous pressure and high energy input of the hydrothermal process accelerates Brownian motion and provides efficient circulation of the ACP [36]. The concentration of ACP at the solution-crystal interface governs the solubility of the HA crystal faces by either rapid growth onto, or dissolution from the different faces depending on the concentration [35]. The atomic structure of the HA unit

cell makes the interfacial free energy of the (001) plane (perpendicular to the *c*-axis) greater than the other faces [37]. At a high critical concentration of ACP in the bulk solution, the chemical potential of the ACP is significantly greater than the chemical potential of the (001) face of HA [35]. At this stage, 1D growth occurs as the metastable ACP colloids migrate to the (001) face, causing the crystals to grow exclusively along the *c*-axis of HA. Such growth gives rise to the constant particle diameter and increasing particle length seen at early hydrothermal times from 6 to 16 h in Figures 2.2-2.4. When the hydrothermal process is extended to 24 h, the concentration of the ACP drops to a level where the overall chemical potential of the bulk solution decreases. This makes it difficult for the diffusion flux of ACP to preferentially go to the (001) face of HA. The result is 3D growth, in which ACP is shared by each face of the HA crystal and both particle diameter and length increase, giving rise to the broad distribution of particle diameters seen at pH 5.20, the skewed distribution at pH 7.50, and the bimodal distribution at pH 13.70.

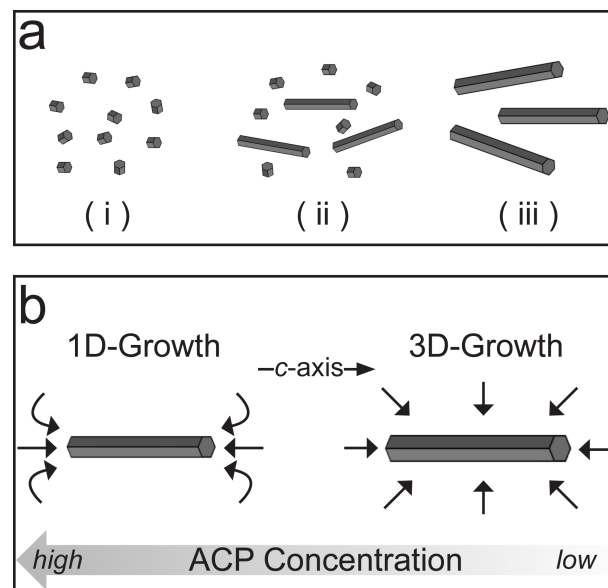


Figure 2.11 Schematic diagram of sol-gel-hydrothermal formation mechanism showing (a) hydrothermal crystallization process involving (i) supersaturation of ACP nanoparticles resulting in the formation of crystalline nuclei, followed by (ii) crystal growth of large nanowires at the cost of smaller, less stable crystals, and (iii) Ostwald ripening process [24, 34]. The growth of HA nanowires is a (b) diffusion-controlled crystal growth process, which is governed by the ACP concentration in the bulk resulting in either 1D or 3D growth of HA [35]. Arrows near the crystal indicate the diffusion direction of the ACP molecules.

As evident from the XRD spectra, the evolution of the HA from 6 to 24 h at each pH value was associated with a relative increase in the (300) reflection. This in turn signifies expansion of the a -plane of HA, which corresponds to crystal growth along the c -axis.

A marked effect of pH on particle diameter was observed. The solubility of HA decreases with increase in pH [1]. As a result of the lower solubility, smaller HA particles precipitate out of solution at higher pH levels as indicated by the significantly lower particle diameter values at 24 h.

During *in vivo* and *in vitro* applications of biomaterials, maintaining the porosity and preventing collapse of the porous structure of scaffolds is a determining factor in their success [4]. In PCL/HA composites, the HA nanowires were uniformly distributed throughout the PCL matrix and mechanical testing demonstrated the reinforcing ability of HA nanowires. Nano-scale HA particles impart the stiffness and strength of bioceramics to the toughness and ductility of PCL. When HA nanoparticles are used as filler materials in polymer matrices, the nanoparticle diameter and aspect ratio govern the strengthening effect. The ideal filler material has the smallest possible particle diameter, while maximizing the particle length and thereby having a large aspect ratio [6, 38]. HA nanowires synthesized at pH 13.70 for 24 h were selected as the filler for reinforcement of PCL composites because the longest observable particle lengths were seen at 24 h and the smallest particle diameters were obtained at pH 13.70. Both the Young's and compressive moduli of PCL/HA composites were significantly greater as compared to unfilled PCL. This increase in stiffness of the composite material will be beneficial for bone tissue engineering scaffolds. Furthermore, the inclusion of nano-scale HA particles

will impart the superior bioactive and osteoconductive properties of HA to the composite materials [3, 16].

In summary, the novel sol-gel-hydrothermal process described above is an effective method for the synthesis of phase-pure HA. The combination of a nanoscale ACP precursor produced by sol-gel chemistry, with a hydrothermal crystallization process results in the formation of HA with micro- and nanowire morphologies. This surfactant- and solvent-free process allows for tunable particle morphology, while maintaining the purity of the final HA product. These HA nanowires are effective fillers for the reinforcement of PCL/HA composites.

2.6 References

- [1] LeGeros RZ. Calcium phosphates in oral biology and medicine. *Monographs in Oral Science*. 1991;15:1-201.
- [2] Hott M, Noel B, Bernache-Assolant D, Rey C, Marie PJ. Proliferation and differentiation of human trabecular osteoblastic cells on hydroxyapatite. *Journal of Biomedical Materials Research*. 1997;37:508-16.
- [3] Okuda T, Ioku K, Yonezawa I, Minagi H, Gonda Y, Kawachi G, et al. The slow resorption with replacement by bone of a hydrothermally synthesized pure calcium-deficient hydroxyapatite. *Biomaterials*. 2008;29:2719-28.
- [4] Lickorish D, Guan L, Davies JE. A three-phase, fully resorbable, polyester/calcium phosphate scaffold for bone tissue engineering: Evolution of scaffold design. *Biomaterials*. 2007;28:1495-502.
- [5] Roeder RK, Sproul MM, Turner CH. Hydroxyapatite whiskers provide improved mechanical properties in reinforced polymer composites. *Journal of Biomedical Materials Research Part A*. 2003;67:801-12.
- [6] Wei G, Ma PX. Structure and properties of nano-hydroxyapatite/polymer composite scaffolds for bone tissue engineering. *Biomaterials*. 2004;25:4749-57.
- [7] Muller F, Gbureck, U., Kasuga, T., Mizutani, Y., Barralet, JE., Lohbauer, U. Whisker-Reinforced Calcium Phosphate Cements. *Journal of the American Ceramic Society*. 2007;90:3694-7.
- [8] Neira IS, Kolen'ko YV, Kommareddy KP, Manjubala I, Yoshimura M, Guitian F. Reinforcing of a Calcium Phosphate Cement with Hydroxyapatite Crystals of Various Morphologies. *Acs Applied Materials & Interfaces*. 2010;2:3276-84.
- [9] Eshtiagh-Hosseini H, Housaindokht MR, Chahkandi M. Effects of parameters of sol-gel process on the phase evolution of sol-gel-derived hydroxyapatite. *Materials Chemistry and Physics*. 2007;106:310-6.
- [10] Liu DM, Troczynski T, Tseng WJ. Water-based sol-gel synthesis of hydroxyapatite: process development. *Biomaterials*. 2001;22:1721-30.
- [11] Fathi MH, Hanifi A. Evaluation and characterization of nanostructure hydroxyapatite powder prepared by simple sol-gel method. *Materials Letters*. 2007;61:3978-83.
- [12] Neira IS, Kolen'ko YV, Lebedev OI, Van Tendeloo G, Gupta HS, Guitian F, et al. An Effective Morphology Control of Hydroxyapatite Crystals via Hydrothermal Synthesis. *Crystal Growth & Design*. 2009;9:466-74.

- [13] Mizutani Y, Hattori M, Okuyama M, Kasuga T, Nogami M. Large-sized hydroxyapatite whiskers derived from calcium tripolyphosphate gel. *Journal of the European Ceramic Society*. 2005;25:3181-5.
- [14] Zhang H, Darvell BW. Synthesis and characterization of hydroxyapatite whiskers by hydrothermal homogeneous precipitation using acetamide. *Acta Biomaterialia*. 2010;6:3216-22.
- [15] Zhou H, Lee J. Nanoscale hydroxyapatite particles for bone tissue engineering. *Acta Biomaterialia*. 2011;7:2769-81.
- [16] Sun F, Zhou H, Lee J. Various preparation methods of highly porous hydroxyapatite/polymer nanoscale biocomposites for bone regeneration. *Acta Biomaterialia*. 2011;7:3813-28.
- [17] Chung EJ, Qiu H, Kodali P, Yang S, Sprague SM, Hwang J, et al. Early tissue response to citric acid-based micro- and nanocomposites. *Journal of Biomedical Materials Research Part A*. 2011;96:29-37.
- [18] Lin KL, Liu XG, Chang J, Zhu YJ. Facile synthesis of hydroxyapatite nanoparticles, nanowires and hollow nano-structured microspheres using similar structured hard-precursors. *Nanoscale*. 2011;3:3052-5.
- [19] Lin KL, Chang J, Liu XG, Chen L, Zhou YL. Synthesis of element-substituted hydroxyapatite with controllable morphology and chemical composition using calcium silicate as precursor. *Crystengcomm*. 2011;13:4850-5.
- [20] Cao MH, Wang YH, Guo CX, Qi YJ, Hu CW. Preparation of ultrahigh-aspect-ratio hydroxyapatite nanofibers in reverse micelles under hydrothermal conditions. *Langmuir*. 2004;20:4784-6.
- [21] Wei K, Lai C, Wang YJ. Solvothermal synthesis of calcium phosphate nanowires under different pH conditions. *Journal of Macromolecular Science Pure and Applied Chemistry*. 2006;43:1531-40.
- [22] Sun YX, Guo GS, Tao DL, Wang ZH. Reverse microemulsion-directed synthesis of hydroxyapatite nanoparticles under hydrothermal conditions. *Journal of Physics and Chemistry of Solids*. 2006;68:373-7.
- [23] Chen JD, Wang YJ, Wei K, Zhang SH, Shi XT. Self-organization of hydroxyapatite nanorods through oriented attachment. *Biomaterials*. 2007;28:2275-80.
- [24] Zhang CM, Yang J, Quan ZW, Yang PP, Li CX, Hou ZY, et al. Hydroxyapatite Nano- and Microcrystals with Multifunctional Morphologies: Controllable Synthesis and Luminescence Properties. *Crystal Growth & Design*. 2009;9:2725-33.
- [25] Cullity BD. *Elements of X-ray diffraction*. Reading, Mass.: Addison-Wesley; 1967.

- [26] Koutsopoulos S. Synthesis and characterization of hydroxyapatite crystals: a review study on the analytical methods. *Journal of Biomedical Materials Research*. 2002;62:600-12.
- [27] American Society for Testing and Materials., Joint Committee on Chemical Analysis by Powder Diffraction Methods. *Powder diffraction file*. Rev. ed. Philadelphia,: American Society for Testing and materials; 1960.
- [28] Chou YF, Chiou WA, Xu YH, Dunn JCY, Wu BM. The effect of pH on the structural evolution of accelerated biomimetic apatite. *Biomaterials*. 2004;25:5323-31.
- [29] Liu DM, Yang Q, Troczynski T, Tseng WJ. Structural evolution of sol-gel-derived hydroxyapatite. *Biomaterials*. 2002;23:1679-87.
- [30] Kalinkin AM, Kalinkina EV, Zalkind OA, Makarova TI. Chemical interaction of calcium oxide and calcium hydroxide with CO₂ during mechanical activation. *Inorganic Materials*. 2005;41:1073-9.
- [31] Gibson IR, Bonfield W. Novel synthesis and characterization of an AB-type carbonate-substituted hydroxyapatite. *Journal of Biomedical Materials Research*. 2002;59:697-708.
- [32] Liu DM, Troczynski T, Tseng WJ. Aging effect on the phase evolution of water-based sol-gel hydroxyapatite. *Biomaterials*. 2002;23:1227-36.
- [33] Hou YD, Hou L, Zhang TT, Zhu MK, Wang H, Yan H. (Na_{0.8}K_{0.2})(_{0.5})Bi_{0.5}TiO₃ nanowires: Low-temperature sol-gel-hydrothermal synthesis and densification. *Journal of the American Ceramic Society*. 2007;90:1738-43.
- [34] Lalena JN. *Inorganic materials synthesis and fabrication*. Hoboken, N.J.: Wiley-Interscience; 2008.
- [35] Peng XG, Peng ZA. Mechanisms of the shape evolution of CdSe nanocrystals. *Journal of the American Chemical Society*. 2001;123:1389-95.
- [36] Yu SH, Liu B, Mo MS, Huang JH, Liu XM, Qian YT. General synthesis of single-crystal tungstate nanorods/nanowires: A facile, low-temperature solution approach. *Advanced Functional Materials*. 2003;13:639-47.
- [37] Kim TG, Park B. Synthesis and growth mechanisms of one-dimensional strontium hydroxyapatite nanostructures. *Inorganic Chemistry*. 2005;44:9895-901.
- [38] Liu TY, Chen SY, Liu DM. Influence of the aspect ratio of bioactive nanofillers on rheological behavior of PMMA-based orthopedic materials. *Journal of Biomedical Materials Research Part B: Applied Biomaterials*. 2004;71B:116-22.

CHAPTER THREE

CONTROL OF SURFACE TOPOGRAPHY IN BIOMIMETIC CALCIUM PHOSPHATE COATINGS¹

¹Chapter 3 has been reproduced (with some modifications) with permission from: Costa, D. O., Allo, B. A., Klassen, R., Hutter, J. L., Dixon, S. J., and Rizkalla, A. S. (2012). Control of Surface Topography in Biomimetic Calcium Phosphate Coatings. *Langmuir*, 28(8), 3871-3880. Copyright © 2012, American Chemical Society.

3.1 Chapter Summary

The behavior of cells responsible for bone formation, osseointegration and bone bonding *in vivo* are governed by both the surface chemistry and topography of scaffold matrices. Bone-like apatite coatings represent a promising method to improve the osteoconductivity and bonding of synthetic scaffold materials to mineralized tissues for regenerative procedures in orthopedics and dentistry. Polycaprolactone (PCL) films were coated with calcium phosphates (CaP) by incubation in simulated body fluid (SBF). We investigated the effect of SBF ion concentration and soaking time on the surface properties of the resulting apatite coatings. CaP coatings were examined by scanning electron microscopy (SEM), X-ray diffraction (XRD), Fourier transform infrared spectrometry (FTIR) and energy dispersive X-ray spectrometry (EDX). Young's modulus (E_s) was determined by nanoindentation, and surface roughness was assessed by atomic force microscopy (AFM) and mechanical stylus profilometry. CaP such as carbonate-substituted apatite were deposited onto PCL films. SEM and AFM images of the apatite coatings revealed an increase in topographical complexity and surface roughness with increasing ion concentration of SBF solutions. Young's moduli (E_s) of various CaP coatings were not significantly different, regardless of the CaP phase or surface roughness. Thus, SBF with high ion concentrations may be used to coat synthetic polymers with CaP layers of different surface topography and roughness to improve the osteoconductivity and bone bonding ability of the scaffold.

3.2 Introduction

It is important that tissue engineering scaffolds possess surface chemistry and topography that promote cell attachment and differentiation [1]. To promote bone healing, a scaffold construct must provide osteogenic, osteoconductive or osteoinductive activity at the defect site [2]. For orthopedic and dental applications, calcium phosphate (CaP) coatings may render synthetic polymer scaffolds bioactive and osteoconductive, as well as improve biocompatibility [3]. Hydroxyapatite (HA) facilitates the attachment, proliferation and differentiation of human osteoblastic cells [4], and promotes the ingrowth of natural bone [5]. *In vivo*, various polymer scaffolds coated with a bone-like apatite layer show improved osteoconductivity and bone ingrowth compared to uncoated implants [6-8]. Apatite coatings have also been cited as a method to overcome fibrous tissue encapsulation of scaffolds, a common problem for synthetic polymers implanted *in vivo* [9].

Surface coatings of HA or bone-like apatite formed by a biomimetic process have been studied previously. Investigators have produced a bone-like apatite layer on various types of organic polymer substrates and titanium metal by soaking in a simulated body fluid (SBF) with ion concentrations nearly equal to those of human blood plasma [10, 11]. However, traditional SBF solutions require lengthy incubation times, typically more than 7 days, to produce a uniform apatite coating [12, 13]. Recent efforts to shorten the time needed for coating have focused on increasing ionic concentrations. A solution with 5x the ion concentrations of typical SBF (5xSBF) is capable of depositing various crystalline CaP coatings, including carbonated-HA [14], octacalcium phosphate (OCP) [15], and dicalcium phosphate dihydrate (DCPD) [16], as well as an amorphous calcium

phosphate (ACP) within 24 h [17]. The ACP coating can subsequently be converted to carbonated-HA by soaking in SBF solutions with crystal growth inhibitors Mg^{2+} and HCO_3^- [18]. Further increasing SBF ion concentrations (10xSBF) shortens the times for CaP deposition to hours [19].

Surface topography, at the micron and submicron level, affect the attachment, proliferation and differentiation of cells on biomaterials [20-23]. Increase in surface porosity and roughness of biomaterials improves cellular attachment, proliferation, differentiation and bone-ingrowth [23, 24]. Furthermore, changes in HA microenvironment has shown an effect on osteoblast proliferation and expression of osteogenic markers, osteocalcin and bone sialoprotein [25]. Bone bonding to biomaterial surfaces is expected to occur if the material possesses topographical features at both the micron level and nanometer range [26]. Discrete nanocrystals of CaP, deposited on titanium implants with micron-scale surface roughness, can impart nano-scale surface complexity [27]. Implants with such coatings have exhibited improved osteoconduction and osseointegration in human clinical trials [28].

In view of the above, it would be beneficial to control the surface porosity and complexity of biomimetic CaP coatings. However, to the best of our knowledge only a few studies have attempted to control surface topography of apatite coatings by altering Mg^{2+} levels or pH of SBF [18, 29]. In the present study, apatite coatings were deposited on functionalized polycaprolactone (PCL) films by incubation in supersaturated SBF solutions. PCL is a biocompatible and biodegradable polymer, having a relatively slow rate of degradation making it an ideal scaffold for bone tissue engineering applications where a slowly degrading material is desired [30, 31]. Our objective was to investigate the effect of ionic concentration, level of crystal growth inhibitors (Mg^{2+} , HCO_3^-) and

soaking time on the surface properties of the resulting CaP coatings deposited on PCL. CaP coatings with tailored surface topography have excellent potential future applications on scaffold matrices for bone tissue engineering and regeneration.

3.3 Materials and Methods

3.3.1 Polycaprolactone (PCL) Film Fabrication and Functionalization

PCL pellets (5 g, molecular weight = 80,000 g/mol, Solvay Chemicals Inc., Houston, TX), were placed in an aluminum foil dish and heated at 120°C to produce a viscous liquid which was cooled in a refrigerator for 10 min. Uniform PCL films with a thickness of 1 mm were produced by heat pressing for 2 min at 70°C and 670 N. Specimens (15 mm diameter) were punched and washed with ethanol for 10 min, then dried at room temperature (RT). Specimens were placed in 10 ml of a 5 M NaOH solution at 50 °C and 75 rpm shaking speed (Max^Q 4000, Barnstead) for 48 h. Specimens were then removed from the NaOH solution and washed ultrasonically with deionized water for 10 min and air dried at RT.

3.3.2 Preparation of Modified Simulated Body Fluid (SBF) Solutions

Modified SBF compositions (Table 3.1) were prepared based on work done previously [10]. Concentrations of ion species (Na^+ , K^+ , Mg^{2+} , Ca^{2+} , Cl^- , HPO_4^{2-} , SO_4^{2-}) were adjusted to produce SBF solutions with approximate 5x (5xSBF-A), 7x (7xSBF-A) and 10x (10xSBF-A) ion concentrations by sequentially dissolving analytical grade CaCl_2 , $\text{MgCl}_2 \cdot 6\text{H}_2\text{O}$, $\text{K}_2\text{HPO}_4 \cdot 3\text{H}_2\text{O}$, Na_2SO_4 , KCl , and NaCl (Sigma-Aldrich, USA) in

deionized water. NaHCO_3 was added separately, prior to the start of the coating procedure (see section 3.3.3). Prior to addition of $\text{K}_2\text{HPO}_4 \cdot 3\text{H}_2\text{O}$, 1 M HCl solution was added to lower the pH to 1.75 to increase solubility. Final pH of (5x, 7x, 10x) SBF-A solutions ranged between 2.00-2.25 and was stable for several days when stored at RT. SBF solution (SBF-B), nominally free of Mg^{2+} , HCO_3^- and SO_4^{2-} , was prepared by sequentially adding analytical grade NaCl, CaCl_2 and $\text{K}_2\text{HPO}_4 \cdot 3\text{H}_2\text{O}$ to deionized water. Prior to addition of $\text{K}_2\text{HPO}_4 \cdot 3\text{H}_2\text{O}$, 1 M HCl solution was added to lower the pH to a final value of 5.75.

3.3.3 Biomimetic Coating Process

The coating process was adopted from Tas *et al.* [19], and modified in which 0.0882 g of NaHCO_3 was added to 50 ml SBF-A solution stirring at 500 RPM and 37 °C to achieve an approximate pH of 5.90. NaOH-treated PCL films were suspended in the SBF-A solution for 24 h, or 48 h (with solution replenishment after 24 h). Following treatment in SBF-A, selected samples were incubated in SBF-B for an additional 48 h. Incubation of the samples was performed at a temperature of 37 °C and 75 rpm. Coated specimens were thoroughly washed with deionized water and air dried.

Table 3.1 Ionic concentrations of human blood plasma, SBF-A and SBF-B [10].

Medium	Ion concentration (mM)							
	Na ⁺	K ⁺	Ca ²⁺	Mg ²⁺	HCO ₃ ⁻	Cl ⁻	HPO ₄ ²⁻	SO ₄ ²⁻
Blood plasma	142	5	2.5	1.5	27	103	1	0.5
10xSBF-A	1420	50	25	15	21	1499	10	5
7xSBF-A	994	35	17.5	10.5	21	1057	7	3.5
5xSBF-A	710	25	12.5	7.5	21	739	5	2.5
SBF-B	1420	20	25	0	0	1470	10	0

Ionic concentrations were calculated assuming complete dissociation in solution.

3.3.4 Physical and Chemical Characterization of CaP Coatings

Surface morphologies of CaP coatings were examined using a scanning electron microscope (SEM) equipped with an energy dispersive X-ray spectrometer (EDX) for elemental analysis (LEO 1540XB FIB/SEM, Carl Zeiss, Oberkochen, Germany). Samples were first coated with 3 nm osmium metal using a Filgen OPC 80T instrument. Cross sectional images of CaP coatings were taken by SEM after disrupting the coating layer by scratching or bending coated PCL substrates. Crystal structure of CaP coatings was determined by X-ray diffraction (XRD) using a rotating anode X-ray diffractometer model RTP300 (Rigaku Rotaflex, Japan) operating on CoK α radiation at 45 kV and 160 mA. Spectra were collected in the 2θ range between 5° and 65° , with 0.05° steps and a $10^\circ/\text{min}$ scan speed. 2θ for equivalent CuK α radiation was obtained using Bragg's Law, $\lambda = 2d\sin \theta$, where $\lambda = 1.54056$ and 1.79026 Å for Cu and Co respectively [32]. Chemical functional groups of CaP coatings were determined using a Bruker Vector 22 (Bruker Optics LTD, Milton, ON) Fourier transform infrared spectrometer (FTIR) fitted

with a Bruker/Pike MIRacle (Pike Technologies, Madison, WI) attenuated total reflection spectrometer. Transmittance spectrums from 4000 to 500 cm^{-1} wavenumbers were collected.

3.3.5 Young's Modulus (E_s) of CaP Coatings

E_s was determined using a nanoindentation technique with a Micro Materials NanoTest Indentation machine (Wrexham, UK). A diamond Berkovich indenter was used to perform 10 indentations with 100 μm spacing between indentations for each specimen. A load-displacement curve was recorded for indentation depths of 500 nm at a loading and unloading rate of 0.06 mN/s. The indentation depth of 500 nm was 10% or less of the CaP thickness and was selected to ensure that the measured Young's modulus was specific to the CaP coating and not influenced by the underlying polymer substrate [33]. The dwell time at maximum load was 2 s and the load-displacement data were used to determine the reduced Young's modulus (E_r). The Young's moduli (E_s) of the samples were then calculated using the following the relationship:

$$\frac{1}{E_r} = \frac{(1-\nu_s^2)}{E_s} + \frac{(1-\nu_i^2)}{E_i}$$

where E_s and ν_s are the Young's modulus and Poisson's ratio of the indented CaP coating, respectively, and E_i and ν_i are the modulus and Poisson's ratio of the diamond Berkovich indenter, having values of 1141 GPa and 0.07 respectively. The Poisson's ratio for universal isotropic pure HA needles of 0.28 was used for ν_s [34].

3.3.6 Surface Roughness

Surface roughness of CaP coatings was measured by atomic force microscopy (AFM) under contact mode with a Multimode AFM with Nanoscope IIIa controller using an NP-S cantilever (Veeco Instruments, Santa Barbara, CA). 3-D height images were obtained for a 20 x 20 μm area, and the AFM imaging software was used to determine the arithmetic mean (R_a) of the absolute values of the height profile deviations from the mean line, and root mean square (R_q) roughness, which represents the square root of the arithmetic mean of the squares of the deviations. The R_a and R_q values obtained by AFM represent the fine (high resolution) surface roughness. To evaluate the coarse (low resolution) surface roughness of CaP coatings, a SurfTest SJ-210 mechanical stylus profilometer surface roughness tester (Mitutoyo, Kanagawa, Japan) was used to determine R_a and R_q values. The coarse surface roughness values were obtained according to accepted standards (ISO 4287:1997) with a cut off length, $\lambda_c = 0.8$ mm and evaluation length of 4 mm.

3.4 Results

3.4.1 Characterization of Coating Morphology by SEM

Functionalized PCL surfaces incubated in 5xSBF-A for 24 h revealed deposition of a uniform coating comprised of spherical globules ranging in diameter from 0.5 to 1 μm as seen in SEM micrographs (Fig. 3.1(A)). The spherical globules, which exhibit no distinct surface features, are typical of ACP. Further increasing the ion concentration (7x and 10x) of SBF solutions produced CaP coatings with distinct surface features. Substrates treated with 7xSBF-A for 24 h had a uniform coating consisting of a highly

porous, nanoscale, surface structure (Fig. 3.1(A)), whereas films treated with 10xSBF-A (24 h) had coatings consisting of micron range surface pores (Fig. 3.1(A)). After further incubation in SBF solutions (SBF-B, devoid of crystal growth inhibitors), samples pre-coated with 5xSBF-A (24 h) showed a distinct change in topography – previously having no distinct surface features, coatings now consisted of smaller globules with a very fine, nano-porosity (Fig. 3.1(A)). Incubating the 7xSBF-A (24 h) samples in SBF-B produced a coarse, microscale porous structure, whereas PCL films coated with 10xSBF-A show increased surface micro-porosity after further treatment in SBF-B.

Incubation of PCL in 5xSBF-A for 48 h (with solution replenishment after the first 24 h) produced a uniform coating nearly identical to the layer produced by 5xSBF-A for 24 h with large spherical globules of 1 to 3 μm (Fig. 3.1(B)). Similarly, substrates treated with 7xSBF-A for 48 h had a uniform coating comparable to that after 24 h, consisting of nanoscale surface features (Fig. 3.1(B)). In contrast, increasing the soaking time to 48 h with 10xSBF-A produced a coating with considerably different surface features consisting of a highly rough topography of micron-sized plates oriented randomly (isotropic). Further soaking in SBF-B had little effect on the coating morphologies with the exception of those produced by 5xSBF-A, which changed from large spherical globules with no distinct surface features to a highly porous, honeycomb-like structure. Both coatings produced from 7xSBF-A and 10xSBF-A largely maintained their morphology.

Cross-sectional images of CaP coatings (Fig. 3.2) demonstrate that the unique topographical features were present within approximately 1-2 μm of the surface, whereas the remainder of the CaP coating consisted of a dense, uniform layer. Little porosity was seen within this deeper layer. The total thickness of the CaP coatings (produced using 7

and 10xSBF-A from 24 to 48 h and further soaked in SBF-B) ranged between 5 and 20 μm .

Thus, incubation of functionalized PCL with SBF of different ionic concentrations (with and without subsequent incubation in the absence of crystal growth inhibitors) can be used to prepare surface coatings with varying topographical features. We next addressed the different phases present after incubating the PCL substrates in different SBF concentrations, as well as the compositions of the resultant CaP coatings.

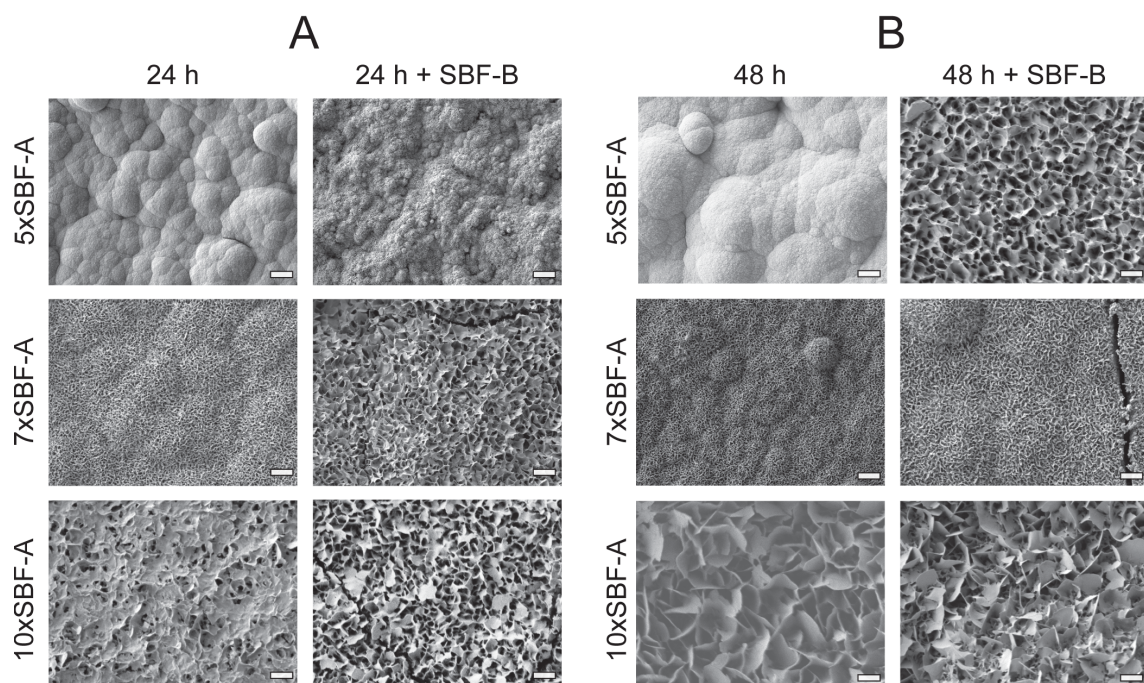


Figure 3.1 SEM micrographs of CaP coatings on PCL films after immersion in various SBF-A solutions for 24 h (A), and 48 h (B) and SBF-B. Scale bars = 1 μm . Images shown are representative of three fields of view taken from three independent samples.

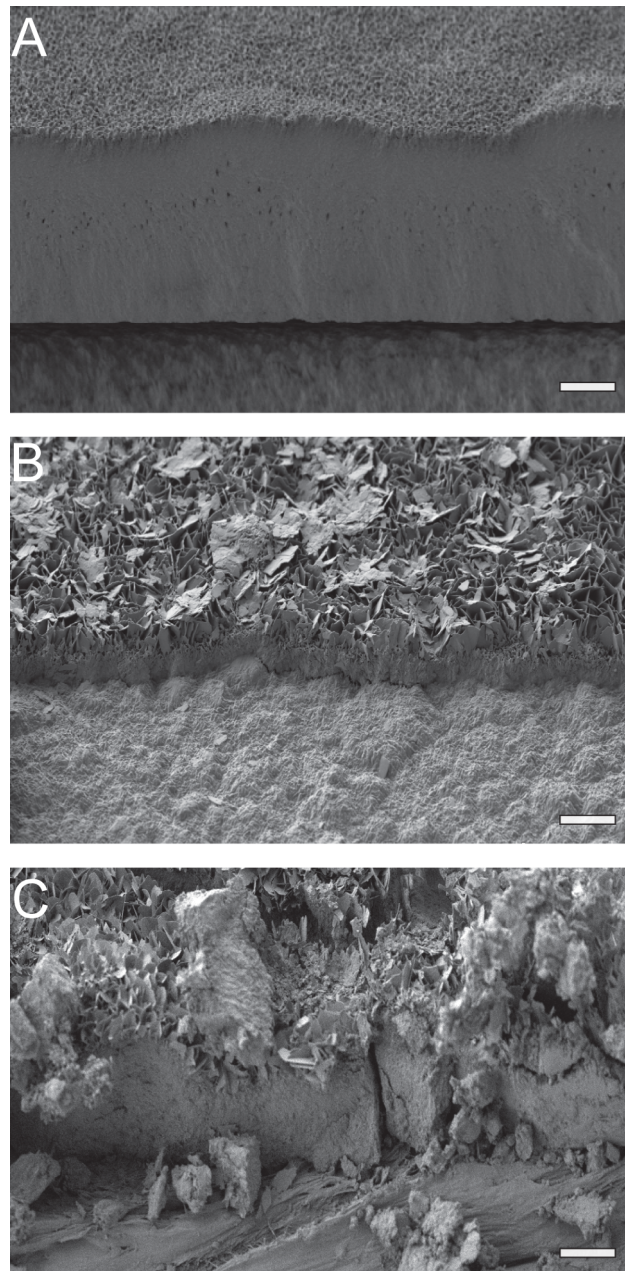


Figure 3.2 SEM micrographs showing cross-section of CaP coatings on PCL films after immersion in various SBF-A solutions for (A) 7xSBF-A (48 h) + SBF-B, (B) 10xSBF-A (24 h) + SBF-B, and (C) 10xSBF-A (48 h) + SBF-B. Scale bars = 5 μm .

3.4.2 XRD of CaP coatings

XRD spectra (Fig. 3.3) of functionalized PCL before and after incubation for 24 h in 5xSBF-A showed similar patterns of peaks (Fig. 3.3(A)), indicating that the deposited layer is likely ACP. Subjecting the 5xSBF-A (24 h) samples to SBF-B resulted in the appearance of a sharp peak at $2\theta = 11.7^\circ$ (Fig. 3.3(A)), which is characteristic of the crystalline structure of DCPD [35]. Contrary to the results obtained for samples incubated in 5xSBF-A, XRD spectra of substrates incubated in 7xSBF-A for 24 h indicated the presence of crystalline CaP as revealed by the small peak at $2\theta = 11.7^\circ$ corresponding to DCPD and sharp peak at $2\theta = 25.8^\circ$ (Fig. 3.3(A)). Indeed, additional incubation of the 7xSBF-A (24 h) coating in SBF-B produced a spectrum with an intense peak at $2\theta = 25.8^\circ$. In addition, a broad peak at $2\theta = 32^\circ$ was observed (Fig. 3.3(A)), corresponding to overlapping of the (211) and (112) diffraction planes, and indicative of a poorly crystalline, bone-like apatite [36]. Moreover, a small peak was observed at $2\theta = 11.7^\circ$, consistent with the presence of DCPD as a minor phase along with HA. XRD analysis of coatings produced using 10xSBF-A revealed an accelerated ability to deposit an apatite layer on PCL substrates, as compared to SBF solutions of lower ion concentrations (i.e. 5x, 7x). XRD spectra of the coating deposited after 24 h contained new peaks at $2\theta = 4.7^\circ$ and 26.1° (Fig. 3.3(A)). The peak at $2\theta = 4.7^\circ$ is likely attributable to the presence of OCP, a precursor of HA; whereas the peak $2\theta = 26.1^\circ$ is indicative of both OCP and apatite [35, 37]. Exposure of this coating to SBF-B converted it to a single phase of poorly crystalline HA, as revealed by the following characteristics:

a) an intense peak at $2\theta = 25.8^\circ$; *b)* a broad peak at $2\theta = 32^\circ$, corresponding to

overlapping of the (211) and (112) diffraction planes; and *c*) a peak at $2\theta = 28.7^\circ$ of the (210) diffraction plane of HA (Fig. 3.3(A)).

Extending the incubation time in 5xSBF-A from 24 to 48 h produced no detectable difference in the XRD spectrum (Fig. 3.3(B)). However, incubation of the 5xSBF-A (48 h) samples in SBF-B resulted in the presence of both DCPD and apatite (Fig. 3.3(B)). In addition to the peak at $2\theta = 11.7^\circ$ typical of DCPD, new peaks at 25.8° , 28.7° and a broad diffraction line at 32° of apatite are visible. Increasing the incubation time in 7xSBF-A from 24 to 48 h enhanced the intensity of the peak at $2\theta = 25.8^\circ$ and brought about the appearance of a large peak at $2\theta = 11.7^\circ$, suggesting a predominance of DCPD (Fig. 3.3(B)). XRD spectra of the 7xSBF (48 h) samples following additional incubation in SBF-B (Fig. 3.3(B)) revealed the formation of apatite only, with characteristic peaks at $2\theta = 25.8, 28.7, 32$ and 53.7° [38]. The DCPD peak at $2\theta = 11.7^\circ$ is noticeably absent. Incubation in 10xSBF-A for 48 h was all that was required to induce apatite formation on the PCL film as indicated by the appearance of a large peak at $2\theta = 25.8^\circ$, as well as the presence of broad peaks at $2\theta = 32, 28.7$ and 53.7° (Fig. 3.3(B)). Additional incubation of these apatite-coated substrates in SBF-B produced no striking change in the phase composition of the coatings (Fig. 3.3(B)), with only peaks characteristic of apatite remaining. However, it should be noted that peaks attributed to the PCL substrate were no longer visible and the relative intensity of the apatite peaks were increased.

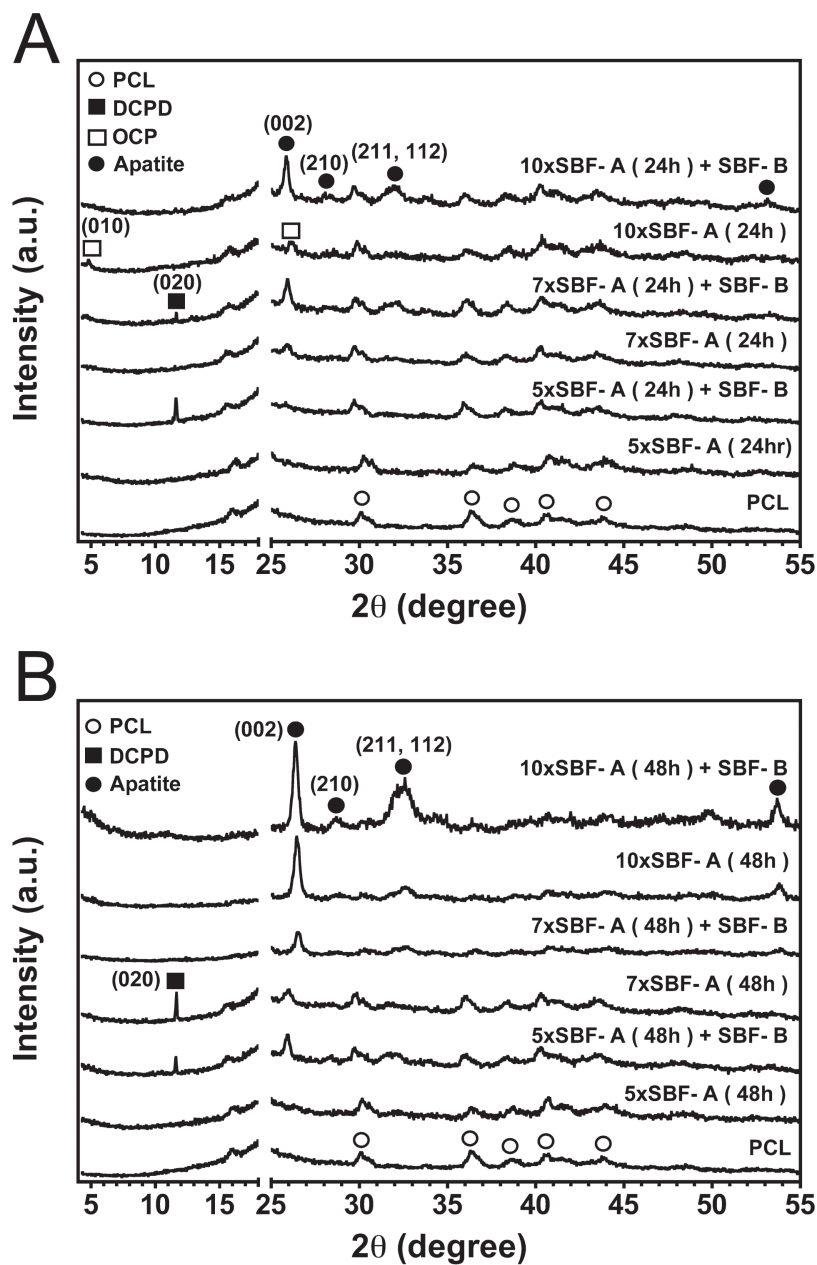


Figure 3.3 XRD pattern of the CaP coatings. PCL films with no treatment and after immersion in various SBF-A solutions for (A) 24 h and (B) 48 h and SBF-B. Standard peak positions and (hkl) values obtained from JCPDS card # 9-432 (HA), 19-272 (carbonated-HA), 9-77 (DCPD), and 26-1056 (OCP).

3.4.3 FTIR of CaP coatings

FTIR spectra (Fig. 3.4) corroborated the formation of various crystalline calcium phosphate coatings. Substrates soaked in 5xSBF-A for 24 h and SBF-B (Fig. 3.4(A)) exhibited major bands for phosphate (1190 , 1110 , 1040 and 980 cm^{-1} for P-O ν_3 mode, and 576 and 525 cm^{-1} for P-O ν_4 mode) and hydrogen-phosphate [790 , and 872 cm^{-1} for P-O(H) ν_1 mode], which are characteristic of DCPD [38], confirming the XRD results. FTIR spectra of the coatings produced from 7xSBF-A and 10xSBF-A for 24 h and SBF-B (Fig. 3.4(A)) showed typical bands associated with a bone-like apatite [38]. Clearly visible is a broad band at 1650 cm^{-1} assigned to -OH bending of H_2O , and intense PO_4^{3-} bands at 1020 cm^{-1} (ν_3), 960 cm^{-1} (ν_1), 600 cm^{-1} and 560 cm^{-1} (ν_4). Carbonate substitution was confirmed by bands at 1430 cm^{-1} and 873 cm^{-1} , typical of a carbonate-substituted HA [35, 38]. HPO_4^{2-} was also detected by FTIR and revealed by a broad shoulder at 1100 cm^{-1} and band at 530 cm^{-1} , and may be due to the presence of minor secondary phases such as DCPD and OCP [39, 40]. Similar spectra were observed for coatings deposited from 5xSBF-A (48 h) and SBF-B (Fig. 3.4(B)), with exception of an increased intensity of the HPO_4^{2-} band at 530 cm^{-1} confirming the XRD observation of a mixed phase coating consisting of both apatite and a significant presence of DCPD. FTIR spectra of coatings produced from both 7xSBF-A and 10xSBF-A for 48 h followed by SBF-B treatment (Fig. 3.4(B)) indicated a predominately single-phase apatite, consistent with the XRD results.

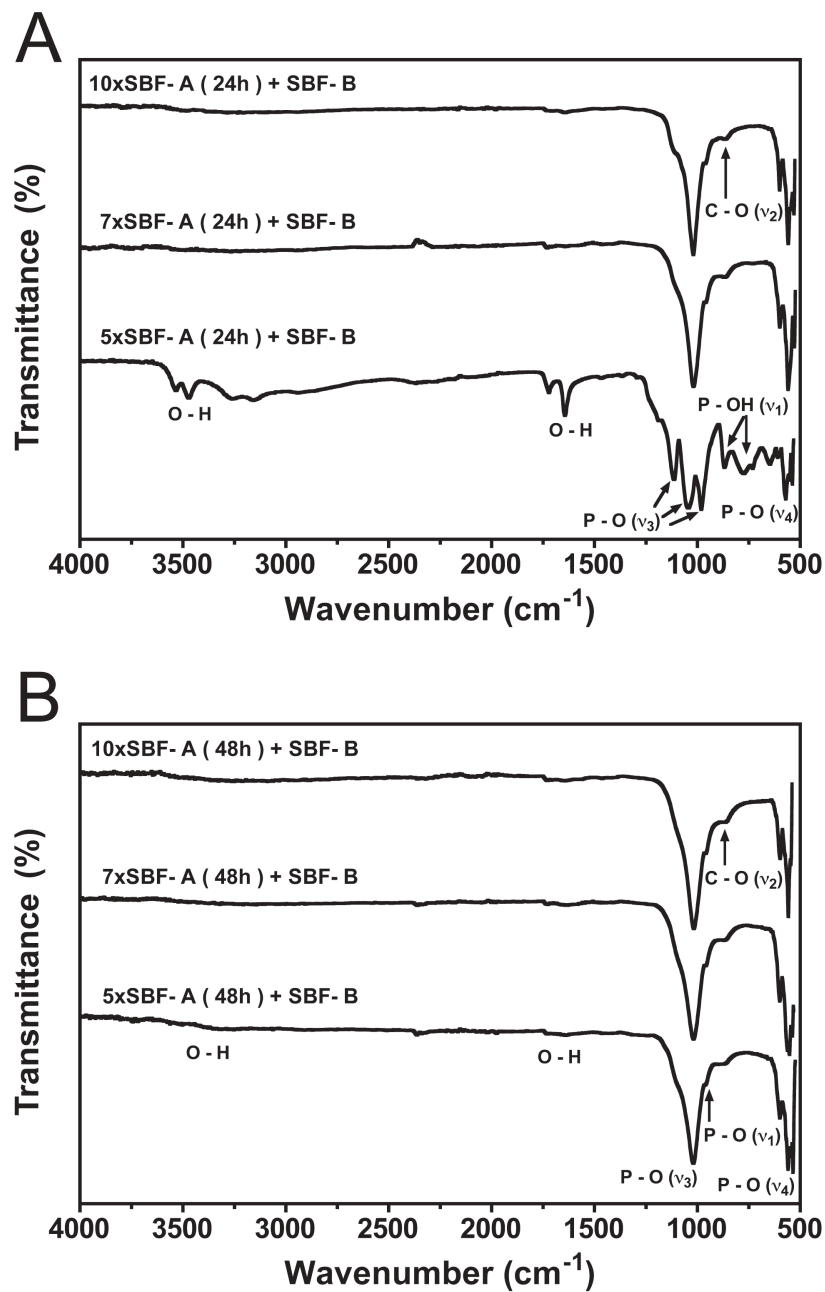


Figure 3.4 FTIR spectra of the CaP coatings. PCL films after immersion in various SBF-A for (A) 24 h and (B) 48 h and after subsequent treatment in SBF-B.

3.4.4 EDX elemental analysis of CaP coatings

EDX analysis of the various coatings revealed Ca/P atomic ratio of coating layers ranging from 1.00 – 1.50, below the stoichiometric value of 1.67 for HA (Table 3.2). There was no significant difference in Ca/P ratio between any of the crystalline CaP coatings produced at 24 h, with only the amorphous CaP layer produced by 5xSBF-A having a significantly lower Ca/P ratio ($p<0.05$). Increasing the soaking time to 48 h had no significant effect on the Ca/P ratio of the CaP coatings. However, at 48 h, CaP coatings produced using 10xSBF-A with and without SBF-B treatment had a significantly greater Ca/P ratio as compared with layers produced using 5xSBF-A. The highest Ca/P ratio (1.50) was measured for coatings produced by 10xSBF-A (48 h) + SBF-B. Deviation of the Ca/P atomic ratio from the stoichiometric value for HA may be due to cation substitutions at the Ca^{2+} sites by Mg^{2+} or Na^+ , or substitution at PO_4^{3-} sites by CO_3^{2-} or HPO_4^{2-} , or a combination of these substitutions. A difference in the measured Mg content of coatings was also observed by EDX. The Mg/Ca ratio was significantly higher ($p<0.05$) for coatings produced by 5xSBF-A as compared to 7x and 10xSBF-A, at both 24 h and 48 h (Table 3.2). There was significantly lower ($p<0.05$), Mg/Ca ratio detected in coatings after treatment with SBF-B (nominally Mg^{2+} -free solution) for all SBF-A concentrations, with the exception of 10xSBF-A at 48 h. The effect of time (24 h vs 48 h) on the Mg/Ca ratio for the CaP layers was only significant ($p<0.05$) for those produced by 5xSBF-A and showed a decrease in the Mg/Ca ratio from 24 h to 48 h.

Table 3.2 Elemental atomic ratio of CaP coatings.

Medium	CO ₃ /P	Ca/P		Mg/Ca	
		24 h	48 h	24 h	48 h
10xSBF-A	2.10	1.283 ^a (0.057)	1.412 ^{AC} (0.189)	0.033 ^d (0.013)	0.024 ^{DE} (0.005)
7xSBF-A	3.00	1.281 ^a (0.041)	1.319 ^{AB} (0.175)	0.051 ^d (0.016)	0.046 ^D (0.009)
5xSBF-A	4.20	0.948 ^b (0.089)	1.161 ^B (0.121)	0.210^f (0.040)	0.140^F (0.020)
10xSBF-A + SBF-B	2.10	1.301 ^a (0.023)	1.500 ^A (0.188)	0.001 ^e (0.001)	0.002 ^E (0.003)
7xSBF-A + SBF-B	3.00	1.273 ^a (0.064)	1.308 ^{AB} (0.036)	0.002 ^e (0.002)	0.003 ^E (0.003)
5xSBF-A + SBF-B	4.20	1.222 ^a (0.026)	1.270 ^{BC} (0.023)	0.004 ^e (0.003)	0.009 ^E (0.011)

CO₃/P ratios were calculated from ion concentrations used in SBF-A preparations. Ca/P and Mg/Ca ratio values are mean (standard deviation) from three EDX spot analyses on three independent samples ($n = 3$). Statistical significance was determined by a two-way ANOVA and a Bonferroni post-test. The effect of different SBF-A and SBF-B were determined at each time, where matching lower case letters indicate no statistical significance ($p > 0.05$) at 24 h and upper case letters indicate no statistical significance ($p > 0.05$) at 48 h. There was no significant difference found between Ca/P ratios at 24 h vs 48 h for any of the SBF treatments. Bolded text denotes a significant ($p < 0.05$) effect of time (24 h vs 48 h) on the Mg/Ca ratio.

The XRD, FTIR, and EDX data establish that various CaP coatings are deposited on PCL films by incubation in SBF solutions with high ionic concentrations (Table 3.3). These results, in conjunction with the SEM micrographs above, demonstrate our ability to produce CaP and carbonated apatite coatings with various surface morphologies by adjusting ion concentration and soaking time.

Table 3.3 Crystal phases of CaP coatings

Medium	Crystal Phase	
	24 h	48 h
5xSBF-A	ACP	ACP
7xSBF-A	DCPD	DCPD
10xSBF-A	OCP/HA	HA
5xSBF-A + SBF-B	DCPD	DCPD/HA
7xSBF-A + SBF-B	HA/DCPD	HA
10xSBF-A + SBF-B	HA	HA

CaP coatings were produced by soaking PCL substrates in 5, 7 or 10xSBF-A for 24 or 48 h, with or without subsequent soaking in SBF-B. CaP crystal phases were determined by XRD, FTIR and EDX. ACP: amorphous calcium phosphate; DCPD: dicalcium phosphate dihydrate; OCP: octacalcium phosphate; HA: hydroxyapatite.

3.4.5 Mechanical properties of CaP coatings

The nanoindentation measurement of E_s of coatings produced from 5xSBF-A (48 h), 7xSBF-A (48 h), 10xSBF-A (48 h) and subsequent incubation in SBF-B is displayed in Fig 3.5. At an indentation depth of 500 nm, there was a significant increase ($p < 0.001$) in the E_s value of the CaP-coated substrates as compared to the uncoated PCL films, however there was no significant difference in the E_s value between the different CaP coatings.

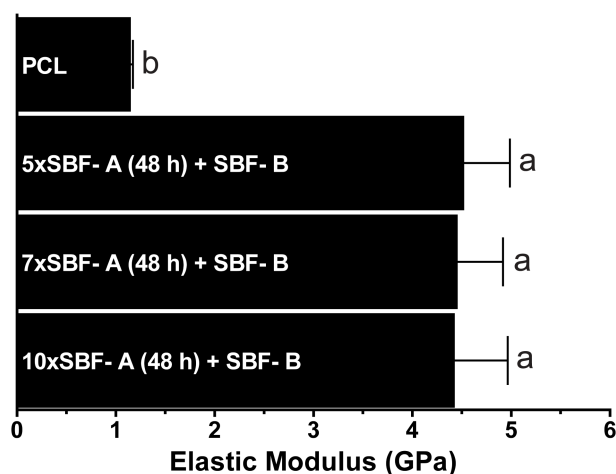


Figure 3.5 Nanoindentation measurement of E_s of PCL films and after immersion in various SBF-A solutions for 48 h and subsequent treatment in SBF-B. E_s values are the mean calculated from 10 indentations performed on two independent samples ($n=20$). Error bars are standard error. Groups with matching letters are not statistically significant ($p > 0.05$) as determined by a one-way ANOVA using Tukey's multiple comparison test.

As indicated by the XRD and FTIR analyses above, the coatings produced from 5xSBF-A (48 h) + SBF-B consist of mixed phases of DCPD and apatite, whereas those produced from 7xSBF-A (48 h) + SBF-B, and 10xSBF-A (48 h) + SBF-B are single phase, poorly crystalline apatite. From the nanoindentation experiments, it is evident that the E_s remains constant for different CaP phases. The indentation study also reveals little to no effect of surface topography or complexity on the mechanical behavior of the CaP coatings.

3.4.6 AFM imaging and surface roughness of CaP coatings

Three CaP coatings, characterized as HA and exhibiting distinct topographies, were selected for further study [7xSBF-A (48 h) + SBF-B, 10xSBF-A (24 h) + SBF-B, 10xSBF-A (48 h) + SBF-B]. AFM height images of these HA coatings revealed fine (high resolution) surface features (Fig. 3.6, left panels); whereas height profiles obtained using a mechanical stylus profilometer revealed coarse (low resolution) surface features (Fig. 3.6, right panels). Apatite coatings were produced by immersing NaOH-treated PCL substrates in 7xSBF-A for 48 h (Fig. 3.6(A)), and 10xSBF-A for 24 h (Fig. 3.6(B)) or 48 h (Fig. 3.6(C)), and subsequently treated with SBF-B. For each apatite coating, 3-D images were obtained for a 20 x 20 μm area and height profiles were measured for a 4 mm evaluation length. Differences in topography are clearly evident from both the 3D height images and height profiles. Apatite coatings produced from 7xSBF-A showed a uniform layer of isotropic (randomly distributed) spherical globules with a height deviation of approximately 600 nm. Substrates soaked in 10xSBF-A showed apatite coatings having an increase in isotropic surface complexity, with many sharp surface

features, numerous peaks and valleys, and a height variation near 1200 nm. Ra and Rq values measured from the AFM images show a significant increase in surface roughness and complexity of apatite coatings when the SBF-A ion concentration was increased from 7 to 10 times (Table 3.4). However, no significant difference was observed in the AFM roughness values of the apatite layers produced by increasing the soaking time in 10xSBF-A from 24 to 48 h. The height profiles (Fig 3.6, right) and the Ra and Rq values measured by mechanical stylus profilometer indicate a significant increase in the roughness when increasing SBF-A concentration from 7x to 10x, and soaking time in 10xSBF-A from 24 to 48 h.

The results obtained from both AFM imaging and the mechanical stylus profilometer indicate differences in the topography of the apatite coatings produced in this study. Roughness of both fine and coarse surface features is dependent on the ion concentration of the SBF-A solutions, whereas soaking time influences the roughness of the coarse surface features.

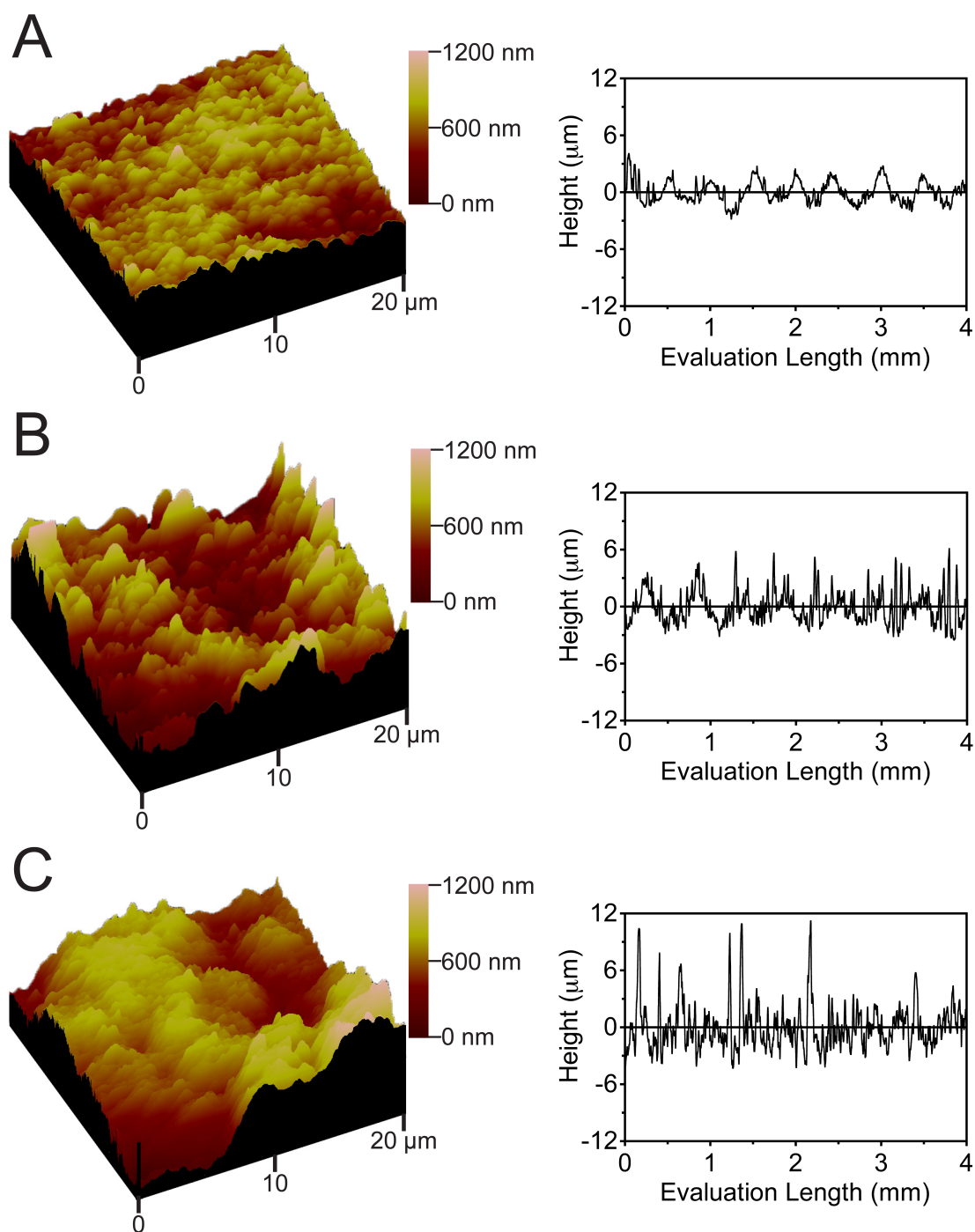


Figure 3.6 Three-dimensional AFM images (left) and mechanical stylus profilometer height profiles (right) of surface topography of HA coatings produced on PCL substrates by immersion in (A) 7xSBF-A (48 h) + SBF-B, (B) 10xSBF-A (24 h) + SBF-B, and (C) 10xSBF-A (48 h) + SBF-B within an area of 20 x 20 μm for AFM and a 4 mm evaluation length for the mechanical stylus profilometer.

Table 3.4 Surface Roughness of CaP Coatings.

Medium	AFM		Mechanical Stylus Profilometer	
	Ra, nm	Rq, nm	Ra, μm	Rq, μm
7xSBF-A (48 h) + SBF-B	194 ^b (28)	255 ^b (39)	1.01 ^a (0.06)	1.26 ^a (0.08)
10xSBF-A (24 h) + SBF-B	316 ^a (26)	402 ^a (32)	1.26 ^a (0.06)	1.61 ^a (0.09)
10xSBF-A (48 h) + SBF-B	363 ^a (38)	454 ^a (44)	1.97 ^b (0.22)	2.56 ^b (0.28)

Ra and Rq values are mean (standard error of the mean) calculated from the average of three different spot analyses on two independent samples ($n = 6$). Statistical significance determined by a one-way ANOVA and Tukey's multiple comparisons test. Effect of SBF-A and SBF-B treatment on surface roughness of substrates were determined for apatite coatings, where matching letters indicate groups with no statistical difference ($p > 0.05$) in Ra and Rq values as measured by AFM and mechanical stylus profilometer.

3.5 Discussion

In the present study, the CaP layer deposited on PCL substrates using 5xSBF-A was identified as an ACP by XRD, which is in accordance to previous studies which demonstrated the ability of a 5xSBF to deposit ACP on titanium substrates [17]. Precipitation of various phases of CaP from solution involves the formation of an ACP as the initial phase prior to hydrolysis and conversion to other crystalline phases [41-43]. The presence of crystal growth inhibitors Mg^{2+} , and HCO_3^- in the 5xSBF-A inhibits the formation of a crystalline CaP phase and, promotes the formation of ACP. Subjecting substrates to 48 h soaking had no observable change in coating crystallinity or topography. Further treating CaP coatings deposited by 5xSBF-A for 24 h with SBF-B,

devoid of crystal growth inhibitors, promoted the transformation to a crystalline DCPD phase. Interestingly, when the substrates were pre-coated with 5xSBF-A for 48 h, soaking in SBF-B promoted the conversion of the ACP coating layer to mixed phases of crystalline DCPD and poorly crystalline carbonated apatite. Given that the CaP coating layers produced by 5xSBF-A for 24 and 48 h showed similar XRD patterns, the difference in phase composition measured after soaking in SBF-B is attributed to the amount of Mg^{2+} incorporated in the amorphous CaP layers during the 5xSBF-A treatments [44, 45].

According to theoretical models based on classical crystallization theory, SBF solutions containing high concentrations of Ca^{2+} and PO_4^{3-} , at pH levels similar to those in this study (SBF-B), favor nucleation of HA compared to both DCPD and OCP [46]. However, the presence of Mg^{2+} ($Mg/Ca > \sim 0.2$) lengthens the total time required for conversion of ACP to HA by prolonging the induction period characteristic of reactions involving nucleation. Mg^{2+} ions poison the surfaces of HA nuclei by adsorbing to the active growth sites, thereby preventing or slowing the HA growth rate and thus allowing other phases to nucleate [43, 44]. The high Mg^{2+} content within the ACP layer formed by the 5xSBF-A for 24 h as compared to 48 h may be responsible for the increased stabilization of the ACP layer in solution, and ultimately delaying the HA formation even after 48 h treatment in SBF-B. At higher ion concentrations and acidic pH, as is the case in the present study, ACP is known to convert initially into DCPD and/or OCP and successively into HA [45]. The delayed dissolution of the ACP phase caused by the incorporated Mg^{2+} ($Mg/Ca = 0.21$) prevented the hydrolysis of DCPD within 48 h soaking in SBF-B. Conversely, the lower Mg^{2+} content within ACP formed by 5xSBF-A after 48 h ($Mg/Ca = 0.14$) was sufficiently low to allow partial hydrolysis of DCPD into

HA after the dissolution of the ACP layer in SBF-B for 48 h. Furthermore, Abbona *et al.* [45], proposed that the slow release of Mg^{2+} from ACP could be an additional cause for delayed HA formation, as Mg^{2+} ions may induce a mechanical strain caused by a lower ionic radius and shorter bond length with oxygen as compared to Ca^{2+} in ACP. These results suggest that the final crystalline phase and kinetics of ACP hydrolysis are governed by the initial Mg^{2+} content in the CaP layer. Increasing the Mg^{2+} content in CaP coating layers delays the conversion to HA and favors other crystalline phases such as DCPD.

Alternatively, XRD for coatings produced after soaking in 7xSBF-A and 10xSBF-A for 24 h indicated the presence of a crystalline phase. The ability of 7xSBF-A and 10xSBF-A solutions to produce a crystalline phase within only 24 h is attributed to the lower Mg^{2+} content within the CaP coatings, and increased level of Ca^{2+} in the SBF-A solutions [47]. Although the initial Mg/Ca atomic ratio in the SBF-A (5x, 7x, 10x) solutions are identical, the carbonate to phosphorous ratio (CO_3/P) varies and has been shown to influence the amount of Mg^{2+} incorporation in synthetic apatite [48]. Mg^{2+} incorporation is known to increase in ACP with an increase in the CO_3/P ratio of the starting solution [48]. Comparing the ion concentrations of the SBF-A (Table 3.1) solutions used in this study, the higher the concentration of SBF-A solution, the lower the corresponding CO_3/P ratio since the carbonate concentration remains constant (approx. 21 mM) for all three conditions. As such, the level of Mg^{2+} incorporation in the CaP coatings decreased with increase in the ion concentration of the SBF-A solutions. EDX analysis showed lower Mg/Ca atomic ratio in the coatings produced by 7xSBF-A and 10xSBF-A as compared to 5xSBF-A. The decrease in Mg^{2+} content measured after 24 h in 10xSBF-A and 7xSBF-A is associated with the lower CO_3/P ratio in the starting

solutions. As evident in this study, treating 10xSBF-A pre-coated substrates (24 h) in SBF-B accelerated the formation of a uniform HA coating, whereas treatment in 7xSBF-A yielded DCPD as a minor phase along with HA. Extending the soaking time in 7x and 10xSBF-A to 48 h consequently increased the apatite content of the above-mentioned coatings.

Deposition of CaP coatings from SBF solutions onto material surfaces occurs via negatively charged functional groups, such as carboxyl and -OH. These surface functional groups act as nucleation sites, first by electrostatic attraction of Ca^{2+} , which adsorb PO_4^{3-} ions from the SBF solution [49]. Once nuclei of critical size are formed on the material surface, they spontaneously grow into a dense CaP layer by further consuming Ca^{2+} and PO_4^{3-} ions from the SBF [11]. Functional groups were produced on the PCL surface by NaOH treatment, which has been previously shown to produce carboxylate and -OH groups on polyester surfaces by hydrolytic cleaving of the ester bonds of PCL [50]. Biomimetic processes using SBF solutions have successfully produced CaP coating layers on various material surfaces, including natural and synthetic polymers, and titanium [10-18, 51]. Therefore, it is expected that the CaP coatings developed in this study can be applied to other materials, given the presence of appropriate surface functional groups.

SEM and AFM micrographs reveal dramatic differences in the coating morphology, with a dense isotropic nano-scale topography produced using 7xSBF-A and an isotropic, highly rough topography composed of micron-sized plates oriented vertically for coatings produced using 10xSBF-A. The difference in the topography of the coatings produced by the various solutions may be due to the difference in the Mg/Ca atomic ratio found in the coating layer prior to SBF-A refresh and/or SBF-B treatment.

EDX results confirmed minor amounts of Mg in all coatings after treatment with SBF-B. The subsequent dissolution and release of Mg^{2+} , as well as the initial Mg^{2+} concentration in solution, would have an influence on coating topography since the presence of Mg^{2+} in solution is capable of reducing the surface roughness and producing apatite coatings exhibiting finer surface structures [29]. These results indicate that apatite coatings with various surface topographies can be produced by adjusting the solution ionic strength and the Mg^{2+} incorporation in coatings prior to immersion in SBF solutions with or without Mg^{2+} .

Apatite coatings with a finer, nano-ordered topography are produced using SBF solutions with lower ion concentrations (i.e. 7xSBF-A), which result in higher incorporation of Mg^{2+} prior to immersion in SBF-B. Coatings consisting of highly defined, randomly ordered plates are produced using SBF solutions with higher ion concentrations (i.e. 10xSBF-A), which deposit CaP coatings with low Mg^{2+} incorporation prior to immersion in SBF-B. The dissolution and release of Mg^{2+} during treatment in refreshed SBF-A, and in SBF-B will be governed by the initial amount of Mg^{2+} in the CaP coatings and will affect the final surface topography.

There is an extensive literature on the influence of surface topography on cell behavior [20-22]. Previous findings indicate that different biological responses would be expected towards the CaP coatings with varying micro- and nano-scale surface roughness developed in the present study. In this regard, surface roughness of approximately $2\ \mu m$ [as observed in our 10xSBF-A (48 h) + SBF-B samples] is proposed by some authors to induce maximal changes in cell behavior compared to smooth surfaces [21]. Further, isotropic nano-scale topography has been shown to increase gene expression of osteogenic markers by cultured human osteoprogenitor cells [52]. However, some

authors have questioned the *in vivo* significance of such nano-scale features, as proteins attaching to the surface after implantation would likely mask such fine topographies [21]. We anticipate that, of the HA coatings synthesized, the 10xSBF-A (48 h) + SBF-B coating would provide the optimal topography for promoting osteoblast attachment and differentiation. Osseointegration and bone-bonding at the bone-implant interface is influenced by surface topography of the implant [26]. Manipulating surface complexity at the micro- and nano-scale level of CaP coatings is vital, as the cement line matrix deposited during osteogenesis is dependent on such surface features for deposition and interlocking [27]. As such, careful control and design of surface roughness and topography are critical for the development of optimal CaP coatings to promote osteoblast differentiation, bone formation and osseointegration of tissue engineering scaffolds and orthopedic implants.

Material stiffness has been shown to influence osteoblast adhesion and maturation [53]. As such, the mechanical properties of the different coatings were measured by nanoindentation to determine their E_s values. Results indicated that the deposited apatite and DCPD/apatite coating layers provided greater E_s values when compared to uncoated PCL films. The E_s value increases nearly 5-fold when a CaP layer is deposited on PCL. No statistical difference was found in E_s between the various coatings produced using the different SBF-A solutions despite the difference in surface porosity and topography. Indeed porosity of HA sintered bodies has been shown to have significant influence on the E_s values [54]. However, a definitive conclusion on the CaP surface topography as the sole influence on mechanical properties cannot be made, as the chemical composition of the CaP coatings may also affect E_s values.

The XRD patterns of coatings deposited from 5xSBF-A show mixed phases of DCPD and apatite, whereas 7x and 10xSBF-A produced single phase apatite coatings. Although coatings from 7x and 10xSBF-A display similar XRD and FTIR spectra, EDX results indicate differences in the Ca/P atomic ratio, which may influence the resulting mechanical properties as ion substitutions in HA are capable of modifying the E_s of HA [55]. The E_s values in this study are comparable to the lower range of those measured for cortical and trabecular bone of the human femur [56].

In summary, bone-like apatite coatings with varying surface topography, roughness and complexity were successfully deposited on functionalized PCL films using SBF solutions with high ion concentrations and adjusted levels of Mg^{2+} and HCO_3^- . Coatings produced with lower concentration SBF solutions had a high initial Mg^{2+} incorporation, showed delayed formation kinetics and reduced surface complexity with a fine surface topography. In contrast, higher concentration SBF solutions had lower Mg^{2+} incorporation, and accelerated apatite formation, producing a highly rough surface, coarse topography consisting of micron-sized plates. The HA coatings produced with higher concentrations SBF solutions had surface roughness values at levels considered optimal for osteoblast attachment and differentiation. Mechanical properties of CaP coatings at the 500 nm range approached those of human bone and were unchanged with coating condition. These bone-like apatite coatings may increase the osteoconductivity and bone bonding ability of synthetic materials.

3.6 References

- [1] Burg KJ, Porter S, Kellam JF. Biomaterial developments for bone tissue engineering. *Biomaterials*. 2000;21:2347-59.
- [2] Bauer TW, Muschler GF. Bone graft materials. An overview of the basic science. *Clinical Orthopaedics and Related Research*. 2000;371:10-27.
- [3] LeGeros RZ. Properties of osteoconductive biomaterials: calcium phosphates. *Clinical Orthopaedics and Related Research*. 2002;395:81-98.
- [4] Hott M, Noel B, Bernache-Assolant D, Rey C, Marie PJ. Proliferation and differentiation of human trabecular osteoblastic cells on hydroxyapatite. *Journal of Biomedical Materials Research*. 1997;37:508-16.
- [5] Nagano M, Nakamura T, Kokubo T, Tanahashi M, Ogawa M. Differences of bone bonding ability and degradation behaviour in vivo between amorphous calcium phosphate and highly crystalline hydroxyapatite coating. *Biomaterials*. 1996;17:1771-7.
- [6] Pek YS, Gao S, Arshad MS, Leck KJ, Ying JY. Porous collagen-apatite nanocomposite foams as bone regeneration scaffolds. *Biomaterials*. 2008;29:4300-5.
- [7] Bigi A, Fini M, Bracci B, Boanini E, Torricelli P, Giavaresi G, et al. The response of bone to nanocrystalline hydroxyapatite-coated Ti13Nb11Zr alloy in an animal model. *Biomaterials*. 2008;29:1730-6.
- [8] Cowan CM, Shi YY, Aalami OO, Chou YF, Mari C, Thomas R, et al. Adipose-derived adult stromal cells heal critical-size mouse calvarial defects. *Nature Biotechnology*. 2004;22:560-7.
- [9] Lickorish D, Guan L, Davies JE. A three-phase, fully resorbable, polyester/calcium phosphate scaffold for bone tissue engineering: Evolution of scaffold design. *Biomaterials*. 2007;28:1495-502.
- [10] Kokubo T, Kushitani H, Sakka S, Kitsugi T, Yamamuro T. Solutions Able to Reproduce In vivo Surface-Structure Changes in Bioactive Glass-Ceramic a-W3. *Journal of Biomedical Materials Research*. 1990;24:721-34.
- [11] Tanahashi M, Yao T, Kokubo T, Minoda M, Miyamoto T, Nakamura T, et al. Apatite Coating on Organic Polymers by a Biomimetic Process. *Journal of the American Ceramic Society*. 1994;77:2805-8.
- [12] Zhang RY, Ma PX. Porous poly(L-lactic acid)/apatite composites created by biomimetic process. *Journal of Biomedical Materials Research*. 1999;45:285-93.
- [13] Kim HM, Kishimoto K, Miyaji F, Kokubo T, Yao T, Suetsugu Y, et al. Composition and structure of the apatite formed on PET substrates in SBF modified with various ionic activity products. *Journal of Biomedical Materials Research*. 1999;46:228-35.

- [14] Barrere F, van der Valk CM, Dalmeijer RAJ, van Blitterswijk CA, de Groot K, Layrolle P. In vitro and in vivo degradation of biomimetic octacalcium phosphate and carbonate apatite coatings on titanium implants. *Journal of Biomedical Materials Research Part A*. 2003;64A:378-87.
- [15] Barrere F, van der Valk CM, Dalmeijer RAJ, Meijer G, van Blitterswijk CA, de Groot K, et al. Osteogenicity of octacalcium phosphate coatings applied on porous metal implants. *Journal of Biomedical Materials Research Part A*. 2003;66A:779-88.
- [16] Barrere F, van Blitterswijk CA, de Groot K, Layrolle P. Influence of ionic strength and carbonate on the Ca-P coating formation from SBFx5 solution. *Biomaterials*. 2002;23:1921-30.
- [17] Barrere F, van Blitterswijk CA, de Groot K, Layrolle P. Nucleation of biomimetic Ca-P coatings on Ti6Al4V from a SBF x 5 solution: influence of magnesium. *Biomaterials*. 2002;23:2211-20.
- [18] Chou YF, Chiou WA, Xu YH, Dunn JCY, Wu BM. The effect of pH on the structural evolution of accelerated biomimetic apatite. *Biomaterials*. 2004;25:5323-31.
- [19] Tas AC, Bhaduri SB. Rapid coating of Ti6Al4V at room temperature with a calcium phosphate solution similar to 10x simulated body fluid. *Journal of Materials Research*. 2004;19:2742-9.
- [20] Unadkat HV, Hulsman M, Cornelissen K, Papenburg BJ, Truckenmuller RK, Post GF, et al. An algorithm-based topographical biomaterials library to instruct cell fate. *Proceedings of the National Academy of Sciences of the United States of America*. 2011;108:16565-70.
- [21] Hayes JS, Czekanska EM, Richards RG. The Cell-Surface Interaction. *Advances in Biochemical Engineering/Biotechnology*. 2012;126:1-31.
- [22] Lim JY, Donahue HJ. Cell sensing and response to micro- and nanostructured surfaces produced by chemical and topographic patterning. *Tissue Engineering*. 2007;13:1879-91.
- [23] Deligianni DD, Katsala ND, Koutsoukos PG, Missirlis YF. Effect of surface roughness of hydroxyapatite on human bone marrow cell adhesion, proliferation, differentiation and detachment strength. *Biomaterials*. 2001;22:87-96.
- [24] Rosa AL, Beloti MM, van Noort R. Osteoblastic differentiation of cultured rat bone marrow cells on hydroxyapatite with different surface topography. *Dental Materials*. 2003;19:768-72.
- [25] Chou YF, Huang WB, Dunn JCY, Miller TA, Wu BM. The effect of biomimetic apatite structure on osteoblast viability, proliferation, and gene expression. *Biomaterials*. 2005;26:285-95.

- [26] Davies JE. Bone bonding at natural and biomaterial surfaces. *Biomaterials*. 2007;28:5058-67.
- [27] Mendes VC, Moineddin R, Davies JE. The effect of discrete calcium phosphate nanocrystals on bone-bonding to titanium surfaces. *Biomaterials*. 2007;28:4748-55.
- [28] Orsini G, Piattelli M, Scarano A, Petrone G, Kenealy J, Piattelli A, et al. Randomized, controlled histologic and histomorphometric evaluation of implants with nanometer-scale calcium phosphate added to the dual acid-etched surface in the human posterior maxilla. *Journal of Periodontology*. 2007;78:209-18.
- [29] Oyane A, Ishikawa Y, Yamazaki A, Sogo Y, Furukawa K, Ushida T, et al. Reduction of surface roughness of a laminin-apatite composite coating via inhibitory effect of magnesium ions on apatite crystal growth. *Acta Biomaterialia*. 2008;4:1342-8.
- [30] Hutmacher DW. Scaffolds in tissue engineering bone and cartilage. *Biomaterials*. 2000;21:2529-43.
- [31] Elfick AP. Poly(epsilon-caprolactone) as a potential material for a temporary joint spacer. *Biomaterials*. 2002;23:4463-7.
- [32] Cullity BD. *Elements of X-ray diffraction*. Reading, Mass.: Addison-Wesley; 1967.
- [33] Pelletier H, Nelea V, Mille P, Muller D. Determination of mechanical properties of pulsed laser-deposited hydroxyapatite thin film implanted at high energy with N⁺ and Ar⁺ ions, using nanoindentation. *Journal of Materials Science*. 2004;39:3605-11.
- [34] Gan L, Wang J, Pilliar RM. Evaluating interface strength of calcium phosphate sol-gel-derived thin films to Ti6Al4V substrate. *Biomaterials*. 2005;26:189-96.
- [35] LeGeros RZ. Calcium phosphates in oral biology and medicine. *Monographs in Oral Science*. 1991;15:1-201.
- [36] Posner AS. Crystal chemistry of bone mineral. *Physiological Reviews*. 1969;49:760-92.
- [37] Barrere F, Layrolle P, van Blitterswijk CA, de Groot K. Biomimetic calcium phosphate coatings on Ti6Al4V: a crystal growth study of octacalcium phosphate and inhibition by Mg²⁺ and HCO₃. *Bone*. 1999;25:107S-11S.
- [38] Koutsopoulos S. Synthesis and characterization of hydroxyapatite crystals: a review study on the analytical methods. *Journal of Biomedical Materials Research*. 2002;62:600-12.
- [39] Rey C, Shimizu M, Collins B, Glimcher MJ. Resolution-enhanced Fourier transform infrared spectroscopy study of the environment of phosphate ion in the early deposits of a solid phase of calcium phosphate in bone and enamel and their evolution with age: 2. Investigations in the nu₃PO₄ domain. *Calcified Tissue International*. 1991;49:383-8.

- [40] Rey C, Shimizu M, Collins B, Glimcher MJ. Resolution-enhanced Fourier transform infrared spectroscopy study of the environment of phosphate ions in the early deposits of a solid phase of calcium-phosphate in bone and enamel, and their evolution with age. I: Investigations in the upsilon 4 PO₄ domain. *Calcified Tissue International*. 1990;46:384-94.
- [41] Abbona F, Madsen HEL, Boistelle R. The Initial Phases of Calcium and Magnesium Phosphates Precipitated from Solutions of High to Medium Concentrations. *Journal of Crystal Growth*. 1986;74:581-90.
- [42] Abbona F, Madsen HEL, Boistelle R. The Final Phases of Calcium and Magnesium Phosphates Precipitated from Solutions of High to Medium Concentration. *Journal of Crystal Growth*. 1988;89:592-602.
- [43] Abbona F, Franchiniangela M. Crystallization of Calcium and Magnesium Phosphates from Solutions of Low Concentration. *Journal of Crystal Growth*. 1990;104:661-71.
- [44] Boskey AL, Posner AS. Magnesium Stabilization of Amorphous Calcium-Phosphate - Kinetic Study. *Materials Research Bulletin*. 1974;9:907-16.
- [45] Abbona F, Baronnet A. A XRD and TEM study on the transformation of amorphous calcium phosphate in the presence of magnesium. *Journal of Crystal Growth*. 1996;165:98-105.
- [46] Lu X, Leng Y. Theoretical analysis of calcium phosphate precipitation in simulated body fluid. *Biomaterials*. 2005;26:1097-108.
- [47] Lu X, Leng Y. TEM study of calcium phosphate precipitation on bioactive titanium surfaces. *Biomaterials*. 2004;25:1779-86.
- [48] LeGeros RZ, Kijkowska R, Bautista C, LeGeros JP. Synergistic effects of magnesium and carbonate on properties of biological and synthetic apatites. *Connective Tissue Research*. 1995;32:525-31.
- [49] Tanahashi M, Matsuda T. Surface functional group dependence on apatite formation on self-assembled monolayers in a simulated body fluid. *Journal of Biomedical Materials Research*. 1997;34:305-15.
- [50] Oyane A, Uchida M, Choong C, Triffitt J, Jones J, Ito A. Simple surface modification of poly(epsilon-caprolactone) for apatite deposition from simulated body fluid. *Biomaterials*. 2005;26:2407-13.
- [51] Lu X, Zhao ZF, Leng Y. Biomimetic calcium phosphate coatings on nitric-acid-treated titanium surfaces. *Materials Science & Engineering C*. 2007;27:700-8.

- [52] Dalby MJ, Gadegaard N, Tare R, Andar A, Riehle MO, Herzyk P, et al. The control of human mesenchymal cell differentiation using nanoscale symmetry and disorder. *Nature materials*. 2007;6:997-1003.
- [53] Keogh MB, O'Brien FJ, Daly JS. Substrate stiffness and contractile behaviour modulate the functional maturation of osteoblasts on a collagen-GAG scaffold. *Acta Biomaterialia*. 2010;6:4305-13.
- [54] Rodriguez-Lorenzo LM, Vallet-Regi M, Ferreira JM, Ginebra MP, Aparicio C, Planell JA. Hydroxyapatite ceramic bodies with tailored mechanical properties for different applications. *Journal of Biomedical Materials Research*. 2002;60:159-66.
- [55] Gross KA, Rodriguez-Lorenzo LM. Sintered hydroxyfluorapatites. Part II: mechanical properties of solid solutions determined by microindentation. *Biomaterials*. 2004;25:1385-94.
- [56] Zysset PK, Guo XE, Hoffler CE, Moore KE, Goldstein SA. Elastic modulus and hardness of cortical and trabecular bone lamellae measured by nanoindentation in the human femur. *Journal of Biomechanics*. 1999;32:1005-12.

CHAPTER FOUR

SURFACE TOPOGRAPHY OF BIOMIMETIC HYDROXYAPATITE COATINGS DIFFERENTIALLY REGULATES OSTEOBLAST AND OSTEOCLAST ACTIVITY¹

¹Chapter 4 has been submitted for publication:

Costa, D. O, Prowse, P. D. H, Chrones, T, Sims, S. M., Hamilton, D. W., Rizkalla, A. S., Dixon, S. J. (2012). Surface Topography of Biomimetic Hydroxyapatite Coatings Differentially Regulates Osteoblast and Osteoclast Activity.

4.1 Chapter Summary

The behavior of bone cells is influenced by the surface chemistry and topography of implants and scaffolds. Our purpose was to investigate how the topography of biomimetic hydroxyapatite (HA) coatings influences the attachment and differentiation of osteoblasts, and the resorptive activity of osteoclasts. Using strategies previously reported [Langmuir 2012;28:3871-80], we directly controlled the surface topography of biomimetic HA coatings on polycaprolactone films. Osteoblasts and osteoclasts were incubated on HA coatings having distinct surface topographies. Osteoblast attachment and differentiation were significantly greater ($p < 0.05$) when cultured on micro-rough HA surfaces ($R_a \sim 2 \mu\text{m}$) than on smoother topographies ($R_a \sim 1 \mu\text{m}$). The Activity of tartrate-resistant acid phosphatase, an osteoclast marker, was greater on smoother than on micro-rough HA surfaces. Furthermore, scanning electron microscopy revealed the presence of resorption lacunae exclusively on smooth HA coatings. Inhibition of resorption on micro-rough HA surfaces was associated with disruption of filamentous actin sealing zones. In conclusion, HA coatings can be prepared with different topographies, which regulate responses of osteoblasts, as well as osteoclastic activity and hence susceptibility to resorption. Thus, it may be possible to design HA coatings, that induce optimal rates of bone formation and degradation specifically tailored for different applications in orthopedics and dentistry.

4.2 Introduction

The surface topography and roughness of biomaterials, at the micrometer and nanometer scale, affect the attachment, signaling, proliferation and differentiation of cells [1-6]. To promote bone regeneration and osseointegration, it is essential that tissue engineering scaffolds provide bioactive, osteogenic and osteoconductive stimuli at the defect site [7, 8]. Therefore, manipulating the surface topography offers an effective and straightforward strategy to improve the biological performance of implant and scaffold materials.

Osteoblasts exhibit increased differentiation and mineralization on roughened substratum topographies compared to smooth surfaces [9, 10]. Previous studies have reported surface roughness (Ra) in the range of 1-7 μm induces maximal changes in cell behavior and stimulation of bone formation [2, 10, 11]. Furthermore, implants having average surface roughness $< 0.5 \mu\text{m}$ are typically encapsulated by fibrous tissue [11]. On the other hand, less is known about the effects of biomaterial characteristics on osteoclast behavior. The chemical composition of resorbable bioceramics has been shown to influence the differentiation and resorption activity of osteoclasts *in vitro* [12-14]. Recently, the effect of HA surface roughness on osteoclast behavior was studied [15]; however, the reported Ra values ($< 0.6 \mu\text{m}$) were considerably lower than those widely accepted as optimal for osteoblast function (Ra $> 1 \mu\text{m}$) [2]. Thus, the effect of high surface roughness (i.e. Ra $> 1.0 \mu\text{m}$) of resorbable biomaterials on osteoclast activity remains poorly defined.

The design of implant and scaffold surface features are dependent on the desired application. Osteoclast inhibition favors implant stability for total hip arthroplasty,

whereas resorbable synthetic biomaterials are intended to be degraded by osteoclastic resorption and physiochemical dissolution [16]. Osteoblast and osteoclast functions are synergistic; both play a role in skeletal healing, development, and remodeling [17] and their complementary activities are a defining feature of the bone-biomaterial interface [18, 19]. Therefore, it is important to assess the interaction of biomaterials with both osteoblasts and osteoclasts. For many applications, it would be beneficial to identify surface features that would be optimal for promoting bone formation by osteoblasts, while suppressing the resorptive activity of osteoclasts. However, only a few studies have investigated the resorption of biomaterial surfaces by osteoclasts [16, 20]. To the best of our knowledge, no previous study has examined the effect of biomaterial topography on both osteoblasts and osteoclasts.

For orthopedic and dental applications, HA coatings can render synthetic biomaterials bioactive and osteoconductive [21], facilitating the attachment and differentiation of cells of the osteoblast lineage [22] and promoting the ingrowth of natural bone [23-25]. Additionally, carbonated-HA coatings exhibit classical resorption lacunae after osteoclastic activity [26]. Surface coatings of HA or bone-like apatite (formed by a biomimetic process) have been deposited on various types of porous polymer scaffolds and titanium metal implants [27, 28]. The biomimetic approach involves soaking substrates in a simulated body fluid (SBF) with ion concentrations similar to those of human blood plasma. Despite numerous studies showing that surface roughness can regulate the osteogenic response to biomaterials, few investigators have attempted to directly control the topography of biomimetic coatings [29]. We recently found that, by varying the ionic concentration of SBF, we could reliably control the topography of biomimetic HA coatings [30]. Solutions with 7 and 10 times the ion

concentration of typical SBF (7xSBF and 10xSBF) lead to the deposition of carbonated bone-like HA coatings with distinct surface topography and roughness, enabling us to systematically study their influence on cell function.

In the present study, bone-like HA coatings with smooth ($R_a = 1.0 \mu\text{m}$) and micro-rough ($R_a = 2.0 \mu\text{m}$) surfaces were deposited on polycaprolactone (PCL) films. Our objective was to determine effects of biomimetic HA coatings with varying surface topography on the behavior of osteoblasts and osteoclasts. We report that increasing the surface complexity of biomimetic HA enhances the attachment and differentiation of primary osteoblasts. Furthermore, we discovered that a high degree of surface roughness suppresses the resorption of HA by authentic, freshly isolated osteoclasts. Thus, an HA surface topography was identified that simultaneously enhances osteoblast function while suppressing osteoclast activity.

4.3 Materials and Methods

4.3.1 Biomimetic HA coating process

Biomimetic HA coatings with varying surface roughness were deposited on PCL films by a method reported previously [30]. Briefly, modified SBF solutions were prepared having approximately 7 times (7xSBF-A) and 10 times (10xSBF-A) the concentration of ion species (Na^+ , K^+ , Mg^{2+} , Ca^{2+} , Cl^- , HPO_4^{2-} , SO_4^{2-}) compared to human blood plasma. An SBF solution (SBF-B), nominally free of Mg^{2+} , HCO_3^- and SO_4^{2-} , was also prepared and used as a crystal growth solution.

NaHCO_3 (0.0882 g) was added to 50 mL of modified SBF-A solution stirring at 500 rpm and 37°C to achieve a pH of 5.90. PCL films (5 g, molecular weight = 80 000

g/mol, Solvay Chemicals Inc., Houston, TX) with a diameter of 15 mm were treated with NaOH and then suspended in the SBF-A solution for 24 and 48 h (with solution replenishment after 24 h) to produce HA coatings with varying surface topography. Following treatment in SBF-A, samples were incubated in SBF-B for an additional 48 h. Incubation of the samples was performed at a temperature of 37°C and stirring at 75 rpm. Coated specimens were thoroughly washed with deionized water and air-dried.

The topography of biomimetic HA surfaces was assessed by scanning electron microscopy (SEM). Samples were coated with 3 nm osmium using a Filgen OPC-80T instrument and then examined using a FIB/SEM LEO 1540XB microscope equipped with an EDX spectrometer for elemental analysis (Carl Zeiss, Jena, Germany).

HA coatings were previously characterized using X-ray diffraction (XRD), Fourier-transform infrared spectroscopy (FTIR), nanoindentation, and energy dispersive X-ray spectroscopy (EDX) [30]. In addition, analysis of the surface topography at high and low resolution was previously performed using atomic force microscopy (AFM, to assess fine submicron-scale topography) and mechanical stylus profilometry (to assess coarse micron-scale topography), respectively. Surface roughness (R_a) was quantified as the arithmetic mean of the absolute values of the height profile deviations from the mean line. Two R_a values are reported for each surface, the first obtained using AFM and the second from profilometry [30]. Analysis of sub-micrometer topography by AFM revealed that PCL substrates incubated in 7xSBF-A for 48 h produced HA coatings with $R_a = 194$ nm, whereas profilometry indicated micro-scale topography with $R_a = 1.0$ μm and are designated as having “smoother” (HA1) topography. Substrates incubated in 10xSBF-A for 24 h produced “submicro-rough” (HA2) surfaces having significantly greater roughness ($R_a = 316$ nm) as measured by AFM, but no difference at low

resolution ($R_a = 1.3 \mu\text{m}$) as determined using profilometry. Incubation in 10xSBF-A for 48 h yielded HA coatings with both submicrometer and micron-scale roughness, with equivalent $R_a = 363 \text{ nm}$ at high resolution (AFM) and significantly increased $R_a = 2.0 \mu\text{m}$ at low resolution (profilometry), and therefore, have a “micro-rough” (HA3) topography.

4.3.2 Osteoblast isolation and culture

Rat calvarial osteoblasts (RCO) were isolated from 0- to 5-day-old neonatal Sprague Dawley rats. All animal procedures were approved by the University Council on Animal Care of The University of Western Ontario and were in accordance with the guidelines of the Canadian Council on Animal Care. Briefly, the parietal and occipital bones were dissected and washed with phosphate-buffered saline (PBS). The harvested bones were minced and subsequently digested by incubation in 700 units/ml of type I collagenase (Sigma-Aldrich, St. Louis, MO) at 37°C . The supernatant of the first digestion was discarded and the calvarial fragments were treated five more times with collagenase (20 min at 37°C), and the subsequent supernatants were collected, combined and sedimented. The resulting cell pellet was re-suspended and cultured in α minimum essential media (α -MEM) supplemented with 10% (v/v) fetal bovine serum (FBS; Life Technologies Inc., Carlsbad, CA), antibiotics and antimycotic (AA; 200 U/mL penicillin, 200 $\mu\text{g}/\text{mL}$ streptomycin, 0.5 $\mu\text{g}/\text{mL}$ amphotericin B) (Gibco, Carlsbad, CA). Primary RCO cultures were maintained in a humidified 5% CO_2 atmosphere at 37°C and, in some cases, stored in liquid nitrogen.

Prior to cell experiments, RCOs were expanded until 80 to 100% confluent and released from 75-cm² tissue culture plastic flasks using a 0.05% trypsin and 0.2 g/L EDTA solution, and cell number was determined using a Multisizer 3 Coulter Counter (Beckman Coulter, Mississauga, ON, Canada). Substrata were sterilized in low-temperature, radio-frequency glow discharge (RFGD) argon plasma using a PDC-32G plasma cleaner (Harrick Plasma, Ithaca, NY) for 4 min. For assessment of cell attachment and fluorescence labeling, RCOs (passage 2-4) were seeded on substrates in 24-well plates at 2.5×10^3 cells/cm²; for differentiation experiments, RCOs (primary or passage 1) were seeded on substrates in 24-well plates at a density of 25×10^3 cell/cm².

4.3.3 Osteoblast attachment and morphology

RCOs were cultured on HA1, HA2 and HA3 surfaces for 6 h. Cells were then fixed using 4% paraformaldehyde (PFA) in PBS, and permeabilized with 0.1% Triton-X 100 in PBS for 5 min. Samples were blocked using 3% bovine albumin (BSA) in PBS for 30 min. To reveal focal adhesions, substrates were incubated with primary antibodies to vinculin (Millipore, Billerica, MA) at 1:100 dilution in 3% BSA in PBS for 1 h. The surfaces were rinsed three times with PBS and then incubated for 1.5 h with Alexa Fluor 488-conjugated goat anti-mouse IgG secondary antibody (1:200 dilution in 3% BSA in PBS, Life Technologies Inc.) for visualization of vinculin, and rhodamine-conjugated phalloidin (1:100 dilution in 3% BSA in PBS, Cytoskeleton Inc., Denver, CO) for visualization of filamentous actin (F-actin). Nuclei were counterstained using Vectashield Mounting Medium (Vector Labs, Burlingame, CA) containing 4',6-diamidino-2-phenylindole (DAPI).

Images were captured using an Axio Observer Z.1 fluorescence microscope (Carl Zeiss, Jena, Germany) and AxioImager software. Osteoblast attachment was determined on each surface by evaluating the total number of nuclei visible from 10 non-overlapping fields of view, selected at random. For quantification of cell spreading, the planar area of the cells was measured using AxioVision Software Release 4.8.0.0. The average cell planar area was determined from 10 cells on each sample. To assess the number of focal adhesions, vinculin labeling was analyzed using ImageJ software (National Institutes of Health, Bethesda, MD). The average number of focal adhesions per cell was determined for 10 cells by an impartial, blinded observer.

4.3.4 Osteoblast differentiation and quantitative assessment of osteoblast marker gene expression

RCOs were incubated on each substratum (HA1, HA2 and HA3) and cultured in α -MEM (supplemented with 10% FBS and AA) for 3 days. Subsequently, RCO's were cultured in osteogenic medium (regular medium described above supplemented with 2 mM β -glycerophosphate and 50 μ g/mL ascorbic acid) and incubated for an additional 7 or 14 days (with medium changed every 2-3 days). Total RNA was extracted using TRIzol (Invitrogen) prior to the addition of osteogenic medium (day 0) and at days 7 and 14. RNA was purified using an RNeasy Micro Kit (Qiagen - Canada, Toronto, ON) and genomic DNA removed using DNase I (Qiagen), according to the manufacturer's instructions. Purified RNA was stored at -80°C until required. The total RNA concentration and purity were determined from absorption at 260 and 280 nm using a Nanodrop spectrophotometer (Thermo Fisher Scientific, Waltham, MA, USA).

Quantitative real-time PCR (RT-qPCR) was performed to determine transcript levels of type I collagen (*Colla2*), tissue non-specific alkaline phosphatase (*Alpl*) and osteocalcin (*Bglap*).

RT-qPCR was performed using the ABI Prism 7900 HT Sequence Detector (Applied Biosystems, Carlsbad, CA, USA) with 15 μ l final reaction volumes containing: 5-25 ng RNA sample; TaqMan One-Step RT-PCR Master Mix Reagents (Applied Biosystems); *Colla2*, *Alpl*, *Bglap* or *18S* ribosomal RNA primers and probes (Applied Biosystems); and RNase-free water. Reverse transcription was performed at 48°C for 30 min followed by 40 cycles of amplification at an annealing temperature of 60°C. *Colla2*, *Alpl* and *Bglap* gene expression was normalized to levels of endogenous *18S* rRNA. Expression is given as fold change relative to day 0 levels for cells cultured on smoother (HA1) substrata, calculated using the delta-delta cycle threshold ($\Delta\Delta C_T$) method. Efficiency was verified using standard curves for each primer-probe set, generated from a dilution series of pooled RNA.

4.3.5 Osteoclast isolation and culture

Authentic osteoclasts were isolated from the long bones of neonatal New Zealand white rabbits as described previously [31]. Briefly, long bones were minced and cells suspended in M199 medium supplemented with 15% FBS, antibiotics and antimycotic (100 U/mL penicillin, 200 μ g/mL streptomycin, 0.5 μ g/mL amphotericin B). Dentin was used as a control substratum. Slices (6 x 6 mm) were prepared from elephant ivory obtained as a gift from the Canadian Wildlife Service and cleaned by sonication in 70% ethanol. Substrata (dentin slices, HA1 and HA3) were sterilized by RFGD argon plasma

and pretreated with FBS for 1 h. Subsequently, 500 μL of osteoclast suspension was carefully added to the top of the dentin, HA1 and HA3 samples and incubated in humidified 5% CO_2 at 37°C for 1 h. Substrates were then washed gently with PBS to remove non-adherent cells, and 1 ml of supplemented M199 medium was added and samples were incubated at 5% CO_2 for 48 h. For evaluation of pit formation and F-actin organization, samples were incubated in humidified 10% CO_2 at 37°C for 48 h, conditions known to decrease medium pH to ~ 7.0 [32], and stimulate of resorptive activity [33].

4.3.6 Tartrate-resistant acid phosphatase (TRAP) activity

After 48 h in culture, the osteoclasts were fixed using 4% PFA in PBS for 10 min and substrata were rinsed three times with PBS. Samples were stained for TRAP activity, an enzymatic marker of osteoclasts, using an acid phosphatase kit (Sigma-Aldrich) according to the manufacturer's protocol without counter-staining with hematoxylin. Images were obtained using a Nikon SMZ 1500 stereoscopic zoom microscope (Nikon Instruments Inc. Melville, NY) equipped with a Fiber-Lite MI-150 high intensity illuminator (Dolan-Jenner Industries, Boxborough, MA) and a Photometrics CoolSNAP *cf* CCD camera (Roper Scientific Photometrics, Tucson, AZ). Micrographs were analyzed to determine the size distribution of the TRAP-positive regions using ImageJ software (to exclude debris, only areas $> 60 \mu\text{m}^2$ were included in the analysis). We quantified the total area of TRAP-positive regions, and the total number of regions with planar area $> 250 \mu\text{m}^2$ (as an indicator of the number of osteoclasts) on five randomly selected fields of view.

4.3.7 Resorption activity

Determination of osteoclastic resorption was also performed by SEM analysis [34]. At the conclusion of the osteoclast incubation (48 h), the majority of non-osteoclastic cells were removed from the test substrata using Pronase E (0.001% in PBS with 0.5 mM EDTA) at 37 °C for 5 min [31]. Samples were then gently washed with PBS, replaced in fresh medium and incubated at 37°C for 2 h to allow osteoclast morphology to recover. Culture medium was then removed and cells fixed with 4% glutaraldehyde solution (Sigma-Aldrich) for 15 min, after which substrata were gently rinsed three times with PBS. To preserve osteoclast morphology [35], samples were dried using hexamethyldisilazane (HMDS; Sigma-Aldrich). Samples were first dehydrated in a series of ethanol dilutions (25%, 50%, 75%, 90%, 95% and 100%) for 5 min at each concentration. Substrata were then submerged in 100% hexamethyldisilazane for 10 min and dried in air. Surface topography of substrata after incubation with and without osteoclasts was examined using the FIB/SEM LEO 1540XB microscope. Resorption pit planar area was determined by measuring the area of 10-15 pits from two independent experiments using ImageJ software.

4.3.8 Fluorescence microscopy

Fluorescence microscopy was used to visualize the F-actin organization within osteoclasts by fluorescence staining. After 48 h in culture, the cells were fixed using 4% PFA in PBS and permeabilized with 0.1% Triton-X 100 in PBS for 5 min. The surfaces were rinsed three times with PBS and the samples were blocked with 3% BSA in PBS

for 30 min. The substrates were incubated for 1.5 h with rhodamine-conjugated phalloidin (1:100 dilution in 3% BSA in PBS). Nuclei were counterstained using DAPI containing Vectashield Mounting Medium. Osteoclasts were identified as multinucleated cells having three or more nuclei.

To monitor organization of actin within live osteoclasts, adenovirus expressing human β -actin-EGFP fusion protein was created using the ViraPower™ adenoviral expression system, according to the manufacturer's protocols (Invitrogen). pAd/CMV/V5-DEST and pENTR1A Gateway vectors were used. A NheI-BamHI fragment containing actin-EGFP was isolated from the pActin-EGFP vector (Clontech, Mountain View, CA) and cloned into the pENTR1A vector. HEK293A cells (Invitrogen) were used for adenovirus amplification. A crude viral lysate was prepared in α -MEM supplemented with 2% FBS. Preliminary experiments were performed to optimize transfection conditions for each virus preparation. Rabbit osteoclasts were isolated and cultured on HA3 samples in a 24-well culture plate for 1 day. Viral lysate was then added onto each sample (200 μ L per sample) and incubated for 20 min at 37°C. Subsequently, 2 mL of supplemented M199 medium was added to each well and cultures were incubated for 24 h before imaging.

A confocal microscope (model LSM 510 META; Zeiss) was used to visualize the actin organization within the actin-EGFP-transfected live osteoclasts and fixed osteoclasts stained with rhodamine-conjugated phalloidin. Images were acquired using Zeiss C-Apochromat 40x water-immersion objective. EGFP was visualized using 488-nm Ar⁺ ion laser excitation and a 500-550 nm emission band pass filter. Rhodamine was visualized using 543-nm HeNe laser excitation and a 565-615 nm emission band pass filter.

4.4 Results

4.4.1 Control of surface topography of biomimetic hydroxyapatite coatings

We prepared HA surface coatings with varying topographical features and roughnesses by incubation of functionalized polycaprolactone (PCL) with simulated body fluid (SBF) of different ionic concentrations and for various soaking times (Fig. 4.1). Detailed characterization of the crystal phase, identification of functional groups, substrate stiffness, and surface roughness of the HA coatings have been described in our previous study [30]. Each of the HA coatings consisted of the same crystal phase (poorly crystalline, bone-like HA) and exhibited carbonate substitution. In addition, EDX analyses revealed virtually identical elemental composition (Figure 4.2) and there were no significant differences in Ca/P or Na/Ca ratios.

As shown previously [30], the HA surface roughness was assessed at high resolution (sub-micrometer) using AFM and at lower resolution (micro-scale) using profilometry. For the purposes of the present study, HA surfaces with $R_a = 190$ nm and 1.0 μm as measured by AFM and profilometry, respectively, were considered to have a smoother (HA1) surface. HA coatings with $R_a = 320$ nm and $R_a = 1.3$ μm were considered to be submicro-rough (HA2, i.e. rough at high resolution). Lastly, HA coatings with $R_a = 360$ nm and $R_a = 2.0$ μm were considered to be micro-rough (HA3) and were rough at both high and low resolution. These materials were used to investigate the effect of surface topography of biomimetic HA coatings on the behavior of osteoblasts and osteoclasts.

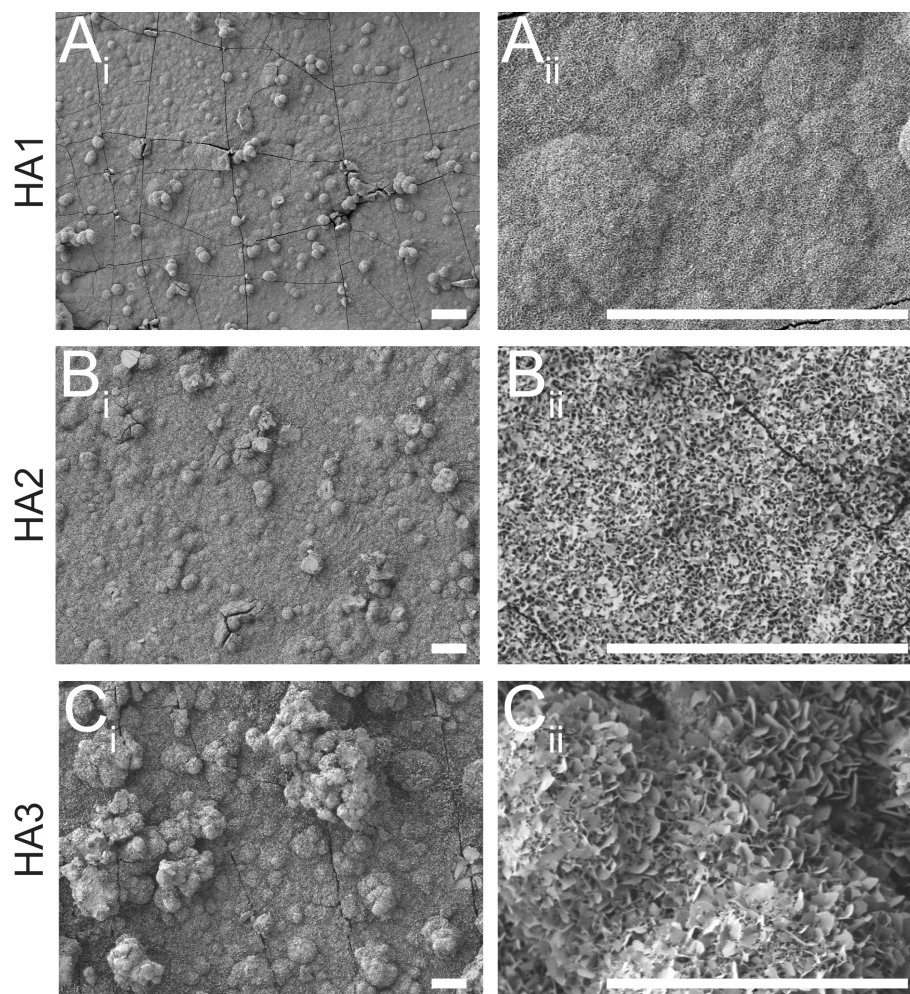


Figure 4.1 Scanning electron microscope (SEM) images of hydroxyapatite (HA) coatings. HA was deposited on polycaprolactone (PCL) discs by immersion in modified simulated body fluid (SBF) of different ionic concentrations. A) Smoother (HA1) topography was obtained by initial incubation in 7xSBF-A for 48 h. B) sub-micrometer rough (HA2) topography was obtained by initial incubation in 10xSBF-A for 24 h. C) Sub-micrometer and micro-rough (HA3) topography was obtained by initial incubation in 10xSBF-A for 48 h. Images are representative of multiple samples from at least 5 independent preparations. Scale bar = 20 μm in all panels.

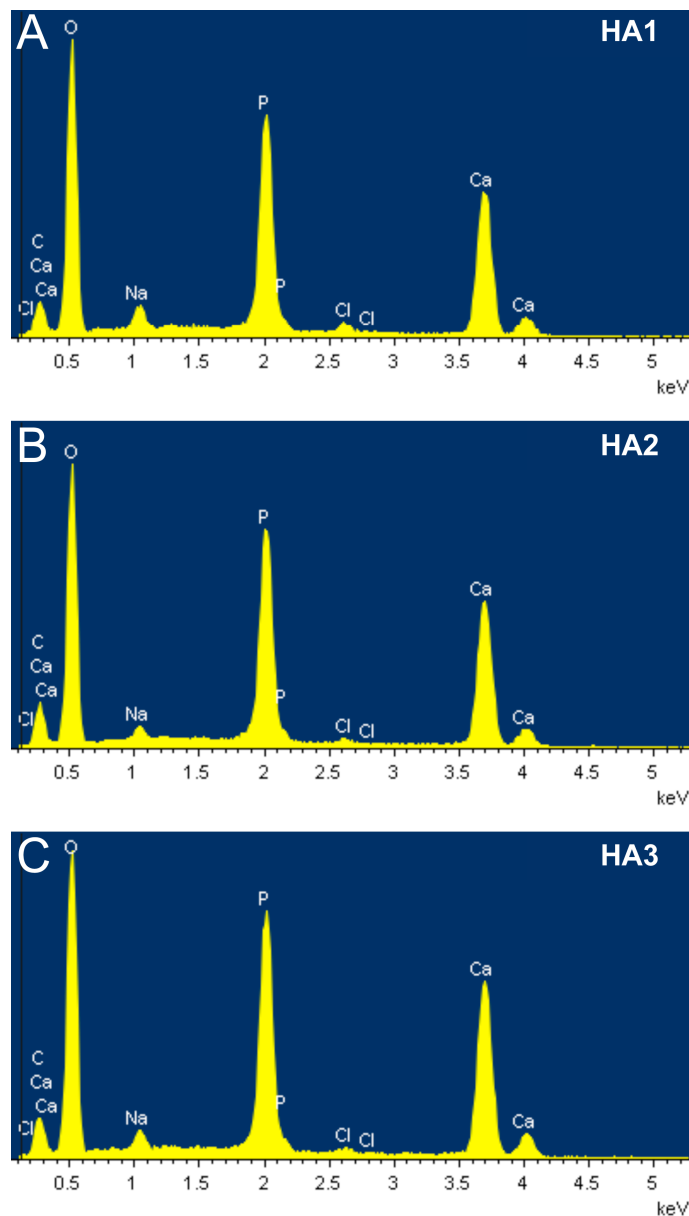


Figure 4.2 Elemental analysis of hydroxyapatite (HA) coatings as determined by energy dispersive X-ray spectroscopy (EDX). HA was deposited on polycaprolactone (PCL) discs by immersion in modified simulated body fluid (SBF) of different ionic concentrations. A) Representative spectrum from smoother (HA1) topography obtained by initial incubation in 7xSBF-A for 48 h. B) Representative spectrum from sub-micrometer-rough (HA2) topography obtained by initial incubation in 10xSBF-A for 24 h. C) Representative spectrum from micro-rough (HA3) topography obtained by initial incubation in 10xSBF-A for 48 h. These data reveal that the elemental composition of all 3 substrata was virtually identical. Spectra are representative of 3 spot analyses from 3 independent preparations.

4.4.2 Effect of HA surface topography on osteoblast attachment, spreading and focal adhesion formation

Rat calvarial osteoblasts (RCOs) were cultured on the different HA coatings for 6 h, then cells were fixed, and nuclei, F-actin and vinculin were labeled. Osteoblast morphology was assessed by fluorescence microscopy of F-actin-labeled cells (Fig. 4.3(A), red label). Morphology was similar for osteoblasts attached to HA1 and HA2 surfaces – cells showed long cytoplasmic extensions, filopodia and stress fiber formation. By contrast, osteoblasts attached to the rougher HA3 coatings displayed fewer cellular projections, lamellipodia, F-actin-rich microspikes and a more diffuse, randomly arranged pattern of cytoplasmic F-actin.

Fluorescence imaging of F-actin and nuclei showed that osteoblasts attached well on each of the HA1, HA2 and HA3 surfaces. Interestingly, osteoblast attachment was greater by ~ 50% on the HA3 coating compared to the smoother HA1 surface (Fig. 4.3(B), $p < 0.05$). Osteoblast spreading was quantified by measuring the planar area of cells and was found to be similar on each surface, with mean values ranging from 870-1050 μm^2 (Fig. 4.3(C), $p > 0.05$). Focal adhesions were observed by immunofluorescence imaging of vinculin-labeled cells (Fig. 4.3(A)). Numerous focal adhesions appeared at the termini of projections from osteoblasts adhered to HA1 and HA2 coatings. In contrast, vinculin showed predominate distribution perinuclear in osteoblasts attached to rougher HA3 surfaces. Quantification revealed a markedly greater number of focal adhesions in osteoblasts attached to HA1 compared to cells on HA3 coatings (Fig. 4.3(D), $p < 0.05$).

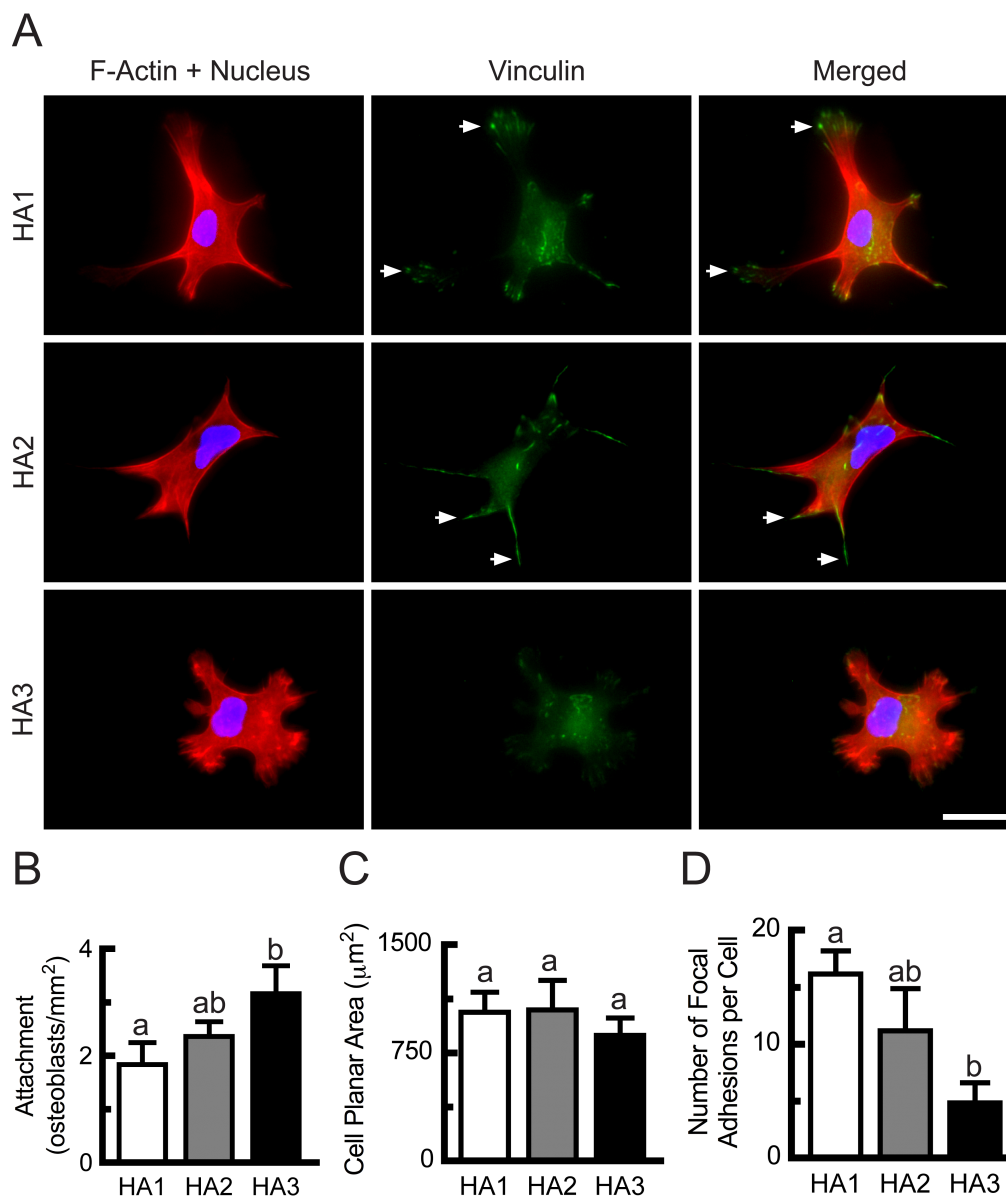


Figure 4.3 Effects of HA surface topography on osteoblast attachment, spreading and focal adhesion formation. Rat calvarial osteoblasts (RCOs) were cultured on the HA coatings for 6 h. Cells were then fixed, labeled for nuclei (blue), F-actin (red) and vinculin (green). A) Representative fluorescence images of single osteoblasts on smoother (HA1), sub-micrometer-rough (HA2) and micro-rough (HA3) coatings. Focal adhesions were revealed by vinculin staining (arrows). Scale bars = 50 µm, and applies to all panels. B) Osteoblast attachment was quantified as the number of cells attached per mm². Data are means ± SEM from 10 fields of view of triplicate samples from $n = 4$ independent experiments. C) Planar cell area was quantified by image analysis. Data are means ± SEM of triplicate samples from $n = 4$ independent experiments. D) Number of focal adhesions per cell was determined by a blinded observer. Data are means ± SEM of $n = 6$ samples from two independent experiments. Data were analyzed by one-way ANOVA and Tukey's multiple comparisons test. Bars labeled with the same lower case letter are not significantly different ($p > 0.05$).

In summary, the surface topography of biomimetic HA coatings influenced osteoblast attachment and focal adhesion formation. Micro-rough HA3 surfaces supported greater attachment, but fewer focal adhesions than did smoother HA1 coatings.

4.4.3 Effect of HA surface topography on markers of osteoblast differentiation

RCOs were plated on HA1, HA2 and HA3 surfaces and cultured for 3 days. Medium was then supplemented with β -glycerophosphate and ascorbic acid to induce osteoblastic differentiation (day 0) and cells were cultured for an additional 7 or 14 days. Quantitative RT-PCR revealed that transcript levels of *Colla2* were not significantly different on day 0. As expected, by day 7 some modest increases were observed in the expression of collagen type I (Fig. 4.4(A)). Interestingly, *Colla2* mRNA levels were significantly greater when osteoblasts were differentiated on the micro-rough HA3 coatings than on the smoother HA1 surfaces ($p < 0.05$).

A classic marker of osteoblast differentiation, tissue-nonspecific alkaline phosphatase, is encoded by *Alpl* and plays a critical role in regulating mineralization of the extracellular matrix [36]. By day 7, there was marked upregulation of *Alpl* expression in osteoblasts on all 3 substrata (Fig. 4.4(B)). Notably, significant increases in *Alpl* transcript levels were more than 2-fold greater in osteoblasts on the rougher HA3 surfaces as compared to HA1 coatings ($p < 0.05$).

Osteocalcin, also known as bone γ -carboxyglutamic acid-containing protein, is secreted only by osteoblasts and is encoded by the gene *Bglap*. Moreover, osteocalcin is expressed by osteoblasts at later stages of differentiation than is tissue-nonspecific

alkaline phosphatase [37]. Consistent with expression at later stages of differentiation, we observed dramatic upregulation of *Bglap* transcript levels after 14 days of culture on all substrata (Fig. 4.4©). In keeping with the changes observed in *Alpl* expression, significant increases in *Bglap* transcript levels were more than 2-fold greater in osteoblasts on HA3 surfaces, as compared to HA2 and HA1 coatings ($p < 0.05$). Taken together, these data indicate that the biomimetic HA coating with greater surface roughness and complexity (HA3, $R_a \sim 360$ nm and $R_a \sim 2$ μ m) promotes osteoblast differentiation.

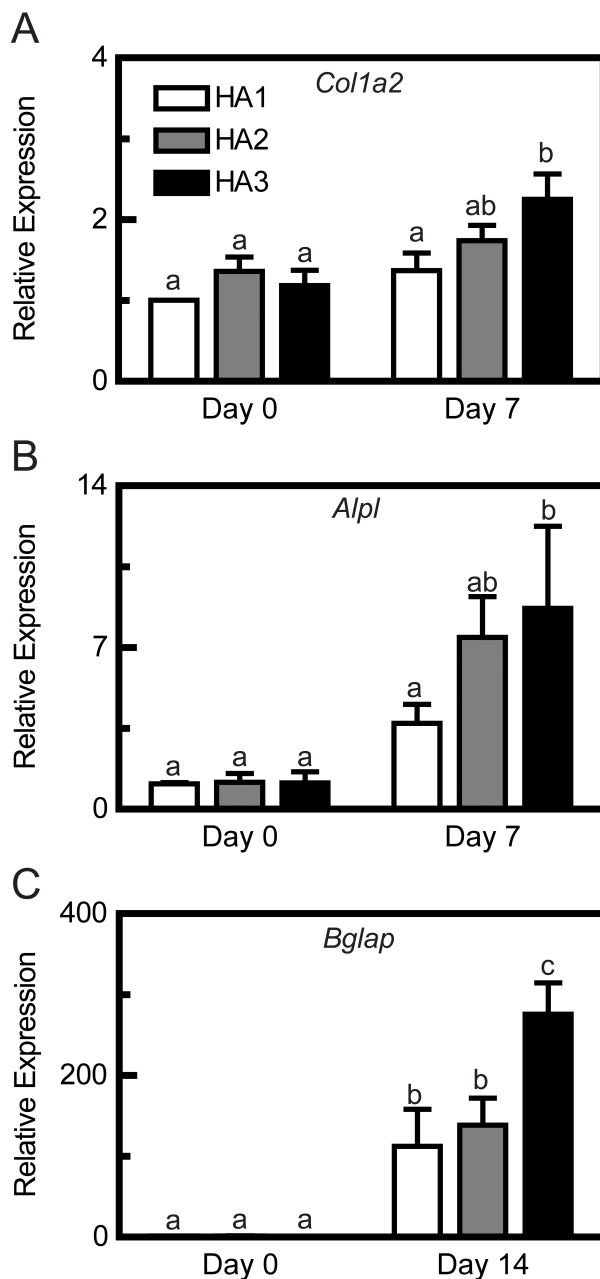


Figure 4.4 Effect of HA surface topography on expression of osteoblast differentiation markers. RCOs were plated on HA1, HA2 and HA3 surfaces and cultured for 3 days. Medium was then supplemented with β -glycerophosphate and ascorbic acid to induce osteoblastic differentiation (day 0) and cells were cultured for an additional 7 or 14 days. Quantitative RT-PCR was performed to assess transcript levels of collagen type I (*Col1a2*, A), tissue-nonspecific alkaline phosphatase (*Alpl*, B) and osteocalcin (*Bglap*, C). Expression was normalized to levels of endogenous 18S rRNA and is reported as fold change relative to day 0 levels for cells cultured on smoother (HA1) substrata. Data are means \pm SEM of triplicate samples from $n = 3$ independent experiments. Data were analyzed by two-way ANOVA with repeated measures and Bonferroni multiple comparisons test. Bars labeled with the same lower case letter are not significantly different ($p > 0.05$).

4.4.4 Effect of HA surface topography on osteoclasts as revealed by staining for tartrate-resistant acid phosphatase (TRAP) activity

Primary osteoclasts and osteoclast precursors were disaggregated from the long bones of neonatal rabbits, plated on test substrata and cultured for 2 days. In these experiments, we compared the effects of the following surfaces: smoother (HA1); micro-rough (HA3), which was superior for osteoblast attachment and differentiation; and dentin slices, which are resorbable by osteoclasts *in vitro* and were used as a positive control.

After 2 days, cultures were stained for TRAP, a well-established histochemical marker of osteoclasts and late osteoclast precursors [38]. In the absence of cells, no TRAP staining was observed on any of the substrata (Fig 4.5(A_i, B_i, C_i)). However, on surfaces plated with cells, positive TRAP staining was observed (Fig. 4.5(A_{ii}, B_{ii}, C_{ii})) with the greatest amount of TRAP staining apparent in cultures plated on the less rough and smoother HA1 coatings (Fig. 4.5(B_{ii})).

Image analysis software was used to quantify the planar area and number of TRAP-stained regions on each substratum. Frequency distribution plots of the areas of TRAP-stained regions were fit by nonlinear regression using a two-phase exponential decay model (Fig. 4.5(A_{iii}, B_{iii}, C_{iii})). The second decay constant was 10-fold smaller for HA1 surfaces, indicating a broader range of larger TRAP-positive cells on the smoother surfaces (Fig. 4.5(D)). Total TRAP-stained area was significantly greater on HA1 surfaces than on HA3 coatings (Fig. 4.5(E), $p < 0.05$), consistent with greater attachment and spreading of osteoclasts and osteoclast precursors on the smoother topography.

Material with planar area less than $60 \mu\text{m}^2$ was considered to be debris; 60 to $250 \mu\text{m}^2$ was consistent with the size of mononucleated osteoclast precursors, while labeled regions greater than $250 \mu\text{m}^2$ most likely represented multinucleated osteoclasts (although we recognize that these could also be contiguous groups of precursors). Using these criteria, we estimated the total number of osteoclasts on each substratum (Fig. 4.5(F)). The number of osteoclasts on smoother HA1 surfaces was approximately 2.5-fold greater than on micro-rough HA3 coatings ($p < 0.05$). Thus, surface topography appears to have a major influence on osteoclast attachment and spreading.

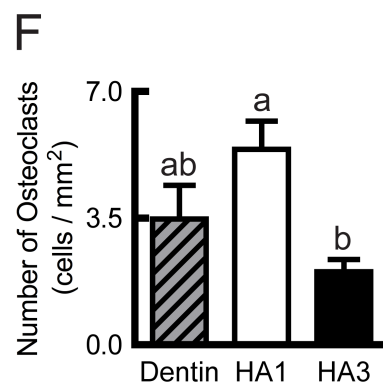
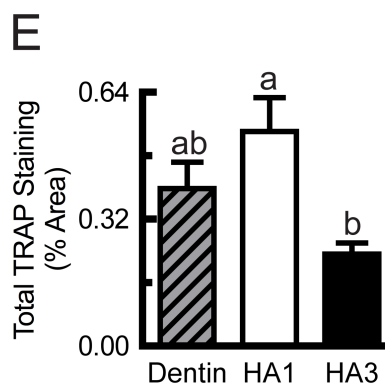
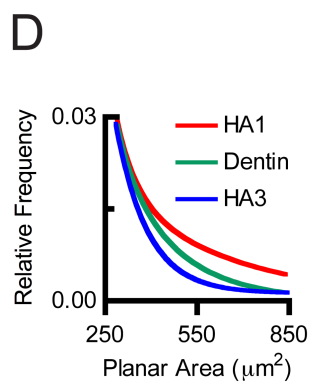
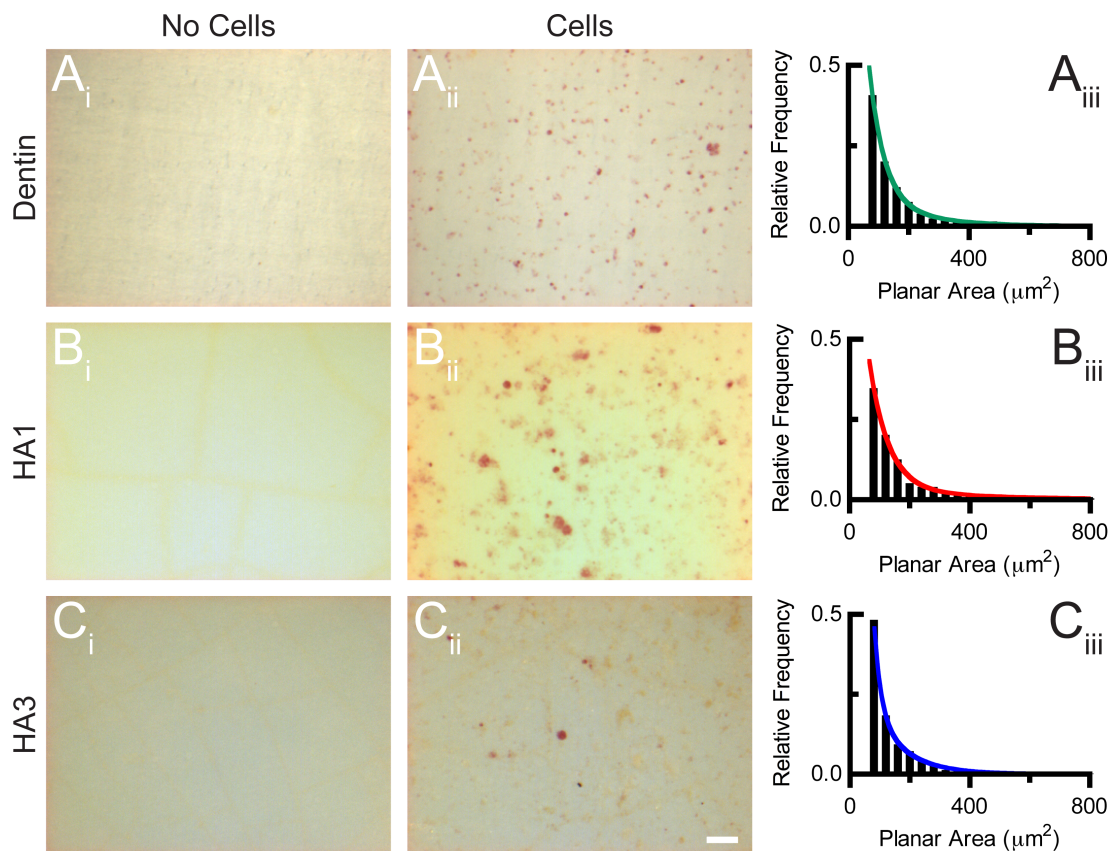


Figure 4.5 Effect of HA surface topography on osteoclasts as revealed by staining for tartrate-resistant acid phosphatase (TRAP) activity. Dentin slices (control, A), smoother HA1 (B) and micro-rough HA3 (C) were incubated for 2 days in the presence and absence of rabbit osteoclasts. Samples were then stained for activity of the osteoclast marker enzyme TRAP (red). Image analysis software was used to quantify the planar area and number of TRAP-stained regions on each substratum. To exclude debris, only areas $> 60 \mu\text{m}^2$ were included in the analysis. A-C) Panels at right illustrate frequency distribution plots of the areas of TRAP-stained regions. Distributions were fit by nonlinear regression using a two-phase exponential decay model. First and second decay constants were (in μm^{-2}): 0.0055 and 0.020 for dentin; 0.016 and 0.0025 for HA1; and 0.0096 and 0.045 for HA3. D) Plot of nonlinear regression curves, fit to the distribution of TRAP regions observed on dentin (green curve), HA1 (red curve) and HA3 (blue curve). E) Area of TRAP staining was quantified as a percentage of the total area of each substratum. F) Number of TRAP-positive osteoclasts (planar area $> 250 \mu\text{m}^2$) was also quantified. Data are means \pm SEM from 5 fields of view of triplicate samples from $n = 3$ independent experiments. Data were analyzed by one-way ANOVA and Tukey's multiple comparisons test. Bars labeled with the same lower case letter are not significantly different ($p > 0.05$). Scale bars = $100 \mu\text{m}$ and applies to all panels.

4.4.5 Effect of HA surface topography on osteoclastic resorption

We next explored the ability of osteoclasts to resorb HA coatings. Smoother (HA1) HA, micro-rough (HA3) HA and dentin slices were incubated for 2 days in the presence and absence of rabbit osteoclasts. Preparations were then fixed and processed for analysis by SEM. Dentin, HA1 and HA3 samples incubated without cells showed no pits or defects that could be mistaken for resorption lacunae formed by osteoclasts (Fig. 4.6(A_i, B_i, C_i)), the planar areas of which are typically of the order of $1-3 \times 10^3 \mu\text{m}^2$ [34]. As expected, osteoclasts produced distinct resorption lacunae on dentin slices showing typical shallow resorption pits, often associated with the presence of an osteoclast (Fig. 4.6(A_{ii})). Numerous mononucleated cells and erythrocytes were also apparent. Osteoclastic resorption pits were observed on smoother HA1 coatings (Fig. 4.6(B_{ii})). However, in contrast to pits on dentin, resorption lacunae on HA1 surfaces showed a markedly distinct morphology, appearing as deep, punched-out pits with smaller planar area (Fig. 4.6(D)). Strikingly, no evidence of resorption pits was seen on any of the micro-rough HA3 surfaces after examination of a total of five surfaces from 3 independent osteoclast preparations. Nevertheless, osteoclasts were observed on HA3 coatings exhibiting typical spread morphology (Fig. 4.6(C_{ii})). In summary, SEM analysis revealed a dramatic effect of topography on the ability of osteoclasts to resorb HA.

Osteoclasts on HA1 substrata were well spread and appeared to be in more intimate contact with the surface (Fig. 4.7(A)) than osteoclasts on HA3 coatings (Fig. 4.6(C_{ii})). Furthermore, osteoclasts on the smoother HA1 substrata appeared to localize selectively to regions devoid of large surface irregularities. Some osteoclasts that appeared to be actively resorbing HA1 substrates were slightly dome shaped (Fig.

4.7(B)), suggesting apico-basal polarization. Other osteoclasts, associated with completely formed resorption lacunae, appeared to be migrating (Fig. 4.7(C)). Fig. 4.7(D) shows a higher magnification image of the resorption lacunae in Fig. 4.7(C). The HA1 appears to be completely removed down to the underlying PCL polymer. A distinct ring-like structure is apparent on the inside periphery of lacunae, which we suggest could represent partial dissolution of HA at the site of the sealing zone.

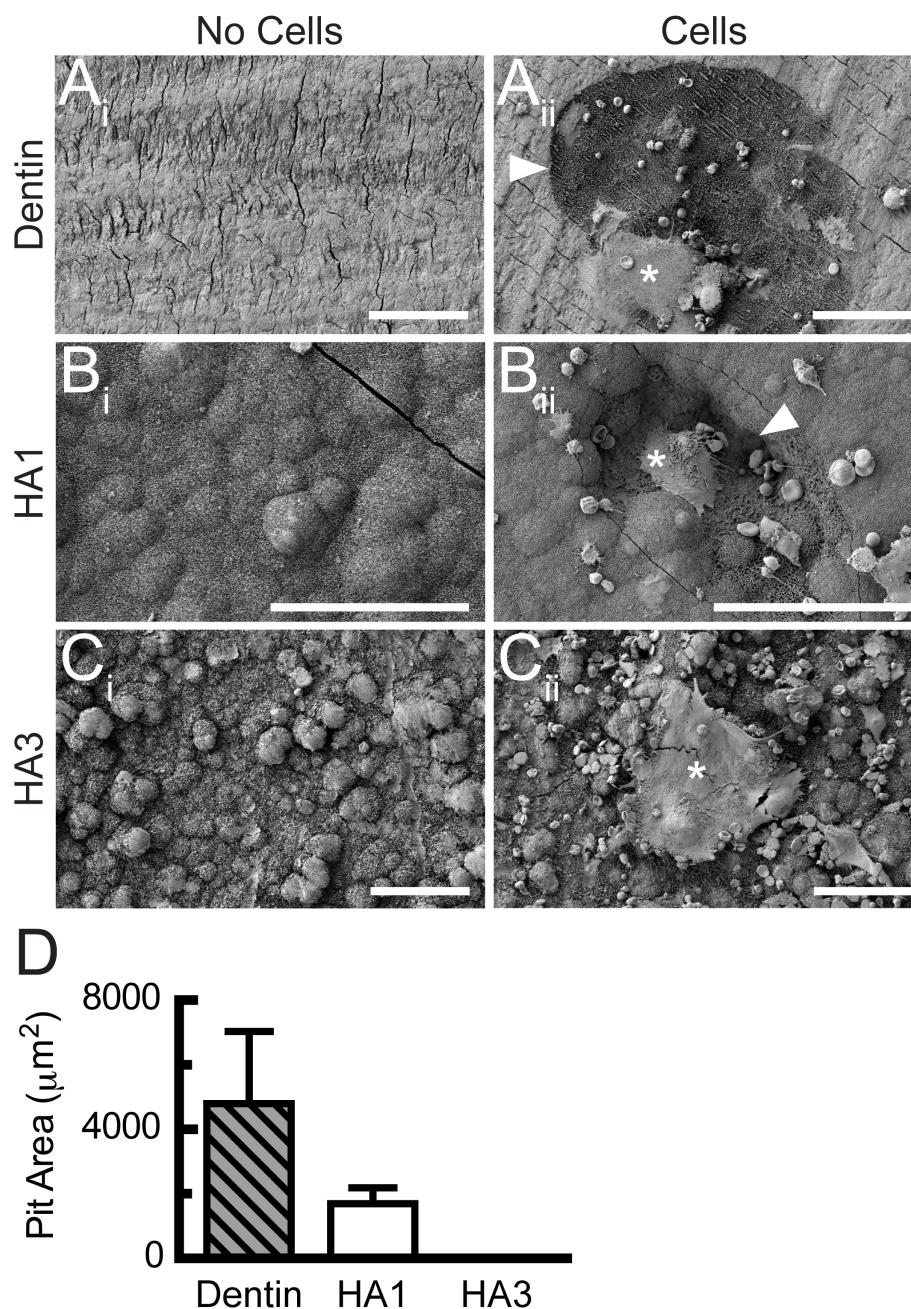


Figure 4.6 Effect of HA surface topography on osteoclastic resorption. Dentin slices (A), and HA with smoother (HA1, B) and micro-rough (HA3, C) topographies were incubated for 2 days in the absence (left panels) and presence (right panels) of rabbit osteoclasts. Preparations were then fixed and processed for analysis by SEM. Arrowheads indicate resorption pits. Asterisks indicate osteoclasts. Scale bars = 50 μm. Images are representative of samples from three independent cell isolations. D) Pit area was quantified using ImageJ software. Data are means ± SEM of $n = 10$ to 15 pits from 2-3 independent cell isolations.

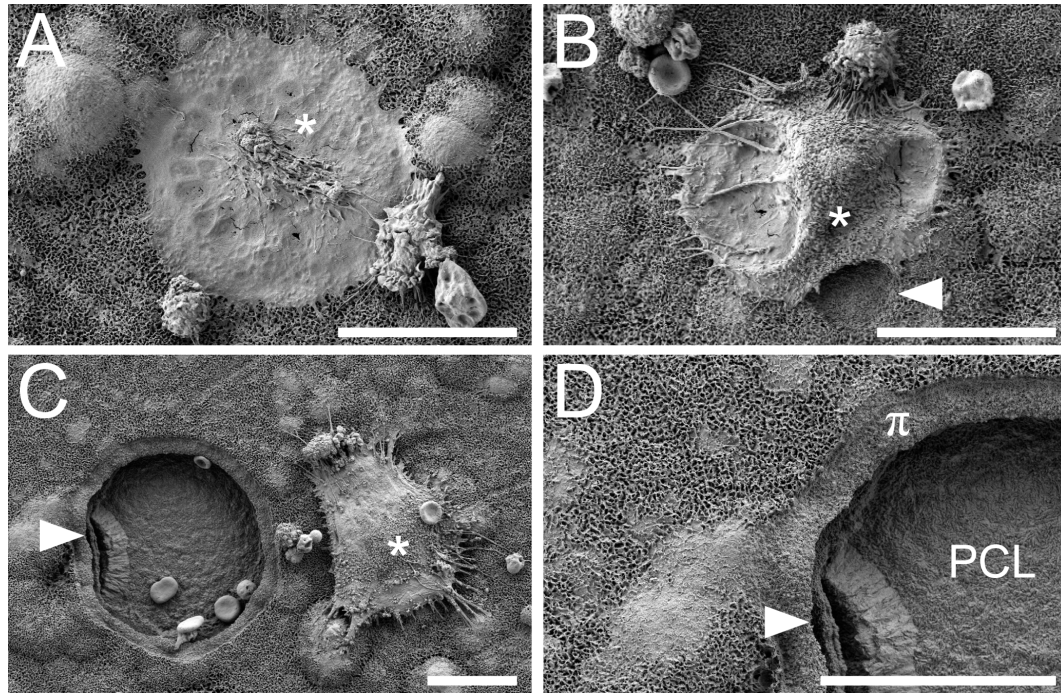


Figure 4.7 Osteoclastic resorption on the smooth HA1 coatings. Rabbit osteoclasts were cultured for 2 days on the smoother HA1 coatings. Preparations were then fixed and processed for analysis by SEM. Arrowheads indicate resorption pits. Asterisks indicate osteoclasts. Scale bars = 20 μm . Three osteoclasts are illustrated. A) Osteoclast is well spread and in intimate contact with the HA1 surface. B) Another slightly dome-shaped osteoclast appeared to be actively resorbing the HA1 substrate. C) A third osteoclast was associated with a distinct resorption lacuna and appeared to be migrating. D) A higher magnification image of a part of the resorption lacunae shown in panel C. HA1 appears to have been completely removed down to the underlying polycaprolactone (PCL) polymer base. A distinct ring-like structure (designated by π) is apparent on the inside periphery of lacunae, which could represent partial dissolution of HA1 at the site of the sealing zone.

4.4.6 Effect of HA surface topography on F-actin organization in osteoclasts

Osteoclasts adhere to substrata via podosomes – dynamic, F-actin-containing structures that self-organize into rings, belts and sealing zones, which are essential for resorption [39, 40]. We next addressed the effect of substratum topography on sealing zone formation by analysis of F-actin organization. Rabbit osteoclasts were cultured on the smoother HA1, micro-rough HA3 and dentin slices for 2 days, the studied by fluorescence microscopy (Fig. 4.8).

On both dentin and smoother HA1 coatings, many osteoclasts exhibited typical F-actin sealing zones (Fig. 4.8(A, B)). Ring-like sealing zones are typically formed by active osteoclasts plated on resorbable substrata. In contrast, osteoclasts cultured on micro-rough HA3 coatings more often displayed disrupted F-actin organization, with individual podosomes and podosome belts along the cell periphery (Fig. 4.8(C)). F-actin belts are typically seen in osteoclasts cultured on non-resorbable substrata such as glass [39]. Quantification of actin organization revealed that 3-fold more osteoclasts exhibited ring-like F-actin sealing zones on HA1 than on HA3 surfaces (Fig. 4.8(D), $p < 0.05$). We also used these data to determine the mean planar area of osteoclasts on HA1 and HA3 surfaces. There was no significant difference in the size of osteoclasts (with comparable number of nuclei) when plated on HA1 or HA3 coatings (Fig. 4.9). This finding argues against the possibility that differences in TRAP-stained area (Fig. 4.5) were due to greater spreading of osteoclasts on the smoother HA1 topography.

We employed confocal microscopy to better characterize the actin structures formed in osteoclasts adhering to the micro-rough HA3 surfaces. First, rabbit osteoclasts

were transduced with adenoviruses expressing actin-EGFP fusion protein. Again, these cells failed to form well defined sealing zone structures (Supplementary Fig. S4). Moreover, we also used confocal microscopy to examine rabbit osteoclasts on HA3 surfaces, expressing actin-EGFP fusion protein and then fixed and labeled for F-actin (Supplementary Fig. S5). These high resolution images revealed the presence of peripheral podosomes and podosome clusters, which were not organized into sealing zones known to be essential for osteoclastic resorption. In addition, co-labeling of F-actin containing podosomes with both EGFP and rhodamine (Supplementary Fig. S5C) validates use of the exogenous actin-EGFP fusion protein for monitoring actin dynamics in living cells.

Taken together, the osteoclast experiments revealed increased presence and activity of osteoclasts on the smoother HA surface. Furthermore, failure to resorb the micro-rough HA coating may be due to the inability of osteoclasts to form an F-actin sealing zone on this more complex topography.

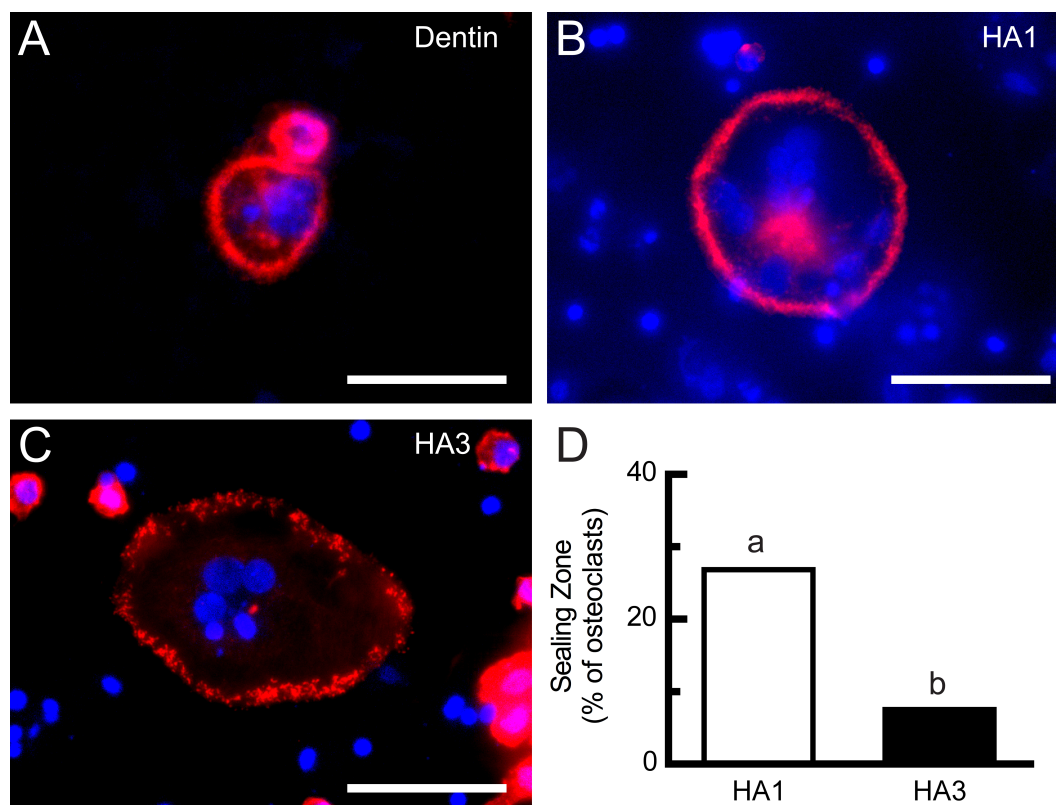


Figure 4.8 Effect of HA surface topography on F-actin organization in osteoclasts. Rabbit osteoclasts were cultured on dentin slices (A), smoother HA1 (B) and micro-rough HA3 (C) for 2 days. Preparations were then fixed, labeled for F-actin (red) and nuclei (blue) and observed by wide-field fluorescence microscopy. On both dentin and HA1 coatings, osteoclasts often exhibited ring-like F-actin sealing zones. In contrast, osteoclasts on rougher HA3 coatings displayed disrupted F-actin organization, with individual podosomes and podosome belts along the cell periphery. Images are representative of multiple samples from five independent cell isolations. Scale bar = 50 μ m. D) The number of osteoclasts exhibiting ring-like F-actin sealing zones was quantified on HA1 and HA3 coatings. Data are expressed as a percentage of the total number of osteoclasts examined (41 on HA1 and 53 on coatings) from five independent cell isolations. F-actin sealing zones were present in a significantly greater proportion of osteoclasts on smoother HA1 than on micro-rough HA3 surfaces ($p < 0.05$, based on Fisher's exact test).

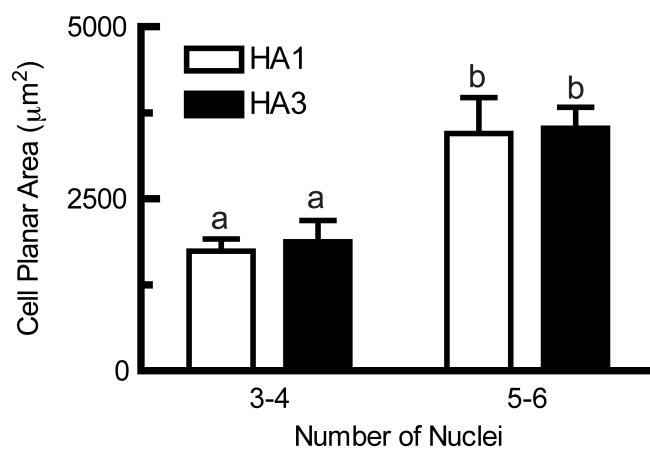


Figure 4.9 Quantification of the effect of HA surface topography on spreading of osteoclasts. Disaggregated rabbit osteoclasts were cultured on smoother HA1 and micro-rough HA3 for 2 days. Preparations were then fixed, labeled for F-actin and nuclei and observed by wide-field fluorescence microscopy. Image analysis software was used to quantify the planar area of osteoclasts having comparable number of nuclei. Data are expressed as a means \pm SEM of $n = 17-20$ (with 3-4 nuclei) and $n = 7-8$ (with 5-6 nuclei) osteoclasts from 5 independent cell isolations. Data were analyzed by two-way ANOVA and a Bonferroni multiple comparisons test. Bars labeled with the same lower case letter are not significantly different ($p > 0.05$). These data reveal that topography did not significantly affect the spreading of osteoclasts.

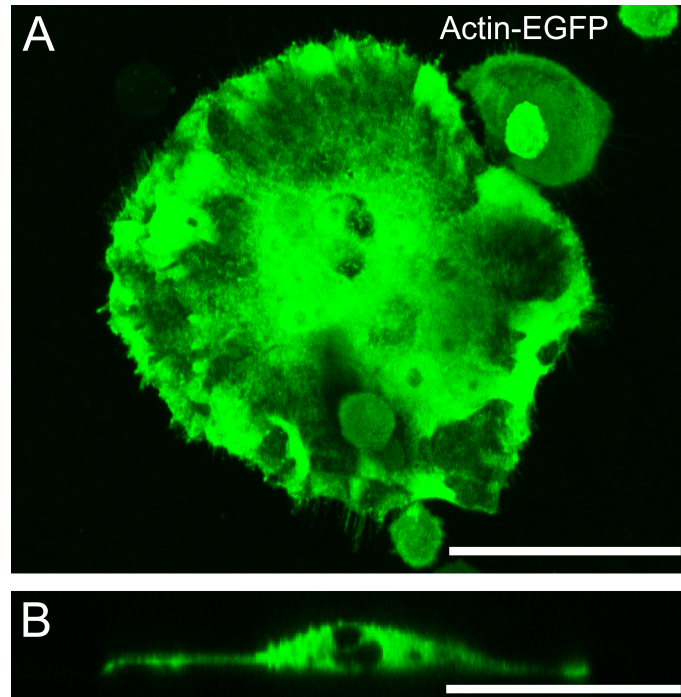


Figure 4.10 Confocal microscopy of actin in living osteoclast adhering to micro-rough HA3 coating. Rabbit osteoclasts were plated on HA3 surfaces and transduced with adenovirus expressing actin-EGFP fusion protein. Cells were then bathed in HEPES-buffered M199 medium with 15% FBS at $\sim 26^{\circ}\text{C}$ and imaged using confocal microscopy (40x objective, Zeiss LSM 510 META confocal microscope). Osteoclasts failed to form well defined sealing zone structures. Scale bar = 100 μm . A) Merged z-stack image of single living osteoclast. B) Orthogonal reconstruction of live osteoclast in panel A.

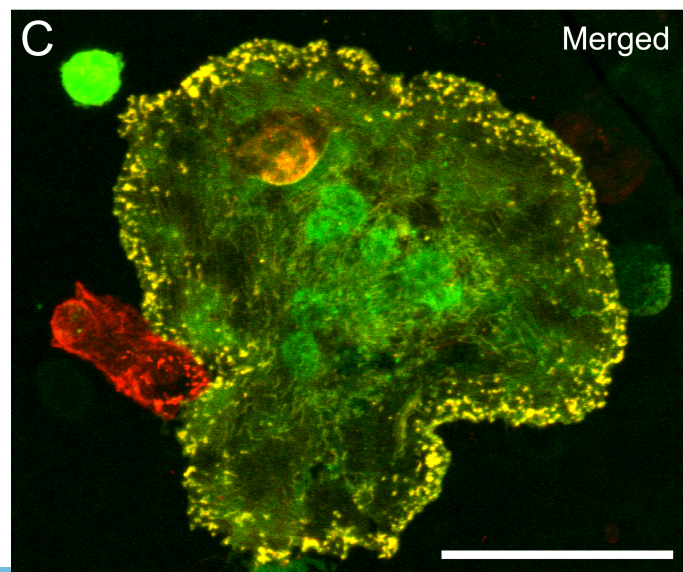
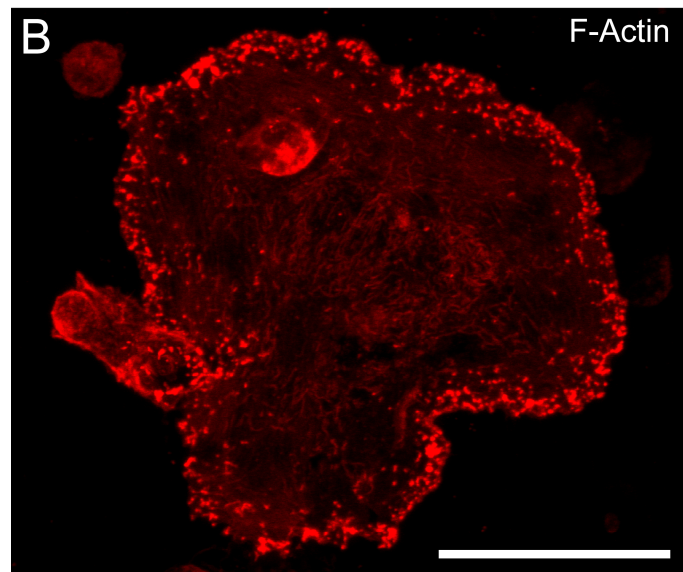
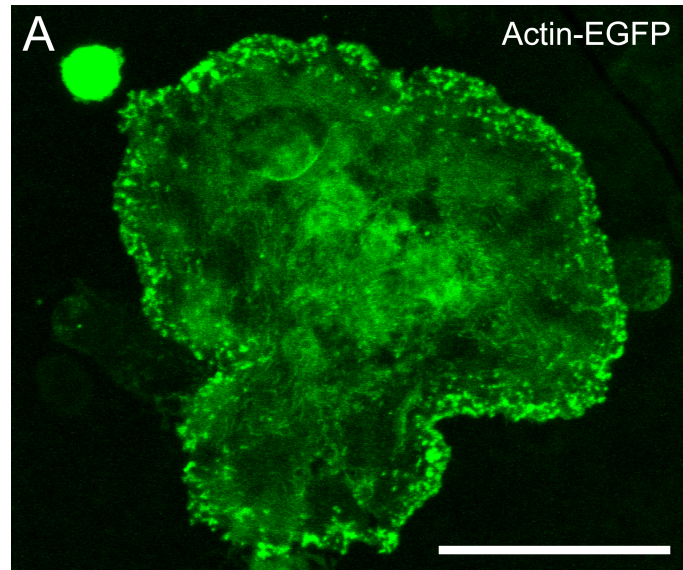


Figure 4.11 Confocal microscopy of actin structures in osteoclast adhering to micro-rough HA3 coating. Rabbit osteoclasts were plated on micro-rough HA3 surfaces and transduced with adenovirus expressing actin-EGFP fusion protein. Cells were subsequently fixed and F-actin was labeled with rhodamine-conjugated phalloidin. Confocal imaging was performed using a 40x objective (Zeiss LSM 510 META confocal microscope). The same osteoclast was imaged for EGFP (A, green), which labels exogenous actin (globular and filamentous), and rhodamine-conjugated phalloidin (B, red), which labels endogenous and exogenous F-actin. C) Merged image. Osteoclast exhibits peripheral F-actin podosomes and podosome clusters, which were not organized into sealing zones, known to be essential for osteoclastic resorption. Co-labeling of F-actin containing podosomes with both EGFP and rhodamine (yellow) validates use of the exogenous actin-EGFP fusion protein for monitoring actin dynamics in living cells. Scale bars = 100 μ m.

4.5 Discussion

Our findings further support an important role for the surface topography of biomaterials in controlling cell behavior. Our approach to controlling the topography of HA coatings offers several advantages compared to other reported techniques. We deposited biomimetic HA coatings on PCL by incubation in modified SBF – a straightforward method to directly modify the complexity and roughness of HA surfaces [30]. This systematic procedure utilizes mild conditions permitting the deposition of coatings on temperature-sensitive materials such as synthetic polymers, in contrast to techniques such as thermal spraying [41]. Moreover, our solution-based biomimetic process allows for the deposition of coatings on complex porous matrices [41], in contrast to grinding and polishing of sintered HA discs [4, 15] or line-of-sight deposition techniques such as thermal spraying [42] and laser cladding [43].

Attachment and spreading define the initial stages of cell-biomaterial interactions. These initial interactions affect the morphology and subsequent downstream cellular processes such as proliferation and differentiation [44]. HA has been previously shown to support the attachment of osteoblastic cells better than glass or pure titanium [45]. In the present study, the attachment of RCOs was enhanced by increasing the surface roughness and complexity of biomimetic HA. This is in keeping with a previous report that roughening of sintered HA discs using grit-polishing increases the attachment of bone marrow stromal cells [4].

Focal adhesions link the cytoskeleton of cells to the extracellular matrix or biomaterial surface. Focal adhesions are composed of proteins including vinculin, which mediates interactions between F-actin and integrins [44]. Focal adhesion proteins

mediate signal transduction and subsequent changes in gene expression initiated by binding to the extracellular matrix or biomaterial surface [46]. The complexity of biomaterial surfaces is known to influence the formation of focal adhesions. For example, a mesenchymal cell line cultured on polydimethylsiloxane showed increased formation of focal adhesions on a micropatterned surface compared to a flat surface [47]. In contrast, we found that, as roughness and surface complexity of the HA surfaces increased, the number of focal adhesions decreased. Moreover, on micro-rough surfaces, osteoblast morphology appeared to be rounded with no stress fiber formation. It is possible that differences in focal adhesion formation and consequent signaling contribute to the effects of topography on osteoblast differentiation observed in longer term cultures.

Osteogenic differentiation is comprised of three phases -- cellular proliferation, cellular maturation, and matrix mineralization [48]. During these phases, a host of collagenous and non-collagenous proteins are expressed. Type I collagen is expressed during the initial period of proliferation and ECM synthesis, whereas alkaline phosphatase expression occurs during maturation of cells and ECM [48, 49]. Furthermore, early stage expression of alkaline phosphatase has been correlated with later stage bone nodule formation *in vitro* [9], consistent with its role in generating inorganic phosphate required for matrix mineralization. Osteocalcin is expressed later, during the final stage of matrix mineralization [48, 49].

Increased levels of surface roughness and complexity enhanced collagen type I and alkaline phosphatase expression, consistent with accelerated differentiation. Furthermore, micro-rough HA coatings having increased levels of submicrometer and micro-scale complexity induced dramatically greater levels of osteocalcin expression.

Therefore, merely depositing calcium phosphate coatings on synthetic materials is not sufficient to produce optimal scaffold and implant biomaterial surfaces. The osteogenic potential of biomimetic HA coatings can be further enhanced by the careful control and design of the surface complexity and roughness.

In the present study, the greatest effects on osteoblast attachment, adhesion and differentiation were found when comparing HA coatings with smoother (HA1) topography to those with micro-rough (HA3) topography. Effects of submicro-rough (HA2) substrata were intermediate, suggesting that topographical features at both the micro, submicro and nano scales contribute to regulating the behavior of osteoblasts. In this regard, some authors have considered nanostructured surfaces as highly desirable for promoting the adhesion, growth and maturation of cells on biomaterials [50]; while, others have questioned the *in vivo* significance of such nanoscale structures, as proteins attaching to the surface after implantation likely mask such fine features [2].

The effect of surface topography on osteoclasts was evaluated using authentic, mature osteoclasts isolated directly from the long bone of neonatal rabbits, a well characterized model for investigating osteoclast behavior [51]. Most previous studies examining resorption of synthetic calcium phosphates *in vitro* have used osteoclast-like cells formed from bone marrow, the RAW 264.7 cell line, or human peripheral blood monocytes [14, 15, 20, 26, 52]. However, primary cultures of authentic osteoclasts are advantageous, as they allow for the assessment of mineral resorption activity independent of effects on osteoclast formation, which can complicate the interpretation of results [49].

In the present study, we found that the surface topography of biomimetic HA coatings has a pronounced effect on their interaction with osteoclasts. Fewer TRAP-

positive cells were observed on HA surfaces with increased levels of topographical complexity and roughness. These results are in contradiction to previous studies using osteoclasts differentiated from rat bone marrow on surface-abraded, sintered HA discs [52]. In another study, authentic osteoclasts isolated from the long bones of rats were cultured on natural versus abraded bone slices [53]. There was no difference in the number of TRAP-positive osteoclasts on each surface. Other investigators differentiated osteoclast-like cells *in vitro* from human peripheral blood monocytes on surface-abraded, sintered HA discs (with addition of receptor activator of nuclear factor κ B ligand (RANKL) and macrophage colony stimulating factor (M-CSF)) [15]. In this case, more osteoclasts formed on the rougher substratum. However, the degree of surface roughness of their sintered HA discs was well below the Ra value of the HA coatings used in the present study, which are considered ideal for biomaterials [2, 11]. Interestingly, the osteoclastic cells derived from human monocytes were decreased on rough HA discs in the presence of human bone marrow stromal cells [15], indicating complex interactions between topography, and cells of the osteoblast and osteoclast lineages.

In regard to osteoblast-osteoclast interactions, rougher micro-topographies have been shown to enhance the production and secretion of osteoprotegerin (OPG) by osteoblast-like cells [54]. OPG is a decoy receptor that selectively binds RANKL limiting osteoclast differentiation, activation and survival [40]. However, it is unlikely that OPG production contributes to the effects of micro-rough topography in the present study, as cells are cultured at low density and relatively few osteoblast precursors are present. As osteoclast spreading did not appear to differ markedly on smooth and micro-rough surfaces, the increased TRAP-staining on HA1 surfaces likely represents increased numbers of osteoclasts and possibly increased osteoclast activity. However, the small

number of cells present in primary cultures of disaggregated rabbit osteoclasts (and their heterogeneity) precluded us from performing gene expression studies using this system.

In the present study, the susceptibility of the biomimetic HA coating to osteoclastic resorption was highly dependent on the surface topography. Resorption lacunae were clearly visible on smoother HA coatings, whereas no evidence of resorption lacunae was visible on rougher HA coatings. Similar trends have been reported previously. For example, slightly fewer pits were formed by osteoclast-like cells cultured on roughened versus smooth sintered HA discs (Ra values not reported) [52]. When rat osteoclasts were cultured on bone slices of various roughnesses, there was a modest effect on resorptive activity, with maximal resorption at Ra = 1.0 μm and approximately 20% less resorption at Ra = 2.9 [53]. In the present study, we identified a dramatic effect of surface roughness on osteoclast activity with no resorption detectable on the rougher HA surfaces having increased complexity at the sub-micrometer- and micrometer scale. Interestingly, a previous study compared the susceptibility to osteoclastic resorption of calcium phosphate coatings, including carbonated apatite and amorphous calcium phosphate *in vitro* [26]. They found distinct resorption lacunae on carbonated apatite (with topography similar to our HA1 coatings), but unexpectedly not on relatively soluble amorphous calcium phosphate (with very rough topography). It is possible that, as in the present study, this difference in susceptibility to resorption was due to substratum topography rather than differences in chemistry or phase.

In the present study, resorption lacunae on HA1 surfaces appeared as deep, punched-out pits, in contrast to pits on dentin, which were shallower with much greater planar area. These differences in pit morphology are due presumably to the presence of

matrix proteins in dentin, but not in biomimetic HA. In this regard, matrix proteins such as osteopontin are known to regulate osteoclast spreading, motility and resorption [55].

The resorption of bone and mineral substrates is dependent on the formation of an actin-rich compartment, known as the sealing zone [40, 56]. The sealing zone constitutes the site where osteoclasts tightly adhere to the substrate forming a diffusion barrier, which in turn establishes an extracellular resorption compartment into which protons are transported and proteolytic enzymes are secreted [39, 56, 57]. In the case of synthetic apatite biomaterials, acidification of this compartment causes mineral dissolution and formation of a resorption lacuna.

In keeping with the decrease in focal adhesions in osteoblasts, we found that osteoclasts plated on micro-rough HA3 coatings displayed disrupted F-actin organization, with individual podosomes and podosome belts along the cell periphery and few cells exhibiting complete sealing zones. Given the essential role for sealing zones in resorption, it is possible that the failure of osteoclasts to resorb HA3 surfaces was due to the presence of surface irregularities that prevented formation of a functional sealing zone. In this regard, the continuity of substrate adhesiveness has been shown to be of critical importance for the formation and growth of the sealing zone [57]. In these studies, when osteoclasts were plated on flat glass substrates, patterned with an array of adhesive and non-adhesive regions, non-adhesive barriers as small as 1 μm were found to inhibit sealing zone formation. It is conceivable that topographical features may similarly disrupt establishment of complete sealing zones.

In other cell types, adhesion has been shown to depend on surface topography, with adhesion decreasing as surface roughness increases [44, 58]. Furthermore, increased

surface roughness is also correlated with decreased number of focal adhesions [58], consistent with the behavior of RCOs observed in the present study.

The inability of osteoclasts to resorb micro-rough HA surfaces may be attributed to the disrupted sealing zone formation. It is also possible that, even if the osteoclast could establish a sealing apparatus, the surface complexity would prevent a functional seal. In other words, pathways would still exist that would permit the diffusion of small molecules between surface irregularities. Thus, protons would diffuse out of resorption compartment and buffers would diffuse in, preventing acidification of the resorption compartment and dissolution of the HA.

Biomimetic HA coatings represent an ideal method to improve osteoconductivity and osseointegration of implants and porous scaffolds [23, 24]. Furthermore, biomimetic HA coatings are effective in preventing the fibrous tissue encapsulation commonly seen for synthetic polymers *in vivo* [25]. Our studies establish that the careful control and design of the surface topography of biomimetic HA offer a straightforward and effective route to improve osteoconductivity of the apatite coatings, while minimizing their susceptibility to osteoclastic resorption.

Synthetic apatite biomaterials are degraded by osteoclasts *in vivo* and, therefore, their susceptibility to osteoclastic resorption is an important characteristic [16, 59]. The results of the present study establish that resorption of biomimetic HA coatings is dramatically dependent on surface topography, wherein increasing roughness and isotropic complexity inhibit degradation, while promoting osteoblast attachment and differentiation. This finding may have important implications in designing scaffolds and implant coatings with complementary bone-forming stimulus and coating degradation rates. If the ultimate goal is for the biomaterial to be used as a synthetic bone substitute,

then the degradation rate should be comparable to bone. However, if the intended application is a permanent implant, then the resorption rate should be minimized [59]. In particular, biomimetic HA coatings have been used as drug delivery systems for the therapeutic release of antibiotics and growth factors [60, 61]. The release kinetics of the target compound is strongly dictated by the solubility and susceptibility to resorption of the mineral coating. We propose that it is possible to design the surface topography of biomimetic HA coatings to specifically control the rate osteoclastic degradation and, subsequently, the release kinetics of incorporated therapeutic agents.

In summary, biomimetic HA coatings with differing surface topographies were evaluated for their osteoconductivity and bioresorption using osteoblasts and osteoclasts. There was a significant increase in osteoblast attachment and expression of osteogenic markers, collagen I, alkaline phosphatase, and osteocalcin, when cultured on biomimetic HA surfaces with increased sub-micro- and micro-scale surface roughness. In addition, F-actin sealing zones were disrupted when authentic osteoclasts were cultured on micro-rough biomimetic HA. Consistent with this observation, osteoclasts failed to resorb HA surfaces with micro-rough topography. These results have important implications for the future design and fabrication of biomimetic coatings for scaffolds and drug delivery systems.

4.6 References

- [1] Unadkat HV, Hulsman M, Cornelissen K, Papenburg BJ, Truckenmuller RK, Post GF, et al. An algorithm-based topographical biomaterials library to instruct cell fate. *Proceedings of the National Academy of Sciences of the United States of America*. 2011;108:16565-70.
- [2] Hayes JS, Czekanska EM, Richards RG. The Cell-Surface Interaction. *Advances in Biochemical Engineering/Biotechnology*. 2012;126:1-31.
- [3] Lim JY, Donahue HJ. Cell sensing and response to micro- and nanostructured surfaces produced by chemical and topographic patterning. *Tissue Engineering*. 2007;13:1879-91.
- [4] Deligianni DD, Katsala ND, Koutsoukos PG, Missirlis YF. Effect of surface roughness of hydroxyapatite on human bone marrow cell adhesion, proliferation, differentiation and detachment strength. *Biomaterials*. 2001;22:87-96.
- [5] Rosa AL, Beloti MM, van Noort R. Osteoblastic differentiation of cultured rat bone marrow cells on hydroxyapatite with different surface topography. *Dental Materials*. 2003;19:768-72.
- [6] Hamilton DW, Brunette DM. The effect of substratum topography on osteoblast adhesion mediated signal transduction and phosphorylation. *Biomaterials*. 2007;28:1806-19.
- [7] Bauer TW, Muschler GF. Bone graft materials. An overview of the basic science. *Clinical Orthopaedics and Related Research*. 2000;371:10-27.
- [8] Allo BA, Costa DO, Dixon SJ, Mequanint K, Rizkalla AS. Bioactive and Biodegradable Nanocomposites and Hybrid Biomaterials for Bone Regeneration. *Journal of Functional Biomaterials*. 2012;3:432-63.
- [9] Perizzolo D, Lacefield WR, Brunette DM. Interaction between topography and coating in the formation of bone nodules in culture for hydroxyapatite- and titanium-coated micromachined surfaces. *Journal of Biomedical Materials Research*. 2001;56:494-503.
- [10] Bachle M, Kohal RJ. A systematic review of the influence of different titanium surfaces on proliferation, differentiation and protein synthesis of osteoblast-like MG63 cells. *Clinical Oral Implants Research*. 2004;15:683-92.
- [11] Hacking SA, Tanzer M, Harvey EJ, Krygier JJ, Bobyn JD. Relative contributions of chemistry and topography to the osseointegration of hydroxyapatite coatings. *Clinical Orthopaedics and Related Research*. 2002;405:24-38.

- [12] Yamada S, Heymann D, Bouler JM, Daculsi G. Osteoclastic resorption of calcium phosphate ceramics with different hydroxyapatite/beta-tricalcium phosphate ratios. *Biomaterials*. 1997;18:1037-41.
- [13] Winkler T, Hoenig E, Gildenhaar R, Berger G, Fritsch D, Janssen R, et al. Volumetric analysis of osteoclastic bioresorption of calcium phosphate ceramics with different solubilities. *Acta Biomaterialia*. 2010;6:4127-35.
- [14] Detsch R, Hagemeyer D, Neumann M, Schaefer S, Vortkamp A, Wuelling M, et al. The resorption of nanocrystalline calcium phosphates by osteoclast-like cells. *Acta Biomaterialia*. 2010;6:3223-33.
- [15] Costa-Rodrigues J, Fernandes A, Lopes MA, Fernandes MH. Hydroxyapatite surface roughness: complex modulation of the osteoclastogenesis of human precursor cells. *Acta Biomaterialia*. 2012;8:1137-45.
- [16] Schilling A, Filke S, Brink S, Korbmacher H, Amling M, Rueger J. Osteoclasts and Biomaterials. *European Journal of Trauma*. 2006;32:107-13.
- [17] Teti A. Bone development: overview of bone cells and signaling. *Current osteoporosis reports*. 2011;9:264-73.
- [18] Costa-Rodrigues J, Fernandes A, Fernandes MH. Reciprocal osteoblastic and osteoclastic modulation in co-cultured MG63 osteosarcoma cells and human osteoclast precursors. *Journal of Cellular Biochemistry*. 2011;112:3704-13.
- [19] Minkin C, Marinho VC. Role of the osteoclast at the bone-implant interface. *Advances in Dental Research*. 1999;13:49-56.
- [20] Yang L, Perez-Amodio S, Barrere-de Groot FY, Everts V, van Blitterswijk CA, Habibovic P. The effects of inorganic additives to calcium phosphate on in vitro behavior of osteoblasts and osteoclasts. *Biomaterials*. 2010;31:2976-89.
- [21] LeGeros RZ. Properties of osteoconductive biomaterials: calcium phosphates. *Clinical Orthopaedics and Related Research*. 2002;395:81-98.
- [22] Hott M, Noel B, Bernache-Assolant D, Rey C, Marie PJ. Proliferation and differentiation of human trabecular osteoblastic cells on hydroxyapatite. *Journal of Biomedical Materials Research*. 1997;37:508-16.
- [23] Pek YS, Gao S, Arshad MS, Leck KJ, Ying JY. Porous collagen-apatite nanocomposite foams as bone regeneration scaffolds. *Biomaterials*. 2008;29:4300-5.
- [24] Bigi A, Fini M, Bracci B, Boanini E, Torricelli P, Giavaresi G, et al. The response of bone to nanocrystalline hydroxyapatite-coated Ti13Nb11Zr alloy in an animal model. *Biomaterials*. 2008;29:1730-6.

- [25] Lickorish D, Guan L, Davies JE. A three-phase, fully resorbable, polyester/calcium phosphate scaffold for bone tissue engineering: Evolution of scaffold design. *Biomaterials*. 2007;28:1495-502.
- [26] Leeuwenburgh S, Layrolle P, Barrere F, de Bruijn J, Schoonman J, van Blitterswijk CA, et al. Osteoclastic resorption of biomimetic calcium phosphate coatings in vitro. *Journal of Biomedical Materials Research*. 2001;56:208-15.
- [27] Kokubo T. Formation of biologically active bone-like apatite on metals and polymers by a biomimetic process. *Thermochimica Acta*. 1996;280:479-90.
- [28] Tanahashi M, Yao T, Kokubo T, Minoda M, Miyamoto T, Nakamura T, et al. Apatite Coating on Organic Polymers by a Biomimetic Process. *Journal of the American Ceramic Society*. 1994;77:2805-8.
- [29] Oyane A, Ishikawa Y, Yamazaki A, Sogo Y, Furukawa K, Ushida T, et al. Reduction of surface roughness of a laminin-apatite composite coating via inhibitory effect of magnesium ions on apatite crystal growth. *Acta Biomaterialia*. 2008;4:1342-8.
- [30] Costa DO, Allo BA, Klassen R, Hutter JL, Dixon SJ, Rizkalla AS. Control of surface topography in biomimetic calcium phosphate coatings. *Langmuir*. 2012;28:3871-80.
- [31] Naemsch LN, Weidema AF, Sims SM, Underhill TM, Dixon SJ. P2X(4) purinoceptors mediate an ATP-activated, non-selective cation current in rabbit osteoclasts. *Journal of Cell Science*. 1999;112 (Pt 23):4425-35.
- [32] Pereverzev A, Komarova SV, Korcok J, Armstrong S, Tremblay GB, Dixon SJ, et al. Extracellular acidification enhances osteoclast survival through an NFAT-independent, protein kinase C-dependent pathway. *Bone*. 2008;42:150-61.
- [33] Arnett TR. Acidosis, hypoxia and bone. *Archives of Biochemistry and Biophysics*. 2010;503:103-9.
- [34] Lapierre DM, Tanabe N, Pereverzev A, Spencer M, Shugg RP, Dixon SJ, et al. Lysophosphatidic acid signals through multiple receptors in osteoclasts to elevate cytosolic calcium concentration, evoke retraction, and promote cell survival. *The Journal of biological chemistry*. 2010;285:25792-801.
- [35] Bray DF, Bagu J, Koegler P. Comparison of hexamethyldisilazane (HMDS), Peldri II, and critical-point drying methods for scanning electron microscopy of biological specimens. *Microscopy Research and Technique*. 1993;26:489-95.
- [36] Yadav MC, Simao AM, Narisawa S, Huesa C, McKee MD, Farquharson C, et al. Loss of skeletal mineralization by the simultaneous ablation of PHOSPHO1 and alkaline phosphatase function: a unified model of the mechanisms of initiation of skeletal calcification. *Journal of Bone and Mineral Research*. 2011;26:286-97.

- [37] Pockwinse SM, Wilming LG, Conlon DM, Stein GS, Lian JB. Expression of cell growth and bone specific genes at single cell resolution during development of bone tissue-like organization in primary osteoblast cultures. *Journal of Cellular Biochemistry*. 1992;49:310-23.
- [38] Minkin C. Bone acid phosphatase: tartrate-resistant acid phosphatase as a marker of osteoclast function. *Calcified Tissue International*. 1982;34:285-90.
- [39] Jurdic P, Saltel F, Chabadel A, Destaing O. Podosome and sealing zone: specificity of the osteoclast model. *European Journal of Cell Biology*. 2006;85:195-202.
- [40] Novack DV, Teitelbaum SL. The osteoclast: friend or foe? *Annual review of pathology*. 2008;3:457-84.
- [41] Kamitakahara M, Ohtsuki C, Miyazaki T. Coating of bone-like apatite for development of bioactive materials for bone reconstruction. *Biomedical materials*. 2007;2:R17-23.
- [42] Gross KA, Muller D, Lucas H, Haynes DR. Osteoclast resorption of thermal spray hydroxyapatite coatings is influenced by surface topography. *Acta Biomaterialia*. 2012;8:1948-56.
- [43] Paital SR, He W, Dahotre NB. Laser pulse dependent micro textured calcium phosphate coatings for improved wettability and cell compatibility. *Journal of materials science Materials in medicine*. 2010;21:2187-200.
- [44] Anselme K. Osteoblast adhesion on biomaterials. *Biomaterials*. 2000;21:667-81.
- [45] Okumura A, Goto M, Goto T, Yoshinari M, Masuko S, Katsuki T, et al. Substrate affects the initial attachment and subsequent behavior of human osteoblastic cells (Saos-2). *Biomaterials*. 2001;22:2263-71.
- [46] Siebers MC, ter Brugge PJ, Walboomers XF, Jansen JA. Integrins as linker proteins between osteoblasts and bone replacing materials. A critical review. *Biomaterials*. 2005;26:137-46.
- [47] Seo CH, Furukawa K, Montagne K, Jeong H, Ushida T. The effect of substrate microtopography on focal adhesion maturation and actin organization via the RhoA/ROCK pathway. *Biomaterials*. 2011;32:9568-75.
- [48] Siggelkow H, Rebenstorff K, Kurre W, Niedhart C, Engel I, Schulz H, et al. Development of the osteoblast phenotype in primary human osteoblasts in culture: comparison with rat calvarial cells in osteoblast differentiation. *Journal of Cellular Biochemistry*. 1999;75:22-35.
- [49] Barrere F, van Blitterswijk CA, de Groot K. Bone regeneration: molecular and cellular interactions with calcium phosphate ceramics. *International journal of nanomedicine*. 2006;1:317-32.

- [50] Bacakova L, Filova E, Parizek M, Ruml T, Svorcik V. Modulation of cell adhesion, proliferation and differentiation on materials designed for body implants. *Biotechnology Advances*. 2011;29:739-67.
- [51] Coxon FP, Rogers MJ, Crockett JC. Isolation and purification of rabbit osteoclasts. *Methods in Molecular Biology*. 2012;816:145-58.
- [52] Gomi K, Lowenberg B, Shapiro G, Davies JE. Resorption of sintered synthetic hydroxyapatite by osteoclasts in vitro. *Biomaterials*. 1993;14:91-6.
- [53] Matsunaga T, Inoue H, Kojo T, Hatano K, Tsujisawa T, Uchiyama C, et al. Disaggregated osteoclasts increase in resorption activity in response to roughness of bone surface. *Journal of Biomedical Materials Research*. 1999;48:417-23.
- [54] Lossdorfer S, Schwartz Z, Wang L, Lohmann CH, Turner JD, Wieland M, et al. Microrough implant surface topographies increase osteogenesis by reducing osteoclast formation and activity. *Journal of Biomedical Materials Research Part A*. 2004;70:361-9.
- [55] Tanabe N, Wheal BD, Kwon J, Chen HH, Shugg RP, Sims SM, et al. Osteopontin signals through calcium and nuclear factor of activated T cells (NFAT) in osteoclasts: a novel RGD-dependent pathway promoting cell survival. *The Journal of biological chemistry*. 2011;286:39871-81.
- [56] Teti A, Marchisio PC, Zallone AZ. Clear zone in osteoclast function: role of podosomes in regulation of bone-resorbing activity. *American Journal of Physiology*. 1991;261:C1-7.
- [57] Anderegg F, Geblinger D, Horvath P, Charnley M, Textor M, Addadi L, et al. Substrate adhesion regulates sealing zone architecture and dynamics in cultured osteoclasts. *PloS one*. 2011;6:e28583.
- [58] Anselme K, Bigerelle M, Noel B, Dufresne E, Judas D, Iost A, et al. Qualitative and quantitative study of human osteoblast adhesion on materials with various surface roughnesses. *Journal of Biomedical Materials Research*. 2000;49:155-66.
- [59] Schilling AF, Linhart W, Filke S, Gebauer M, Schinke T, Rueger JM, et al. Resorbability of bone substitute biomaterials by human osteoclasts. *Biomaterials*. 2004;25:3963-72.
- [60] Stigter M, de Groot K, Layrolle P. Incorporation of tobramycin into biomimetic hydroxyapatite coating on titanium. *Biomaterials*. 2002;23:4143-53.
- [61] Suarez-Gonzalez D, Barnhart K, Migneco F, Flanagan C, Hollister SJ, Murphy WL. Controllable mineral coatings on PCL scaffolds as carriers for growth factor release. *Biomaterials*. 2012;33:713-21.

CHAPTER FIVE

GENERAL DISCUSSION

5.1 Summary and Conclusions

One- and Three-Dimensional Growth of Hydroxyapatite Nanowires during Sol-Gel-Hydrothermal Synthesis – Chapter 2 is the first report of HA nanowire and nanorod synthesis via combination of sol-gel chemistry and hydrothermal treatment. Amorphous nano-scale CaP gel was produced using sol-gel chemistry and it was found that conversion to crystalline HA occurred after hydrothermal treatment. Morphologies of the HA powders varied from nanorods of low aspect ratio, to high-aspect ratio nanowires. The particle diameter and length was tunable by adjusting the hydrothermal pH and reaction time, respectively. We also found that the nanorods and nanowires were a phase-pure HA and carbonate substitution was introduced using high pH hydrothermal treatment.

1. Replacement of traditional high-temperature calcination of amorphous CaP gel with hydrothermal crystallization produced HA nanorods and nanowires.
2. Adjustment of hydrothermal pH and temperature allowed for tunable HA particle morphology, including nanorods and high aspect ratio nanowires, through a one- and three-dimensional crystal growth mechanism.
3. Characterization of hydrothermal powders revealed phase-pure stoichiometric and carbonate-substituted HA.
4. Discrete HA nanowires dispersed uniformly within a PCL matrix and provided effective reinforcement of PCL/HA composites, with improvement in tensile and compressive properties.

Control of Surface Topography in Biomimetic Calcium Phosphate Coatings – In Chapter 3, we reported our discovery that adjusting the ionic concentration of SBF solutions and incubation time can effectively control the surface topography of biomimetic CaP coatings deposited on PCL films. Various CaP coatings (consisting of DCPD, OCP, HA and mixed phases) were obtained from the different SBF preparations. The fine-resolution topography of HA coatings was dependent on the ionic concentration, whereas the coarse-resolution topography was influenced by soaking time.

1. Bone-like HA coatings with varying topography and levels of isotropic surface complexity were deposited on PCL by incubation in modified SBF solutions.
2. SBF concentration affects high resolution HA surface roughness.
3. Soaking time affects low resolution HA surface roughness.
4. The deposited calcium phosphate coatings included DCPD, OCP, and carbonated-HA with Ca/P ratio ranging from 1.30 to 1.50.
5. The surface roughness of apatite coatings varied from 194 to 363 nm measured at high resolution, and 1 to 2 μm at low resolution.

Surface Topography of Biomimetic Hydroxyapatite Coating Differentially Regulates Osteoblast Osteoclast Activity – Chapter 4 describes the effect of surface topography and roughness of the biomimetic HA described in Chapter 3 on the *in vitro* behavior of osteoblasts and osteoclasts. In particular, rat calvarial osteoblasts showed enhanced osteogenic response to biomimetic HA coatings with increased isotropic surface complexity and roughness. In contrast, osteoclast activity was suppressed when authentic rabbit-derived osteoclasts were cultured on biomimetic HA with greater surface

complexity and roughness. In keeping with this observation, the formation of distinct resorption lacunae was not observed on rough HA coatings, whereas resorption pits were observed on biomimetic HA surfaces with less surface roughness and complexity.

1. Osteoblast attachment to rough HA surfaces was greater than attachment to smoother, less complex surfaces.
2. Formation of focal adhesions by osteoblasts was suppressed when cultured on rough HA surfaces.
3. Osteoblast differentiation was enhanced when cultured on biomimetic HA coatings with greater levels of roughness at both high and low resolution.
4. Osteoclast activity is dependent on surface roughness, with increased TRAP staining and greater numbers of osteoclasts on smoother biomimetic HA surfaces.
5. Osteoclasts produced resorption lacunae when cultured on smoother biomimetic HA surfaces with ($R_a = 194 \text{ nm}$ and $1 \text{ }\mu\text{m}$ at high and low resolution, respectively).
6. Osteoclasts failed to produce resorption lacunae when cultured on rougher, more complex biomimetic HA surfaces ($R_a = 363 \text{ nm}$ and $2 \text{ }\mu\text{m}$ at high and low resolution, respectively).
7. Osteoclasts showed greater propensity to form sealing zone (as indicated by formation of F-actin ring-like structure) when cultured on smoother HA surfaces.

5.2 Contributions of the Research to the Current State of Knowledge

Historical perspective and general significance – An extensive number of research contributions in the field of bone tissue engineering has led to the understanding of several critical design parameters for biomaterials intended for bone regeneration. Brekke *et al.* [1] compiled a comprehensive list of the design considerations determined from a literature review. Design parameters included [1-4]:

1. Biocompatible material that does not induce soft tissue growth at the bone/implant interface.
2. Material provides initial mechanical strength and stiffness matching that of the surrounding tissue to allow normal patient activity and provide mechanical stimuli to cells.
3. Biodegradable material that resorbs in a predictable and controllable manner in concert with bone regeneration.
4. Material possesses the surface chemistry and topography that promote cellular adhesion, proliferation and appropriate differentiation of osteogenic cells.
5. Material is osteoconductive, supporting the ingrowth of capillaries and cells from host to promote bone ingrowth. Allows for the attachment, proliferation, migration, and differentiation of bone cells.

The overall objective of the current research project was the design and development of composite biomaterials suitable for use as synthetic bone graft

substitutes. Biomaterials were designed to meet as many of the above criteria as possible in order to promote the repair and regeneration of bone defects.

Synthesis of HA Nanowires and Application in Composite Biomaterials –

Although a goal of biomaterial design for bone regeneration is the development of materials with comparable stiffness and strength, scaffolds often fall short due to the requirement for a high degree of macroporosity [5]. However, scaffold materials are required to be, at the very least, capable of withstanding the *in vivo* stresses and tractional forces produced by cells and the contractile forces exerted by the natural remodeling process [3, 6]. Therefore, the use of ceramic fillers, in combination with polymer matrices, helps to increase the stiffness of composites and help maintain their structural integrity by preventing the collapse of the porous structure *in vivo* [7].

The rationale for biomaterial design was based, in part, on the natural nanocomposite structure of bone tissue. Specifically, the composite biomaterial consisted of a synthetic organic biodegradable polymer matrix, PCL, in combination with nano-scale synthetic HA. Thus, the synthetic composite mimics the mineral-collagen composite nature of bone. Addition of nano-scale HA as a filler material reinforced the PCL matrix and improved the tensile and compressive properties of the composite. It is expected that the nano-HA would also provide a continuous bioactive and osteoconductive component, as well as help to buffer the acid arising from polymer degradation [5].

Traditionally, HA ceramics are commonly produced by wet chemical methods, including sol-gel chemistry. Sol-gel chemistry is a well understood and widely used synthesis procedure for production of amorphous inorganic materials, including CaP.

The sol-gel technique provides molecular mixing of chemical precursors, allowing for control of composition and chemical homogeneity, and produces nano-scale amorphous products [8, 9]. However, sol-gel-derived amorphous inorganics require calcination at elevated temperatures in the presence of air to produce crystalline ceramics, such as HA. The calcination step is often accompanied by the formation of secondary phases such as calcium oxide and tricalcium phosphate (TCP) [8, 9], and granular particle shapes [9, 10]. We have shown for the first time that high temperature calcination can be replaced by a hydrothermal crystallization process to produce phase-pure, and carbonated-HA nanowires and nanorods with tunable aspect ratio. The facile sol-gel-hydrothermal process offers a simple, cost effective, and environmentally friendly synthesis route. Furthermore, by simply adjusting the composition of the sol-gel precursor, it is anticipated that various CaP-based products, including silica and strontium substituted ceramics could be easily synthesized [11].

Control of Surface Topography of HA Coatings and Characterization of Their Interaction with Bone Cells In Vitro – A unique solution-based process was developed for the purpose of depositing surface coatings of carbonated-HA on PCL. The coating was designed to provide an ideal surface chemistry and topography for enhancing osteoblast attachment and differentiation, thereby rendering the biomaterial surface osteoconductive and bioactive.

Deposition of biomimetic HA coatings on PCL, using a modified SBF incubation process, offers a facile method to directly modify the complexity, and roughness of HA surfaces. The one-step deposition of HA coatings from modified SBF solutions, with direct control of surface features is advantageous over typical approaches, which use

grinding or polishing of sintered HA discs [12, 13], or various line-of-sight deposition techniques such as thermal spraying [14], or laser cladding [15]. To the best of our knowledge, we have developed for the first time a technique to control the surface topography of a bone-like carbonated-HA coating on a biodegradable synthetic polymer. The mild conditions of the biomimetic process allows for the deposition of coatings on temperature-sensitive materials such as synthetic polymers, whereas the solution-based approach makes it possible to apply the technique to complex porous matrices [16].

Despite the extensive literature reporting the benefits of roughened surfaces on osteoblast behavior and bone formation, few studies have integrated this knowledge into the rational design of surface coatings. A previous study investigated the effect of biomimetic HA crystal size and morphology on viability, proliferation and gene expression in MC3T3-E1 preosteoblastic cells [17]. The authors suggested a differential cell response to small changes in apatite microstructure. However, the authors failed to characterize macroscopic surface topography and roughness. Therefore, it is not known if the changes in osteoblast behavior were due to differences in apatite crystal structure or modification of surface topography. We have shown that changes in the ionic concentration of SBF and soaking time are critical parameters that affect the biomimetic HA surface topography.

In vitro experiments with osteoblasts revealed dramatic differences in the expression of osteogenic markers, indicating that, by simply controlling the surface characteristics of the deposited HA, enhancements in cell differentiation can be achieved. Furthermore, experiments using authentic osteoclasts indicated for the first time, that a specific surface topography inhibits the formation of resorption lacunae. This finding may have important implications for the future design of HA surface coatings, because

the ideal biomaterial would integrate into the physiological bone formation and remodeling process [18] and, therefore, control over resorption kinetics is critical. Furthermore, biomimetic HA coatings have been developed as drug delivery systems for antibiotics and growth factors [19, 20]. Investigations have shown that the release kinetics of the target compound is strongly dictated by the solubility of the mineral coating [20]. *In vivo*, degradation of biomaterials is influenced by several factors including body fluid-mediated dissolution, as well as degradation by enzymatic activity, body movements and cellular resorption. Our results have shown that the surface topography of biomimetic HA coatings can be specifically designed to control the rate of osteoclastic degradation, and, therefore, the release kinetics of therapeutic compounds.

5.3 Limitations of the Research and Suggestions for Future Studies

Fabrication of 3D Porous Scaffolds – The objective of this research project was to synthesize and characterize calcium phosphate-based resorbable composite biomaterials for applications in bone tissue engineering. However, for the promising biomaterials to achieve application in bone regeneration, the materials need to be fabricated into scaffold constructs with 3D porous structures (with appropriate pore size, porosity, and interconnectivity between pores) to allow for cell and tissue ingrowth [4, 21]. Additionally, high porosity and interconnectivity are critical for the necessary diffusion of nutrients and oxygen, and removal of metabolic wastes [21, 22].

For bone regeneration, scaffold architecture should ideally mimic that of trabecular bone, which is characterized by a random pore structure [1]. It was initially

thought that a pore size of 100 μm was the minimum requirement due to cell size, and migration, and diffusion issues. However, more recent studies have identified a pore size in the range of 200–400 μm as optimal for cell and bone ingrowth, and sufficient vascularization [1, 3, 4, 21]. For example, an *in vitro* and *in vivo* study [23], which tested PCL scaffolds with different a range of different pore sizes, showed that both chondrocytes and osteoblasts preferred larger pore diameters in the range of 380–405 μm when cultured *in vitro*. In contrast, when implanted *in vivo* (cranial defects of rabbits), PCL scaffolds with lower pore diameters (ranging from 290–310 μm) showed more new bone formation, which progressed further into the center of the scaffold.

In view of critical scaffold design parameters and their application in bone tissue engineering, a number of techniques have been used investigated to fabricate 3D scaffolds with high porosity and surface area. The conventional methods for scaffold fabrication include drop-on-demand printing [24], gas foaming [25-27], solvent casting/particulate leaching [28-32], precipitation casting [33], electrospinning [34], microsphere sintering/particulate leaching [28, 32, 35-38], freeze-drying [39] or combination of these techniques.

Correlating In Vitro Characteristics with In Vivo Behavior – In Chapter 4, of topographically modified biomimetic HA coatings were evaluated using *in vitro* cell culture of osteoblasts (bone formation) and osteoclasts (biomaterial resorption). Osteoblast attachment and gene expression experiments highlighted the potential for enhancement of bone formation by using roughened biomimetic HA, whereas osteoclast experiments illustrated potential control over cell resorption. However, these experiments were performed on 2D film, and, as described above, the application of these

biomaterials ultimately requires fabrication of porous 3D scaffolds. Osteoblast proliferation, differentiation and protein synthesis may vary when cultured in 3D constructs as compared to 2D planar substrates of the same biomaterial [40]. Conversely, cell behavior on 2D substrates has been shown to correspond to 3D behavior when planar substrates are fabricated with complex micro-roughness [41].

In vivo confirmation of the results obtained from *in vitro* experiments using osteoblasts and osteoclasts, will be required before these materials can be tested in a clinical setting. Although *in vitro* osteogenic markers are often indicative of *in vivo* bone formation [42] and isolated rabbit osteoclasts are considered an ideal model of osteoclastic behavior *in vivo* [43], the effects of biomimetic surface roughness on bone formation and osteoclastic resorption *in vivo* are poorly defined. As such, it would be beneficial to use a preclinical animal model to ascertain whether increased surface roughness of HA coatings evokes greater bone formation compared to less rough surfaces *in vivo*. Moreover, it would be useful to determine the effects of the surface topography on osteoclastic resorption *in vivo*, as well as the overall effect of these surface on the balance between bone formation and resorption.

In this project, osteoclastic resorption was evaluated using SEM analysis of the substratum surface. Although no distinct resorption lacunae were observed on the rougher HA surfaces (Chapter 4), osteoclastic resorption may have been limited to mild surface erosion.

Development of Osteoinductive Biomaterials – Ideally, synthetic bone graft substitutes are bioactive, osteoconductive and osteoinductive [44, 45]. In the case of noncritical size defects, bioactive and osteoconductive materials are sufficient to

accelerate bone regeneration by providing cell anchorage sites and adequate stimulation for ECM formation to bridge the defect [5]. However, for nonunion or critical size defects, an additional osteoinductive stimulus is necessary to promote bone regeneration [44]. CaP biomaterials are considered inherently considered non-osteoinductive, although this remains controversial, with some investigators reporting possible osteoinductive activity [46]. Nevertheless, the CaP biomaterials could be synthesized so as to incorporate osteoinductive growth factors by co-precipitation with the biomimetic HA [20]. The biomimetic process used to control the surface topography of deposited HA requires low temperature and mild pH, therefore, is a suitable system to incorporate therapeutic compounds. Moreover, the topographies produced during the biomimetic process may offer a method to control the degradation kinetics, and subsequently, the release kinetics.

Combining PCL/HA nanocomposites with CaP Coatings having Tailored Topography – The technologies developed in these studies represent promising biomaterials for the fabrication of scaffolds for bone regeneration. However, the biomaterials need to be combined into a cohesive scaffold material in order to meet the clinical needs in orthopedics and dentistry. The next critical step in the development of scaffolds include: 1) the fabrication of PCL/HA nanocomposites having a macro-porous structure, as described above, and 2) application of CaP coating to the surface of the PCL/HA porous nanocomposite. The combination of the HA nanowires having high aspect ratio, with a biodegradable polymer would produce osteoconductive nanocomposites with appropriate stiffness and strength. Moreover, as described in these studies, the CaP coating could be deposited onto the surface of the macro-porous

nanocomposite scaffold to meet the different requirements of bone forming stimulus and biodegradation, as necessary for the intended application. The CaP-coated nanocomposites scaffolds would be ideal for use in pre-clinical animal models to test the efficacy for the eventual clinical applications as a synthetic bone-graft substitute.

5.4 References

- [1] Brekke JH, Toth JM. Principles of tissue engineering applied to programmable osteogenesis. *Journal of Biomedical Materials Research*. 1998;43:380-98.
- [2] Hutmacher DW. Scaffolds in tissue engineering bone and cartilage. *Biomaterials*. 2000;21:2529-43.
- [3] Hutmacher DW, Schantz JT, Lam CX, Tan KC, Lim TC. State of the art and future directions of scaffold-based bone engineering from a biomaterials perspective. *Journal of tissue engineering and regenerative medicine*. 2007;1:245-60.
- [4] Burg KJ, Porter S, Kellam JF. Biomaterial developments for bone tissue engineering. *Biomaterials*. 2000;21:2347-59.
- [5] Allo BA, Costa DO, Dixon SJ, Mequanint K, Rizkalla AS. Bioactive and Biodegradable Nanocomposites and Hybrid Biomaterials for Bone Regeneration. *Journal of Functional Biomaterials*. 2012;3:432-63.
- [6] Vacanti CA, Bonassar LJ. An overview of tissue engineered bone. *Clinical Orthopaedics and Related Research*. 1999:S375-81.
- [7] Lickorish D, Guan L, Davies JE. A three-phase, fully resorbable, polyester/calcium phosphate scaffold for bone tissue engineering: Evolution of scaffold design. *Biomaterials*. 2007;28:1495-502.
- [8] Eshtiagh-Hosseini H, Housaindokht MR, Chahkandi M. Effects of parameters of sol-gel process on the phase evolution of sol-gel-derived hydroxyapatite. *Materials Chemistry and Physics*. 2007;106:310-6.
- [9] Liu DM, Troczynski T, Tseng WJ. Water-based sol-gel synthesis of hydroxyapatite: process development. *Biomaterials*. 2001;22:1721-30.
- [10] Fathi MH, Hanifi A. Evaluation and characterization of nanostructure hydroxyapatite powder prepared by simple sol-gel method. *Materials Letters*. 2007;61:3978-83.
- [11] Lin KL, Chang J, Liu XG, Chen L, Zhou YL. Synthesis of element-substituted hydroxyapatite with controllable morphology and chemical composition using calcium silicate as precursor. *Crystengcomm*. 2011;13:4850-5.
- [12] Deligianni DD, Katsala ND, Koutsoukos PG, Missirlis YF. Effect of surface roughness of hydroxyapatite on human bone marrow cell adhesion, proliferation, differentiation and detachment strength. *Biomaterials*. 2001;22:87-96.
- [13] Costa-Rodrigues J, Fernandes A, Lopes MA, Fernandes MH. Hydroxyapatite surface roughness: complex modulation of the osteoclastogenesis of human precursor cells. *Acta Biomaterialia*. 2012;8:1137-45.

- [14] Gross KA, Muller D, Lucas H, Haynes DR. Osteoclast resorption of thermal spray hydroxyapatite coatings is influenced by surface topography. *Acta Biomaterialia*. 2012;8:1948-56.
- [15] Paital SR, He W, Dahotre NB. Laser pulse dependent micro textured calcium phosphate coatings for improved wettability and cell compatibility. *Journal of materials science Materials in medicine*. 2010;21:2187-200.
- [16] Kamitakahara M, Ohtsuki C, Miyazaki T. Coating of bone-like apatite for development of bioactive materials for bone reconstruction. *Biomedical materials*. 2007;2:R17-23.
- [17] Chou YF, Huang WB, Dunn JCY, Miller TA, Wu BM. The effect of biomimetic apatite structure on osteoblast viability, proliferation, and gene expression. *Biomaterials*. 2005;26:285-95.
- [18] Schilling A, Filke S, Brink S, Korbmacher H, Amling M, Rueger J. Osteoclasts and Biomaterials. *European Journal of Trauma*. 2006;32:107-13.
- [19] Stigter M, de Groot K, Layrolle P. Incorporation of tobramycin into biomimetic hydroxyapatite coating on titanium. *Biomaterials*. 2002;23:4143-53.
- [20] Suarez-Gonzalez D, Barnhart K, Migneco F, Flanagan C, Hollister SJ, Murphy WL. Controllable mineral coatings on PCL scaffolds as carriers for growth factor release. *Biomaterials*. 2012;33:713-21.
- [21] Yang S, Leong KF, Du Z, Chua CK. The design of scaffolds for use in tissue engineering. Part I. Traditional factors. *Tissue Engineering*. 2001;7:679-89.
- [22] Salgado AJ, Coutinho OP, Reis RL. Bone tissue engineering: state of the art and future trends. *Macromolecular Bioscience*. 2004;4:743-65.
- [23] Oh SH, Park IK, Kim JM, Lee JH. In vitro and in vivo characteristics of PCL scaffolds with pore size gradient fabricated by a centrifugation method. *Biomaterials*. 2007;28:1664-71.
- [24] Mondrinos MJ, Dembzyński R, Lu L, Byrapogu VK, Wootton DM, Lelkes PI, et al. Porogen-based solid freeform fabrication of polycaprolactone-calcium phosphate scaffolds for tissue engineering. *Biomaterials*. 2006;27:4399-408.
- [25] Xu Q, Ren XW, Chang YN, Wang JW, Yu L, Dean K. Generation of microcellular biodegradable polycaprolactone foams in supercritical carbon dioxide. *Journal of Applied Polymer Science*. 2004;94:593-7.
- [26] Jenkins MJ, Harrison KL, Silva MMCG, Whitaker MJ, Shakesheff KM, Howdle SM. Characterisation of microcellular foams produced from semi-crystalline PCL using supercritical carbon dioxide. *European Polymer Journal*. 2006;42:3145-51.

- [27] Di Maio E, Mensitieri G, Iannace S, Nicolais L, Li W, Flumerfelt RW. Structure optimization of polycaprolactone foams by using mixtures of CO₂ and N₂ as blowing agents. *Polymer Engineering and Science*. 2005;45:432-41.
- [28] Reignier J, Huneault MA. Preparation of interconnected poly(epsilon-caprolactone) porous scaffolds by a combination of polymer and salt particulate leaching. *Polymer*. 2006;47:4703-17.
- [29] Grenier S, Sandig M, Mequanint K. Polyurethane biomaterials for fabricating 3D porous scaffolds and supporting vascular cells. *Journal of Biomedical Materials Research Part A*. 2007;82A:802-9.
- [30] Hou QP, Grijpma DW, Feijen J. Porous polymeric structures for tissue engineering prepared by a coagulation, compression moulding and salt leaching technique. *Biomaterials*. 2003;24:1937-47.
- [31] Murphy WL, Dennis RG, Kileny JL, Mooney DJ. Salt fusion: An approach to improve pore interconnectivity within tissue engineering scaffolds. *Tissue Engineering*. 2002;8:43-52.
- [32] Yang Q, Chen L, Shen XY, Tan ZQ. Preparation of polycaprolactone tissue engineering scaffolds by improved solvent casting/particulate leaching method. *Journal of Macromolecular Science Part B-Physics*. 2006;45:1171-81.
- [33] Coombes AG, Rizzi SC, Williamson M, Barralet JE, Downes S, Wallace WA. Precipitation casting of polycaprolactone for applications in tissue engineering and drug delivery. *Biomaterials*. 2004;25:315-25.
- [34] Wutticharoenmongkol P, Sanchavanakit N, Pavasant P, Supaphol P. Preparation and characterization of novel bone scaffolds based on electrospun polycaprolactone fibers filled with nanoparticles. *Macromol Biosci*. 2006;6:70-7.
- [35] Izquierdo R, Garcia-Giralt N, Rodriguez MT, Caceres E, Garcia SJ, Gomez Ribelles JL, et al. Biodegradable PCL scaffolds with an interconnected spherical pore network for tissue engineering. *Journal of biomedical materials research Part A*. 2008;85:25-35.
- [36] Lebourg M, Sabater Serra R, Mas Estelles J, Hernandez Sanchez F, Gomez Ribelles JL, Suay Anton J. Biodegradable polycaprolactone scaffold with controlled porosity obtained by modified particle-leaching technique. *Journal of materials science Materials in medicine*. 2008;19:2047-53.
- [37] Hou Q, Grijpma DW, Feijen J. Preparation of interconnected highly porous polymeric structures by a replication and freeze-drying process. *J Biomed Mater Res B Appl Biomater*. 2003;67:732-40.
- [38] Draghi L, Resta S, Pirozzolo MG, Tanzi MC. Microspheres leaching for scaffold porosity control. *Journal of materials science Materials in medicine*. 2005;16:1093-7.

- [39] Thein-Han WW, Misra RDK. Biomimetic chitosan-nanohydroxyapatite composite scaffolds for bone tissue engineering. *Acta Biomaterialia*. 2009;5:1182-97.
- [40] Mancini L, Tamma R, Settanni M, Camerino C, Patano N, Greco G, et al. Osteoblasts cultured on three-dimensional synthetic hydroxyapatite implanted on a chick allantochorial membrane induce ectopic bone marrow differentiation. *Annals of the New York Academy of Sciences*. 2007;1116:306-15.
- [41] Ghibaud M, Trichet L, Le Digabel J, Richert A, Hersen P, Ladoux B. Substrate topography induces a crossover from 2D to 3D behavior in fibroblast migration. *Biophysical Journal*. 2009;97:357-68.
- [42] Jaquiere C, Schaeren S, Farhadi J, Mainil-Varlet P, Kunz C, Zeilhofer HF, et al. In vitro osteogenic differentiation and in vivo bone-forming capacity of human isogenic jaw periosteal cells and bone marrow stromal cells. *Annals of Surgery*. 2005;242:859-67, discussion 67-8.
- [43] Coxon FP, Rogers MJ, Crockett JC. Isolation and purification of rabbit osteoclasts. *Methods in Molecular Biology*. 2012;816:145-58.
- [44] Laurencin CT, Khan Y, Kofron M, El-Amin S, Botchwey E, Yu X, et al. The ABJS Nicolas Andry Award: Tissue engineering of bone and ligament: a 15-year perspective. *Clinical Orthopaedics and Related Research*. 2006;447:221-36.
- [45] Bauer TW, Muschler GF. Bone graft materials. An overview of the basic science. *Clinical Orthopaedics and Related Research*. 2000;371:10-27.
- [46] LeGeros RZ. Properties of osteoconductive biomaterials: calcium phosphates. *Clinical Orthopaedics and Related Research*. 2002;395:81-98.

APPENDIX A

Copyright Permissions



MINERALOGICAL SOCIETY OF AMERICA

3635 Concorde Pkwy Ste 500 • Chantilly VA
20151-1110 • USA
Tel: 1 (703) 652-9950 • Fax: 1 (703) 652-9951 • Internet:
www.minsocam.org

September 13, 2012

Daniel O. Costa
The University of Western Ontario

Dear Mr. Costa:

I received your e-mail message of 2012-09-13 requesting permission to reproduce the following figure in your thesis, *Calcium Phosphate Based Resorbable Biomaterials for Bone Regeneration*, at the University of Western Ontario:

□ Figure 2 from Jill D. Pasteris, Brigitte Wopenka, and Eugenia Valsami-Jones, Phosphates and Global Sustainability: Bone and Tooth Mineralization: Why Apatite?, *ELEMENTS*, April 2008, v. 4, p. (2): 97-104

It is with pleasure that we grant you permission to reproduce this figure without cost on the condition that the authors are properly cited and that reference is given to the original publication of the Mineralogical Society of America.

Sincerely,

J. Alexander Speer
Executive Director, MSA

**ELSEVIER LICENSE
TERMS AND CONDITIONS**

Sep 13, 2012

This is a License Agreement between Daniel Costa ("You") and Elsevier ("Elsevier") provided by Copyright Clearance Center ("CCC"). The license consists of your order details, the terms and conditions provided by Elsevier, and the payment terms and conditions.

All payments must be made in full to CCC. For payment instructions, please see information listed at the bottom of this form.

Supplier	Elsevier Limited The Boulevard, Langford Lane Kidlington, Oxford, OX5 1GB, UK
Registered Company Number	1982084
Customer name	Daniel Costa
Customer address	The University of Western Ontario London, ON N6A 5C1
License number	2987180229883
License date	Sep 13, 2012
Licensed content publisher	Elsevier
Licensed content publication	Bone
Licensed content title	Unique alignment and texture of biological apatite crystallites in typical calcified tissues analyzed by microbeam x-ray diffractometer system
Licensed content author	T Nakano, K Kaibara, Y Tabata, N Nagata, S Enomoto, E Marukawa, Y Umakoshi
Licensed content date	October 2002
Licensed content volume number	31
Licensed content issue number	4
Number of pages	9
Start Page	479
End Page	487
Type of Use	reuse in a thesis/dissertation
Portion	figures/tables/illustrations
Number of figures/tables/illustrations	1
Format	both print and electronic

9/13/12

Rightslink Printable License

Are you the author of this Elsevier article?	No
Will you be translating?	No
Order reference number	
Title of your thesis/dissertation	Calcium Phosphate-Based Resorbable Biomaterials for Bone Regeneration
Expected completion date	Oct 2012
Estimated size (number of pages)	250
Elsevier VAT number	GB 494 6272 12
Permissions price	0.00 USD
VAT/Local Sales Tax	0.0 USD / 0.0 GBP
Total	0.00 USD
Terms and Conditions	

INTRODUCTION

1. The publisher for this copyrighted material is Elsevier. By clicking "accept" in connection with completing this licensing transaction, you agree that the following terms and conditions apply to this transaction (along with the Billing and Payment terms and conditions established by Copyright Clearance Center, Inc. ("CCC"), at the time that you opened your Rightslink account and that are available at any time at <http://myaccount.copyright.com>).

GENERAL TERMS

2. Elsevier hereby grants you permission to reproduce the aforementioned material subject to the terms and conditions indicated.

3. Acknowledgement: If any part of the material to be used (for example, figures) has appeared in our publication with credit or acknowledgement to another source, permission must also be sought from that source. If such permission is not obtained then that material may not be included in your publication/copies. Suitable acknowledgement to the source must be made, either as a footnote or in a reference list at the end of your publication, as follows:

“Reprinted from Publication title, Vol /edition number, Author(s), Title of article / title of chapter, Pages No., Copyright (Year), with permission from Elsevier [OR APPLICABLE SOCIETY COPYRIGHT OWNER].” Also Lancet special credit - “Reprinted from The Lancet, Vol. number, Author(s), Title of article, Pages No., Copyright (Year), with permission from Elsevier.”

4. Reproduction of this material is confined to the purpose and/or media for which permission is hereby given.

5. Altering/Modifying Material: Not Permitted. However figures and illustrations may be altered/adapted minimally to serve your work. Any other abbreviations, additions, deletions and/or any other alterations shall be made only with prior written authorization of Elsevier Ltd. (Please contact Elsevier at permissions@elsevier.com)

<https://s100.copyright.com/AppDispatchServlet>

2/5

6. If the permission fee for the requested use of our material is waived in this instance, please be advised that your future requests for Elsevier materials may attract a fee.
7. **Reservation of Rights:** Publisher reserves all rights not specifically granted in the combination of (i) the license details provided by you and accepted in the course of this licensing transaction, (ii) these terms and conditions and (iii) CCC's Billing and Payment terms and conditions.
8. **License Contingent Upon Payment:** While you may exercise the rights licensed immediately upon issuance of the license at the end of the licensing process for the transaction, provided that you have disclosed complete and accurate details of your proposed use, no license is finally effective unless and until full payment is received from you (either by publisher or by CCC) as provided in CCC's Billing and Payment terms and conditions. If full payment is not received on a timely basis, then any license preliminarily granted shall be deemed automatically revoked and shall be void as if never granted. Further, in the event that you breach any of these terms and conditions or any of CCC's Billing and Payment terms and conditions, the license is automatically revoked and shall be void as if never granted. Use of materials as described in a revoked license, as well as any use of the materials beyond the scope of an unrevoked license, may constitute copyright infringement and publisher reserves the right to take any and all action to protect its copyright in the materials.
9. **Warranties:** Publisher makes no representations or warranties with respect to the licensed material.
10. **Indemnity:** You hereby indemnify and agree to hold harmless publisher and CCC, and their respective officers, directors, employees and agents, from and against any and all claims arising out of your use of the licensed material other than as specifically authorized pursuant to this license.
11. **No Transfer of License:** This license is personal to you and may not be sublicensed, assigned, or transferred by you to any other person without publisher's written permission.
12. **No Amendment Except in Writing:** This license may not be amended except in a writing signed by both parties (or, in the case of publisher, by CCC on publisher's behalf).
13. **Objection to Contrary Terms:** Publisher hereby objects to any terms contained in any purchase order, acknowledgment, check endorsement or other writing prepared by you, which terms are inconsistent with these terms and conditions or CCC's Billing and Payment terms and conditions. These terms and conditions, together with CCC's Billing and Payment terms and conditions (which are incorporated herein), comprise the entire agreement between you and publisher (and CCC) concerning this licensing transaction. In the event of any conflict between your obligations established by these terms and conditions and those established by CCC's Billing and Payment terms and conditions, these terms and conditions shall control.
14. **Revocation:** Elsevier or Copyright Clearance Center may deny the permissions described in this License at their sole discretion, for any reason or no reason, with a full refund payable to you. Notice of such denial will be made using the contact information provided by you. Failure to receive such notice will not alter or invalidate the denial. In no event will Elsevier or Copyright Clearance Center be responsible or liable for any costs, expenses or damage

incurred by you as a result of a denial of your permission request, other than a refund of the amount(s) paid by you to Elsevier and/or Copyright Clearance Center for denied permissions.

LIMITED LICENSE

The following terms and conditions apply only to specific license types:

15. **Translation:** This permission is granted for non-exclusive world **English** rights only unless your license was granted for translation rights. If you licensed translation rights you may only translate this content into the languages you requested. A professional translator must perform all translations and reproduce the content word for word preserving the integrity of the article. If this license is to re-use 1 or 2 figures then permission is granted for non-exclusive world rights in all languages.

16. **Website:** The following terms and conditions apply to electronic reserve and author websites:

Electronic reserve: If licensed material is to be posted to website, the web site is to be password-protected and made available only to bona fide students registered on a relevant course if:

This license was made in connection with a course,

This permission is granted for 1 year only. You may obtain a license for future website posting,

All content posted to the web site must maintain the copyright information line on the bottom of each image,

A hyper-text must be included to the Homepage of the journal from which you are licensing at <http://www.sciencedirect.com/science/journal/xxxxx> or the Elsevier homepage for books at <http://www.elsevier.com> , and

Central Storage: This license does not include permission for a scanned version of the material to be stored in a central repository such as that provided by Heron/XanEdu.

17. **Author website** for journals with the following additional clauses:

All content posted to the web site must maintain the copyright information line on the bottom of each image, and the permission granted is limited to the personal version of your paper. You are not allowed to download and post the published electronic version of your article (whether PDF or HTML, proof or final version), nor may you scan the printed edition to create an electronic version. A hyper-text must be included to the Homepage of the journal from which you are licensing at <http://www.sciencedirect.com/science/journal/xxxxx> . As part of our normal production process, you will receive an e-mail notice when your article appears on Elsevier's online service ScienceDirect (www.sciencedirect.com). That e-mail will include the article's Digital Object Identifier (DOI). This number provides the electronic link to the published article and should be included in the posting of your personal version. We ask that you wait until you receive this e-mail and have the DOI to do any posting.

Central Storage: This license does not include permission for a scanned version of the material to be stored in a central repository such as that provided by Heron/XanEdu.

18. **Author website** for books with the following additional clauses:

Authors are permitted to place a brief summary of their work online only.

A hyper-text must be included to the Elsevier homepage at <http://www.elsevier.com> . All content posted to the web site must maintain the copyright information line on the bottom of each image. You are not allowed to download and post the published electronic version of your chapter, nor may you scan the printed edition to create an electronic version.

Central Storage: This license does not include permission for a scanned version of the material to be stored in a central repository such as that provided by Heron/XanEdu.

19. **Website** (regular and for author): A hyper-text must be included to the Homepage of the journal from which you are licensing at <http://www.sciencedirect.com/science/journal/xxxx>. or for books to the Elsevier homepage at <http://www.elsevier.com>

20. **Thesis/Dissertation**: If your license is for use in a thesis/dissertation your thesis may be submitted to your institution in either print or electronic form. Should your thesis be published commercially, please reapply for permission. These requirements include permission for the Library and Archives of Canada to supply single copies, on demand, of the complete thesis and include permission for UMI to supply single copies, on demand, of the complete thesis. Should your thesis be published commercially, please reapply for permission.

21. **Other Conditions**:

v1.6

If you would like to pay for this license now, please remit this license along with your payment made payable to "COPYRIGHT CLEARANCE CENTER" otherwise you will be invoiced within 48 hours of the license date. Payment should be in the form of a check or money order referencing your account number and this invoice number RLNK500857059.

Once you receive your invoice for this order, you may pay your invoice by credit card. Please follow instructions provided at that time.

Make Payment To:
Copyright Clearance Center
Dept 001
P.O. Box 843006
Boston, MA 02284-3006

For suggestions or comments regarding this order, contact RightsLink Customer Support: customercare@copyright.com or +1-877-622-5543 (toll free in the US) or +1-978-646-2777.

Gratis licenses (referencing \$0 in the Total field) are free. Please retain this printable license for your reference. No payment is required.

**ELSEVIER LICENSE
TERMS AND CONDITIONS**

Sep 13, 2012

This is a License Agreement between Daniel Costa ("You") and Elsevier ("Elsevier") provided by Copyright Clearance Center ("CCC"). The license consists of your order details, the terms and conditions provided by Elsevier, and the payment terms and conditions.

All payments must be made in full to CCC. For payment instructions, please see information listed at the bottom of this form.

Supplier	Elsevier Limited The Boulevard, Langford Lane Kidlington, Oxford, OX5 1GB, UK
Registered Company Number	1982084
Customer name	Daniel Costa
Customer address	The University of Western Ontario London, ON N6A 5C1
License number	2987180357994
License date	Sep 13, 2012
Licensed content publisher	Elsevier
Licensed content publication	Journal of Solid State Chemistry
Licensed content title	Crystal Structure of Calcium-Deficient Carbonated Hydroxyapatite. Thermal Decomposition
Licensed content author	T.I. Ivanova, O.V. Frank-Kamenetskaya, A.B. Kol'tsov, V.L. Ugolkov
Licensed content date	September 2001
Licensed content volume number	160
Licensed content issue number	2
Number of pages	10
Start Page	340
End Page	349
Type of Use	reuse in a thesis/dissertation
Intended publisher of new work	other
Portion	figures/tables/illustrations
Number of figures/tables/illustrations	1
Format	both print and electronic

9/13/12

Rightslink Printable License

Are you the author of this Elsevier article?	No
Will you be translating?	No
Order reference number	
Title of your thesis/dissertation	Calcium Phosphate-Based Resorbable Biomaterials for Bone Regeneration
Expected completion date	Oct 2012
Estimated size (number of pages)	250
Elsevier VAT number	GB 494 6272 12
Permissions price	0.00 USD
VAT/Local Sales Tax	0.0 USD / 0.0 GBP
Total	0.00 USD
Terms and Conditions	

INTRODUCTION

1. The publisher for this copyrighted material is Elsevier. By clicking "accept" in connection with completing this licensing transaction, you agree that the following terms and conditions apply to this transaction (along with the Billing and Payment terms and conditions established by Copyright Clearance Center, Inc. ("CCC"), at the time that you opened your Rightslink account and that are available at any time at <http://myaccount.copyright.com>).

GENERAL TERMS

2. Elsevier hereby grants you permission to reproduce the aforementioned material subject to the terms and conditions indicated.

3. Acknowledgement: If any part of the material to be used (for example, figures) has appeared in our publication with credit or acknowledgement to another source, permission must also be sought from that source. If such permission is not obtained then that material may not be included in your publication/copies. Suitable acknowledgement to the source must be made, either as a footnote or in a reference list at the end of your publication, as follows:

“Reprinted from Publication title, Vol /edition number, Author(s), Title of article / title of chapter, Pages No., Copyright (Year), with permission from Elsevier [OR APPLICABLE SOCIETY COPYRIGHT OWNER].” Also Lancet special credit - “Reprinted from The Lancet, Vol. number, Author(s), Title of article, Pages No., Copyright (Year), with permission from Elsevier.”

4. Reproduction of this material is confined to the purpose and/or media for which permission is hereby given.

5. Altering/Modifying Material: Not Permitted. However figures and illustrations may be altered/adapted minimally to serve your work. Any other abbreviations, additions, deletions and/or any other alterations shall be made only with prior written authorization of Elsevier Ltd. (Please contact Elsevier at permissions@elsevier.com)

<https://s100.copyright.com/AppDispatchServlet>

2/5

6. If the permission fee for the requested use of our material is waived in this instance, please be advised that your future requests for Elsevier materials may attract a fee.
7. **Reservation of Rights:** Publisher reserves all rights not specifically granted in the combination of (i) the license details provided by you and accepted in the course of this licensing transaction, (ii) these terms and conditions and (iii) CCC's Billing and Payment terms and conditions.
8. **License Contingent Upon Payment:** While you may exercise the rights licensed immediately upon issuance of the license at the end of the licensing process for the transaction, provided that you have disclosed complete and accurate details of your proposed use, no license is finally effective unless and until full payment is received from you (either by publisher or by CCC) as provided in CCC's Billing and Payment terms and conditions. If full payment is not received on a timely basis, then any license preliminarily granted shall be deemed automatically revoked and shall be void as if never granted. Further, in the event that you breach any of these terms and conditions or any of CCC's Billing and Payment terms and conditions, the license is automatically revoked and shall be void as if never granted. Use of materials as described in a revoked license, as well as any use of the materials beyond the scope of an unrevoked license, may constitute copyright infringement and publisher reserves the right to take any and all action to protect its copyright in the materials.
9. **Warranties:** Publisher makes no representations or warranties with respect to the licensed material.
10. **Indemnity:** You hereby indemnify and agree to hold harmless publisher and CCC, and their respective officers, directors, employees and agents, from and against any and all claims arising out of your use of the licensed material other than as specifically authorized pursuant to this license.
11. **No Transfer of License:** This license is personal to you and may not be sublicensed, assigned, or transferred by you to any other person without publisher's written permission.
12. **No Amendment Except in Writing:** This license may not be amended except in a writing signed by both parties (or, in the case of publisher, by CCC on publisher's behalf).
13. **Objection to Contrary Terms:** Publisher hereby objects to any terms contained in any purchase order, acknowledgment, check endorsement or other writing prepared by you, which terms are inconsistent with these terms and conditions or CCC's Billing and Payment terms and conditions. These terms and conditions, together with CCC's Billing and Payment terms and conditions (which are incorporated herein), comprise the entire agreement between you and publisher (and CCC) concerning this licensing transaction. In the event of any conflict between your obligations established by these terms and conditions and those established by CCC's Billing and Payment terms and conditions, these terms and conditions shall control.
14. **Revocation:** Elsevier or Copyright Clearance Center may deny the permissions described in this License at their sole discretion, for any reason or no reason, with a full refund payable to you. Notice of such denial will be made using the contact information provided by you. Failure to receive such notice will not alter or invalidate the denial. In no event will Elsevier or Copyright Clearance Center be responsible or liable for any costs, expenses or damage

incurred by you as a result of a denial of your permission request, other than a refund of the amount(s) paid by you to Elsevier and/or Copyright Clearance Center for denied permissions.

LIMITED LICENSE

The following terms and conditions apply only to specific license types:

15. **Translation:** This permission is granted for non-exclusive world **English** rights only unless your license was granted for translation rights. If you licensed translation rights you may only translate this content into the languages you requested. A professional translator must perform all translations and reproduce the content word for word preserving the integrity of the article. If this license is to re-use 1 or 2 figures then permission is granted for non-exclusive world rights in all languages.

16. **Website:** The following terms and conditions apply to electronic reserve and author websites:

Electronic reserve: If licensed material is to be posted to website, the web site is to be password-protected and made available only to bona fide students registered on a relevant course if:

This license was made in connection with a course,

This permission is granted for 1 year only. You may obtain a license for future website posting,

All content posted to the web site must maintain the copyright information line on the bottom of each image,

A hyper-text must be included to the Homepage of the journal from which you are licensing at <http://www.sciencedirect.com/science/journal/xxxxx> or the Elsevier homepage for books at <http://www.elsevier.com> , and

Central Storage: This license does not include permission for a scanned version of the material to be stored in a central repository such as that provided by Heron/XanEdu.

17. **Author website** for journals with the following additional clauses:

All content posted to the web site must maintain the copyright information line on the bottom of each image, and the permission granted is limited to the personal version of your paper. You are not allowed to download and post the published electronic version of your article (whether PDF or HTML, proof or final version), nor may you scan the printed edition to create an electronic version. A hyper-text must be included to the Homepage of the journal from which you are licensing at <http://www.sciencedirect.com/science/journal/xxxxx> . As part of our normal production process, you will receive an e-mail notice when your article appears on Elsevier's online service ScienceDirect (www.sciencedirect.com). That e-mail will include the article's Digital Object Identifier (DOI). This number provides the electronic link to the published article and should be included in the posting of your personal version. We ask that you wait until you receive this e-mail and have the DOI to do any posting.

Central Storage: This license does not include permission for a scanned version of the material to be stored in a central repository such as that provided by Heron/XanEdu.

18. **Author website** for books with the following additional clauses:

Authors are permitted to place a brief summary of their work online only.

A hyper-text must be included to the Elsevier homepage at <http://www.elsevier.com> . All content posted to the web site must maintain the copyright information line on the bottom of each image. You are not allowed to download and post the published electronic version of your chapter, nor may you scan the printed edition to create an electronic version.

Central Storage: This license does not include permission for a scanned version of the material to be stored in a central repository such as that provided by Heron/XanEdu.

19. **Website** (regular and for author): A hyper-text must be included to the Homepage of the journal from which you are licensing at <http://www.sciencedirect.com/science/journal/xxxx>. or for books to the Elsevier homepage at <http://www.elsevier.com>

20. **Thesis/Dissertation**: If your license is for use in a thesis/dissertation your thesis may be submitted to your institution in either print or electronic form. Should your thesis be published commercially, please reapply for permission. These requirements include permission for the Library and Archives of Canada to supply single copies, on demand, of the complete thesis and include permission for UMI to supply single copies, on demand, of the complete thesis. Should your thesis be published commercially, please reapply for permission.

21. **Other Conditions**:

v1.6

If you would like to pay for this license now, please remit this license along with your payment made payable to "COPYRIGHT CLEARANCE CENTER" otherwise you will be invoiced within 48 hours of the license date. Payment should be in the form of a check or money order referencing your account number and this invoice number RLNK500857061.

Once you receive your invoice for this order, you may pay your invoice by credit card. Please follow instructions provided at that time.

**Make Payment To:
Copyright Clearance Center
Dept 001
P.O. Box 843006
Boston, MA 02284-3006**

For suggestions or comments regarding this order, contact RightsLink Customer Support: customercare@copyright.com or +1-877-622-5543 (toll free in the US) or +1-978-646-2777.

Gratis licenses (referencing \$0 in the Total field) are free. Please retain this printable license for your reference. No payment is required.

**NATURE PUBLISHING GROUP LICENSE
TERMS AND CONDITIONS**

Sep 13, 2012

This is a License Agreement between Daniel Costa ("You") and Nature Publishing Group ("Nature Publishing Group") provided by Copyright Clearance Center ("CCC"). The license consists of your order details, the terms and conditions provided by Nature Publishing Group, and the payment terms and conditions.

All payments must be made in full to CCC. For payment instructions, please see information listed at the bottom of this form.

License Number	2987370089835
License date	Sep 13, 2012
Licensed content publisher	Nature Publishing Group
Licensed content publication	IBMS BonekEy
Licensed content title	Cathepsin K - A new molecular target for osteoporosis
Licensed content author	Sevgi B Rodan, Le T Duong
Licensed content date	Jan 1, 2008
Volume number	5
Issue number	1
Type of Use	reuse in a thesis/dissertation
Requestor type	academic/educational
Format	print and electronic
Portion	figures/tables/illustrations
Number of figures/tables/illustrations	1
High-res required	no
Figures	Figure 1
Author of this NPG article	no
Your reference number	
Title of your thesis / dissertation	Calcium Phosphate-Based Resorbable Biomaterials for Bone Regeneration
Expected completion date	Oct 2012
Estimated size (number of pages)	250
Total	0.00 USD
Terms and Conditions	Terms and Conditions for Permissions

Nature Publishing Group hereby grants you a non-exclusive license to reproduce this material for this purpose, and for no other use, subject to the conditions below:

1. NPG warrants that it has, to the best of its knowledge, the rights to license reuse of this material. However, you should ensure that the material you are requesting is original to Nature Publishing Group and does not carry the copyright of another entity (as credited in the published version). If the credit line on any part of the material you have requested indicates that it was reprinted or adapted by NPG with permission from another source, then you should also seek permission from that source to reuse the material.
 2. Permission granted free of charge for material in print is also usually granted for any electronic version of that work, provided that the material is incidental to the work as a whole and that the electronic version is essentially equivalent to, or substitutes for, the print version. Where print permission has been granted for a fee, separate permission must be obtained for any additional, electronic re-use (unless, as in the case of a full paper, this has already been accounted for during your initial request in the calculation of a print run). NB: In all cases, web-based use of full-text articles must be authorized separately through the 'Use on a Web Site' option when requesting permission.
 3. Permission granted for a first edition does not apply to second and subsequent editions and for editions in other languages (except for signatories to the STM Permissions Guidelines, or where the first edition permission was granted for free).
 4. Nature Publishing Group's permission must be acknowledged next to the figure, table or abstract in print. In electronic form, this acknowledgement must be visible at the same time as the figure/table/abstract, and must be hyperlinked to the journal's homepage.
 5. The credit line should read:
 Reprinted by permission from Macmillan Publishers Ltd: [JOURNAL NAME]
 (reference citation), copyright (year of publication)
 For AOP papers, the credit line should read:
 Reprinted by permission from Macmillan Publishers Ltd: [JOURNAL NAME],
 advance online publication, day month year (doi: 10.1038/sj.[JOURNAL
 ACRONYM].XXXXX)
- Note: For republication from the *British Journal of Cancer*, the following credit lines apply.**
 Reprinted by permission from Macmillan Publishers Ltd on behalf of Cancer Research UK: [JOURNAL NAME] (reference citation), copyright (year of publication) For AOP papers, the credit line should read:
 Reprinted by permission from Macmillan Publishers Ltd on behalf of Cancer Research UK: [JOURNAL NAME], advance online publication, day month year (doi: 10.1038/sj.[JOURNAL ACRONYM].XXXXX)
6. Adaptations of single figures do not require NPG approval. However, the adaptation

should be credited as follows:

Adapted by permission from Macmillan Publishers Ltd: [JOURNAL NAME]
(reference citation), copyright (year of publication)

Note: For adaptation from the *British Journal of Cancer*, the following credit line applies.

Adapted by permission from Macmillan Publishers Ltd on behalf of Cancer Research UK: [JOURNAL NAME] (reference citation), copyright (year of publication)

7. Translations of 401 words up to a whole article require NPG approval. Please visit <http://www.macmillanmedicalcommunications.com> for more information. Translations of up to a 400 words do not require NPG approval. The translation should be credited as follows:

Translated by permission from Macmillan Publishers Ltd: [JOURNAL NAME]
(reference citation), copyright (year of publication).

Note: For translation from the *British Journal of Cancer*, the following credit line applies.

Translated by permission from Macmillan Publishers Ltd on behalf of Cancer Research UK: [JOURNAL NAME] (reference citation), copyright (year of publication)

We are certain that all parties will benefit from this agreement and wish you the best in the use of this material. Thank you.

Special Terms:

v1.1

If you would like to pay for this license now, please remit this license along with your payment made payable to "COPYRIGHT CLEARANCE CENTER" otherwise you will be invoiced within 48 hours of the license date. Payment should be in the form of a check or money order referencing your account number and this invoice number RLNK500857313.

Once you receive your invoice for this order, you may pay your invoice by credit card. Please follow instructions provided at that time.

**Make Payment To:
Copyright Clearance Center
Dept 001
P.O. Box 843006
Boston, MA 02284-3006**

For suggestions or comments regarding this order, contact RightsLink Customer Support: customercare@copyright.com or +1-877-622-5543 (toll free in the US) or +1-978-646-2777.

Gratis licenses (referencing \$0 in the Total field) are free. Please retain this printable license for your reference. No payment is required.

MDPI Journals A-Z For Authors About Open Access Policy Submit My Manuscript Login Register


 Title / Keyword Journal Volume
 Author Section Issue
 Article Type Special Issue Page

MDPI Open Access Information and Policy

All articles published by MDPI are made available under an open access license worldwide immediately. This means:

everyone has free and unlimited access to the full-text of all articles published in MDPI journals, and everyone is free to re-use the published material given proper accreditation/citation of the original publication. open access publication is supported by authors' institutes or research funding agency by payment of a comparatively low Article Processing Charge (APC) for accepted articles.

External Open Access Resources

MDPI is a [RoMEO green publisher](#) — RoMEO is a database of Publishers' copyright and self-archiving policies hosted by the [University of Nottingham](#)

If you are new to the concept of open access, you may visit one of the following websites or watch the below 'Open Access 101' video:

[Wikipedia article on 'Open Access'](#)
[Peter Suber's 'Open Access Overview'](#)
[Information Platform Open Access \[in English, in German\]](#)
[SHERPA's 'Authors and Open Access'](#)

Meaning of Open Access

In MDPI's understanding, which is in accordance with major definitions of open access to scientific literature (namely the Budapest, Berlin and Bethesda declarations), *open access* means:

- peer-reviewed literature is freely available without subscription or price barriers,
- literature is immediately released in open access format (no embargo period), and
- published material can be re-used without obtaining permission as long as a correct citation to the original publication is given.

Up to 2008 most articles published by MDPI contained the note "© year by MDPI (<http://www.mdpi.org>). Reproduction is permitted for noncommercial purposes". During 2008 MDPI journals started to publish articles under the [Creative Commons Attribution License](#). However, all articles published by MDPI before and during 2008 should be considered as released under the same Creative Commons Attribution License since 2008.

This means that all articles published in MDPI journals, including data, graphics and supplements, can be linked from outside in, crawled by search engines, re-used by text mining applications or websites, blogs, etc. free of charge under the sole condition of proper accreditation of the source and original Publisher. MDPI believes that open access publishing can foster the exchange of research results amongst scientists from different disciplines, thus facilitating interdisciplinary research, whilst providing access to research results to researchers world-wide, including from developing countries, as well as to an interested general public. Although MDPI publishes all of its journals under the open access model, we believe that open access is an enriching part of the scholarly communication process that can and should co-exist with other forms of communication and publication, such as society-based publishing and conferencing activities.

Important Note: some articles (especially *Reviews*) may contain figures, tables or text taken from other publications, for which MDPI does not hold the copyright or the right to re-license the published material. Please note that you should inquire with the original copyright holder (usually the original Publisher or the original authors), if this material can be further re-used.

Advantages of Open Access for Authors

High Availability and High Visibility of open access articles is guaranteed through the free and unlimited accessibility of the publication over the Internet without any restrictions. Everyone can freely access and download the full-text of all articles published with MDPI. Readers, mostly other researchers, of open access journals do not need to pay any subscription or pay-per-view charges to read articles published by MDPI. open access publications are also more easily included and searchable in search engines and indexing databases.

Higher Citation Impact of open access articles due to their high publicity and availability. It has been demonstrated that open access publications are more frequently cited [1,2].

Less Costly — Open Access Publishers cover their costs for editorial handling and editing of a paper by charging authors' institutes or research funding agency. The cost of handling and the production of an article is covered through the one-time payment of an **Article Processing Charge (APC)** for each accepted article. The APC of Open Access Publishers are only a fraction of the average income per paper that traditional, subscription-based Publishers have been earning. MDPI's **Article Processing Charge (APC)** is regardless of the length of an article, because we wish to encourage publication of long papers with complete results and full experimental or computational details [3].

Faster Publication in MDPI's open access journals is achieved by the online-only availability. Accepted articles are typically published online more rapidly in MDPI journals than traditional, subscription-based and printed journals [4].

Links and Notes

1. Open access citation impact advantage: http://en.wikipedia.org/wiki/Open_access#Authors_and_researchers. For example, a standard research paper "Shutalev, A.D.; Kishko, E.A.; Sivova, N.V.; Kuznetsov, A.Y. *Molecules* **1998**, *3*, 100-106" has been cited 51 times, the highest number among

SPARC Open Access 101 Video



8/24/12

Rightslink® by Copyright Clearance Center



RightsLink®

Home

Create Account

Help

ACS Publications
High quality. High impact.

Title: One- and Three-Dimensional Growth of Hydroxyapatite Nanowires during Sol-Gel-Hydrothermal Synthesis

Author: Daniel O. Costa, S. Jeffrey Dixon, and Amin S. Rizkalla

Publication: Applied Materials

Publisher: American Chemical Society

Date: Mar 1, 2012

Copyright © 2012, American Chemical Society

User ID
<input type="text"/>
Password
<input type="text"/>
<input type="checkbox"/> Enable Auto Login
<input type="button" value="LOGIN"/>
Forgot Password/User ID?
If you're a copyright.com user , you can login to RightsLink using your copyright.com credentials. Already a RightsLink user or want to learn more?

PERMISSION/LICENSE IS GRANTED FOR YOUR ORDER AT NO CHARGE

This type of permission/license, instead of the standard Terms & Conditions, is sent to you because no fee is being charged for your order. Please note the following:

- Permission is granted for your request in both print and electronic formats, and translations.
- If figures and/or tables were requested, they may be adapted or used in part.
- Please print this page for your records and send a copy of it to your publisher/graduate school.
- Appropriate credit for the requested material should be given as follows: "Reprinted (adapted) with permission from (COMPLETE REFERENCE CITATION). Copyright (YEAR) American Chemical Society." Insert appropriate information in place of the capitalized words.
- One-time permission is granted only for the use specified in your request. No additional uses are granted (such as derivative works or other editions). For any other uses, please submit a new request.

Copyright © 2012 [Copyright Clearance Center, Inc.](#) All Rights Reserved. [Privacy statement.](#)
Comments? We would like to hear from you. E-mail us at customercare@copyright.com

<https://s100.copyright.com/AppDispatchServlet>

1/1

8/24/12

Rightslink® by Copyright Clearance Center



RightsLink®

Home

Create Account

Help

ACS Publications
High quality. High impact.

Title: Control of Surface Topography in Biomimetic Calcium Phosphate Coatings

Author: Daniel O. Costa, Bedilu A. Allo, Robert Klassen, Jeffrey L. Hutter, S. Jeffrey Dixon, and Amin S. Rizkalla

Publication: Langmuir

Publisher: American Chemical Society

Date: Feb 1, 2012

Copyright © 2012, American Chemical Society

User ID
<input type="text"/>
Password
<input type="text"/>
<input type="checkbox"/> Enable Auto Login
<input type="button" value="LOGIN"/>
Forgot Password/User ID?
If you're a copyright.com user , you can login to RightsLink using your copyright.com credentials. Already a RightsLink user or want to learn more?

PERMISSION/LICENSE IS GRANTED FOR YOUR ORDER AT NO CHARGE

This type of permission/license, instead of the standard Terms & Conditions, is sent to you because no fee is being charged for your order. Please note the following:

- Permission is granted for your request in both print and electronic formats, and translations.
- If figures and/or tables were requested, they may be adapted or used in part.
- Please print this page for your records and send a copy of it to your publisher/graduate school.
- Appropriate credit for the requested material should be given as follows: "Reprinted (adapted) with permission from (COMPLETE REFERENCE CITATION). Copyright (YEAR) American Chemical Society." Insert appropriate information in place of the capitalized words.
- One-time permission is granted only for the use specified in your request. No additional uses are granted (such as derivative works or other editions). For any other uses, please submit a new request.

Copyright © 2012 [Copyright Clearance Center, Inc.](#) All Rights Reserved. [Privacy statement.](#)
Comments? We would like to hear from you. E-mail us at customercare@copyright.com

<https://s100.copyright.com/AppDispatchServlet>

1/1

APPENDIX B

Animal Ethics Approval

2008-097::2:

Submitted by IACUC:

Turner, Andrew M Protocol

Number: 2008-097.

Title: In Vitro and In Vivo Influence of Substratum Topography and Chemistry on

Osteoblast, Osteoclast, and Fibroblast Physiology

A YEARLY RENEWAL to Animal Use Protocol 2008-097 has been approved.

1. This number must be indicated when ordering animals for this project.
2. Animals for other projects may not be ordered under this number.
3. If no number appears please contact this office when grant approval is received. If the application for funding is not successful and you wish to proceed with the project, request that an internal scientific peer review be performed by the Animal Use Subcommittee office.
4. Purchases of animals other than through this system must be cleared through the ACVS office. Health certificates will be required.

REQUIREMENTS/COMMENTS

Please ensure that individual(s) performing procedures on live animals, as described in this protocol, are familiar with the contents of this document.

The holder of this Animal Use Protocol is responsible to ensure that all associated safety components (biosafety, radiation safety, general laboratory safety) comply with institutional safety standards and have received all necessary approvals. Please consult directly with your institutional safety officers.

Regards,
Animal Use Subcommittee

The University of Western Ontario
Animal Use Subcommittee / University Council on Animal Care
Health Sciences Centre, London, Ontario CANADA – N6A 5C1
<http://www.uwo.ca/animal/website/AUS/index.htm>



AUP Number: 2008---043---06

PI Name: Sims, Stephen M

AUP Title: Role Of Cytosolic Calcium In The Regulation Of Osteoclasts And Bone Resorption// Ion Transport And Signalling In Skeletal Cells: P2 Nucleotide Receptor Function In Bone

Approval Date: 08/08/2012

Official Notice of Animal Use Subcommittee (AUS) Approval: Your new Animal Use Protocol (AUP) entitled "Role Of Cytosolic Calcium In The Regulation Of Osteoclasts And Bone Resorption// Ion Transport And Signalling In Skeletal Cells: P2 Nucleotide Receptor Function In Bone

" has been APPROVED by the Animal Use Subcommittee of the University Council on Animal Care. This approval, although valid for four years, and is subject to annual Protocol Renewal.2008-043-06::5

1. This AUP number must be indicated when ordering animals for this project.
2. Animals for other projects may not be ordered under this AUP number.
3. Purchases of animals other than through this system must be cleared through the ACVS office. Health certificates will be required.

The holder of this Animal Use Protocol is responsible to ensure that all associated safety components (biosafety, radiation safety, general laboratory safety) comply with institutional safety standards and have received all necessary approvals. Please consult directly with your institutional safety officers.

Submitted by: Copeman, Laura
on behalf of the Animal Use Subcommittee
University Council on Animal Care

CURRICULUM VITAE

Contact Information

Last Name Costa
 First Name Daniel O.
 Position Graduate Student, Ph.D. candidate

Office address: Biomaterial Science Laboratory
 Department of Chemical and Biochemical Engineering
 Faculty of Engineering
 The University of Western Ontario
 London, Ontario, Canada, N6A 5C1

Post-secondary Education and Degrees

2006-2012 Ph.D. candidate, Chemical and Biochemical Engineering
 The University of Western Ontario
 London, Ontario Canada
 Supervisors: Dr. Amin S. Rizkalla and Dr. S. Jeffrey Dixon

2002-2006 B.E.Sc., Chemical and Biochemical Engineering
 The University of Western Ontario
 London, Ontario, Canada

Honours and Awards

2010-2011 CIHR Ph.D. Graduate fellow in Musculoskeletal Health Research
 2006-2011 Western Graduate Research Scholarship
 2009-2010 Province of Ontario Graduate Scholarship in Science and Technology
 (OGSST)
 2005, 2006 Undergraduate Deans Honor List

Related Work Experience

2006-2011 Teaching Assistant
 Engineering Thermodynamics, Engineering Communications, Chemical Engineering
 Thermodynamics, Plant Design and Safety, Introduction to Biomaterials
 The University of Western Ontario

2006-2012 Research Assistant
 Biomaterial Science Laboratory and Bone Physiology Laboratory
 The University of Western Ontario

Publications

1. **Costa, D. O.**, Allo, B. A., Klassen, R., Hutter, J. L., Dixon, S. J., and Rizkalla, A. S. Control of Surface Topography in Biomimetic Calcium Phosphate Coatings. *Langmuir*, 2012; 28(8), 3871-3880.
2. **Costa, D. O.**, Dixon, S. J., and Rizkalla, A. S. One- and three-dimensional growth of hydroxyapatite nanowires during sol-gel-hydrothermal synthesis. *ACS Applied Materials & Interfaces*, 2012; 4(3), 1490-1499.
3. Allo, B. A., **Costa, D. O.**,* Dixon, S. J., Mequanint, K., and Rizkalla, A. S. Bioactive and Biodegradable Nanocomposites and Hybrid Biomaterials for Bone Regeneration (Review). *Journal of Functional Biomaterials*, 2012; 3(2), 432-463.
 *Co-first author.

Submitted:

4. Saadaldin, S. A., **Costa, D. O.**, Dixon, S. J., Rizkalla, A. S. Synthesis of Bioactive and Machinable Miserite Glass-Ceramics for Dental Implant Applications.
5. **Costa, D. O.**, Prowse, P. H. D., Chrones, T., Hamilton, D., Rizkalla, A. S., and Dixon, S. J. Surface Topography of Biomimetic Hydroxyapatite Coating Differentially Regulates Osteoblast and Osteoclast Activity.

Conference Proceedings

1. **Costa, D. O.**, Dixon, S. J., and Rizkalla, A. S. Biomimetic Apatite Coatings on Polycaprolactone. *2009 Canadian Biomaterials Conference*. The University of Laval; Quebec City, Quebec, Canada. Selected for oral presentation.
2. **Costa, D. O.**, Hamilton, D., Dixon, S. J., and Rizkalla, A. S. Carbonated Hydroxyapatite Coatings on Polycaprolactone. *2009 Biomedical Engineering Society*. The University of Pittsburgh; Pittsburgh, Pennsylvania, U.S.A. Selected for poster presentation.
3. **Costa, D. O.**, Hamilton, D., Dixon, S. J., and Rizkalla, A. S. Hydroxyapatite Nano-wire Synthesis by a Sol-gel Hydrothermal Process. *2009 Biomedical Engineering Society*. The University of Pittsburgh; Pittsburgh, Pennsylvania, U.S.A. Selected for poster presentation.

4. **Costa, D. O.**, Dixon, S. J., and Rizkalla, A. S. Synthesis of Hydroxyapatite Nanowires. *2010 Canadian Biomaterials Conference*. Queens University; Kingston, Ontario, Canada. Selected for oral presentation.
5. **Costa, D. O.**, Prowse, P., Hamilton, D., Dixon, S. J., and Rizkalla, A. S. Surface Topography of Biomimetic Calcium Phosphate Coatings Regulates Osteoclastic Resorption. *2012 Canadian Connective Tissue Conference*. University of Toronto; Toronto, Ontario, Canada. Selected for poster presentation.